Iron electronic states in minerals of the Earth's mantle

---

eingereicht an der **Bayreuther Graduiertenschule für Mathematik und Naturwissenschaften (BayNAT)**

submitted to the **Bayreuth Graduate School of Mathematics and Natural Sciences (BayNAT)**

zur Erlangung der Würde eines Doktors der Naturwissenschaften
— Dr. rer. nat. —

Dissertation

vorgelegt durch

Denis Vasiukov

aus Tula (Russland)

Bayreuth, 2018

This doctoral thesis was prepared at the department of Crystallography at the University of Bayreuth from 02/2015 until 05/2018 and was supervised by Prof. Dr. Natalia Dubrovinskaia.

This is a full reprint of the dissertation submitted to obtain the academic degree of Doctor of Natural Sciences (Dr. rer. nat.) and approved by the Bayreuth Graduate School of Mathematical and Natural Sciences (BayNAT) of the University of Bayreuth.

Date of submission: 14.05.2018

Date of defence: 10.07.2018

Acting director: Prof. Dr. Dirk Schüler

Doctoral committee:

Prof. Dr. Leonid Dubrovinsky (reviewer)

Prof. Dr. Daniel Frost (reviewer)

Prof. Dr. Hans Keppler (chairman)

Dr. Gerd Steinle-Neumann

Summary

Iron is an important constituent of the Earth's silicate mantle. As one of the transition metal elements, iron can adopt different electronic states (i.e., oxidation, spin states, *etc.*) that gives rise to diverse behavior in mantle minerals at corresponding pressure-temperature conditions. The electronic state of iron can be influenced by important parameters of the mantle such as the conditions at which mantle minerals and their assemblies were formed (for example oxygen fugacity), and changes in the electronic state of iron can directly affect geophysical and geochemical properties of mantle assemblages (such as elasticity, element partitioning, diffusion, *etc.*). This PhD thesis focusses on to the evolution and changes of the electronic state of iron in important mantle minerals and their influence on mineral properties. In particular, the following problems have been studied:

- the effect of Fe^{3+} in the octahedral site (Y-site) on the sound velocities of garnet solid solutions,
- the iron oxidation state in majoritic garnet inclusions from diamond originating from the lowermost upper mantle and transition zone and estimation of the corresponding oxygen fugacities,
- systematics of the pressure-induced spin transition of Fe^{3+} in the oxygen coordination octahedron and correlations of hyperfine parameters with octahedron geometry,
- iron electronic state in bridgmanite synthesized *in situ* in a diamond anvil cell.

The high-pressure study of skiagite (77 mol. %)-iron-majorite garnet revealed that sound velocities are significantly lower than the sound velocities of the silicate garnet end-members, such as grossular, pyrope, Mg-majorite, andradite, and almandine. In addition, sound velocities of the two garnet end-members with Fe^{3+} in the Y-site, skiagite and khoharite, were estimated. The neglect of Fe^{3+} in the Y-site of the garnet structure may result in an overestimation of up to 1 % of the sound velocities of the garnet solid solution that are relevant to the mantle transition zone .

Thirteen garnet inclusions from diamonds of mantle origin were studied using Mössbauer spectroscopy and single-crystal X-ray diffraction. The studied garnet inclusions show a systematic increase of the iron oxidation state with increase of the formation depth. The determined oxygen fugacities appear to be higher than the stability field of Fe metal. This implies that the iron disproportionation reaction ($3Fe^{2+} \rightarrow 2Fe^{3+} + Fe^{0}$) cannot be responsible for the high Fe^{3+} content in the studied mantle garnets, but the hypothesis that carbonate was the oxidizing agent might be valid.

The comparative study of the spin transition in $Fe^{3+}O_6$ octahedra in $FeBO_3$, Fe_2O_3, $Fe_3(Fe_{1.766(2)}Si_{0.234(2)})(SiO_4)_3$, FeOOH, $CaFe_2O_4$ and $Ca_3Fe_2(SiO_4)_3$ showed that the spin transition of Fe^{3+} begins within a narrow range of octahedron volumes (8.9–9.3 $Å^3$). Taking into account the compressibility of the $Fe^{3+}O_6$ octahedra, this volume range corresponds to a 45–60 GPa pressure range. It was demonstrated that a simple model of an ideal octahedron based on crystal field theory predicts transition volumes with reasonable accuracy if the iron octahedron is not significantly distorted. It was found that, in the case of octahedral coordination, the center shift of high-spin iron depends linearly on octahedral volume with the same slope, independent of the oxidation state.

Spin transitions usually lead to an isosymmetric structural transition that can progress as either supercritical crossover or a first-order phase transition. The position of the critical point on the phase diagram is determined to a large extent by elastic interactions between ions in different spin states. Our experimental results suggest a cooperative behavior of iron ions at room temperature if iron octahedra share common oxygen atoms. As mantle minerals are solid solutions with relatively low concentrations of iron, the cooperative behavior of iron ions is unlikely. Therefore, the crossover behavior at iron spin transitions in Earth's mantle minerals is more probable, especially taking into account the high mantle temperatures at spin-transition pressures.

Experiments on the synthesis of bridgmanite in the laser-heated diamond anvil cell revealed that the $Fe^{3+}/\Sigma Fe$ ratio in bridgmanite depends on the iron oxidation state of the precursor that was used. We demonstrated that Fe^{3+} in bridgmanite is formed due to iron disproportionation in case of synthesis from a reduced precursor at pressures below 60 GPa. All products of the iron disproportionation reaction, including Fe metal, were identified *in situ*.

The $Fe^{3+}/\Sigma Fe$ ratio in bridgmanite synthesized from a reduced precursor at pressures between 35 and 60 GPa and $\sim$ 2400 K is about 25 %. In bridgmanite synthesized at 86 GPa and $\sim$ 2800 K, Fe^{3+} adopts the low-spin state and the $Fe^{3+}/\Sigma Fe$ ratio reaches 60 %. However, despite this high Fe^{3+} content, we could not detect the presence of Fe metal, which leaves open the question regarding the origin of the large amount of Fe^{3+}. We argue that the appearance of the doublet with extremely high quadrupole splitting in Mössbauer spectra of bridgmanite above 30 GPa is related not to the spin transition of Fe^{2+} in the pseudo-dodecahedral site, but to a transition between the non-degenerate and Jahn-Teller active electronic terms without any change in the spin quantum number.

Zusammenfassung

Eisen ist ein wichtiger Bestandteil des Silikatmantels der Erde. Als Übergangsmetall kann es unterschiedliche elektronische Zustände annehmen (*z.B.* Oxidationsstufe, Spinzustand, *usw.*), was in den Mantelmineralen bei entsprechenden Druck- und Temperaturbedingungen zu vielfältigem Verhalten führt. Der elektronische Zustand von Eisen wird von wichtigen Parametern des Mantels beeinflusst, wie etwa die Bedingungen, bei denen Mantelminerale und ihre Vergesellschaftungen geformt wurden (*z.B.* Sauerstofffugazität); Änderungen im elektronischen Zustand von Eisen kann direkt die geophysikalischen und geochemischen Eigenschaften der Mineralvergesellschaftungen im Mantel beeinflussen (*z.B.* Elastizität, Elementpartitionierung, Diffusion, *usw.*). Diese Dissertation richtet sich auf Entwicklung und Änderungen des elektronischen Zustands von Eisen in wichtigen Mantelmineralen und ihr Einfluss auf die Mineraleigenschaften. Insbesondere wurden folgende Probleme untersucht:

- Auswirkung von Fe^{3+} auf der Oktaederlage (Y-Lage) auf die Schallgeschwindigkeit in Granatmischkristallen,
- Eisen-Oxidationsstufe in Majorit-Granateinschlüssen in Diamant aus dem untersten Obermantel und der Übergangszone und die Abschätzung der entsprechenden Sauerstofffugazitäten,
- Systematik des druckinduzierten Spinübergangs von Fe^{3+} in oktaedrischer Sauerstoffkoordination und Korrelationen der Hyperfeinparameter mit der Oktaedergeometrie,
- elektronischer Zustand von Eisen im *in situ* in einer Diamantstempelzelle synthetisierten Bridgmanit.

Die Hochdruckstudie an Skiagit (77 mol. %)-Eisen-Majorit zeigte, dass die Schallgeschwindigkeiten signifikant niedriger sind, als bei Silikatgranatendgliedern wie Grossular, Pyrop, Mg-Majorit, Andradit und Almandin. Weiter wurden die Schallgeschwindigkeiten der zwei Endglieder mit Fe^{3+} auf der Y-Lage, Skiagit und Khoharit, abgeschätzt. Die Vernachlässigung von Fe^{3+} auf der Y-Lage kann zu einer Überschätzung der Schallgeschwindigkeit in Granatmischkristallen von bis zu 1 % führen, was für die Übergangszone relevant ist.

Dreizehn Granateinschlüsse aus Manteldiamanten wurden mittels Mößbauerspektroskopie und Einkristallröntgenstrahlbeugung untersucht. Die Granateinschlüsse zeigen eine zunehmende Eisen-Oxidationsstufe mit zunehmender Ursprungstiefe. Die ermittelten Sauerstofffugazitäten sind höher als das Stabilitätsfeld von metallischem Eisen erwarten lässt. Das bedeutet, dass die Eisen-Disproportionierung ($3Fe^{2+} \rightarrow 2Fe^{3+} + Fe^{0}$) nicht für den

hohen Fe^{3+} Gehalt in den untersuchten Mantelgranaten verantwortlich ist, sondern dass die Hypothese von Karbonaten als Oxidationsmittel richtig sein kann.

Die vergleichende Studie des Spinübergangs in $Fe^{3+}O_6$ Oktaedern in $FeBO_3$, Fe_2O_3, $Fe_3(Fe_{1.766(2)}Si_{0.234(2)})(SiO_4)_3$, FeOOH, $CaFe_2O_4$ und $Ca_3Fe_2(SiO_4)_3$ zeigte, dass der Spinübergang von Fe^{3+} in einem schmalen Bereich des Oktaedervolumens (8.9–9.3 $Å^3$) beginnt. Unter Berücksichtigung der Kompressibilität des $Fe^{3+}O_6$ Oktaeders entspricht dieses Volumen dem Druckbereich 45–60 GPa. Es zeigte sich, dass ein einfaches auf der Kristallfeldtheorie basierendes Modell des idealen Oktaeders die Übergangsvolumina mit guter Genauigkeit vorhersagt, wenn der Eisenoktaeder nicht signifikant verzerrt ist. Im Fall der Oktaederkoordination hängt die zentrale Verschiebung des High-Spin Eisens linear mit dem Oktaedervolumen zusammen, unabhängig von der Oxidationsstufe.

Spinübergänge führen gewöhnlich zu isosymmetrischen Strukturübergängen, entweder als superkritische Übergänge oder als Phasenumwandlungen erster Ordung. Die Lage des kritischen Punktes im Phasendiagramm ist zu einem großen Teil von elastischen Wechselwirkungen zwischen den Ionen in unterschiedlichem Spinzustand bestimmt. Gemäß unseren experimentellen Ergebnissen haben Eisenionen bei Zimmertemperatur ein kooperatives Verhalten, wenn Eisenoktaeder ein gemeinsames Sauerstoffatom teilen. In Mantelmineralen als Mischkristallen mit relativ niedriger Eisenkonzentration ist das kooperative Verhalten unwahrscheinlich. Wahrscheinlicher ist der superkritische Übergang beim Eisenspinübergang, besonders unter Berücksichtigung der hohen Manteltemperaturen und Spinübergangsdrücken.

Versuche zur Synthese von Bridgmanit in Laser-geheizten Diamantstempelzellen zeigten, dass das $Fe^{3+}/\Sigma Fe$ Verhältnis in Bridgmanit von der Eisenoxidationsstufe des verwendeten Prekursors abhängt. Fe^{3+} in Bridgmanit bildet sich gemäß der Eisendisproportionierung bei einer Synthese mit reduziertem Prekursor und Drücken unter 60 GPa. Alle Produkte der Eisendisproportionierung, einschließlich metallischem Eisem, wurden *in situ* nachgewiesen.

Das $Fe^{3+}/\Sigma Fe$ Verhältnis in Bridgmanit, synthetisiert mit reduziertem Prekursor und bei Drücken zwischen 35 and 60 GPa und $\sim$ 2400 K, ist etwa 25 %. In Bridgmanit, synthtisiert bei 86 GPa und $\sim$ 2800 K, nimmt Fe^{3+} den Low-Spin Zustand ein, das $Fe^{3+}/\Sigma Fe$ Verhältnis reicht bis 60 %. Trotz dieses hohen Fe^{3+} Gehalts konnten wir kein metallisches Eisen nachweisen, was die Frage nach dem Ursprung des hohen Fe^{3+} Gehalts offen läßt. Wir nehmen an, dass das Dublett mit extrem hoher Quadrupolaufspaltung in den Mößbauerspektren von Bridgmanit oberhalb 30 GPa nicht dem Spinübergang des Fe^{2+} in der Pseudo-Dodekaederlage zuzuordnen ist, sondern einem Übergang zwischen nicht-degenerierten und Jahn-Teller aktiven elektronischen Termen ohne jegliche Änderung in der Spinquantenzahl.

Acknowledgments

I am grateful to my supervisors Leonid Dubrovinsky and Natalia Dubrovinskaia for their supervision, patience, and especially for their assistance in overcoming all of the difficult situations during my PhD. These four years in the University of Bayreuth were a very important experience in my life from many aspects.

I deeply acknowledge Catherine McCammon for the many helpful discussions and her struggle (not a vain!) with my radical standpoints and English. I thank Andreas Schönleber who always found time to help me and for his translation of my thesis summary into German. I am deeply indebted to Alexander Kurnosov who aided me many times. Denise Kelk-Huth provided me with invaluable help on administrative and many other issues. I am also grateful to Lydia Kison-Herzing, Petra Buchert, Sven Linhardt, and Franz Fischer for their help. I thank Dan Frost, Hans Keppler, Tiziana Boffa Balaran, Alexander Chumakov, Vladimir Dmitriev, and Dmitry Chernyshov for the fruitful scientific discussions that sparked many good ideas.

I thank all my friends, namely Georgios Aprilis, Ilya Kupenko, Valerio Cerantola, Leyla Ismailova, Ines Collings, Maxim and Elena Bykovy, Stella Chariton, Dariia Simonova, Anna Pakhomova, Sylvain Petitgirard, Robert Arato, Egor and Iuliia Koemets, Timofey Fedotenko, Saiana Khandarkhaeva, Ananya Mallik, Ingrid Blanchard, and Esther Posner for their ideas, help, participation in experiments, and for the good times that we spent together.

Finally, I am grateful to Irina Chuvashova just for ... something.

Contents

1 Introduction

The Earth's interior can be divided in two chemically distinct parts: the core (solid inner and liquid outer), composed primarily of iron, and the silicate mantle with thin crust. While O, Si, Mg are the main elements of the mantle, the Fe contribution (along with Al and Ca) is also significant (McDonough and Sun, 1995). The chemical and physical properties of iron are essentially different from the other major chemical elements of the mantle because iron belongs to a transition metal family.

Transition metals feature a partially filled valence d subshell which can adopt different electronic states. The electronic states depend on the amount of d-electrons and how they occupy d-orbitals. The number of d-electrons determines an *electronic configuration* (that is directly connected with the oxidation state) while the particular occupancy of d-orbitals determines an *electronic term*. Both electronic configuration and term significantly influence the ionic radius of the cation, the covalence of chemical bonds with ligands, the force constants that, in turn, influence the macroscopic properties of compound (e.g., density, compressibility, thermal conductivity etc.). In the Earth's interior the electronic state of iron in minerals is affected by thermodynamical parameters of the mantle such as pressure, temperature and oxygen fugacity and can significantly vary with depth and rock assemblage.

The most common oxidation states of iron in minerals are +2 and +3 (and 0 for iron metal and alloys) with d^6 and d^5 configurations, respectively. The iron oxidation state (or $Fe^{3+}/\Sigma Fe$ ratio) in the mantle minerals is of particular importance for geophysics and geochemistry. Apart from the influencing the physical properties of the rock this ratio is related to the oxygen fugacity (f_{O_2}) that is a key parameter for the chemical and physical behavior of the mantle. The oxygen fugacity controls the speciation of volatile fluids that has important role in magmatic and metasomatic processes, the deep carbon cycle, mantle degassing and evolution of the hydrosphere and atmosphere (see review Frost and McCammon, 2008, and references therein).

The reliable data on f_{O_2} are only available for the shallow upper mantle. While the uppermost mantle has f_{O_2} close to fayalite-magnetite-quartz buffer (FMQ), the garnet xenoliths data show the general trend of decreasing f_{O_2} with depth (Frost and McCammon, 2008). Extrapolation of the shallow mantle data to higher pressures Ballhaus (1995), Woodland and Koch (2003) and experiments by Rohrbach et al (2007) all agree that f_{O_2} can cross iron-wüstite buffer (IW) at depths deeper than 250 km[1]. This is an important conjecture meaning stabilization of the Fe-Ni alloy in the lower part of the upper mantle and possi-

[1]note, however, that this estimate should be shifted towards 300–350 km taking into account the improved garnet oxythermobarometer from Stagno et al (2013).

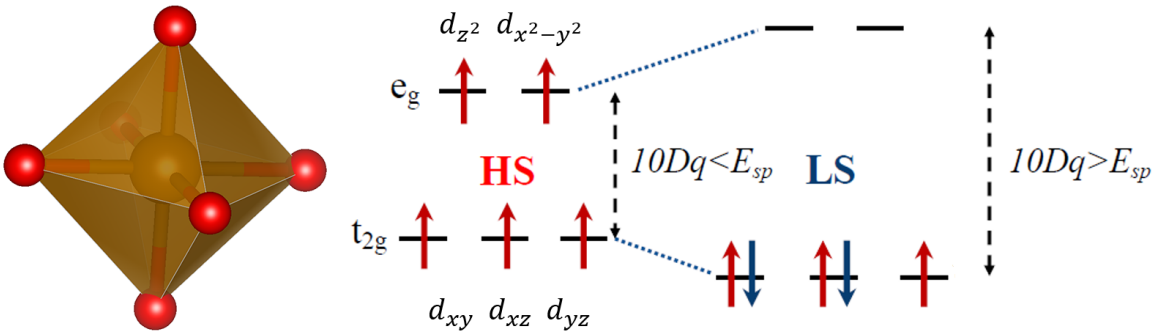

Figure 1. Crystal field splitting in an octahedron: the high-spin ($^6A_{1g}$) and low-spin ($^2T_{2g}$) electronic terms for the d^5 electronic configuration.

bility of the iron disproportionation reaction ($3Fe^{2+} \rightarrow Fe^0 + 2Fe^{3+}$) with counterintuitive appearance of the ferric iron at highly reduced conditions.

This disproportionation reaction is of particular importance for the bridgmanite, $(Mg,Fe)(Si,Al)O_3$, the volumetrically dominant mineral of the lower mantle. The bridgmanite samples synthesized in multianvil press (at 26 GPa) contain a large amount of Fe^{3+} ($Fe^{3+}/\Sigma Fe \geq 50$ %) independently of f_{O_2} (Frost et al, 2004). These data led to the conclusion that the lower mantle contains about 1 wt% of a metallic iron-rich alloy due to the disproportionation of ferrous iron Frost et al (2004).

Besides the iron oxidation state, the ground electronic term of the partially filled $3d$ electronic subshell becomes an important degree of freedom at pressures of the lower mantle. The ground electronic term is determined by electronic configuration and the filling (or "building-up") principle of $3d$-subshell by electrons. While for a free ion all orbitals in d-subshell are degenerated and the filling order of d-orbitals is determined by Hund's rules, the case of transition metal cation bounded in crystal is more complicated. In crystal the energy of the d-orbitals are affected by the neighboring ligands that breaks their degeneracy. Such breaking of degeneracy leads to many possible electronic terms comparing to the free ion case and can modified the filling principle of the d subshell.

Let us consider the octahedral coordination. In this case the crystal field splits d-orbitals on two manifolds (e_g and t_{2g}, Fig. 1). Depending on the magnitude of this splitting ($10Dq$) the transition metal ion can adopt different electronic states, also known as spin states. At small Dq the filling of the d-orbitals is determined by the first Hund's rule (so electronic term tends to have a maximal spin quantum number, i.e. the maximal possible amount of an unpaired spins) and called high spin (HS) state. If Dq exceeds some critical value (so if $10Dq$ larger than the spin-pairing energy), the electronic state with paired spins on the t_{2g} manifold is preferable (so in this case electrons fill the low-energy orbitals at first) and such

state is called low spin (LS, see Fig. 1).

The value of the crystal field splitting increases with decrease of a cation-ligand distance r ($Dq \propto r^{-5}$ for an *ideal* octahedron, see ch. 2 in Figgis and Hitchman, 2000), so the LS state can become energetically favorable at high pressures leading to the HS-LS transition. The possibility of the spin transition in the Earth's mantle was pointed out by Fyfe (1960), and the first experimental confirmation was obtained for ferropericlase by Badro et al (2003). The HS-LS transition of iron may have many important consequences for the properties of lower mantle (such as density, compressibility, element partitioning etc., see review Lin et al, 2013, and references therein).

Numerous aspects of the spin transition in lower mantle minerals remain controversial and highly debatable. There is an especially tangled problem of iron electronic states in bridgmanite. Bridgmanite crystallizes in the distorted $GdFeO_3$-type perovskite structure with two cationic sites — pseudo-dodecahedral A-site and octahedral B-site. In bridgmanite iron adopts both +2 and +3 oxidation states and Fe^{2+} prefers the A-site only. It is generally believed that Fe^{3+} can occupy both A- and B-sites (Lin et al, 2013), however, the structure refinements of the single-crystal diffraction data show that Fe^{3+} also prefers A-site (Vanpeteghem et al, 2006).

High pressure can stabilize LS Fe^{3+} in the B-site that can strongly affect site distribution of the iron and aluminum in bridgmanite structure. This conjecture receives support from the first-principle calculations (Hsu et al, 2012) but experiments show controversial results (Catalli et al, 2010, Glazyrin et al, 2014). The A-site Fe^{2+} behavior is even more puzzled: Mössbauer data show appearance of the new component with very high quadrupole splitting (QS) that was interpreted as Fe^{2+} in the intermediate spin state ($S = 1$) (Lin et al, 2008, McCammon et al, 2008). However, first-principles theoretical calculations do not support this conclusion but argue that high QS component appears due to different local ligand configuration around A-site Fe^{2+} (Hsu et al, 2010). To date, we are still far away from the consensus about iron behavior in bridgmanite despite its fundamental importance for geophysics.

2 Motivation

The above-mentioned examples show the importance the iron electronic states in the mantle minerals for the composition, chemical and physical properties of the Earth's mantle. This thesis is dedicated to the study of iron behavior in the major minerals of the Earth's mantle and its influence on their properties at the respective P, T-conditions. I have focused on the

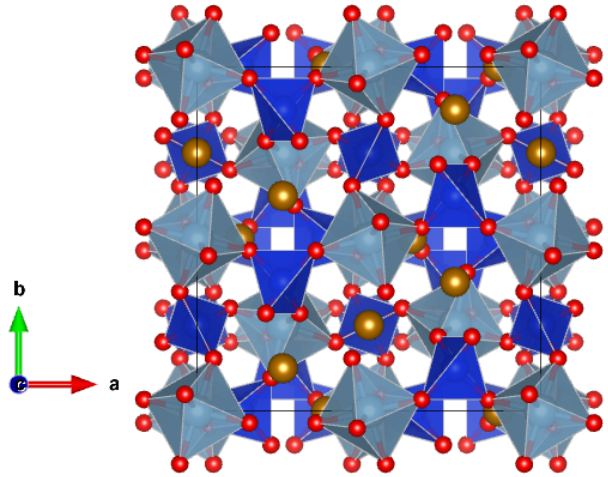

Figure 2. Garnet crystal structure. Its framework is formed by alternating corner-shared SiO_4 tetrahedra (Z-site, blue) and octahedra with trivalent cation (Y-site, grey). The distorted cubic voids (X-site) are populated by large divalent cation (depicted as golden isolated atoms).

four particular problems described in more details below.

2.1 Sound velocity of skiagite-iron-majorite solid solution

Garnets are an abundant group of silicate minerals crystallizing in a cubic structure (space group $Ia\bar{3}d$, Fig. 2) with general formula $X_3^{2+}Y_2^{3+}(SiO_4)_3$. Its structure is able to accommodate variety of divalent (Mg, Fe, Ca, Mn at the X-site) and trivalent cations (Al, Fe, Cr at the Y-site) that leads to formation of the complex solid solutions. Garnets constitute a significant part of the upper mantle and mantle transition zone (MTZ) therefore their elastic properties are important for the interpretation of seismological data from this part of the mantle.

Starting from lower half of the upper mantle pyroxene progressively dissolves in garnet leading to excess of Si^{4+} that is incorporated in the Y-site. Such garnets are called "majoritic" (or containing "majorite" component) and Si^{4+} is balanced either by Mg^{2+} in Y-site (Mg-majorite, $Mg_3(Mg,Si)(SiO_4)_3$) or by Na^+ in the X-site (Na-majorite, $(Na_2,Mg)Si_2(SiO_4)_3$). Because of pyroxene dissolution the garnet fraction in the MTZ can reach up to 35 and 95 vol% in rock with pyrolite and eclogite compositions, respectively (Wood et al, 2013).

The elastic moduli of a natural complex garnet solid solution can be calculated as a linear combination of elastic moduli of the corresponding end-members (Lacivita et al, 2014). High-pressure studies of the elastic properties of garnets have focused mostly on

the end-members with Mg, Ca and Fe^{2+} populating the X-site, and Al, (Mg,Si) on the Y-site (Arimoto et al, 2015, Chantel et al, 2016, Gwanmesia et al, 2014, Jiang et al, 2004, Kono et al, 2010, Zhou et al, 2014, Zou et al, 2012). However, the general trend of increase in $Fe^{3+}/\Sigma Fe$ ratio with depth in garnet xenoliths (Frost and McCammon, 2008) and the possible iron disproportionation reaction (Ballhaus, 1995, Rohrbach et al, 2007, Woodland and Koch, 2003) point out the importance of the garnet end-members with ferric iron on the Y-site. Indeed, the recent investigations of natural samples (Kiseeva et al, 2018, Xu et al, 2017) show that majoritic garnets from deep mantle contain significant amount of Fe^{3+}.

Here, I investigate sound velocities of the skiagite, the iron end-member of silicate garnet family with formula $Fe_3^{2+}Fe_2^{3+}(SiO_4)_3$ using Nuclear Inelastic Scattering. These data can be used for the analysis of the Y-site Fe^{3+} influence on the sound velocities on the garnet solid solution with composition relevant to the MTZ.

2.2 Iron oxidation state in the natural majoritic inclusions

The deepest natural samples used for the determination of f_{O_2} are the garnet peridotite xenoliths which cover depth range down to about 200 km (Frost and McCammon, 2008). The information about oxidation state of the deeper mantle can be obtained only from inclusions in diamonds which can be brought to the surface from depth down to the very top of the lower mantle. However, only inclusions which are evidently originated from the lowermost upper mantle and MTZ are suitable for the f_{O_2} characterization. The majoritic garnet satisfies this requirement because the above-mentioned pyroxene dissolution in garnet makes the Si excess in the garnet composition an unambiguous sign of its high-pressure formation. Unfortunately, such majoritic garnets inclusions are very rare, only about 250 crystals were reported in literature (Kiseeva et al, 2013).

To shed light on the oxygen fugacity of the lowermost upper mantle and MTZ the iron oxidation state in the series of the thirteen majoritic inclusions with pyroxenitic composition from Jagersfontein kimberlite (South Africa) was investigated. Their composition was characterized by electron microprobe analysis in Tappert et al (2005) and Si content of the garnets of interest varies in range from 3.08 to 3.54 pfu that covers a wide range of depths including MTZ.

2.3 Pressure-induced spin transition of Fe^{3+} in the oxygen octahedron

The spin transition is a fascinating electronic phenomenon occurring in transition metal compounds. It was discovered in coordination complexes (Cambi and Szegö, 1931) and remains an active research area until now (Gütlich, 2013). The change of the $3d$-shell electronic state from HS to LS leads to many important consequences. In fact, the spin transition can be considered as a substitution of a transition metal ion by another one with absolutely different properties (such as ionic radius, force constants, type of the degeneracy of the electronic configuration, which determines favorable distortions of the polyhedron, magnetic moment etc.). This may lead to the drastic changes in many physical properties of the material: density, elastic moduli, element partitioning, magnetic and transport behavior.

The minerals relevant to the bulk mantle contain only one kind of the anion — oxygen. Iron cations coordinated by oxygen adopt only the HS state at ambient pressure. As explained in the introduction section, high pressure in general favors a LS state at some point and indeed experimental studies show that LS becomes a ground state at pressures of the lower mantle (Lin et al, 2013).

However, to date there are large discrepancies in the reported spin transition pressures (Lin et al, 2013), some works even report its beginning at ambient pressure (Dorfman et al, 2016). Apparently, such difference in the reported pressures is related to use of the polycrystalline samples with large pressure gradients and intergrain strains, and ambiguity in the interpretation of the spectroscopic data. The first-principle theoretical calculations also predict transition pressure with a large spread because results of the calculations depend in a sensitive way on the used approach (Hsu et al, 2012) or the on-site Hubbard repulsion parameter U (Leonov et al, 2016, see the footnote 36).

The two widely used experimental techniques for determination of the iron spin states at high pressure are X-ray emission spectroscopy (XES) and nuclear forward scattering (NFS). Unfortunately, the interpretation of the experimental data from both technique can be not so straightforward as it seems at a first sight, especially if the sample contain iron cations in different electronic states simultaneously. The analysis of the XES spectra in terms of two features, main line and satellite, is often insufficient (Vankó and de Groot, 2007) and pressure-induced broadening effects of the $K\beta'$ satellite peak can significantly complicate data analysis (Lin et al, 2013). The NFS spectra in general do not provide information about center shift (so, among hyperfine parameters only the quadrupole splitting and hyperfine magnetic field are used to distinguish spin states) and represent an ill-posed mathematical problem in case of the complex spectrum with several distinct components.

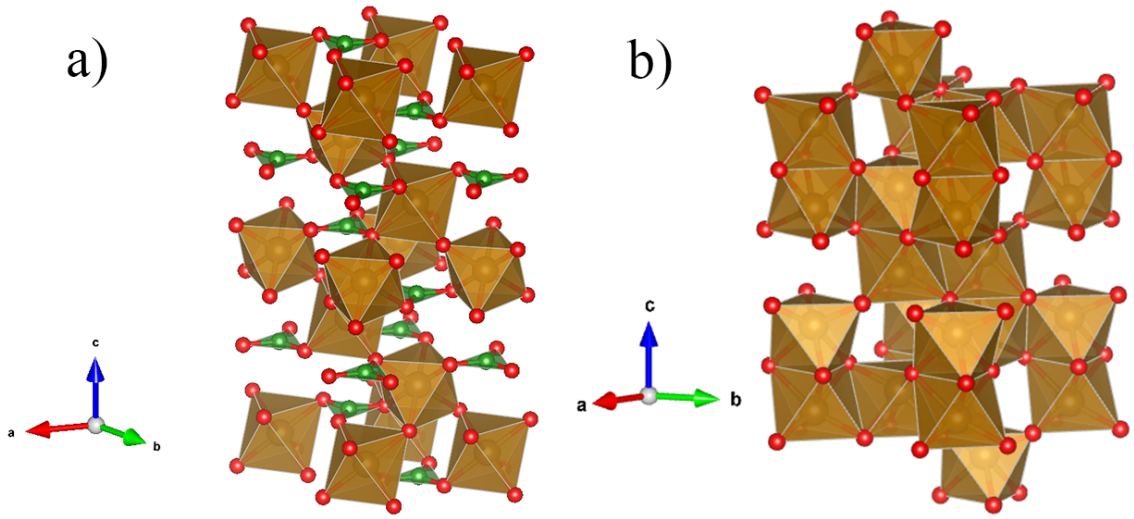

Figure 3. Crystal structures of iron borate and hematite. a) $FeBO_3$ has a calcite-type ($CaCO_3$) structure and is comprised by corner-shared $Fe^{3+}O_6$ octahedra and BO_3 triangles perpendicular to the 3-fold axis. b) α-Fe_2O_3 crystallizes in a corundum-type (Al_2O_3) structure consisting only of $Fe^{3+}O_6$ octahedra. Each octahedron connects with three neighbors via edges in honeycomb-like layers and the layers are interconnected through common triangular faces of octahedra.

To clarify the conditions of the spin transition approach, the systematic comparative study of the spin transition of Fe^{3+} in oxygen octahedra has been performed. It was aimed at establishing regularities in the pressure-induced spin transition of trivalent iron in the oxygen octahedron. To provide solid foundation for the interpretation of the hyperfine parameters this study was founded on the Mössbauer spectroscopy with synchrotron Mössbauer source in combination with single-crystal XRD data. This approach provides the basis to search a correlation between crystal chemistry and hyperfine parameters.

The main focus was put on the stoichiometric phases with different structures: iron borate ($FeBO_3$, Fig. 3a), hematite (α-Fe_2O_3, Fig. 3b) and skiagite-iron-majorite solid solution ($Fe_3(Fe_{1.766(2)}Si_{0.234(2)})(SiO_4)_3$, Fig. 2). Additionally, the high-quality literature experimental data for goethite (FeOOH, Xu et al, 2013), calcium ferrite ($CaFe_2O_4$ Greenberg et al, 2013, Merlini et al, 2010) and andradite ($Ca_3Fe_2(SiO_4)_3$ Friedrich et al, 2014) is used for the comparative analysis. The obtained regularities were used for analysis of iron electronic states in bridgmanite (see below).

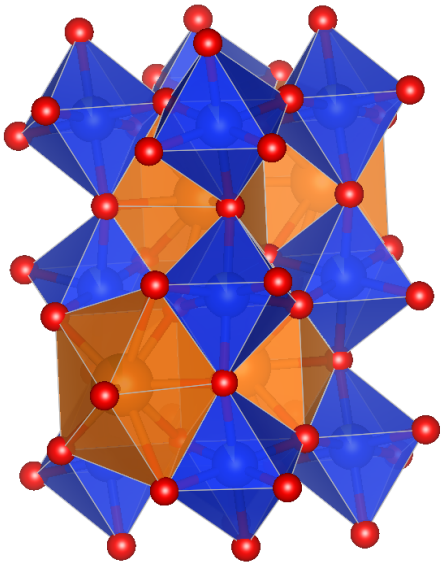

Figure 4. Crystal structure of bridgmanite. Its perovskite-like framework is formed by corner-shared octahedra populated by Si^{4+} and Al^{3+} (B-site, blue) with large 8-12 coordinated cavities occupied by Mg^{2+} and Fe^{2+} (A-site, orange). The Fe^{3+} can occupy both sites depending on the electronic state.

2.4 Iron behavior in the Fe,Al-bearing bridgmanite

The Earth's lower mantle can be assumed as a primarily triminerallic rock consisting of Fe,Al-bearing bridgmanite, (Mg,Fe)O ferropericlase and $CaSiO_3$ perovskite. While the exact mineral proportions are not well constrained and highly debatable, the estimates of bridgmanite part range from 75 wt.% and higher (Murakami et al, 2012, Ricolleau et al, 2009).

Bridgmanite crystallizes in the distorted perovskite-type structure with two cationic sites (space group *Pbnm*, Fig. 4). The Fe^{2+} substitutes Mg^{2+} in the large A-site and above 30 GPa the Mössbauer data show appearance of new Fe^{2+}_A (the subscript designates crystallographic site) component with high QS. Taking into account previously observed in XES spectra reduction of the Fe $K\beta'$ satellite intensity (Li et al, 2004) this new component was initially interpreted as an intermediate spin state of Fe^{2+}_A (Lin et al, 2008, McCammon et al, 2008). However, the first-principle theoretical calculations do not support this conjecture but show that ferrous iron remains in the HS state at pressures of the lower mantle and component with high QS is related to the different local oxygen arrangement around Fe^{2+}_A (Bengtson et al, 2009, Hsu et al, 2010).

The site preference of the Fe^{3+} is an important and debatable matter. Experiments show that the Al^{3+} presence significantly enhance the $Fe^{3+}/\Sigma Fe$ ratio (Lauterbach et al, 2000) that is attributed to a charge-coupled substitution Fe^{3+}_A–Al^{3+}_B. Indeed, this strong preference

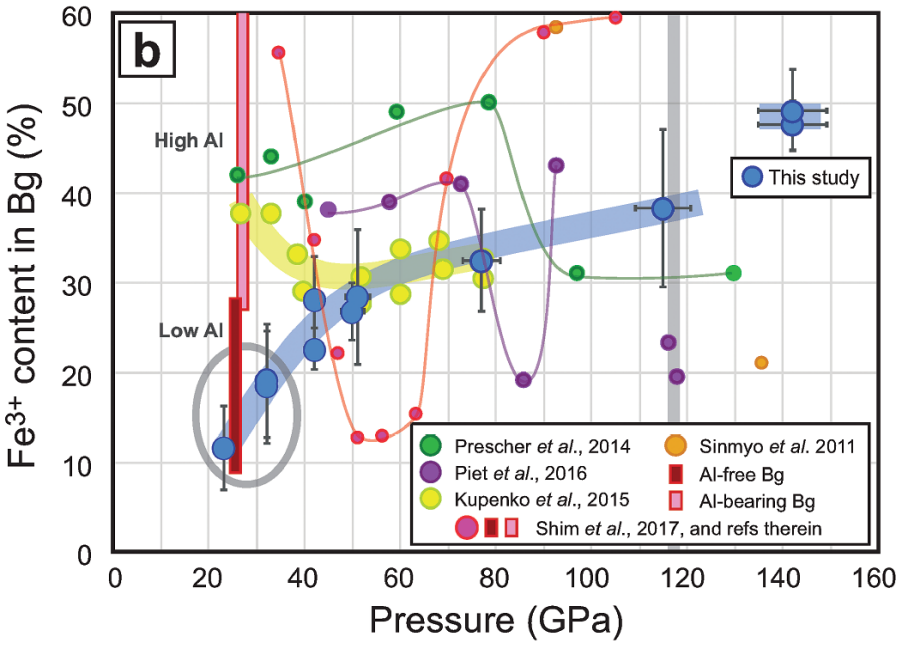

Figure 5. The comparison of $Fe^{3+}/\Sigma Fe$ ratio in bridgmanite at different pressures after laser heating, from work Andrault et al (2018).

of the A-site by Fe^{3+} is confirmed by the direct determination of the site occupancies from X-ray diffraction for samples of Fe,Al-bearing bridgmanite synthesized in multi-anvil press (Vanpeteghem et al, 2006). Regarding Fe^{3+}_A both experimental and theoretical works are in agreement that ferric iron in the A-site remains in the HS state at P–T conditions of the lower mantle (Lin et al, 2013).

However at moderate pressures (above 50 GPa) the LS state of Fe^{3+} in the B-site can be stabilized and this may lead to redistribution of ferric iron between A- and B-sites. Such diffusion process requires high temperatures and will not be visible at room temperature compression experiments. To date, the possible redistribution of ferric iron remains a debatable topic, and while theoretical calculations supports this possibility (Hsu et al, 2012) the different experimental studies came to the opposite conclusions (for instance, see Catalli et al, 2010, Glazyrin et al, 2014). In work Kurnosov et al (2017) the modelling of seismic wave velocities based on elasticity data of Fe,Al-bearing bridgmanite shows the divergence with Preliminary Reference Earth Model (PREM, Dziewonski and Anderson, 1981) at depths below 1200 km.

The changes in the iron electronic states may potentially influence the $Fe^{3+}/\Sigma Fe$ ratio in the bridgmanite that in turn may affect the presence of the iron-rich alloy proposed by Frost et al (2004) in the lower mantle. Indeed, the recent experimental study of iron oxidation state in bridgmanite synthesized *in situ* in laser-heated diamond anvil cell (DAC) at different

pressures found significant variations of $Fe^{3+}/\Sigma Fe$ ratio with synthesis pressure (Shim et al, 2017). However, to date the agreement between different experimental studies is poor, see Fig. 5.

In order to clarify iron behavior at lower mantle P–T conditions study of bridgmanite synthesized *in situ* in laser-heated DAC at different pressures have been performed. Because to date there are no *in situ* evidences for the iron disproportionation reaction (as the multi-anvil press is not a closed system with respect to oxygen) the especial attention was paid to confirm presence of all outcomes of the iron disproportionation reaction.

2.5 Aims of the thesis project

- Investigation of the skiagite sound velocities as function of pressure and analysis of the effect of Fe^{3+} in the Y-site on the sound velocities of the garnets with compositions relevant to the mantle transition zone.
- Determination of the iron oxidation state in the series of the natural majoritic inclusions and modelling of the oxygen fugacity at which the inclusions were formed.
- Establishing regularities of the pressure-induced spin transition in $Fe^{3+}O_6$ octahedra and search of correlations between polyhedron geometry and hyperfine parameters.
- Study of iron oxidation and spin states in Fe,Al-bearing bridgmanite synthesized *in situ* in laser-heated DAC at different pressures and confirmation of iron disproportionation reaction at bridgmanite synthesized from the reduced precursor.

3 Experimental techniques

The diamond anvil cell (see also review Bassett, 2009, for its historical development) is an indispensable tool for high-pressure research. It covers fully the pressure range of the Earth's mantle (and even the whole Earth interior) and the transparency of diamond anvils in a wide range of electromagnetic spectrum allows to apply numerous experimental techniques based on the sample interaction with electromagnetic radiation (e.g., spectroscopic and X-ray diffraction techniques). The temperature can also be varied in a wide range: DAC's compactness allows to use the cell in set-ups with cryostat while high temperatures can be obtained using either resistive heating (up to 1000 °C) or laser heating for higher temperatures, so the achievable temperature range is from few mK to $\sim 10^4$ K.

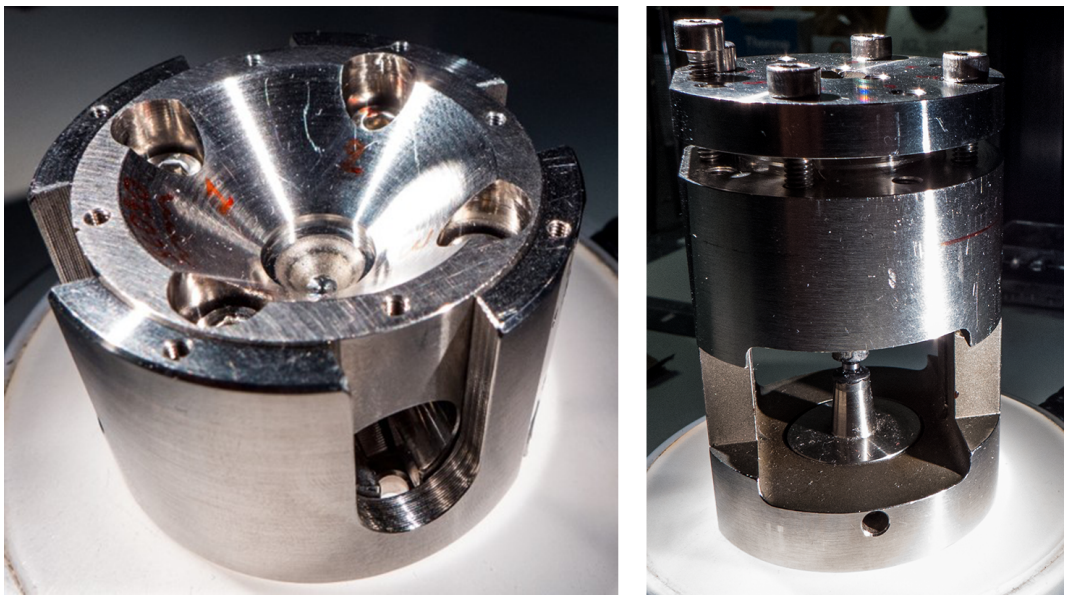

Figure 6. The piston-cylinder type BX90 (left) and panoramic (right) diamond anvil cells. The panoramic cell was used only for the nuclear inelastic scattering experiments.

In this PhD project the piston-cylinder BX90 DAC with rhenium gaskets was used for pressure generation (Kantor et al, 2012, Fig. 6). As a pressure transmitting medium noble gases neon and argon were pumped inside pressure chamber with a gas loading system of Bayerisches Geoinstitut (Kurnosov et al, 2008). The pressure inside DAC was determined using ruby fluorescence method (shift of the Al_2O_3:Cr^{3+} R_1 peak, see Syassen, 2008) or from the lattice parameters of pressure medium using its equation of state in case of the X-ray diffraction experiments (Fei et al, 2007). In some experiments pressure were controlled using high-wavenumber edge of the Raman band of the diamond anvil (which is related to the normal stress of the diamond culet face, Akahama and Kawamura, 2006).

The double-sided laser heating system was used for the *in situ* bridgmanite synthesis (Aprilis et al, 2017, Kupenko et al, 2012). The system uses two near-infrared fiber lasers ($\lambda = 1070 \pm 10$ nm) and a π-shapers to form a Gaussian TEM_{00} beam into a flat-top one (Laskin and Laskin, 2011) that minimizes the effects of the thermophoresis (also known as thermal diffusion, see Sinmyo and Hirose, 2010).

For the nuclear inelastic scattering experiments the special panoramic DAC with large side openings (Fig. 6) was used because in this set-up detectors for the inelastic signal should be installed perpendicular to the beam path as close as possible to the sample. In order to decrease the absorption of the scattered radiation (14.4 keV) by gasket, beryllium was used as a gasket material for these experiments.

One of the most powerful experimental techniques for investigation of iron electronic

states is the Mössbauer spectroscopy. However, the conventional transmission Mössbauer spectroscopy encounters with difficulties (described below) in case of the DAC experiments. Fortunately, during recent decades nuclear resonance techniques have developed greatly on synchrotron facilities and they are an experimental foundation of this thesis. The experiments in DAC benefits particularly from use of the synchrotron radiation due to its low divergency and small beam spot size. These features eliminate many potential experimental uncertainties and allow to carry out experiments with single crystals. The nuclear resonance experiments are complemented by X-ray diffraction techniques which provide reliable phase determination and detailed structural information making interpretation of spectroscopic data much less ambiguous. The principal experimental techniques of this thesis are described in more details below. All nuclear resonance experiments of this PhD project were carried out on the Nuclear Resonance beamline (ID18) at ESRF (Rüffer and Chumakov, 1996).

3.1 Nuclear resonance techniques

3.1.1 Mössbauer effect

The classical Mössbauer spectroscopy and nuclear resonance techniques are based on the Mössbauer effect i.e. the resonance recoilless absorption/emission of the γ-radiation by atomic nucleus that is directly connected with nuclear resonance fluorescence. Such resonance fluorescence is well-known for atomic electronic transition and for the first time was demonstrated more than century ago in sodium vapor (Wood, 1904). While atomic resonance fluorescence can be easily observed, it is not the case for nuclear resonance fluorescence.

The energy of the excited state E_e of the quantum system with mean lifetime τ cannot be measured exactly due to Heisenberg's uncertainty principle ($\Delta E \geq \hbar/\tau$) whereas the energy of the ground state E_g can determined accurately because of its infinite lifetime. As a result, the transition energy from excited to ground state of the nuclei or atom at rest is not a Dirac delta function but smeared around the mean energy $E_0 = E_e - E_g$. The intensity distribution of the radiation as a function of energy E is a Lorentzian curve and given by the Breit-Wigner equation:

$$I(E) = \frac{\Gamma/(2\pi)}{(E - E_0)^2 + (\Gamma/2)^2}, \tag{1}$$

where Γ is the full width of the emission line at half maximum (FWHM). The absorption line has the same intensity distribution.

The transition of the quantum system from excited to ground state releases the energy E_0.

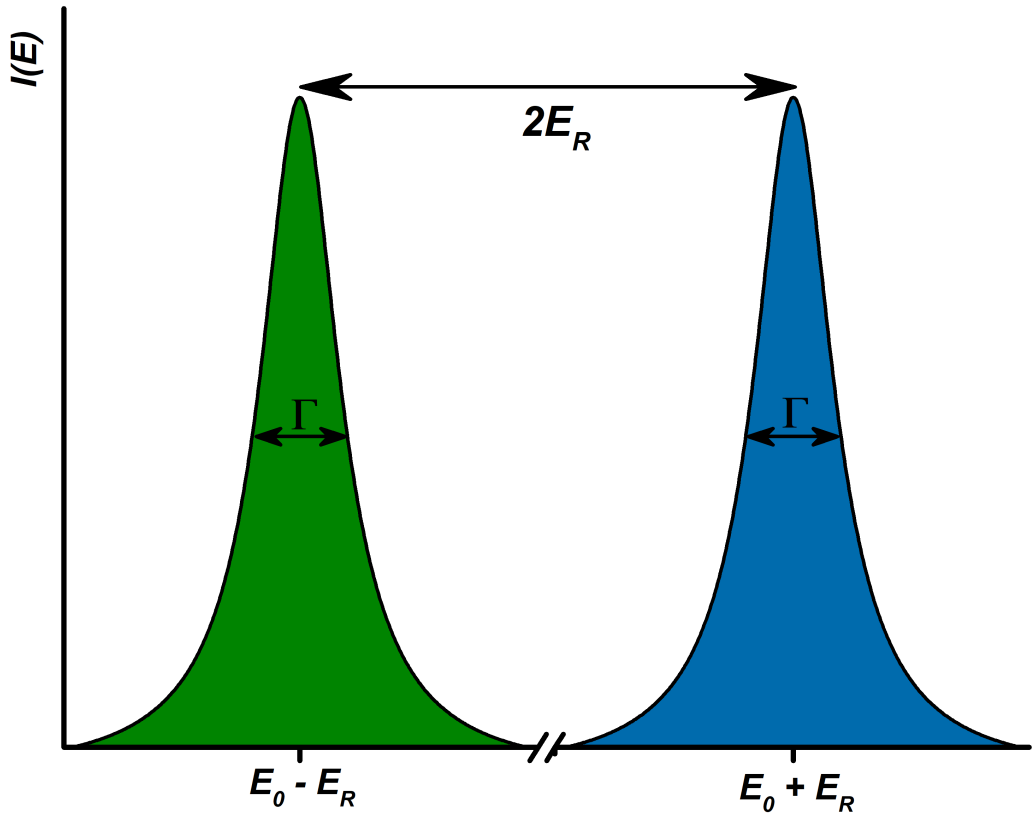

Figure 7. Energy separation of γ-emission (green) and absorption (blue) lines caused by recoil of a "bare" resting nuclei.

Because the emitted photon has momentum the radiant source should experience a recoil with the same but oppositely directed momentum, according to the momentum conservation law. As result, the energy of emitted photon is smaller than transition energy by recoil energy, $E_\gamma = E_0 - E_R$. The recoil energy is

$$E_R = \frac{1}{2}Mv^2 = \frac{(Mv)^2}{2M} = \frac{p_\gamma^2}{2M} = \frac{E_\gamma^2}{2Mc^2} \approx \frac{E_0^2}{2Mc^2}, \tag{2}$$

here it is reasonable to assume that $E_\gamma \approx E_0$ because $E_R \ll E_0$. The analogous process of the photon absorption also requires additional energy for recoil that creates $2E_R$ energy separation between emission and absorption lines (Fig. 7).

The overlap of the emission and absorption lines is required to observe the resonance fluorescence. The principal difference between the nuclear and electronic transitions is significantly different transition energies (10^4–10^5 *vs* 1–10 eV, respectively). While for the electronic transitions the E_R is small comparing to the line width and does not impede observation of resonance fluorescence, for the nuclear transition E_R exceed line widths by several orders of magnitude (for the ^{57}Fe $E_R = 1.95 \cdot 10^{-3}$ eV whereas $\Gamma = 4.55 \cdot 10^{-9}$ eV) making the nuclear

resonance fluorescence impossible to observe.

The outstanding discovery of Rudolf Mössbauer (awarded by a Nobel Prize in Physics in 1961) was that the nuclei bounded in crystal can absorb/emitt γ-quants recoilessly (Mössbauer, 1958a,b, 1959). The point is that in solid state the nuclei is not able to recoil freely and participates only in collective vibrations with neighboring atoms which can be treated as a gas of quasi-particles, phonons. The recoil energy is, therefore, expended on the phonon excitation in crystal but phonon energies, E_{vib}, are again orders of magnitude larger than line width of the nuclear transition. However, due to quantized nature of phonons, there is a certain finite probability that nuclei emits/absorbs γ-quant without exitation/absorption of phonons, the so-called zero-phonon process. In this case the recoil momentum is given not to the single emitting nuclei but is shared with crystal as whole. Therefore, the crystal mass $M_{crystal}$ should be used in eq. (2) making the recoil energy negligibly small. The emission and absorption lines are not shifted from mean energy E_0 and nuclear resonance fluorescence can be observed.

The probability of recoilless emission/absorption is given by the Lamb-Mössbauer or simply f-factor (Greenwood and Gibb, 1971):

$$f = \exp\left[-\frac{\langle x^2\rangle E_\gamma^2}{(\hbar c)^2}\right], \tag{3}$$

where $\langle x^2\rangle$ is the expectation value of the squared vibrational amplitude (or the mean-squared displacement) in the direction of γ-propagation.

3.1.2 Hyperfine parameters

The nuclear quantum states are characterized by the total spin I and its projection m_I along some allocated direction. The values of m_I can range from $-I$ to $+I$ (so $2I+1$ states in total). In the absence of electric and magnetic field the nuclear substates with different m_I are degenerated. The electromagnetic interactions of the nucleus with neighboring charges (own electrons and neighboring atoms) can shift energy of nuclear states and remove degeneracy by splitting nuclear substates with different m_I. These interactions are called hyperfine and they provide valuable information about electronic state of the Mössbauer atom and its local environment in the crystal.

Only three kind of electromagnetic interactions should be considered (because the even electric and magnetic moments of atomic nucleus equal to zero): the electric monopole interaction, the electric quadrupole interaction, and the magnetic dipole interaction. These interactions are characterized by three hyperfine parameters of Mössbauer spectra: the isomer shift, the quadrupole spitting, and the hyperfine magnetic field, respectively.

Isomer shift The electric monopole interaction, leading to the isomer shift, appears due to the different radii of the nuclei in the excited and ground states. This interaction acts by shifting the energy of the single resonance line or the centroid (center of mass) in case of the line multiplet (see scheme of nuclear level in Fig. 8, the second case).

The isomer shift determined from fit of the spectrum is reported relative to the isomer shift of some reference compound at ambient conditions. Nowadays, the α-iron is the most common standard and it was used in all works of this PhD project. However, in practice, one determines not the isomer shift but the centre shift (δ_{CS}) that is a sum of isomer shift (δ_{IS}) and second-order Doppler (SOD, δ_{SOD}) shift. The SOD shift results in reduction of γ-ray energy due to relativistic time dilation in the reference frame associated with the moving nucleus. The difference between δ_{CS} and δ_{IS} is often ignored because the δ_{SOD} is almost the same in case of the spectra measured at the same temperature and one can identify the center shift with the isomer shift. For more details about SOD shift see Menil (1985) or one of the resulting preprint of this PhD project Vasiukov et al (2017b).

The physical meaning of isomer shift is a measure of the electron density at the Mössbauer nucleus which is almost fully created by s-electrons (within relativistic considerations there is also a minor p-electron contribution). One can write it in the following form (Greenwood and Gibb, 1971):

$$\delta_{IS} = \frac{2\pi}{3} Ze^2[\langle r_e^2\rangle - \langle r_g^2\rangle]\Delta\psi^2(0) = \alpha \cdot \Delta\psi^2(0), \tag{4}$$

where Z is the proton number, e is the electron charge, $\langle r_{e,g}^2\rangle$ is the mean-squared nuclear radius of the excited and ground states, respectively, and $\Delta\psi^2(0)$ is the difference in electron density at the nucleus between the measured and reference compounds. The constant α is negative in the case of ^{57}Fe.

The isomer shift of the ^{57}Fe obeys to several systematic trends that are used for the data interpretation:

- The isomer shift decrease with increase of oxidation state. The divalent iron (d^6 configuration) has a very distinct range of δ_{IS} values that makes its identification very simple from Mössbauer spectra. For instance, in skiagite-iron-majorite solid solution the center shift of the Y-site HS Fe^{3+} and the X-site HS Fe^{2+} are 0.23(2) and 1.169(12) mm/s, respectively (see spectrum in Fig. 8).
- The isomer shift decrease with decrease of the iron coordination number.
- The isomer shift decrease with decrease of the ligand electronegativity.
- The isomer shift of the LS state is smaller than for the HS state (for the same electronic configuration).

- The isomer shift is affected by the adjacent bonds of the iron ligands or, in other words, by the type of atoms in the second coordination sphere of iron. This so-called inductive effect was found by Menil (1985).

- The first-principle calculations also show that isomer shift in general decreases with iron-ligand bond length (Neese, 2002). The changes in isomer shift with applying pressures can be related to this effect.

Quadrupole splitting The magnitude of the electric quadrupole interaction depends on the electric field gradient (EFG) created by electrons and neighboring charges at the nucleus. The EFG is a second-rank tensor of the second derivatives of the electric potential $V(\vec{r})$ at nucleus (so $r = 0$):

$$\mathrm{EFG} = \nabla\nabla V = \begin{pmatrix} V_{xx} & V_{xy} & V_{xz} \\ V_{yx} & V_{yy} & V_{yz} \\ V_{zx} & V_{zy} & V_{zz} \end{pmatrix}, \tag{5}$$

where ∇ is the nabla operator, V_{ij} designates the second derivatives $\partial^2 V/\partial x_i \partial x_j$. This tensor is symmetric (so $V_{ij} = V_{ji}$) and can be diagonalized by rotation to a principal axis system for which non-diagonal elements vanish ($V_{i\neq j} = 0$). By convention, the principal axes are chosen such way that $|V_{zz}| \geq |V_{yy}| \geq |V_{xx}|$. The Laplace's equation

$$\Delta V = V_{xx} + V_{yy} + V_{zz} = 0, \tag{6}$$

where Δ is Laplacian, shows that EFG in the principal axis system has only two independent components. These are chosen to be the largest z-component of the EFG (V_{zz}, often designated as eq) and the *asymmetry parameter*, η:

$$\eta = \frac{V_{yy} - V_{xx}}{V_{zz}}. \tag{7}$$

In the proper principal axis system the asymmetry parameter values lie in the range $0 \leq \eta \leq 1$.

In case of the $3/2 \rightarrow 1/2$ transition in ^{57}Fe the EFG results in the quadrupole splitting of the substates of the exited nuclear state ($I = 3/2$) on two Kramers doublets with $m_I = \pm 3/2$ and $\pm 1/2$ (Fig. 8). The magnitude of the quadrupole splitting is given by formula

$$\Delta E_Q = \frac{eQV_{zz}}{2}\sqrt{1 + \frac{1}{3}\eta^2} \tag{8}$$

where Q is the nuclear quadrupole moment. In the absence of magnetic field on the iron nucleus the quadrupole interaction leads to the quadrupole doublet in Mössbauer spectra (Fig. 8).

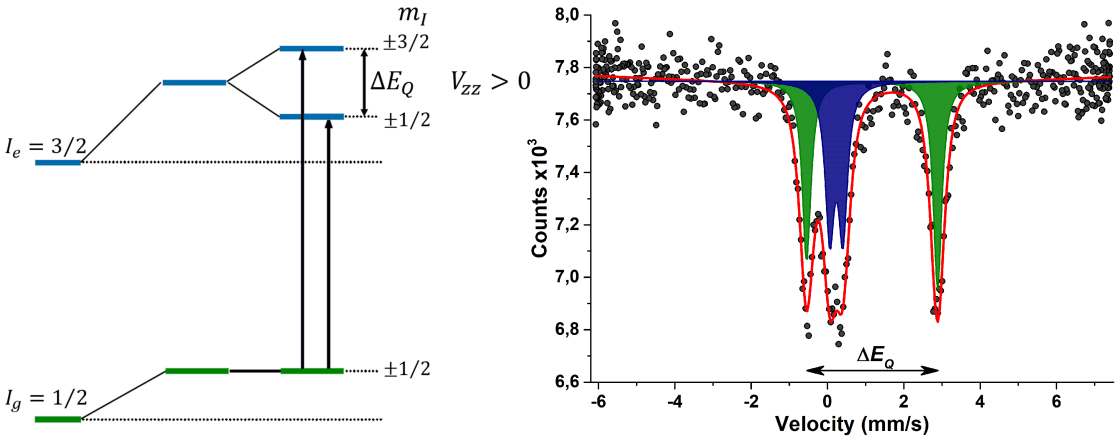

Figure 8. The energy scheme of ^{57}Fe nuclear levels in the presence of electric quadrupole interactions and Mössbauer spectrum of skiagite-iron-majorite solid solution at 50 GPa and room temperature. The energy scheme represents the following cases (from left to right): the "bare" nucleus → the shift of nuclear levels by electric monopole interactions with electrons ($V_{zz} = 0$) → the splitting of the nuclear levels by electric quadrupole interactions ($V_{zz} \neq 0$). There is no splitting of the ^{57}Fe ground state because the nuclear state with spin 1/2 has no electric quadrupole moment ($Q = 0$). Note, that quadrupole interactions remove degeneracy of nuclear levels only for *absolute value* of m_I in case of ^{57}Fe. On the spectrum the blue and green doublets correspond to the Y-site HS Fe^{3+} and the X-site HS Fe^{2+}, respectively. These two iron electronic states have very distinct δ_{CS} and ΔE_Q values.

There are two principal contribution to the EFG: the contribution of the electronic cloud and the lattice contribution from the neighboring ions:

$$V_{zz} = (1 - R)V_{zz}^e + (1 - \gamma_\infty)V_{zz}^i, \tag{9}$$

where V_{zz}, V_{zz}^e and V_{zz}^i are the electric field gradient (total, electronic and lattice contributions, respectively), and R and γ_∞ are the Sternheimer factors of shielding and antishielding, respectively Greenwood and Gibb (1971). Since the electric field gradient (EFG) is proportional to r^{-3}, the electronic contribution generally dominates the EFG. In case of iron the electronic EFG is related to the 3*d*-electrons, as *s*-electrons and fully-filled subshells do not contribute to the EFG. Due to this fact the ΔE_Q values are sensitive to the electronic term and the symmetry of local environment of iron cation. As an example, see spectrum of skiagite-iron-majorite solid solution in Fig. 8. In case of the Y-site HS Fe^{3+} the lattice contribution is the main term in EFG, whereas the electronic contribution dominates EFG of the X-site HS Fe^{2+}. This results in very different quadrupole splitting values (0.34(3) and 3.43(3) mm/s, respectively).

Let us consider Fe^{3+} in the octahedral environment which splits 3*d*-orbitals into e_g and

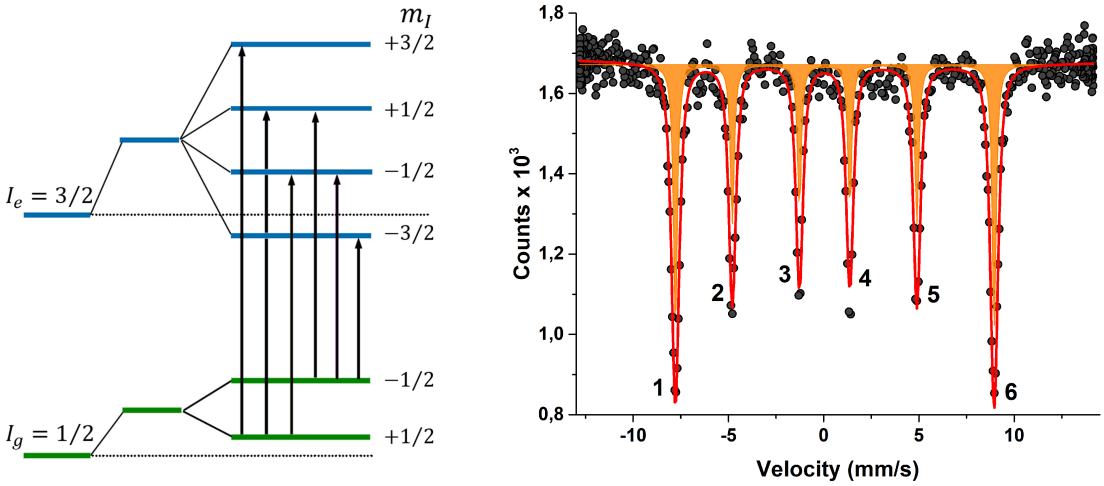

Figure 9. The energy scheme of ^{57}Fe nuclear levels in the presence of magnetic dipole interactions and Mössbauer spectrum of α-Fe_2O_3 single crystal at 26 GPa and room temperature. The energy scheme represents the following cases (from left to right): the "bare" nucleus $\rightarrow$ the shift of nuclear levels by electric monopole interactions with electrons ($V_{zz} = 0$; $H_{hf} = 0$) $\rightarrow$ the splitting of the nuclear levels by magnetic dipole interactions ($V_{zz} = 0$; $H_{hf} \neq 0$). The magnetic field totally removes degeneracy of nuclear levels. Note that line positions in spectrum of α-Fe_2O_3 are not symmetric due to the quadrupole shift.

t_{2g} manifolds (Fig. 1). Because the fully-filled or half-filled e_g and t_{2g} orbitals do not produce an EFG (see Table 4.2 in Gütlich et al (2010)), the quadrupole splitting in the case of HS Fe^{3+} ($^6A_{1g}$ term) is mainly related to the lattice contribution and is generally small. However Fe^{3+} in the LS state ($^2T_{2g}$ term) has one unpaired electron on the t_{2g} level and, therefore, the main contribution to the EFG changes from lattice to electronic (for ferrous iron the situation is opposite). This should cause a significant increase of the quadrupole splitting and, indeed, ΔE_Q values usually change significantly across HS$\rightarrow$LS transition. However, for the degenerated electronic terms the electronic EFG depends on the t_{2g} manifold splitting and temperature Ingalls (1964) that can strongly influence the difference of ΔE_Q between HS and LS states.

Hyperfine magnetic field The magnetic dipole interactions appears in the presence of the magnetic field and remove the degeneracy of the nuclear substates totally (Fig. 9). There is six magnetic dipole-allowed transitions (selection rules are $\Delta m_I = 0, \pm 1$) that give rise to the six line Mössbauer spectrum (Fig. 9). In the case of ^{57}Fe the Mössbauer spectrum of the powder sample show magnetic sextet with relative line intensities 3:2:1:1:2:3 (if the quadrupole interactions are absent).

However, the pure magnetic hyperfine interaction without electric quadrupole interaction is a very rare case in practical Mössbauer spectroscopy. For compounds of interest of this PhD project it is important to mention a high-field case when the energy of magnetic interaction is much larger than energy of the quadrupole interaction (for more detailed discussion of combined electric quadrupole and magnetic hyperfine interactions see Gütlich et al, 2010). In this case the quadrupole interaction can be treated as a perturbation and manifests itself as an additional *quadrupole shift* (ε) of the magnetic sextet lines: the two outer lines (1st and 6th) are shifted by ε to some side (depending on the sign of V_{zz}) whereas inner quartet of lines (from 2nd to 5th) moves to the opposite direction by same value ε (see spectrum of α-Fe_2O_3 in Fig. 9).

The non-zero hyperfine magnetic field appears in case of the magnetic ordering of iron cations in the sample below magnetic critical point[2] (Néel or Curie temperature). The hyperfine magnetic field determined from Mössbauer spectra can be expressed as a sum of three contributions[3]: Fermi contact interaction (H_c) and a dipolar interaction with orbital and spin momenta (H_L and H_S, respectively) of the electrons Greenwood and Gibb (1971):

$$H_{hf} = H_c + H_L + H_S, \tag{10}$$

$$H_c = \frac{8\pi}{3} g_e \mu_B \langle \mathbf{S} \rangle \sum_{ns} \left[\left| \psi^{\uparrow}_{ns}(0) \right|^2 - \left| \psi^{\downarrow}_{ns}(0) \right|^2 \right], \tag{11}$$

$$H_L = g_e \mu_B \langle \frac{1}{r^3} \rangle \langle \mathbf{L} \rangle, \tag{12}$$

$$H_S = g_e \mu_B \langle 3\mathbf{r}(\mathbf{S} \cdot \mathbf{r}) \frac{1}{r^5} - \mathbf{S} \frac{1}{r^3} \rangle, \tag{13}$$

where g_e is the electron spin g-factor, μ_B is the Bohr magneton, $\left| \psi^{\uparrow\downarrow}_{ns}(0) \right|^2$ is the electron density at the nucleus for a given ns shell with spin parallel or antiparallel to the expectation value of the net electronic spin $\langle \mathbf{S} \rangle$, $\langle \mathbf{L} \rangle$ is the expectation value of the orbital momentum and r is the radial coordinate of electrons. The H_{hf} is proportional to the expectation value of the iron magnetic moment and can be approximated by a Brilloiun function which reaches saturation at low temperatures. Because all terms in eq. (10) depend on the $\langle \mathbf{S} \rangle$ and/or $\langle \mathbf{L} \rangle$ the saturated value of the hyperfine magnetic field is closely related to the electronic term of iron $3d$ subshell.

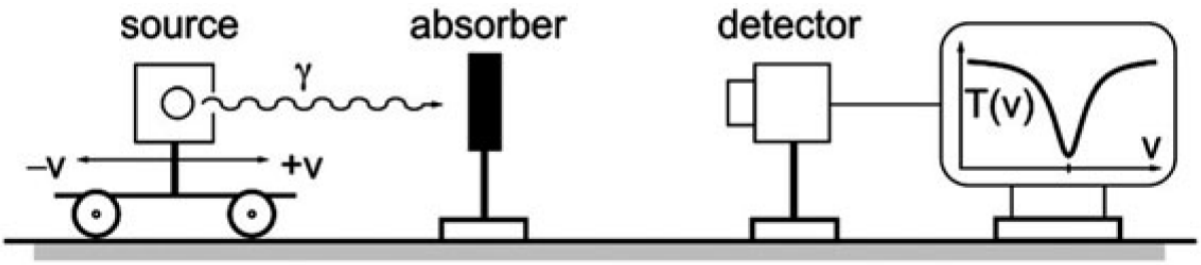

Figure 10. Schematic representation of a transmission Mössbauer spectrometer. Modified after Gütlich et al (2010).

3.1.3 The conventional Mössbauer spectroscopy and its limitations

To measure the usual transmission Mössbauer spectrum (such as in Figs. 8 or 9) one need a source of resonant γ-photons. In conventional Mössbauer spectroscopy the radioactive source are used with a long-living radioactive parent isotope, the decay of which produces the desired Mössbauer isotope in the required excited state. A common radioactive source for the ^{57}Fe spectroscopy is ^{57}Co, which decays to the ^{57}Fe isotope via K-electron capture. The cobalt atoms are diffused to the thin rhodium foil with cubic crystal lattice and such sources give narrow unsplitted Mössbauer line.

To observe nuclear resonance absorption by the sample, in which the nuclear substates are shifted and splitted due to the hyperfine interactions, energy of the source emission line should be modulated. This is implemented by means of a Doppler effect, attaching the radioactive source to the electro-mechanical velocity transducer (Fig. 10). The transducer moves the source according to some periodical law, with velocity $+v$ toward and $-v$ away from the absorber. This motion modulates the energy of the emitted γ-quants by the factor $1 + \vec{v}/c$, so $E_\gamma = E_0(1 + \vec{v}/c)$. Thus, the source emission line scans energy in the interval $E_0 \pm E_0 v/c$ and the Mössbauer transmission spectrum comes out as a convolution of the emission line with absorber spectrum.

Apart from the resonant 14.4 keV line, the ^{57}Co radioactive source produces two additional γ-lines at 122 and 136 keV, and X-ray lines of Fe and Rh (at 6.4 keV and 20.1 keV). These additional unwanted photons should be ignored during data collection, otherwise they would contribute to a large non-resonant background which significantly worsen the statistical accuracy of the data. This is achieved by measuring the so-called pulse-height energy

[2] the slow paramagnetic relaxation phenomena (Gütlich et al, 2010) are not related to the compounds of interest of this thesis.

[3] there is also a magnetic field from dipolar interactions with magnetic moments of neighboring atoms but its value is usually less than 1 T and can be neglected

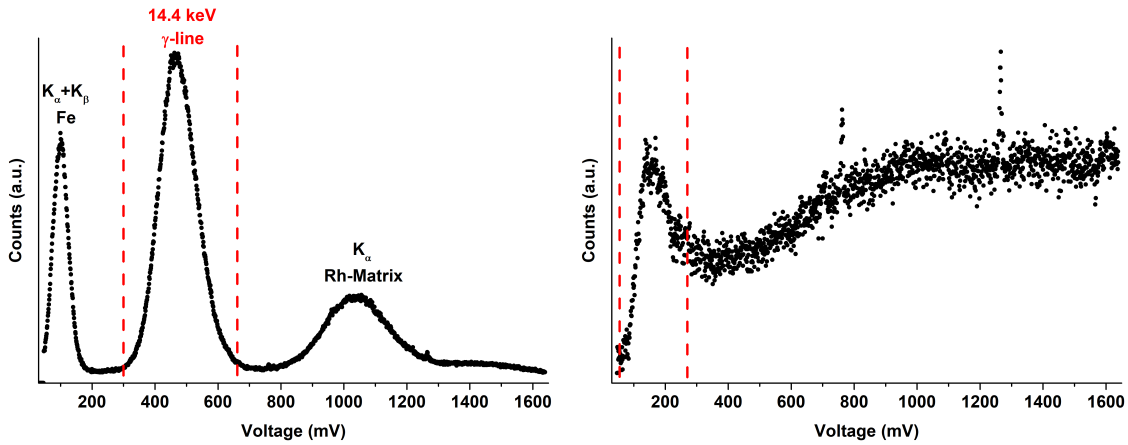

Figure 11. The measured energy emission spectrum of the ^{57}Co(Rh) point source in experimental set-up without DAC (left) and with DAC (right). These pulse-height spectra were acquired on the Mössbauer spectrometer installed in Bayerisches Geoinstitut (BGI) equipped with gas-proportional counter. The dashed lines mark the discriminated energy interval with 14.4 keV resonance line.

spectrum of the source and discriminating desirable resonance line (see left panel in Fig. 11).

Use of the diamond anvil cell significantly limits the sample size and strongly decrease count-rate and a useful signal intensity. The high-energy γ-radiation excite strong X-ray fluorescence in the Re gasket what significantly changes the pulse-height spectrum (right panel in Fig. 11). In this case the discriminated energy interval inevitably contain a large part of the non-resonant radiation that gives an enormous non-resonant background in the acquired Mössbauer spectra.

To improve the quality of the experimental data, a focused beam of resonant γ-quants is required. A way out is experiments on the nuclear resonance beamline at synchrotron facilities.

3.1.4 Nuclear resonance techniques on synchrotron facilities

To observe the nuclear resonance absorption, one need a radiation with extremely narrow energy width (of the order of neV in case of ^{57}Fe) that could be satisfied only with radioactive sources in the past. Nowadays the superior spectral density and brilliance of the third generation of synchrotron source allow to routinely perform experiments with the nuclear resonance processes that led to a swift development of nuclear resonance techniques (Rüffer and Chumakov, 1996). Two most commonly used techniques are Nuclear Inelastic Scattering and Nuclear Forward Scattering. Whereas the latter technique gives information about

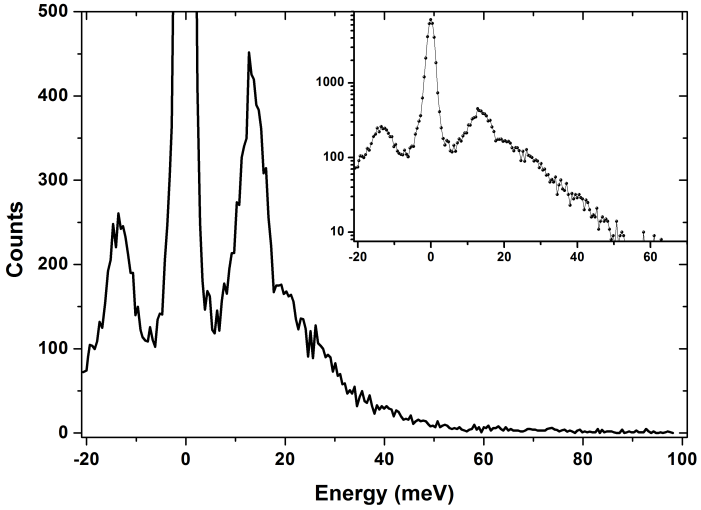

Figure 12. Example of the NIS spectrum. The elastic peak at 0 meV is surrounded by phonon creation (positive energy) and annihilation (negative energy) wings. The inset shows same spectrum in logarithmic scale. The sample is skiagite-iron-majorite solid solution at ambient conditions, from Vasiukov et al (2017a).

hyperfine parameters (as conventional Mössbauer spectroscopy but in time-domain mode), the former one provides information about lattice dynamics utilizing the dependence of the Mössbauer effect on lattice vibrations (Chumakov and Rüffer, 1998).

Nuclear Inelastic Scattering Very soon after discovery of the Mössbauer effect it was proposed to use nuclear resonance absorption to study lattice vibrations (Visscher, 1960). However, this proposal faced insurmountable experimental challenges which were overcome only in the middle of the nineties on the third generation synchrotrons (Seto et al, 1995) and this led to the development of the Nuclear Inelastic Scattering technique (NIS, see Chumakov and Rüffer, 1998).

The NIS technique provides information about lattice dynamics via nuclear resonant *inelastic* absorption, so when the absorption process is accompanied by phonon excitation or annihilation. The typical phonon energies are of the order of dozens of meV that is 10^6–10^7 larger than natural line width of the ^{57}Fe nuclear resonance line. To make such energy difference with Doppler shift the radioactive source should be moved with enormous velocities ~ 1 km/s. However, such energy scans can be easily performed with synchrotron radiation.

The NIS spectrum consists of the elastic peak and inelastic wings (Fig. 12). The elastic peak corresponds to zero-phonon process i.e. the resonance recoilless absorption. Because

characteristic energy scale of the hyperfine interactions is much smaller comparing to the instrumental function (2.3 meV FWHM) the conventional Mössbauer spectrum of the sample can be considered as the δ-function, therefore the resulting convolution is just the instrumental function. The inelastic wings correspond to absorption processes with phonon creation (positive energy) and annihilation (negative energy). These wings are symmetrical and their relative intensity is connected via the Boltzmann factor, similar to the Stokes and anti-Stokes lines in the Raman spectra.

From the NIS spectrum the partial (atomic) phonon density of states (pDOS) can be extracted, an important integral characteristic of the lattice vibrations. The NIS data processing involves removal of the elastic peak and subtraction of background multi-phonon contributions, followed by determination of the pDOS. A visual illustration of all the main steps in NIS data analysis can be found in Hu et al (1999). The detailed mathematical treatment is given in Kohn et al (1998).

The main parameters evaluated from the pDOS are related to thermodynamical and vibrational properties (such as the vibrational contribution to entropy, specific heat etc.). Additional geophysical application of the NIS data is determination of the sound velocities from pDOS function (Sturhahn and Jackson, 2007). The low-energy part of the pDOS contains information about dispersion of the acoustic phonons that can be used for evaluation of the Debye sound velocity (Hu et al, 2003). The latter depends quadratically on the energy and can be written in the following form (Achterhold et al, 2002, Hu et al, 2003):

$$\mathcal{D}(E) = \left(\frac{\tilde{m}}{m}\right) \frac{E^2}{2\pi^2\hbar^3 n V_D^3}, \tag{14}$$

where $\tilde{m}$ is the mass of the nuclear resonant isotope (^{57}Fe in our case), m is the average atomic mass, n is the density of atoms and V_D is Debye sound velocity.

The Debye sound velocity can be expressed as

$$\frac{3}{V_D^3} = \frac{1}{V_p^3} + \frac{2}{V_s^3}, \tag{15}$$

where V_p is the average velocity of the *primary* (compression) wave and V_s is the average velocity of the *secondary* (shear) wave. There is additional relationship between V_p and V_s:

$$V_p = \sqrt{\frac{K + 4/3G}{\rho}}, \qquad V_s = \sqrt{\frac{G}{\rho}},$$
$$=> \frac{K}{\rho} = V_k^2 = V_p^2 - \frac{4}{3}V_s^2, \tag{16}$$

where K is the adiabatic bulk modulus, G is the shear modulus and ρ is the density. The system of equations (15) and (16) has an approximate solution according to the corrected

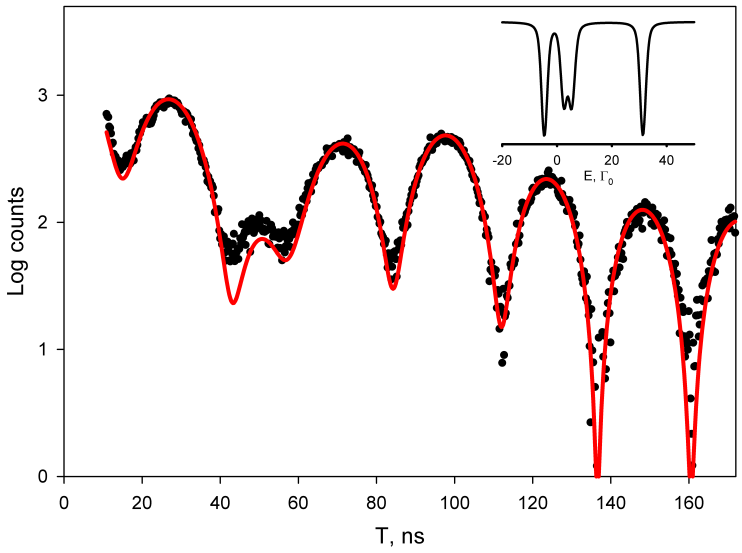

Figure 13. The Nuclear Forward Scattering (NFS) spectrum of the skiagite-iron-majorite solid solution at ambient conditions. The inset is the corresponding Mössbauer spectrum.

formula from Sturhahn and Jackson (2007):

$$V_p = \sqrt{1.002V_k^2 - 0.104V_kV_D + 1.208V_D^2}, \qquad V_s = 0.952V_D - 0.041V_k. \tag{17}$$

Therefore, using known equation of state (for instance obtained from the diffraction compression experiment), both V_p and V_s can be evaluated from the NIS data.

Nuclear Forward Scattering and Synchrotron Mössbauer source There is another approach to observe hyperfine splitting of nuclear substates, fundamentally different from conventional Mössbauer spectroscopy. The synchrotron radiation has a continuous spectrum so the sample irradiation by beam with energy close to the nuclear transition energy leads to the nuclear resonance absorption of some part of the incident photons. The lifetime of the excited nuclear state ($\tau = 97.8$ ns in case of the ^{57}Fe) is much larger comparing to the characteristic time of electronic scattering. The synchrotron radiation has a pulsed structure, so using properly synchronized detectors the pure decay signal of the nuclear excited states (nuclear scattering) can be observed after prompt electronic scattering of the non-resonant radiation (the incident beam typically has 1 meV FWHM).

In general, the nuclear excited states should show the well-known exponential decay ($N(t) = N_0e^{-t/\tau}$) but in the considered case of the forward geometry it is a *coherent* decay. For the coherent process the hyperfine splitting of the nuclear substates leads to the quantum beats in the decay signal (see Fig. 13) and for this reason NFS technique is also

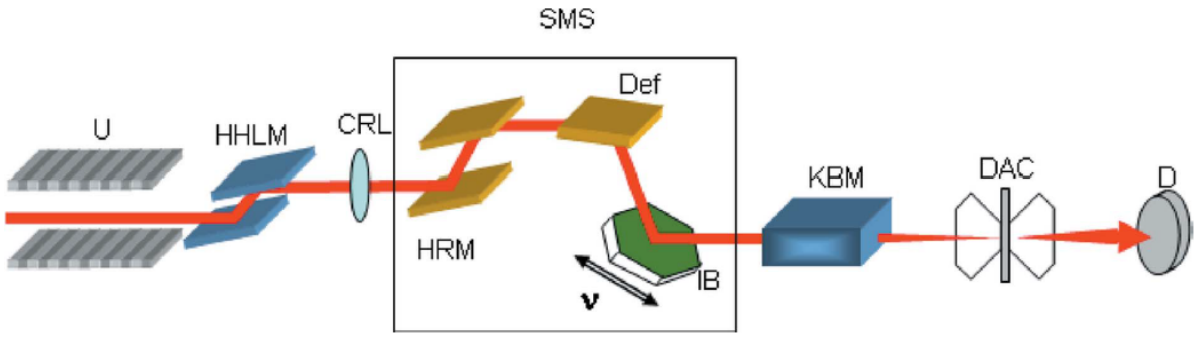

Figure 14. Optical scheme of experimental set-up with the Synchrotron Mössbauer Source. U, undulator; HHLM, high-heat-load monochromator; CRL, compound refractive lens; SMS, the Synchrotron Mössbauer Source: HRM, high-resolution monochromator; Def, Si (311) deflector; IB, iron borate crystal inside the furnace with the four magnets and mounted on the Mössbauer transducer; KBM, Kirkpatrick–Baez mirrors; DAC, diamond anvil cell; D, avalanche photodiode detector. From work Potapkin et al (2012).

called Mössbauer spectroscopy in the time-domain mode (whereas conventional Mössbauer spectroscopy measures hyperfine interactions in the energy-domain mode).

However, the NFS technique has several serious drawbacks. Firstly, NFS in general do not provide information about isomer shift, because shift of nuclear substates do not introduce any modifications to the exponential decay signal. One can extract only the *relative difference* in isomer shift between different components in case of the *multicomponent* spectra. Secondly, the fit of the multicomponent NFS spectra represent the ill-posed mathematical problem with many possible solutions. This problem is even more aggravated by the fact that the usual line broadening in the conventional Mössbauer spectra introduces additional *dynamic* beats to the NFS spectra with their own period (Grünsteudel et al, 1998).

These problems motivated development of the technique that would allow to obtain Mössbauer spectra with the synchrotron radiation in the energy-domain mode. Let us consider diffraction of the beam with energy of nuclear transition. In this case additionally to the usual electronic diffraction nuclei in the crystal absorb and re-emit coherently photons with exact resonance energy. Usually this phenomenon provides negligible contribution to the diffraction process. However, such discriminated *pure nuclear* reflection can be used as a source of the radiation consisting of only resonant γ-quants. Recently, based on this principle the Synchrotron Mössbauer Source (SMS) was developed (Potapkin et al, 2012).

The main element of the SMS optical scheme (Fig. 14) is the high-quality iron borate $^{57}FeBO_3$ single crystal (space group $R\bar{3}c$). Due to its symmetry, all (NNN) reflections with odd N (like (111), (333) *etc.*) are forbidden for electronic diffraction. However, iron borate

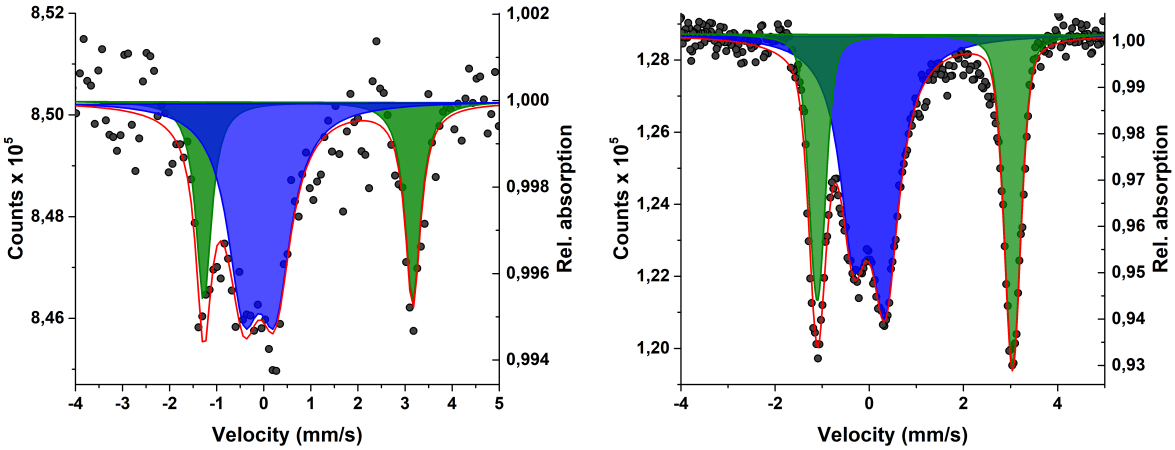

Figure 15. The comparison of the Mössbauer spectra of bridgmanite synthesized *in situ* in the laser-heated DAC measured with the conventional Mössbauer point source (left, spectrum from the work McCammon et al, 2010, Fig. 3c in original publication) and the SMS (right). The relative absorption and collection time for the spectrum with conventional source are about 0.5 % and one week, while for the spectrum with SMS they are 7 % and 8 hours, respectively.

is a canted antiferromagnet, so below Néel temperature T_N the antiferromagnetic ordering of the iron magnetic moments doubles the magnetic unit cell that gives the constructive interference for pure nuclear reflection in the (NNN)-type reflections. Therefore, in the geometry of (NNN) reflection with odd N, the pure nuclear reflection is observed, consisting of only resonant γ-quants.

The energy width of the synchrotron radiation after the undulator initially reduced by two premonochromators (HHLM and HRM, Fig. 14) to decrease heat load on the iron borate crystal. To obtain narrow unsplitted emission line the iron borate crystal is heated close to its T_N (348.35 K) with the applied external magnetic field (Potapkin et al, 2012). As in conventional Mössbauer spectroscopy, the energy modulation of the emission line is performed using the velocity transducer (Fig. 14), which moves the iron borate crystal in the plane parallel to the crystal surface.

The SMS source is analogous to the conventional radioactive source with several important advantages: 100 % linear polarization (due to initial polarization of the synchrotron radiation), absence of the non-resonant radiation and small beam spot size (about 10–15 μm). The spectra obtained with SMS are identical to the spectra from conventional Mössbauer spectroscopy except for the shape of the source line only. In the first approximation the shape of SMS emission line can be considered as a squared Lorentzian distribution (Smirnov et al, 2011) and should be taken into account using a transmission integral fit in

MossA software (Prescher et al, 2012). The small beam spot size of the SMS allows to carry out experiments with single crystals in the DAC that eliminates the potential experimental uncertainties related to the pressure gradient and inter-grain strain.

For the sake of comparison, the Mössbauer spectra of bridgmanite measured by conventional source and SMS are plotted in the Fig. 15. In both cases the bridgmanite was synthesized *in situ* in laser-heated DAC: the left spectrum is bridgmanite synthesized from polycrystalline majorite with composition $Mg_{0.82}Fe_{0.18}SiO_3$ from the work McCammon et al (2010) while the right spectrum is bridgmanite synthesized from glass with composition $Mg_{0.9}Fe_{0.1}Si_{0.9}Al_{0.1}O_3$ during this PhD project. Despite the lower amount of iron and the significantly shorter collection time the statistical accuracy of spectrum measured with SMS is much better.

3.2 X-ray diffraction

For more than a century the X-ray diffraction (XRD) remains the most important experimental technique for the determination of the atomic arrangement in the solid state. The study of diffraction phenomena began with visible light but eventually it became clear that it is a general phenomenon for any kind of matter or field with wave-like properties.

The diffraction effects are most pronounced when the dimensions of the diffracting object is comparable to the wavelength of waves. For the interatomic distances (of the order of several Å) in the solid state the corresponding electromagnetic radiation belongs to the X-rays. In this case the three-dimensional periodic structure of the crystal can be considered as a diffraction grating for the X-rays.

The diffraction patterns appear because of the wave interference. In case of the X-ray diffraction from the crystal lattice planes the condition for the constructive interference is given by a Bragg's law (or Wulff–Bragg's condition):

$$2d \sin\theta = n\lambda, \tag{18}$$

where d is the interplane distance, θ is the scattering angle (the angle between the lattice plane and the X-rays), n is a positive integer and λ is the wavelength of the incident wave. The physical meaning of this law is that if the path difference between two waves acquired during reflection by the lattice planes is multiple to the wavelength λ, they remain in phase and the constructive interference is observed (Fig. 16).

The diffraction experiment can be performed with single crystal or powder sample. In the former case the diffraction gives a pattern with set of the distinct diffraction peaks whereas in

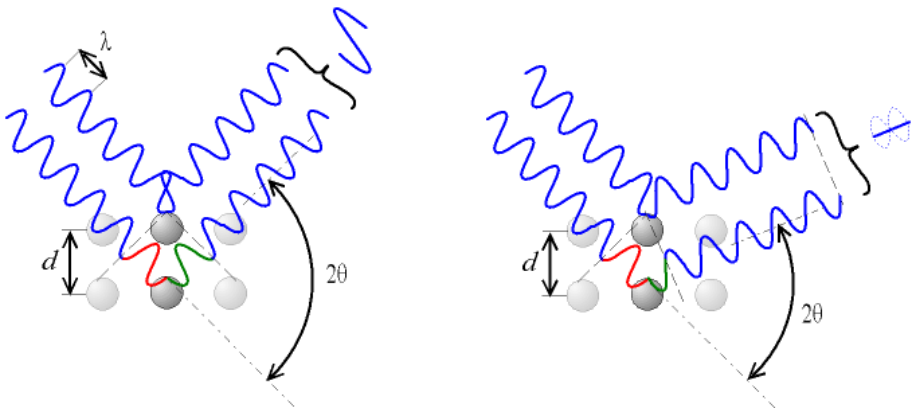

Figure 16. Illustration of the Bragg's law: the phase shift causes constructive (left figure) or destructive (right figure) interferences of the incident radiation. Modified after wikipedia.org.

the latter case the diffraction pattern will be formed by set of rings with center on the incident beam path because the powder consist of crystallites with random orientation. Powder XRD is commonly used to identify phases and to measure lattice constants while single-crystal XRD is more suitable for determination of the atomic arrangement in the studied crystal.

Using a monochromatic radiation with known λ one can determine the lattice spacing in the sample according to the Bragg's law. After indexation of diffraction peaks or rings (in case of the powder diffraction) by Miller indices, hkl, the symmetry of the crystal lattice can be determined (a space group) together with dimensions of the unit cell.

The information about the atomic positions in the unit cell can be obtained from the analysis of the diffraction peak intensities. The peak intensities depend on a structure factor that determines the scattering power of different lattice planes and directly related to the unit cell content (Giacovazzo, 2002)

$$F_{hkl} = \sum_{j=1}^{N} f_j e^{[-2\pi i(hx_j + ky_j + lz_j)]}, \tag{19}$$

where the summation is over all atoms in the unit cell, x_j, y_j and z_j are the positional coordinates of the jth atom, and f_j is the scattering factor of the jth atom.

The DAC has a limited opening angle ($\pm 38°$ with Boehler-Almax-type diamonds in the BX90 cell) that significantly reduces the covered range of θ values. Use of the hard X-rays improves situation because, according to the Bragg's law, the scattering angle decreases for the shorter wavelengths (eq. 18). The synchrotrons are ideal sources of high-energy X-rays and XRD experiments additionally benefit from the high brilliance and low divergence of the synchrotron radiation.

For the works of this PhD project the XRD experiments were important for the prod-

uct phase identification of the *in situ* bridgmanite synthesis in the laser-heated DAC and refinement of the iron distribution among different crystallographic sites in the bridgmanite and majoritic garnet inclusions. The single-crystal structural data of the iron coordination polyhedra were extensively used in the study of the pressure-induced spin transition of Fe^{3+} in the oxygen octahedra. Besides, XRD was used for the pre-selection of single crystals for the high-pressure experiments.

4 Synopsis of Results

This chapter summarizes major findings and conclusions of the four topics of interest of my PhD research. A complete description of these works can be found in the accompanying articles of this thesis.

4.1 Sound velocity of skiagite-iron-majorite solid solution

The single-crystals of skiagite-iron-majorite solid solution from work (Ismailova et al, 2015) were used. The studied material has composition $Fe_3^{2+}(Fe^{3+}_{1.532(2)}Fe^{2+}_{0.234(2)}Si_{0.234(2)})(SiO_4)_3$ based on single-crystal XRD refinement and microprobe analysis (Ismailova et al, 2015), and, therefore, the solid solution contains approximately 23 mol. % of iron-majorite component ($Fe_3(Fe^{2+},Si)(SiO_4)_3$). The NIS spectra were collected at compression up to 56 GPa in DAC at room temperature (RT).

Fig. 17 shows the obtained values of V_p and V_s as function of pressure in comparison with sound velocities of grossular ($Ca_3Al_2(SiO_4)_3$, Kono et al, 2010), pyrope ($Mg_3Al_2(SiO_4)_3$, Zou et al, 2012), Mg-majorite (Zhou et al, 2014), andradite ($Ca_3Fe_2(SiO_4)_3$, Jiang et al, 2004) and almandine ($Fe_3Al_2(SiO_4)_3$, Arimoto et al, 2015). A linear fit gives the following pressure dependencies of sound velocities at ambient temperature:

$$V_p = 7.43(9) + 0.039(4) \times P, \qquad V_s = 3.56(12) + 0.012(6) \times P \tag{20}$$

Here, V_p and V_s are in km/s and pressure is in GPa. The determined sound velocities of the skiagite-iron-majorite solid solution are substantially lower than for all other considered garnet end-members, while the pressure derivatives of both V_p and V_s are comparable (Fig. 17). Among garnet end-members with Fe^{3+} in the Y-site, only the elastic properties of andradite have been studied in detail (Jiang et al, 2004). Due to the lack of experimental data for pure skiagite, its elastic moduli have been estimated based on the solid solution considerations.

For a solid solution formed by atomic substitution on multiple distinct crystallographic

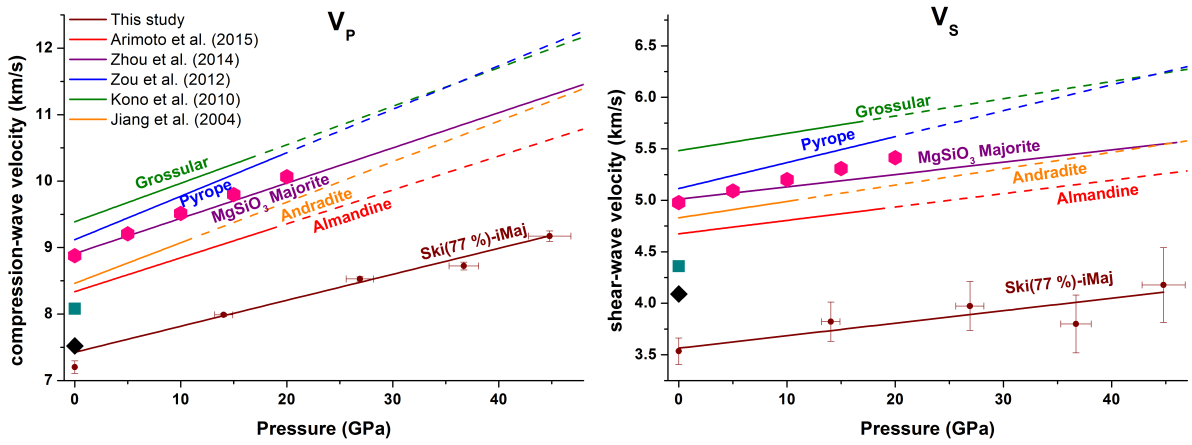

Figure 17. Sound velocities of the skiagite-iron-majorite solid solution and some silicate garnet end-members as a function of pressure at ambient temperature. The black diamonds, cyan squares and pink hexagons are estimated sound velocities of pure skiagite, khoharite and JF-55A inclusion, respectively. The solid lines conform to the pressure range investigated in the corresponding studies while dashed lines designate regions of extrapolation.

sites, the unknown elastic moduli and sound velocities of end-members can be estimated from solid solution with a particular composition. Let us consider the hypothetical garnet solid solution $(Fe_{2.4}Ca_{0.6})(Fe_{0.4}Al_{1.6})(SiO_4)_3$ for estimation of sound velocities of pure skiagite. The composition has two equivalent representations using end-members: 20% And + 80% Alm $\equiv$ 20% Gro + 20% Ski + 60% Alm. Assuming the validity of Vegard's law and that elastic moduli of the solid solution depend linearly on those of the end-members, we got for pure skiagite a unit cell length 11.73 Å, an aggregate adiabatic bulk modulus of 156.6 GPa, a shear modulus of 76.4 GPa, and Poisson's ratio of 0.29. Using these values we obtain the values $V_p = 7.52$ km/s and $V_s = 4.09$ km/s for skiagite at ambient conditions (plotted in Fig. 17 as black diamonds). Comparing our experimental data of skiagite-iron-majorite solid solution and estimated sound velocities of pure skiagite (Fig. 17), one can see that the presence of iron-majorite strongly decreases V_s. The cause of this behavior requires further investigation.

Recently reported majoritic inclusions in host garnet from an eclogite xenolith (Xu et al, 2017) contain a considerable amount (from 40 to 48 % depending on the particular end-member representation) of khoharite, $Mg_3Fe_2(SiO_4)_3$. The khoharite sound velocities were estimated in a similar way as performed above for skiagite. The hypothetical solid solution with composition $(Mg_{2.4}Ca_{0.6})(Al_{1.6}Fe_{0.4})(SiO_4)_3$ can be represented as 20% And + 80% Pyr $\equiv$ 20% Gro + 20% Kho + 60% Pyr. We obtain the following values for khoharite: $a = 11.66$ Å, $\rho = 3.859$ g/cm^3, $K = 153.9$ GPa, $G = 73.4$ GPa. The sound velocities for khoharite at ambient conditions are then $V_p = 8.08$ km/s and $V_s = 4.36$ km/s (plotted in Fig. 17 as cyan squares). As seen in the figure, khoharite also has lower sound velocities

compared to other silicate garnets, but occupies an intermediate position between andradite and skiagite in the series of garnets with Fe^{3+} in the Y-site.

In petrological models of the upper mantle and MTZ, iron ions are conventionally assumed to be divalent. This is also a common assumption when reducing electron microprobe data of natural samples from the deep mantle. In the case of garnet, Fe^{2+} is assigned to the X-site. It is therefore important to estimate the extent to which the presence of Fe^{3+} in the Y-site can influence sound velocities of the complex garnet solid solution. The most important consequences would be for the seismic profile in the 400-600 km depth interval where pyroxene completely dissolves into garnet and the volume fraction of the latter reaches a maximum (Wood et al, 2013).

As a representative example of Y-site Fe^{3+} influence, we consider the JF-55A inclusion (formation depth of 440 km) with pyroxenitic composition from the Jagersfontein kimberlite (Kiseeva et al, 2018). This is the most oxidized garnet from the series, so it is ideal as a limiting case. Based on electron microprobe and Mössbauer data, the composition of JF-55A from single-crystal structure refinement is $(Na_{0.06}Fe^{2+}_{0.42}Ca_{0.57}Mg_{1.97})(Fe^{3+}_{0.15}Mg_{0.38}Si_{0.44}Al_{1.01})(SiO_4)_3$ (Kiseeva et al, 2018). Therefore, the end-member representation is 3% Na-maj + 38% Mg-maj + 27% Pyr + 13% Alm + 11.5% Gro + 7.5% And.

In the original publication, all iron was assumed to be ferrous in the reduction of electron microprobe data (Tappert et al, 2005). There is no unique chemical formula that can be written from these data. Indeed, it is impossible to derive a composition without excess cations or the presence of vacancies based on normal assumptions about site charges. To proceed, we consider the following end-member representation: 3% Na-maj + 38% Mg-maj + 27% Pyr + 16% Alm + 16% Gro.

The differences between the two representations are the amount of almandine and grossular, and the presence of andradite. From Fig. 17 one can see that consideration of Y-site Fe^{3+} should decrease the resulting sound velocities. Indeed, the calculations for composition with Fe^{3+} give $V_p = 8.88$ km/s and $V_s = 4.98$ km/s (Fig. 17), while for the "Fe^{2+} only" composition the result is $V_p = 8.96$ km/s and $V_s = 5.03$ km/s at ambient conditions. Therefore, Y-site ferric iron decreases sound velocities by 1 % in this case. At 20 GPa and 300 K the difference remains 0.08 and 0.05 km/s for V_p and V_s, respectively. In terms of the 400—600 km depth interval in the preliminary reference Earth model (Dziewonski and Anderson, 1981), it corresponds to a 16 km depth difference.

However, if instead of using the experimental unit cell parameter for both compositions, the values calculated using Vegard's law are used, the difference in the velocities decreases to 0.05 and 0.03 km/s at ambient conditions for V_p and V_s, respectively. Moreover, the

non-uniqueness of the "Fe^{2+} only" composition substantially spreads the range of this difference. Therefore, the assumption that garnet contains only ferrous iron may lead to a overestimation of sound velocities up to 1% in case of garnet solid solution relevant to MTZ.

4.2 Iron oxidation state in the natural majoritic inclusions

The inclusions were released by crushing the host diamonds, mounted in epoxy disks with 0.7 mm thickness supported by brass rings and then polished. All measurements described here were performed on the samples mounted in epoxy. Due to the small size of the inclusions (typical lateral dimension is about 100–150 μm) and low natural abundance of the ^{57}Fe it is a very challenging or even impossible task to measure $Fe^{3+}/\Sigma Fe$ ratio by conventional Mössbauer spectroscopy with a reasonable precision. We used Mössbauer spectroscopy with SMS (Potapkin et al, 2012) for determination of the iron oxidation state. The inclusions were also studied by synchrotron XRD and confirmed as garnet single crystals (with few exceptions in the form of multidomain crystals with small amount of polycrystalline phases, see Kiseeva et al, 2018).

The studied garnet inclusions belong to the pyroxenite rock type and their compositions yield pressures of formation of 7.7–17.9 GPa using the Beyer–Frost majorite geobarometer (Beyer and Frost, 2017). The obtained Mössbauer spectra do not show the presence of Fe^{2+} in the Y site that, together with published results in McCammon and Ross (2003), Xu et al (2017), confirms a strong preference to balance Si^{4+} in the Y-site by Mg^{2+} (not Fe^{2+}) in the garnet structure.

Because the Y-site contains only ferric iron, the refinement of the Y-site iron amount provides independent estimate of the $Fe^{3+}/\Sigma Fe$ ratio from XRD data. The structural refinements of all garnets were performed with the following composition constraints: (*i*) each crystallographic site of garnet is fully occupied, (*ii*) only O, Si, Mg, Al, Fe and Ca are considered and the presence of other elements is neglected, (*iii*) in the Y site, Mg, Si and Al are refined as a single "Al" atom (X-ray scattering by equiproportional mixture of Si and Mg is the same as scattering by Al) and (*iiii*) the amount of Ca in the X site is fixed based on the microprobe data (Tappert et al, 2005).

The $Fe^{3+}/\Sigma Fe$ ratio obtained from the XRD data is in a good agreement with the Mössbauer spectroscopy results and has significantly smaller random errors (Fig. 18). Our results show a clear approximately linear trend of increase of Fe^{3+} part with formation pressure (Fig. 18).

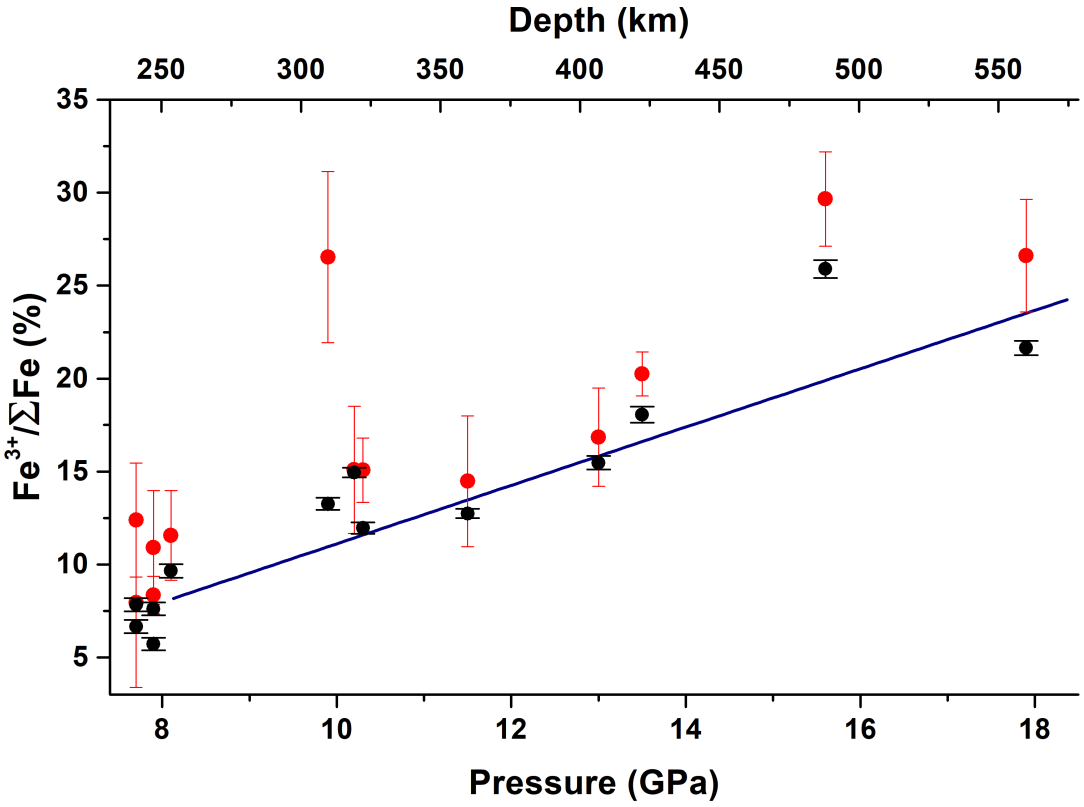

Figure 18. The dependence of the garnet inclusion oxidation state on the formation depth. The red circles are results of the Mössbauer spectroscopy while the black circles is part of the octahedral Y-site Fe according to refinement of the single-crystal XRD data. The blue line is a linear fit of the XRD data.

To estimate the corresponding oxygen fugacities the following equilibrium was used:

$$2Ca_3Al_2(SiO_4)_3 + 4/3Fe_3Al_2(SiO_4)_3 + 2.5Mg_3(Mg,Si)(SiO_4)_3 + O_2 = 2Ca_3Fe_2(SiO_4)_3 + 10/3Mg_3Al_2(SiO_4)_3 + 4SiO_2 \quad (21)$$

The reliability of our thermodynamical calculation method was checked using data from work Rohrbach et al (2007) in which garnets were synthesized in equilibrium with Fe metal. For 4 of the 5 iron metal-saturated experiments the calculated $\log f_{O_2}$ are, as expected, just below Fe–FeO equilibrium (Fig. 19) confirming the validity of our approach.

For the analysed garnets the corresponding oxygen fugacities range from 0.26 $\log f_{O_2}$ units below to about 3 $\log f_{O_2}$ units above the IW buffer (Fig. 19), implying that they were not in equilibrium with Fe metal and not oxidized by disproportionation of Fe^{2+} to Fe^{3+} plus Fe^0. It has previously been suggested that the pyroxenite substrates in which the garnets and their host diamonds crystallized were generated by reactions between subducted eclogite and peridotite aided by carbonate melt (Kiseeva et al, 2016) and that diamond and oxidized

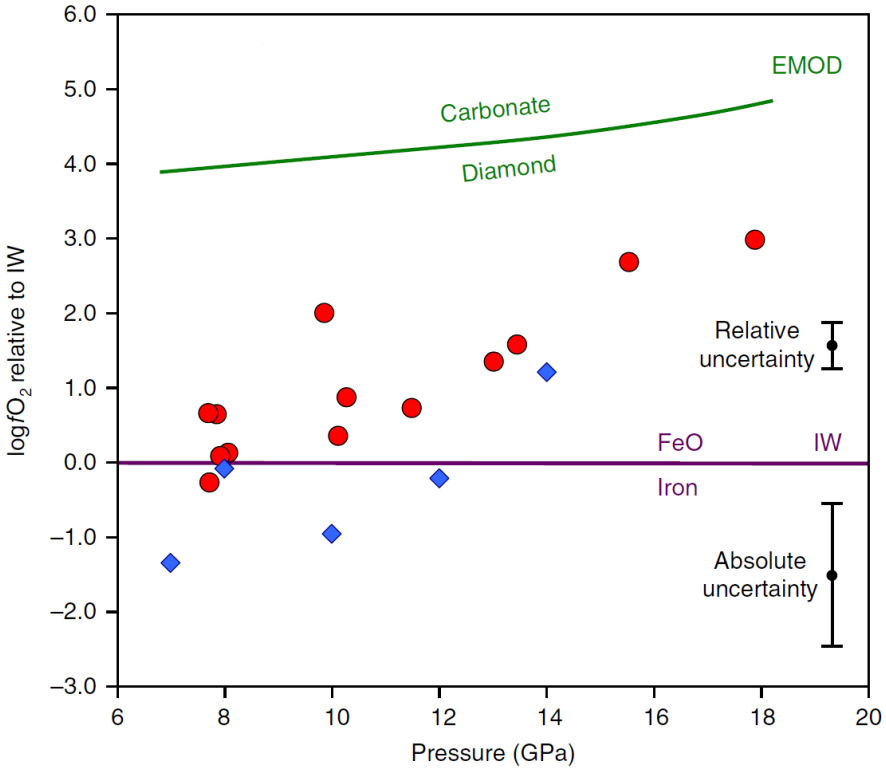

Figure 19. Calculated oxygen fugacities of the studied majoritic inclusions (red circles) and of garnets crystallized in coexistence with Fe metal (blue diamonds Rohrbach et al, 2007). IW means the iron-wüstite buffer, EMOD is the enstatite-magnesite-olivine-diamond buffer.

majoritic garnet are products of this interaction. Indeed, the comparison of our results to a carbon–carbonate equilibrium (EMOD in Fig. 19) shows that our inclusions are in the (reduced) diamond stability field and that they approach EMOD with increasing pressure, which means that oxidation of Fe^{2+} during the reduction of carbonate in a fluid or melt phase is a plausible mechanism for generating the Fe^{3+} present in the garnets.

4.3 Pressure-induced spin transition of Fe^{3+} in the oxygen octahedron

As mentioned above (section 2.3), to date there is a poor agreement between different studies in the reported spin transition pressures. This discrepancy is caused by the fact that most of the experiments are performed with powder samples. In this case the non-hydrostatic conditions inside pressure chamber lead to the enormous broadening of the transition region (see comparison of the single-crystal and powder experiments in Cerantola et al, 2015) that additionally may result in wrong conclusions about manner of the spin transition (crossover *vs* phase transition).

Table 1: The difference in δ_{CS} values and ΔE_Q of ferric iron before and after the pressure-induced spin transition. All parameters refer to ambient temperature if not given explicitly.

Compound	${}^{HS}\delta_{CS} - {}^{LS}\delta_{CS}$, mm/s	ΔE_Q, mm/s	
		before	after
$FeBO_3$	0.13(3)	0.06(9)	1.98(3)
$Fe_3(Fe_{1.766}Si_{0.234})(SiO_4)_3$	0.19(2)	0.25(6)	0.89(1)
$CaFe_2O_4$	0.16(3) at 5 K	0.6 & 1.2	1.1 & 1.6
FeOOH	0.3 at 6 K	—	2.5 at 50 K
Fe_2O_3	0.22(3)	0.71(2)	0.76(3)

We have investigated pressure-induced spin transition in iron borate, iron sesquioxide and skiagite-iron-majorite solid solution using Mössbauer spectroscopy with SMS. In order to eliminate potential influence of the pressure gradients and inter-grain strains we have carried out experiments with single crystals and used neon as a pressure transmitting medium. The obtained results were used in the comparative analysis together with literature data for goethite, calcium ferrite and andradite. In search of regularities in behavior of spin transition and hyperfine parameters the structural data about geometry of iron octahedra in the compounds of interest were extensively used. We relied only on the reliable single-crystal crystallographic data in the comparative analysis.

Hyperfine parameters at spin transitions in $Fe^{3+}O_6$ octahedra The data on hyperfine parameters of ferric iron in compounds of interest before and after spin transition are compiled in Table 1. All considered compounds demonstrate similar behavior through spin transitions. The main features are *(i)* drop in the δ_{CS} value, *(ii)* disappearance of magnetic order at room temperature, and *(iii)* LS state of ferric iron ion characterized by doublet with higher quadrupole splitting (relative to the values of HS Fe^{3+}).

There is a large spread of ΔE_Q values of the Fe^{3+} LS state at RT (from 0.76 mm/s in Fe_2O_3 to 2.5 mm/s in FeOOH) that is apparently related to the different degree of the iron octahedron distortion. In section 3.1.2 it was shown that at spin transition of Fe^{3+} in octahedral environment the main contribution to the EFG changes from the lattice to the electronic one, that should lead to the significant increase in the ΔE_Q values. Despite this fact, there is an overlap between ΔE_Q values of Fe^{3+} in HS and LS state (Table 1). These observations demonstrate that an identification of the LS state based solely on the

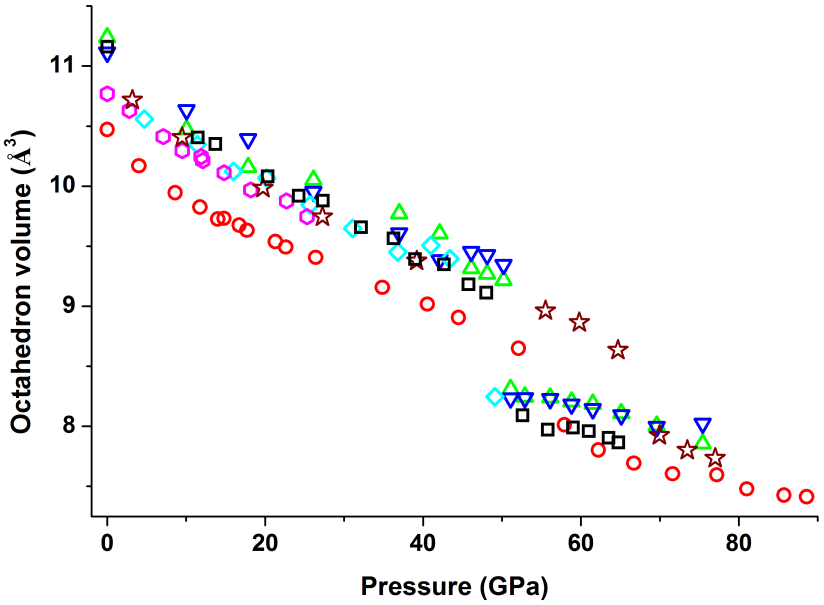

Figure 20. Volume of $Fe^{3+}O_6$ octahedra as a function of pressure for different compounds. Black squares correspond to iron borate, red circles to skiagite-iron-majorite solid solution, green and blue triangles to two different structural positions in calcium ferrite, cyan diamonds to goethite, magenta hexagons to hematite and brown stars to andradite. The deviation of the skiagite-iron-majorite data from the rest compounds is related to the mixed occupancy of the Y-site by Fe and Si.

quadrupole splitting values (that is a common case for NFS data) might be ambiguous.

Our data show that much more reliable sign of the spin transition is decrease in δ_{CS} value. Using NIS data we have demonstrated that the SOD contribution is not higher than 10 % at RT. Therefore, it is the difference in isomer shift between HS and LS states that is mainly responsible for decrease in center shift value. According to the modern density functional theory calculations the metal-ligand bond length strongly influences δ_{IS} value (Neese, 2002), therefore, the lower δ_{IS} in LS state is related to the shorter bond length relative to the HS state.

Volume of $Fe^{3+}O_6$ octahedron at spin transition Fig. 20 shows the dependence of the octahedron volumes in the studied compounds as a function of pressure. One can see that the spin transition of Fe^{3+} starts in the pressure range 45–60 GPa and over a remarkably narrow range of octahedron volume — 8.9–9.3 Å^3. This suggests that the spin transition is controlled by the electronic density inside the octahedron.

The transition bond length at which the spin transition should happen can be estimated using Tanabe-Sugano diagrams (Tanabe and Sugano, 1954a,b). For the ideal octahedron we

Table 2: Crystal field parameters and the estimated polyhedron volumes from eq. (22) at transition onset.

Compound	$10D_q$ (cm^{-1})	B (cm^{-1})	β	V_0 (Å^3)	est. V_t (Å^3)	exp. V_t (Å^3)
$FeBO_3$	12700	680	0.68	11.16	9.0	9.1
Fe_2O_3	14000	540	0.54	10.77	10.2	9.0
FeOOH	15320	590	0.59	10.81	10.3	9.3
$Ca_3Fe_2(SiO_4)_3$	12600	593	0.59	10.88	9.2	8.9
$FeCO_3$	10325	747	0.84	13.2	10.6	10.3

can write:

$$V_t = V_0 \left(\frac{D_q^0}{D_q^t} \right)^{3/5}, \tag{22}$$

where V is the octahedron volume, and the indices 0 and t correspond to ambient pressure and at the spin transition, respectively. The results of this estimation for the compounds under consideration are collected in Table 2. One can see that this simplest model overestimates the transition volume notably in the case of hematite and goethite. If predictions would be accurate, the spin transition in these compounds would take place at 20–25 GPa.

This discrepancy is most likely related to octahedral distortions. In both hematite and goethite, octahedral Fe-O bonds divide into two groups (three bonds in each) with different lengths: approximately 1.95 and 2.10 Å at ambient conditions. Electrostatic potentials with symmetry lower than cubic contain additional terms that have different power dependencies on r (for instance, the term $\propto r^{-3}$ for a trigonally distorted octahedron, see ch. 2 in Figgis and Hitchman, 2000). Therefore, consideration of the proper electrostatic potentials for hematite and goethite should lead to a correct estimation of the transition volumes, but such an examination was beyond the scope of this work.

In all studied compounds, iron octahedra show very similar compressibility (Fig. 20). The isothermal bulk moduli of $Fe^{3+}O_6$ octahedra in different compounds at ambient conditions vary between 170 and 210 GPa. In the vicinity of the spin transition the average value of K is around 400 GPa (iron borate has the lowest value of 340(20) GPa). As LS ferric iron has a significantly smaller ionic radius, one can expect that the elastic moduli should increase at the HS→LS transition. Indeed, an comparison of the equations of state of HS and LS $Fe^{3+}O_6$ octahedra shows that at 50 GPa the bulk modulus changes from 340(20) GPa to 410(70) GPa and from 400(20) GPa to 510(50) GPa for $FeBO_3$ and $CaFe_2O_4$, respectively.

Cooperativity at spin transition Available single-crystal XRD data show that the pressure-induced spin transitions in inorganic compounds have a strong tendency to result in isosymmetric transitions[4]. From the phenomenological theory of phase transitions, it follows that they can proceed either as first-order transitions or, beyond the critical point, as a crossover (supercritical manner) in which there is no discontinuity in any free-energy derivative (Christy, 1995).

The abundance ratio of different spin states would be controlled by Boltzmann factor if the cations change spin states independently. However, because cations in different spin states have different ionic radii, a spin transition of one ion introduces a strain field into the crystal lattice (one can consider the ion in a different spin state as an impurity). The coupling of the cations with this strain field determines the strength of cooperative behavior at the spin transition and, accordingly, the critical temperature (T_{cp}) at which the first-order phase transition is changed by crossover behavior.

For the compounds considered in this study the condition of cooperativity is as follows: if iron octahedra share common oxygen atoms and form an infinite framework, the compound shows strong cooperative behavior at pressure-induced spin transitions (by "strong" we mean that the critical point lies above room temperature). If this condition is fulfilled there are favorable conditions for magnetic ordering by means of superexchange interactions. Indeed, all such studied compounds ($FeBO_3$, α-Fe_2O_3, FeOOH and $CaFe_2O_4$) in the HS state are magnetically ordered at room temperature in the vicinity of the spin transition (see supplemental material in Vasiukov et al, 2017b). However, if the magnetic ordering disappears in the LS state, when, strictly speaking, the transition could not be isosymmetric, because at such transition the symmetry relative to time reversal is changed. This leads to important consequences: (i) the spin transition in magnetically-ordered compounds can only proceed as a first-order phase transition, and (ii) the temperature of the critical point cannot be lower than the Néel (Curie) temperature of the HS phase in the vicinity of the spin transition. These conclusions are valid if the spin transition is the driving force of the transition.

The spin transitions in the Y-site of the garnet structure (andradite and skiagite–iron-majorite solid solution) show explicit crossover behavior at room temperature within $\sim$ 10 GPa. This is in agreement with the formulated cooperativity condition, since Y-site octahedra do not share oxygen atoms (Fig. 2). Note that this is a clear structure feature, where the spin transition of Mn^{3+} (d^4 configuration) in the octahedral site of the hydrogarnet henritermierite proceeds in the same way (Friedrich et al, 2015).

[4]At isosymmetric transition the space group preserves and the atoms do not change their Wyckoff positions. In the literature it is also often called isostructural.

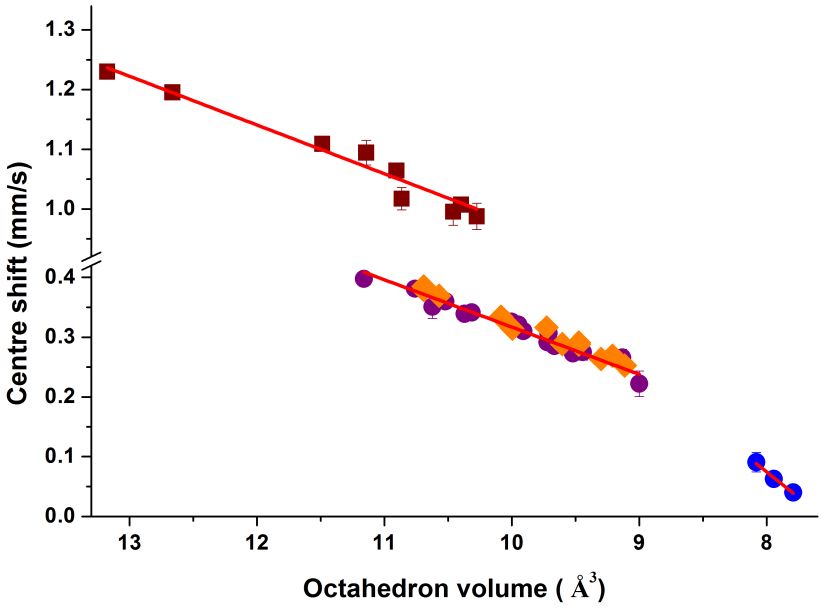

Figure 21. Center shift as a function of the octahedron volume shows a linear dependence. Purple and blue circles are data of $FeBO_3$ (HS and LS, respectively), orange diamonds correspond to α-Fe_2O_3, and brown squares belong to $FeCO_3$ (single-crystal data from Cerantola et al, 2015). The red lines are linear fits to the underlying points (the middle line is a fit of the $FeBO_3$ HS points). In the HS state, slope values are the same for both ferric ($FeBO_3$, α-Fe_2O_3) and ferrous ($FeCO_3$) iron ions.

In the case of solid solutions, the highest T_{cp} value will be seen in the iron end-member. Reduction of the amount of iron in the system will decrease the cooperativity of iron octahedra and, accordingly, the critical point temperature. In natural systems pressure-induced spin transitions are inferred to occur in the Earth and exoplanet interiors. In view of the above considerations the iron spin transition in the Earth's mantle should tend to crossover behavior for the following reasons: (*i*) mantle minerals are solid solutions with relatively low concentrations of iron that promote a decrease of the cooperativity of iron ions, and (*ii*) the temperatures of the mantle are high (> 2000 K) at spin-transition pressures.

Center shift *vs* polyhedron volume Single-crystal XRD experiments provide a unique opportunity to study the dependence of δ_{CS} on the polyhedron volume (Fig. 21). In addition to the compounds measured in this work, we also used for comparison single-crystal Mössbauer data of Fe^{2+} in siderite ($FeCO_3$) from Cerantola et al (2015).

In all studied compounds the center shift varies linearly with octahedron volume. It is interesting that for the HS octahedra, linear fits have the same slope (Fig. 21) within un-

certainty, regardless of valence state: 0.079(4), 0.079(5) and 0.082(4) mm/s·Å^{-3} for $FeBO_3$, α-Fe_2O_3 and $FeCO_3$, respectively. This similarity of slopes suggests that the volume dependence of δ_{CS} is governed by the same mechanism in all investigated compounds. The noted difference in pressure dependence of isomer shift between Fe^{2+} and Fe^{3+} compounds (Williamson, 1978) is therefore simply related to the higher compressibility of ferrous iron (at least in the case of octahedral coordination).

The skiagite-iron-majorite data demonstrate that volume dependence of CS is distinct for different coordination polyhedra. The volume dependence of δ_{CS} of the cubic X-site Fe^{2+} is nonlinear in the investigated pressure range and considerably weaker than for the case of the octahedron.

Based on the obtained volume dependence for δ_{CS} and compressibility data we can constrain possible range of center shift values for the HS Fe cations coordinated by oxygen octahedra. The average decrease in δ_{CS} before the beginning of the pressure-induced spin transition is 0.15 ± 0.03 mm/s for Fe^{3+} and 0.25 ± 0.05 mm/s for Fe^{2+}. The δ_{CS} of LS state Fe after pressure-induced spin transition should be smaller by 0.28 ± 0.05 mm/s for Fe^{3+} and 0.55 ± 0.1 mm/s for Fe^{2+} than δ_{CS} of HS state Fe at ambient pressure.

4.4 Iron behavior in the Fe,Al-bearing bridgmanite

As a precursor for the *in situ* bridgmanite synthesis in DAC two kind of glass with composition $Mg_{0.9}Fe_{0.1}Si_{0.9}Al_{0.1}O_3$ (according to electron microprobe data) and different $Fe^{3+}/\Sigma Fe$ ratio 0 and 50 % (determined by Mössbauer spectroscopy) were used. The glass stoichiometry approximately corresponds to the expected lower mantle composition and crystallization of the material from it at appropriate conditions can give a product consisting of bridgmanite as the only phase. In our experiments the products of the glass crystallization and electronic states of iron were studied by synchrotron XRD diffraction and Mössbauer spectroscopy with SMS, respectively.

Change in the ground state of the A-site Fe^{2+} In agreement with previous Mössbauer studies (Lin et al, 2013) we observe the doublet with high quadrupole splitting (> 3.7 mm/s) above 30 GPa (see Fig. 24). As mentioned in the section 2.4 there are two interpretations of this component: an intermediate spin state of Fe_A^{2+} (Lin et al, 2008, McCammon et al, 2008) or Fe_A^{2+} in different local oxygen arrangement (Bengtson et al, 2009, Hsu et al, 2010).

In discussion of the possible spin states of the Fe_A^{2+} the crystal field splitting scheme of the cuboctahedron is used in literature (Lin et al, 2013). However, the real coordination

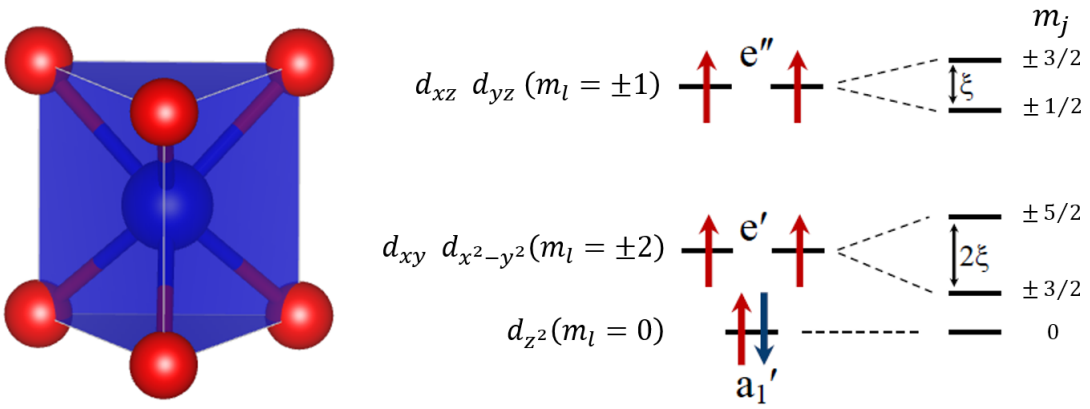

Figure 22. Crystal field splitting in a trigonal prism, the z-axis is collinear to the 3-fold axis of the trigonal prism. Note that in case of the high-spin state of d^6 configuration there is a competition between ${}^5E'$ and ${}^5A_1'$ electronic terms for the ground state because of the spin-orbit splitting of e' level.

polyhedron of the bridgmanite A-site is a bicapped trigonal prism which has considerably different splitting scheme of the d-orbitals. Let us approximate crystal fields splitting of the A-site by trigonal prism (Huisman et al, 1971, Fig. 22). The influence of two capping atoms can be considered as a small perturbation because of their longer Fe-O distances and be neglected in the first approximation. The validity of this assumption is supported by results of the molecular orbital analysis in Burdett et al (1978) where the obtained crystal field splitting scheme of bicapped trigonal prism is similar to the trigonal prism.

Looking on Fig. 22, it is easy to see that spin transition of d^6 configuration should lead to LS state with $S = 0$ and appearance of any intermediate spin state is unlikely. However, the HS-LS transition can be excluded because both Fe_A^{2+} doublets with high and low quadrupole splitting (Fig. 24a) have the same center shift values. Therefore, the more plausible candidate for the doublet with high quadrupole splitting is Fe_A^{2+} with more subtle changes in the electronic state than the spin transition.

We note, that the energy difference between a_1' and e' levels depends in a sensitive way on the geometry of trigonal prism (as D_{3h} point group allows arbitrary height of the trigonal prism). Moreover, crystal field of the trigonal prism does not quench orbital moment of the d-orbitals and e' level can be splitted by strong spin-orbit coupling with magnitude 2ξ (Fig. 22). As result, it is not self-evident which electronic term, ${}^5E'$ or ${}^5A_1'$, will be adopted as ground state.

Therefore, we conclude that the appearance of the Fe_A^{2+} doublet with high quadrupole splitting is related to the transition between these electronic terms. Such interpretation is

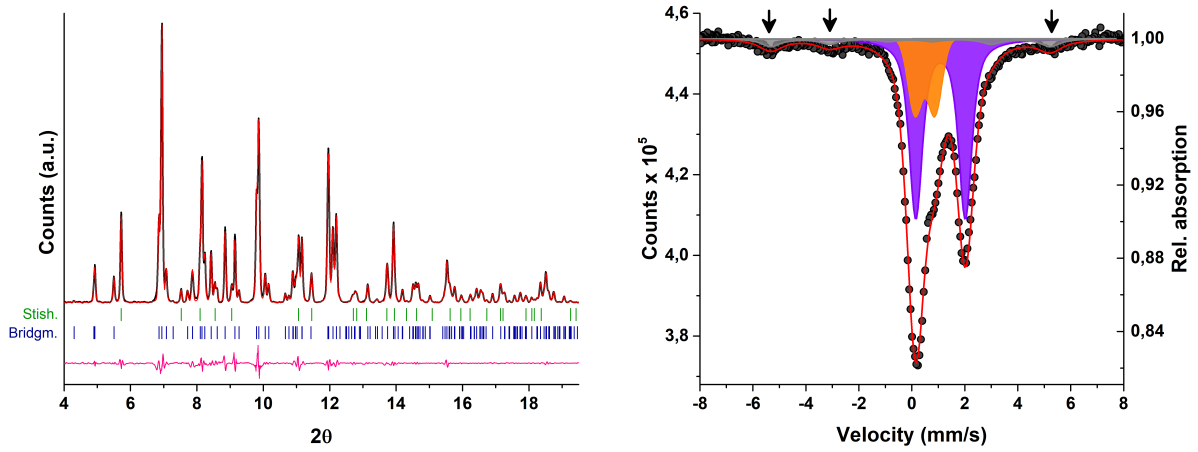

Figure 23. Powder XRD pattern and Mössbauer spectrum of the decompressed sample synthesized from reduced glass at 35 GPa and 2500 K. While the bridgmanite dominates diffraction pattern, the first two peaks of stishovite, (110) and (101), are clearly visible. On the Mössbauer spectrum, apart from Fe^{2+}_A and Fe^{3+}_A in bridgmanite (violet and orange doublets, respectively), one can see signal of α-iron (grey sextet). The evident sextet lines (1st, 2nd and 6th), which are not overlapped with bridgmanite components, are marked by arrows.

in agreement with theoretical predictions (Bengtson et al, 2009, Hsu et al, 2010) because $^5E'$ term is a Jahn-Teller active state and, due to Jahn-Teller theorem, will have a different local ligand arrangement comparing to the non-degenerated $^5A'_1$ term. The difference in quadrupole splitting between these two terms can be enhanced by mixing of $3d$-orbitals (see Burdett et al, 1978).

***In situ* evidence of the iron disproportionation reaction and evolution of the iron oxidation state with synthesis pressure** The abundance of bridgmanite and its strong preference to accommodate Fe^{3+} make the redox reaction generating trivalent iron important for the composition of lower mantle. For instance, the proposed 1 wt.% Fe metal in lower mantle (based on multianvil experiments, Frost et al, 2004) is a reduced product of the Fe^{2+} disproportionation. However, high-pressure assemblage in multianvil press is an open system with respect to oxygen so the experimental artefacts leading to the changes in iron oxidation state cannot be unambiguously ruled out. The DAC is a closed system with respect to oxygen and appearance of metallic iron in synthesis of bridgmanite from precursor containing only Fe^{2+} would be a strong evidence of the ferrous iron disproportionation.

The disproportionation of ferrous iron in a simple ionic form is $3Fe^{2+} \rightarrow 2Fe^{3+} + Fe^0$. However, taking into account that we are dealing with Fe^{2+} in bridgmanite, the complete

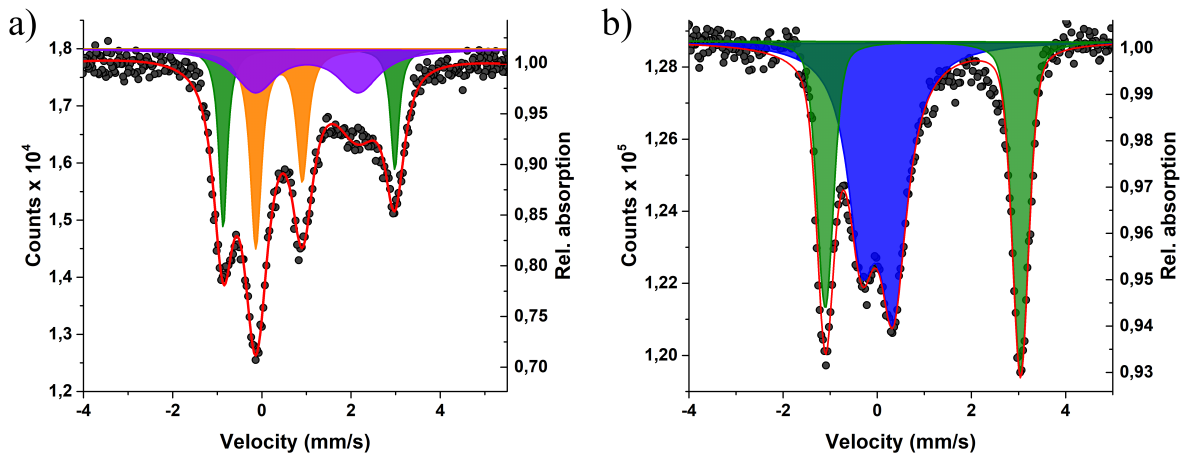

Figure 24. Examples of Mössbauer spectra of bridgmanite after synthesis at high pressures. These bridgmanites were synthesized from oxidized precursor at 45 GPa (a) and reduced precursor at 86 GPa (b). The green doublet corresponds to the different electronic term of Fe^{2+}_A (see text) while the blue doublet is low-spin Fe^{3+}, most likely in the B-site. The rest components conform to those in Fig. 23.

reaction is

$$3Fe^{2+}SiO_3 \rightarrow Fe^{3+}Fe^{3+}O_3 + 3SiO_2 + Fe^0 \quad (23)$$

and Fe^{2+} disproportionation produces 3 moles of stishovite for every mole of iron metal. Taking into account that the precursor is comprised by 90 % of $MgSiO_3$, the Fe metal should be the least abundant phase in the synthesized sample and difficult for identification.

In our experiments, the powder diffraction pattern of the samples synthesized from reduced precursor is dominated by bridgmanite but stishovite is also clearly visible (Fig. 23). The presence of Fe metal could not be reliably established since its diffraction peaks would overlap with bridgmanite ones. The Rietveld refinement cannot be used in this case because laser heating in DAC produces polycrystalline material with significant texturing.

In Mössbauer spectra of the samples synthesized at high pressures because the expected singlet of ε-Fe would totally overlap with strong bridgmanite signal. However, this problem can be overcome by decompression of the material, as Fe metal (if present) have to transforms to another allotrope, α-Fe, which is ferromagnetic with distinguishable magnetic sextet. Indeed, on the Mössbauer spectrum of the decompressed sample one can distinctly see separate peaks of the α-Fe sextet (Fig. 23). These results unambiguously confirm that the iron disproportionation produces Fe^{3+} in this case. The experiments with oxidized precursor around 50 GPa show that $Fe^{3+}/\Sigma Fe$ ratio slightly decreases relative to the precursor value (from 47(3) to 37(4)%). This points out on the absence of Fe^{2+} disproportionation in this case and, indeed, we did not observe stishovite peaks on the powder diffraction pattern.

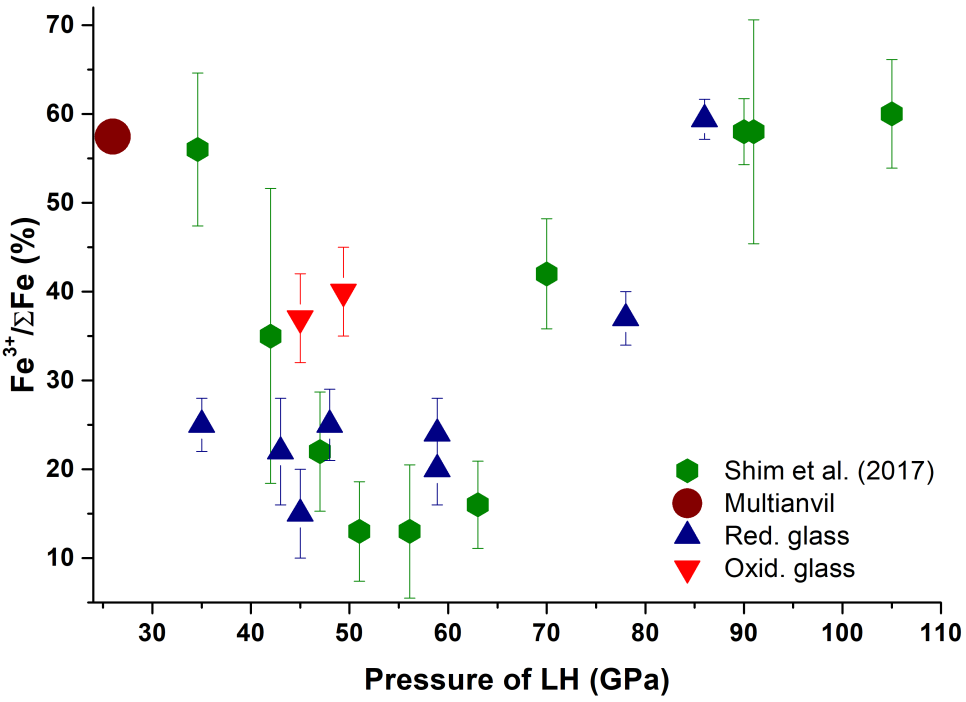

Figure 25. Dependence of the Fe^{3+} content in bridgmanite on the synthesis pressure. Our results are compared with data from Shim et al (2017).

We were able to identify all products of the Fe^{2+} disproportionation in the syntheses from reduced precursor at pressures between 35 and 60 GPa. However, the Mössbauer spectrum of the sample synthesized at 86 GPa (Fig. 24b) is quantitatively different from spectra of the samples synthesized at lower pressures (like Fig. 24a). In this case the spectrum is superposition of only two doublets, one is the high-pressure electronic term of Fe^{2+}_A and another is a new doublet with $\delta_{CS} = 0.00(2)$ mm/s and $\Delta E_Q = 0.68(2)$ mm/s (at 87 GPa and RT) which was not observed at lower pressures. Note that doublet with similar hyperfine parameters was observed in McCammon et al (2010) after laser heating of majorite at 125 GPa and in Kupenko et al (2015) after laser heating of bridgmanite above 40 GPa. In the former work this doublet was interpreted as a LS Fe^{2+}_A, whereas authors of the latter work treat it as a LS Fe^{3+}_B.

The center shift of the blue doublet on Fig. 24b is lower by 0.35 mm/s than the corresponding value of HS Fe^{3+}_A around 50 GPa. The volume dependence of center shift cannot explain such big difference. According to results of section 4.3 (see Vasiukov et al, 2017b), center shift of 0.00(2) mm/s is too low to correspond with any electronic state of Fe^{2+}, even with its low-spin state, but it is close to characteristic values of LS Fe^{3+} in oxygen octahedron. As mentioned in section 2.4, the theoretical studies predict redistribution of ferric iron between A- and B-sites above 50 GPa (Hsu et al, 2012). Therefore, we interpret the blue

doublet in Fig. 24b as LS Fe_B^{3+} in agreement with work Kupenko et al (2015).

This stabilization of LS Fe^{3+} together with redistribution of iron between A- and B-site apparently has a significant effect on the $Fe^{3+}/\Sigma Fe$ ratio in the synthesized bridgmanite (Fig. 25). While our data show rather constant Fe^{3+} content between 35 and 60 GPa ($\sim$ 25 %) there is a clear increase of $Fe^{3+}/\Sigma Fe$ ratio above this pressure interval. Generally, our results are in agreement with recent work Shim et al (2017) but authors of this study did not observe the doublet of LS Fe_B^{3+} at high pressures.

We also note that there is no space for ε-Fe singlet on the spectrum of the sample synthesized at 86 GPa (Fig. 24b) and we do not observe any sign of α-Fe in Mössbauer spectrum of the decompressed sample. In principle, Fe^{3+} in bridgmanite can be produced by another type of redox reaction where Mg, Al or Si are reduced with formation of bridgmanite with cationic vacancies. Any of these three compounds will be difficult to detect by powder XRD as strong bridgmanite signal should obscure their peaks. However, our powder XRD data show presence of stishovite which should not appear in such redox reactions. Therefore, the question regarding the redox reaction which produces the large amount of Fe^{3+} at pressures above 60 GPa remains open.

4.5 List of manuscripts and statement of author's contribution

1. Vasiukov, D. M., Ismailova, L., Kupenko, I., Cerantola, V., Sinmyo, R., Glazyrin, K., McCammon, C., Chumakov, A. I., Dubrovinsky, L, Dubrovinskaia, N. (2017). Sound velocities of skiagite–iron–majorite solid solution to 56 GPa probed by nuclear inelastic scattering. *Physics and Chemistry of Minerals*. DOI: 10.1007/s00269-017-0928-8.

   L.I. synthesized and pre-selected the studied single crystals. I.K., V.C., R.S., K.G., C.M., A.I.C and L.D. performed the NIS experiments. D.M.V. processed and interpreted the NIS data. D.M.V., N.D., L.D. and C.M. wrote the manuscript. My contribution is 60 %.

2. Kiseeva, E. S., Vasiukov, D. M., Wood, B. J., McCammon, C., Stachel, T., Bykov, M., Bykova, E., Chumakov, A., Cerantola, V., Harris, J. F., Dubrovinsky, L. (2018). Oxidized iron in garnets from the mantle transition zone. *Nature Geoscience*, **11**, 144–147.

   Work was initiated and planned by E.S.K. and L.D. T.S. and J.W.H. provided the samples and their detailed description. M.B., D.M.V., E.B. and L.D. performed the X-ray diffraction measurements. D.M.V., M.B., E.B. and L.D. processed and analysed the diffraction data. D.M.V., V.C., A.C. and C.M. collected, processed and analysed the Mössbauer spectra. E.S.K. and B.J.W. interpreted the data, performed the ther-

modynamic calculations and prepared the manuscript. My contribution is 40 %.

3. Vasiukov, D. M., Dubrovinsky, L., Kupenko, I., Cerantola, V., Aprilis, G., Ismailova, L., Bykova, E., McMammon, C., Prescher, C., Chumakov, A. I., Dubrovinskaia, N. (2017). Pressure-induced spin transition of Fe^{3+} in oxygen octahedra. arXiv preprint arXiv:1710.03192. *Physical Review B*, under review.

   D.M.V., I.K., V.C., G.A., L.I., L.D., C.P., C.M. and A.I.C. performed the Mössbauer experiments. E.B. prepared diffraction data. D.M.V. processed and interpreted the Mössbauer data and developed the discussion. D.M.V., L.D., N.D. and C.M. wrote the manuscript. My contribution is 90 %.

4. Vasiukov, D. M., van Driel, J., Bykova, E., Bykov, M., Aprilis, G., Cerantola, V., Kupenko, I., McCammon, C., Schönleber, A., Glazyrin, K., Prakapenka, V., Liermann, H.-P., Hanfland, M., Chumakov, A.I., Dubrovinsky, L., Dubrovinskaia, N. Iron behaviour in Fe,Al-bearing bridgmanite between 35–80 GPa. To be submitted to *Earth and Planetary Science Letters*.

   J.v.D. synthesized the glass used for bridgmanite synthesis. D.M.V., G.A., V.C., I.K., L.D., C.M. and A.I.C. performed the Mössbauer experiments. E.B., M.B., L.D., G.A., K.G., V.P., H.-P.L. and M.H. carried out diffraction experiments. D.M.V. processed and interpreted the Mössbauer data. The diffraction data were treated by D.M.V., E.B., M.B., A.S., L.D. D.M.V., N.D. and L.D. wrote the manuscript. My contribution is 50 %.

References

Achterhold K, Keppler C, Ostermann A, Van Bürck U, Sturhahn W, Alp E, Parak F (2002) Vibrational dynamics of myoglobin determined by the phonon-assisted Mössbauer effect. Phys Rev E 65(5):051,916

Akahama Y, Kawamura H (2006) Pressure calibration of diamond anvil Raman gauge to 310 GPa. J Appl Phys 100(4):043,516

Andrault D, Muñoz M, Pesce G, Cerantola V, Chumakov A, Kantor I, Pascarelli S, Rüffer R, Hennet L (2018) Large oxygen excess in the primitive mantle could be the source of the great oxygenation event. Geochemical Perspectives Letters 6:5–10

Aprilis G, Strohm C, Kupenko I, Linhardt S, Laskin A, Vasiukov D, Cerantola V, Koemets E, McCammon C, Kurnosov A, et al (2017) Portable double-sided pulsed laser heating system for time-resolved geoscience and materials science applications. Rev Sci Instrum 88(8):084,501

Arimoto T, Gréaux S, Irifune T, Zhou C, Higo Y (2015) Sound velocities of $Fe_3Al_2Si_3O_{12}$ almandine up to 19 GPa and 1700 K. Phys Earth Planet Inter 246:1–8

Badro J, Fiquet G, Guyot F, Rueff JP, Struzhkin VV, Vankó G, Monaco G (2003) Iron partitioning in Earth's mantle: toward a deep lower mantle discontinuity. Science 300(5620):789–791

Ballhaus C (1995) Is the upper mantle metal-saturated? Earth Planet Sci Lett 132(1-4):75–86

Bassett WA (2009) Diamond anvil cell, 50th birthday. High Pressure Res 29(2):163–186

Bengtson A, Li J, Morgan D (2009) Mössbauer modeling to interpret the spin state of iron in (Mg,Fe)SiO_3 perovskite. Geophys Res Lett 36(15)

Beyer C, Frost DJ (2017) The depth of sub-lithospheric diamond formation and the redistribution of carbon in the deep mantle. Earth Planet Sci Lett 461:30–39

Burdett JK, Hoffmann R, Fay RC (1978) Eight-coordination. Inorganic Chemistry 17(9):2553–2568

Cambi L, Szegö L (1931) Über die magnetische Susceptibilität der komplexen Verbindungen. Eur J Inorg Chem 64(10):2591–2598

Catalli K, Shim SH, Prakapenka VB, Zhao J, Sturhahn W, Chow P, Xiao Y, Liu H, Cynn H, Evans WJ (2010) Spin state of ferric iron in $MgSiO_3$ perovskite and its effect on elastic properties. Earth Planet Sci Lett 289(1-2):68–75

Cerantola V, McCammon C, Kupenko I, Kantor I, Marini C, Wilke M, Ismailova L, Solopova N, Chumakov A, Pascarelli S, Dubrovinsky L (2015) High-pressure spectroscopic study of siderite ($FeCO_3$) with a focus on spin crossover. Am Mineral 100(11-12):2670–2681

Chantel J, Manthilake GM, Frost DJ, Beyer C, Ballaran TB, Jing Z, Wang Y (2016) Elastic wave velocities in polycrystalline $Mg_3Al_2Si_3O_{12}$-pyrope garnet to 24 GPa and 1300 K. Am Mineral 101(4):991–997

Christy AG (1995) Isosymmetric structural phase transitions: phenomenology and examples. Acta Crystallogr, Sect B: Struct Sci 51(5):753–757

Chumakov A, Rüffer R (1998) Nuclear inelastic scattering. Hyperfine Interact 113(1):59–79

Dorfman SM, Dutton SE, Potapkin V, Chumakov AI, Rueff JP, Chow P, Xiao Y, Cava RJ, Duffy TS, McCammon CA, et al (2016) Electronic transitions of iron in almandine-composition glass to 91 GPa. Am Mineral 101(7):1659–1667

Dziewonski AM, Anderson DL (1981) Preliminary reference Earth model. Phys Earth Planet Inter 25(4):297–356

Fei Y, Ricolleau A, Frank M, Mibe K, Shen G, Prakapenka V (2007) Toward an internally consistent pressure scale. PNAS 104(22):9182–9186

Figgis BN, Hitchman M (2000) Ligand field theory and its applications. Special topics in inorganic chemistry, Wiley-VCH

Friedrich A, Winkler B, Morgenroth W, Ruiz-Fuertes J, Koch-Müller M, Rhede D, Milman V (2014) Pressure-induced spin collapse of octahedrally coordinated Fe^{3+} in $Ca_3Fe_2[SiO_4]_3$ from experiment and theory. Phys Rev B 90(9):094,105

Friedrich A, Winkler B, Morgenroth W, Perlov A, Milman V (2015) Pressure-induced spin collapse of octahedrally coordinated Mn^{3+} in the tetragonal hydrogarnet henritermierite $Ca_3Mn_2[SiO_4]_2[O_4H_4]$. Phys Rev B 92(1):014,117

Frost DJ, McCammon CA (2008) The redox state of Earth's mantle. Annu Rev Earth Planet Sci 36:389–420

Frost DJ, Liebske C, Langenhorst F, McCammon CA, Trønnes RG, Rubie DC (2004) Experimental evidence for the existence of iron-rich metal in the Earth's lower mantle. Nature 428(6981):409

Fyfe W (1960) The possibility of *d*-electron coupling in olivine at high pressures. Geochim Cosmochim Acta 19(2):141–143

Giacovazzo C (2002) Fundamentals of Crystallography. IUCr texts on crystallography, Oxford University Press

Glazyrin K, Ballaran TB, Frost D, McCammon C, Kantor A, Merlini M, Hanfland M, Dubrovinsky L (2014) Magnesium silicate perovskite and effect of iron oxidation state on its bulk sound velocity at the conditions of the lower mantle. Earth Planet Sci Lett 393:182–186

Greenberg E, Rozenberg GK, Xu W, Pasternak MP, McCammon C, Glazyrin K, Dubrovinsky LS (2013) Mott transition in $CaFe_2O_4$ at around 50 GPa. Phys Rev B 88(21):214,109

Greenwood N, Gibb T (1971) Mössbauer Spectroscopy. Chapman and Hall Ltd, London

Grünsteudel H, Haas M, Leupold O, Mandon D, Matzanke BF, Meyer-Klaucke W, Paulsen H, Realo E, Rüter HD, Trautwein AX, et al (1998) Mössbauer spectroscopy with synchrotron radiation: a new technique entering biological inorganic chemistry. Inorg Chim Acta 275:334–339

Gütlich P (2013) Spin crossover–quo vadis? Eur J Inorg Chem 2013(5-6):581–591

Gütlich P, Bill E, Trautwein A (2010) Mössbauer Spectroscopy and Transition Metal Chemistry: Fundamentals and Applications. Springer Berlin Heidelberg

Gwanmesia GD, Wang L, Heady A, Liebermann RC (2014) Elasticity and sound velocities of polycrystalline grossular garnet ($Ca_3Al_2Si_3O_{12}$) at simultaneous high pressures and high temperatures. Phys Earth Planet Inter 228:80–87

Hsu H, Umemoto K, Blaha P, Wentzcovitch RM (2010) Spin states and hyperfine interactions of iron in (Mg,Fe)SiO_3 perovskite under pressure. Earth Planet Sci Lett 294(1-2):19–26

Hsu H, Yonggang GY, Wentzcovitch RM (2012) Spin crossover of iron in aluminous $MgSiO_3$ perovskite and post-perovskite. Earth Planet Sci Lett 359:34–39

Hu M, Sturhahn W, Toellner T, Hession P, Sutter J, Alp E (1999) Data analysis for inelastic nuclear resonant absorption experiments. Nucl Instrum Methods Phys Res, Sect A 428(2):551–555

Hu MY, Sturhahn W, Toellner TS, Mannheim PD, Brown DE, Zhao J, Alp EE (2003) Measuring velocity of sound with nuclear resonant inelastic X-ray scattering. Phys Rev B 67(9):094,304

Huisman R, De Jonge R, Haas C, Jellinek F (1971) Trigonal-prismatic coordination in solid compounds of transition metals. J Solid State Chem 3(1):56–66

Ingalls R (1964) Electric-field gradient tensor in ferrous compounds. Phys Rev 133(3A):A787

Ismailova L, Bobrov A, Bykov M, Bykova E, Cerantola V, Kantor I, Kupenko I, McCammon C, Dyadkin V, Chernyshov D, Pascarelli S, Chumakov A, Dubrovinskaia N, Dubrovinsky L (2015) High-pressure synthesis of skiagite-majorite garnet and investigation of its crystal structure. Am Mineral 100(11-12):2650–2654

Jiang F, Speziale S, Shieh SR, Duffy TS (2004) Single-crystal elasticity of andradite garnet to 11 GPa. J Phys: Condens Matter 16(14):S1041

Kantor I, Prakapenka V, Kantor A, Dera P, Kurnosov A, Sinogeikin S, Dubrovinskaia N, Dubrovinsky L (2012) BX90: A new diamond anvil cell design for X-ray diffraction and optical measurements. Rev Sci Instrum 83(12):125,102

Kiseeva E, Wood B, Ghosh S, Stachel T (2016) The pyroxenite-diamond connection. Geochem Perspect Lett 2:1–9

Kiseeva ES, Yaxley GM, Stepanov AS, Tkalčić H, Litasov KD, Kamenetsky VS (2013) Metapyroxenite in the mantle transition zone revealed from majorite inclusions in diamonds. Geology 41(8):883–886

Kiseeva ES, Vasiukov DM, Wood BJ, McCammon C, Stachel T, Bykov M, Bykova E, Chumakov A, Cerantola V, Harris JW, Dubrovinsky L (2018) Oxidised iron in garnets from the mantle transition zone. Nat Geosci 11:144–147

Kohn V, Chumakov A, Rüffer R (1998) Nuclear resonant inelastic absorption of synchrotron radiation in an anisotropic single crystal. Phys Rev B 58(13):8437

Kono Y, Gréaux S, Higo Y, Ohfuji H, Irifune T (2010) Pressure and temperature dependences of elastic properties of grossular garnet up to 17 GPa and 1650 K. J Earth Sci 21(5):782–791

Kupenko I, Dubrovinsky L, Dubrovinskaia N, McCammon C, Glazyrin K, Bykova E, Ballaran TB, Sinmyo R, Chumakov A, Potapkin V, Kantor A, Rüffer R, Hanfland M, Crichton W, Merlini M (2012) Portable double-sided laser-heating system for Mössbauer spectroscopy and X-ray diffraction experiments at synchrotron facilities with diamond anvil cells. Rev Sci Instrum 83(12):124,501

Kupenko I, McCammon C, Sinmyo R, Cerantola V, Potapkin V, Chumakov A, Kantor A, Rüffer R, Dubrovinsky L (2015) Oxidation state of the lower mantle: *In situ* observations of the iron electronic configuration in bridgmanite at extreme conditions. Earth Planet Sci Lett 423:78–86

Kurnosov A, Kantor I, Boffa-Ballaran T, Lindhardt S, Dubrovinsky L, Kuznetsov A, Zehnder BH (2008) A novel gas-loading system for mechanically closing of various types of diamond anvil cells. Rev Sci Instrum 79(4):045,110

Kurnosov A, Marquardt H, Frost D, Ballaran TB, Ziberna L (2017) Evidence for a Fe^{3+}-rich pyrolitic lower mantle from (Al, Fe)-bearing bridgmanite elasticity data. Nature 543(7646):543

Lacivita V, Erba A, Dovesi R, D'Arco P (2014) Elasticity of grossular–andradite solid solution: an *ab initio* investigation. Phys Chem Chem Phys 16(29):15,331–15,338

Laskin A, Laskin V (2011) πShaper–refractive beam shaping optics for advanced laser technologies. In: J. Phys.: Conf. Ser., IOP Publishing, vol 276, p 012171

Lauterbach S, McCammon C, Van Aken P, Langenhorst F, Seifert F (2000) Mössbauer and ELNES spectroscopy of (Mg,Fe)(Si,Al)O_3 perovskite: a highly oxidised component of the lower mantle. Contrib Mineral Petrol 138(1):17–26

Leonov I, Pourovskii L, Georges A, Abrikosov I (2016) Magnetic collapse and the behavior of transition metal oxides at high pressure. Phys Rev B 94(15):155,135

Li J, Struzhkin VV, Mao Hk, Shu J, Hemley RJ, Fei Y, Mysen B, Dera P, Prakapenka V, Shen G (2004) Electronic spin state of iron in lower mantle perovskite. Proc Natl Acad Sci 101(39):14,027–14,030

Lin JF, Watson H, Vankó G, Alp EE, Prakapenka VB, Dera P, Struzhkin VV, Kubo A, Zhao J, McCammon C, Evans WJ (2008) Intermediate-spin ferrous iron in lowermost mantle post-perovskite and perovskite. Nat Geosci 1(10):688

Lin JF, Speziale S, Mao Z, Marquardt H (2013) Effects of the electronic spin transitions of iron in lower mantle minerals: Implications for deep mantle geophysics and geochemistry. Rev Geophys 51(2):244–275

McCammon C, Ross N (2003) Crystal chemistry of ferric iron in (Mg,Fe)(Si,Al)O_3 majorite with implications for the transition zone. Phys Chem Miner 30(4):206–216

McCammon C, Kantor I, Narygina O, Rouquette J, Ponkratz U, Sergueev I, Mezouar M, Prakapenka V, Dubrovinsky L (2008) Stable intermediate-spin ferrous iron in lower-mantle perovskite. Nat Geosci 1(10):684

McCammon C, Dubrovinsky L, Narygina O, Kantor I, Wu X, Glazyrin K, Sergueev I, Chumakov A (2010) Low-spin Fe^{2+} in silicate perovskite and a possible layer at the base of the lower mantle. Phys Earth Planet Inter 180(3-4):215–221

McDonough WF, Sun SS (1995) The composition of the Earth. Chem Geol 120(3-4):223–253

Menil F (1985) Systematic trends of the ^{57}Fe Mössbauer isomer shifts in (FeO_n) and (FeF_n) polyhedra. Evidence of a new correlation between the isomer shift and the inductive effect of the competing bond $T-X$ ($\rightarrow$Fe) (where X is O or F and T any element with a formal positive charge). J Phys Chem Solids 46(7):763–789

Merlini M, Hanfland M, Gemmi M, Huotari S, Simonelli L, Strobel P (2010) Letter: Fe^{3+} spin transition in $CaFe_2O_4$ at high pressure. Am Mineral 95(1):200–203

Mössbauer RL (1958a) Kernresonanzabsorption von gammastrahlung in Ir^{191}. Naturwissenschaften 45(22):538–539

Mössbauer RL (1958b) Kernresonanzfluoreszenz von gammastrahlung in Ir^{191}. Zeitschrift für Physik 151(2):124–143

Mössbauer RL (1959) Kernresonanzabsorption von γ-strahlung in Ir^{191}. Zeitschrift für Naturforschung A 14(3):211–216

Murakami M, Ohishi Y, Hirao N, Hirose K (2012) A perovskitic lower mantle inferred from high-pressure, high-temperature sound velocity data. Nature 485(7396):90

Neese F (2002) Prediction and interpretation of the ^{57}Fe isomer shift in Mössbauer spectra by density functional theory. Inorg Chim Acta 337:181–192

Potapkin V, Chumakov AI, Smirnov GV, Celse JP, Rüffer R, McCammon C, Dubrovinsky L (2012) The ^{57}Fe synchrotron Mössbauer source at the ESRF. J Synchrotron Radiat 19(4):559–569

Prescher C, McCammon C, Dubrovinsky L (2012) MossA: a program for analyzing energy-domain Mössbauer spectra from conventional and synchrotron sources. J Appl Crystallogr 45(2):329–331

Ricolleau A, Fei Y, Cottrell E, Watson H, Deng L, Zhang L, Fiquet G, Auzende AL, Roskosz M, Morard G, Prakapenka V (2009) Density profile of pyrolite under the lower mantle conditions. Geophys Res Lett 36(6)

Rohrbach A, Ballhaus C, Golla-Schindler U, Ulmer P, Kamenetsky VS, Kuzmin DV (2007) Metal saturation in the upper mantle. Nature 449(7161):456–458

Rüffer R, Chumakov AI (1996) Nuclear resonance beamline at ESRF. Hyperfine Interact 97(1):589–604

Seto M, Yoda Y, Kikuta S, Zhang X, Ando M (1995) Observation of nuclear resonant scattering accompanied by phonon excitation using synchrotron radiation. Phys Rev Lett 74(19):3828

Shim SH, Grocholski B, Ye Y, Alp EE, Xu S, Morgan D, Meng Y, Prakapenka VB (2017) Stability of ferrous-iron-rich bridgmanite under reducing midmantle conditions. Proc Natl Acad Sci 114(25):6468–6473

Sinmyo R, Hirose K (2010) The Soret diffusion in laser-heated diamond-anvil cell. Phys Earth Planet Inter 180(3-4):172–178

Smirnov G, Chumakov A, Potapkin V, Rüffer R, Popov S (2011) Multispace quantum interference in a ^{57}Fe synchrotron Mössbauer source. Phys Rev A 84(5):053,851

Stagno V, Ojwang DO, McCammon CA, Frost DJ (2013) The oxidation state of the mantle and the extraction of carbon from Earth's interior. Nature 493(7430):84

Sturhahn W, Jackson JM (2007) Geophysical applications of nuclear resonant spectroscopy. In: Ohtani E (ed) Advances in High-pressure Mineralogy, Geological Society of America

Syassen K (2008) Ruby under pressure. High Pressure Res 28(2):75–126

Tanabe Y, Sugano S (1954a) On the absorption spectra of complex ions. I. J Phys Soc Jpn 9(5):753–766

Tanabe Y, Sugano S (1954b) On the absorption spectra of complex ions II. J Phys Soc Jpn 9(5):766–779

Tappert R, Stachel T, Harris JW, Muehlenbachs K, Ludwig T, Brey GP (2005) Diamonds from Jagersfontein (South Africa): messengers from the sublithospheric mantle. Contrib Mineral Petrol 150(5):505–522

Vankó G, de Groot FM (2007) Comment on "Spin crossover in (Mg,Fe)O: A Mössbauer effect study with an alternative interpretation of X-ray emission spectroscopy data". Phys Rev B 75(17):177,101

Vanpeteghem CB, Angel R, Ross N, Jacobsen S, Dobson D, Litasov K, Ohtani E (2006) Al, Fe substitution in the $MgSiO_3$ perovskite structure: A single-crystal X-ray diffraction study. Phys Earth Planet Inter 155(1-2):96–103

Vasiukov D, Ismailova L, Kupenko I, Cerantola V, Sinmyo R, Glazyrin K, McCammon C, Chumakov A, Dubrovinsky L, Dubrovinskaia N (2017a) Sound velocities of skiagite–iron–majorite solid solution to 56 GPa probed by nuclear inelastic scattering. Phys Chem Miner DOI 10.1007/s00269-017-0928-8

Vasiukov DM, Dubrovinsky L, Kupenko I, Cerantola V, Aprilis G, Ismailova L, Bykova E, McCammon C, Prescher C, Chumakov AI, Dubrovinskaia N (2017b) Pressure-induced spin pairing transition of Fe^{3+} in oxygen octahedra. arXiv preprint arXiv:171003192v1

Visscher WM (1960) Study of lattice vibrations by resonance absorption of nuclear gamma rays. Ann Phys 9(2):194–210

Williamson D (1978) Influence of pressure on isomer shifts. In: Shenoy G, Wagner F (eds) Mössbauer isomer shifts, North-Holland Publ.

Wood BJ, Kiseeva ES, Matzen AK (2013) Garnet in the Earth's Mantle. Elements 9(6):421–426

Wood RW (1904) A quantitative determination of the anomalous dispersion of sodium vapor in the visible and ultra-violet regions. In: Proceedings of the American Academy of Arts and Sciences, JSTOR, vol 40, pp 365–396

Woodland A, Koch M (2003) Variation in oxygen fugacity with depth in the upper mantle beneath the Kaapvaal craton, Southern Africa. Earth Planet Sci Lett 214(1):295–310

Xu C, Kynickỳ J, Tao R, Liu X, Zhang L, Pohanka M, Song W, Fei Y (2017) Recovery of an oxidized majorite inclusion from Earth's deep asthenosphere. Sci Adv 3(4):e1601,589

Xu W, Greenberg E, Rozenberg GK, Pasternak MP, Bykova E, Boffa-Ballaran T, Dubrovinsky L, Prakapenka V, Hanfland M, Vekilova OY, Simak SI, Abrikosov IA (2013) Pressure-induced hydrogen bond symmetrization in iron oxyhydroxide. Phys Rev Lett 111(17):175,501

Zhou C, Gréaux S, Nishiyama N, Irifune T, Higo Y (2014) Sound velocities measurement on $MgSiO_3$ akimotoite at high pressures and high temperatures with simultaneous in situ X-ray diffraction and ultrasonic study. Phys Earth Planet Inter 228:97–105

Zou Y, Irifune T, Gréaux S, Whitaker ML, Shinmei T, Ohfuji H, Negishi R, Higo Y (2012) Elasticity and sound velocities of polycrystalline $Mg_3Al_2(SiO_4)_3$ garnet up to 20 GPa and 1700 K. J Appl Phys 112(1):014,910

Sound velocities of skiagite-iron-majorite solid solution to 56 GPa probed by Nuclear Inelastic Scattering

D.M. Vasiukov*[a,b], L. Ismailova[c], I. Kupenko[d], V. Cerantola[e], R. Sinmyo[b], K. Glazyrin[f], C. McCammon[b], A.I. Chumakov[e], L. Dubrovinsky[b], N. Dubrovinskaia[a]

[a] *Laboratory of Crystallography, Universität Bayreuth, Universitätsstr. 30, D-95447 Bayreuth, Germany*
[b] *Bayerisches Geoinstitut, Universität Bayreuth, Universitätsstr. 30, D-95447 Bayreuth, Germany*
[c] *Skolkovo Institute of Science and Technology, Skolkovo Innovation Center, ul. Nobelya 3,143026 Moscow, Russia*
[d] *Institut für Mineralogie, Universität Münster, Corrensstr. 24, D-48149 Münster, Germany*
[e] *ESRF-The European Synchrotron CS40220 38043 Grenoble Cedex 9 France*
[f] *Photon Science, Deutsches Elektronen-Synchrotron, Notkestr. 85, D-22603 Hamburg, Germany*

*vasyukov@physics.msu.ru
*orcid.org/0000-0003-0906-7087

High-pressure experimental data on sound velocities of garnets are used for interpretation of seismological data related to the Earth's upper mantle and the mantle transition zone. We have carried out a Nuclear Inelastic Scattering study of iron-silicate garnet with skiagite (77 mol. %)-iron-majorite composition in a diamond anvil cell up to 56 GPa at room temperature. The determined sound velocities are considerably lower than sound velocities of a number of silicate garnet end-members, such as grossular, pyrope, Mg-majorite, andradite, and almandine. The obtained sound velocities have the following pressure dependencies: V_p [km/s] = 7.43(9)+0.039(4)$\times P$ [GPa] and V_s [km/s] = 3.56(12)+0.012(6)$\times$ P [GPa]. We estimated sound velocities of pure skiagite and khoharite and conclude that the presence of the iron-majorite component in skiagite strongly decreases V_s. We analysed the influence of Fe^{3+} on sound velocities of garnet solid solution relevant to the mantle transition zone and consider that it may reduce sound velocities up to 1 % relative to compositions with only Fe^{2+} in the cubic site.

Keywords Nuclear Inelastic Scattering · Sound velocities · Skiagite · Khoharite · Garnet · Mantle transition zone

Acknowledgements

The authors are grateful to Dr. R. Mittal for the provided data. We thank the European Synchrotron Radiation Facility for the provision of synchrotron radiation (ID18). N.D. thanks the German Research Foundation (Deutsche Forschungsgemeinschaft, DFG, projects no. DU 954-8/1 and DU 954-11/1) and the Federal Ministry of Education and Research, Germany (BMBF, grants no. 5K13WC3 and 5K16WC1) for financial support. C.M. and L.D. acknowledge DFG funding through projects MC 3-18/1 and MC 3-20/1 and the CarboPaT Research Unit FOR2125. Partial support was also provided by the German Academic Exchange Service (DAAD).

1 Introduction

Garnets are an abundant group of minerals that are stable down to the top of the lower mantle ($\sim$ 720 km). Their elastic properties are important for interpretation of seismological data as they

constitute a substantial part of the upper mantle and mantle transition zone (MTZ). The fraction of garnet in peridotite and eclogite assemblages can increase up to 35 and 95 vol. %, respectively, at MTZ conditions as pyroxenes progressively dissolve in garnet with increasing depth (Irifune and Ringwood, 1993, Irifune et al, 1986, Litasov and Ohtani, 2005, Ricolleau et al, 2010, Ringwood, 1991, Wood et al, 2013).

Silicate garnets have the general formula $X_3^{2+}Y_2^{3+}(SiO_4)_3$ and crystallize in a cubic structure (space group $Ia\bar{3}d$, Fig. 1). The distorted cubic site (X-site) is occupied by large divalent cations (Mg, Fe, Ca, Mn), while the octahedral site (Y-site) is populated by trivalent (Al, Fe, Cr) cations. Pyroxene dissolution in garnet at high-pressure high-temperature (HPHT) conditions leads to an excess of silicon that is incorporated in the Y-site. In such garnets Si^{4+} is balanced either by divalent cations in the Y-site (mainly Mg, $Mg_3(Mg,Si)(SiO_4)_3$) or by sodium in the X-site ($(Na_2,Mg)Si_2(SiO_4)_3$). Therefore, the presence of such a majorite component is an unambiguous indication of a high-pressure formation of the garnet.

Up until now, HPHT studies of the elastic properties of garnets have focused on the end-members with Mg, Ca, and Fe^{2+} populating the X-site and Al, (Mg,Si) on the Y-site (Arimoto et al, 2015, Chantel et al, 2016, Gwanmesia et al, 2014, Kono et al, 2010, Zhou et al, 2014, Zou et al, 2012). However, there is strong evidence to support the hypothesis of reducing conditions and stabilization of Fe-Ni alloy below 250 km depth (Rohrbach et al, 2007, Woodland and Koch, 2003), so one should consider the disproportionation reaction $Fe^{2+} \rightarrow Fe^{3+} + Fe^0$ and a subsequent incorporation of ferric iron into garnet. Recently, highly oxidized majoritic inclusions from deep mantle xenoliths were found (Xu et al, 2017) and majoritic inclusions from deep mantle diamonds (Kiseeva et al, 2018) revealed that the amount of Fe^{3+} in the Y-site increases considerably with depth (up to 25-30 % of total iron at 500 km). These data indicate that garnets such as andradite ($Ca_3Fe_2(SiO_4)_3$) and skiagite ($Fe_3^{2+}Fe_2^{3+}(SiO_4)_3$) are potentially important for the Earth's upper mantle and MTZ.

Here we present an experimental high-pressure study of skiagite-iron-majorite ($Fe_3(Fe^{2+},Si)(SiO_4)_3$) solid solution in a diamond anvil cell (DAC) at room temperature using Nuclear Inelastic Scattering (NIS, also known as NRIXS — Nuclear Resonant Inelastic X-ray Scattering).

2 Experimental methods

The single crystals of skiagite-iron-majorite were synthesized in a multi-anvil apparatus at 9.5 GPa and 1100 °C from a powdered mixture of chemically pure oxides $Fe_{1-x}O$, $^{57}Fe_2O_3$ and SiO_2 (Ismailova et al, 2015). The material that we studied has composition $Fe_3^{2+}(Fe^{3+}_{1.532(2)}Fe^{2+}_{0.234(2)}Si_{0.234(2)})(SiO_4)_3$ based on single-crystal X-ray diffraction and microprobe analysis (Ismailova et al, 2015), and therefore the samples contain approximately 23 mol. % of iron-majorite component. High-quality crystals were selected based on the quality of their diffraction peak profiles using a three-circle Bruker diffractometer equipped with a SMART APEX CCD detector and a high-brilliance Rigaku rotating anode (Rotor Flex FR-D, Mo-K_α radiation) with Osmic focusing X-ray optics.

For pressure generation we used panoramic DACs designed and manufactured in Bayerisches Geoinstitut. The size of the diamond culets was 250 μm. The isometric crystals of the garnet with typical linear dimension of $\sim$ 15 μm and a small ruby sphere were loaded into the pressure chamber in beryllium gaskets (the indentation thickness and the hole diameter were 30 μm and 120 μm, respectively). Several garnet crystals were loaded, and all measurements expect the one at 56 GPa were performed on the single crystal that gave the strongest NIS signal. The data point at 56 GPa was collected from another garnet crystal in a separate another DAC. Neon was used as pressure transmitting medium. Pressure in the DAC was determined by ruby fluorescence (Dewaele et al,

2008). It was measured before and after each data collection and the average value was used.

The single-crystal NIS experiments were performed at ambient temperature at the Nuclear Resonance Beamline (ID18, Rüffer and Chumakov, 1996) of the European Synchrotron Radiation Facility. The synchrotron ring was operated in hybrid mode (one clean 4 mA single bunch diametrically opposed to a $\sim$ 196 mA multi-bunch beam composed of 24 groups of bunches spread over 3/4 of the storage ring circumference). The data were collected at ambient temperature over a range of -20 to 100 meV relative to the ^{57}Fe nuclear resonance energy (14.4 keV) with 0.5 meV step. The energy bandwidth and the beam spot size were 2.3 meV and $7 \times 13\,\mu\text{m}^2$, respectively. The data were processed using DOS software (Kohn and Chumakov, 2000).

3 Experimental results

The NIS technique provides information about lattice dynamics via nuclear resonant inelastic absorption and has its roots in the Mössbauer effect (see Chumakov and Rüffer, 1998, for a review of the development of the method). The NIS spectrum consists of the elastic (the recoilless absorption, i.e., the Mössbauer effect) and inelastic part (which appears due to inelastic interactions with phonons in the studied sample). Data processing involves removal of the elastic peak and subtraction of background multi-phonon contributions, followed by determination of the partial (atomic) phonon density of states (pDOS). The raw NIS spectrum of the studied solid solution at ambient conditions is shown in Fig. 2 (for pressure evolution of the NIS spectra see the Supplementary Information). A visual illustration of all the main steps in NIS data analysis can be found in Hu et al (1999). For the detailed mathematical treatment, the reader is referred to Kohn et al (1998).

3.1 Partial phonon density of states

Garnet has 4 formula units (80 atoms) per primitive unit cell. The phonon density of states (DOS) of garnet is therefore related to 240 vibrational branches. Garnet has a phonon band gap between 80 and 100 meV and the high-energy band is composed of 48 modes mainly related to the vibrations of tetrahedral subunit (Baima et al, 2016, Mittal et al, 2001, Papagelis et al, 2002). The measured iron pDOS (Fig. 3) therefore consists of 192 vibrational branches (3 acoustic and 189 optical).

The studied crystals have cubic symmetry, therefore the obtained pDOS does not have directional dependence (Kohn et al, 1998) and represents the average pDOS of the crystal, not the projected one. The thermodynamic and vibrational parameters extracted from the iron pDOS are presented in Table 1. Because iron populates two crystallographic sites (X and Y), the parameters are the averaged values in the first approximation. However, it is not an *exact* averaging because contributions of the X- and Y-sites are weighted by the corresponding Lamb-Mössbauer factors which are distinct (see discussion in Sturhahn and Chumakov, 1999).

So far there has been no theoretical investigation of the phonon properties of skiagite or iron-majorite. Nevertheless, the contributions of the different crystallographic sites to the iron pDOS at ambient conditions (Fig. 4) can be assigned using the theoretical iron pDOS of almandine ($Fe_3Al_2(SiO_4)_3$) and/or andradite. This is possible because the potential wells of the X- and Y-sites in skiagite-iron-majorite solid solutions should be similar to those of X-site Fe^{2+} in almandine and Y-site Fe^{3+} in andradite, respectively. Hence, this approach is also valid for the iron pDOS. In the literature, only the pDOS of X-site Fe^{2+} in almandine has been reported (Mittal et al, 2000, 2001) as obtained from semi-empirical interatomic potential calculations. Comparing it with our experimental iron pDOS (Fig. 4), one can judge that the 15 meV peak is dominated by vibrations of X-site Fe^{2+}. Accordingly,

after subtracting the X-site contribution from experimental pDOS, one can see that the noticeable contribution of Y-site Fe appears above 18 meV and the low intensity 55–80 meV band is formed only by its vibrations.

3.2 Sound velocities

The determination of the sound velocities from the NIS data is based on the evaluation of the Debye sound velocity from the low-energy part of the pDOS (Hu et al, 2003). The latter depends quadratically on the energy and can be written in the following form (Achterhold et al, 2002, Hu et al, 2003):

$$\mathcal{D}(E) = \left(\frac{\tilde{m}}{m}\right) \frac{E^2}{2\pi^2\hbar^3 n V_D^3} \tag{1}$$

where $\tilde{m}$ is the mass of the nuclear resonant isotope (^{57}Fe in our case), m is the average atomic mass, n is the density of atoms and V_D is Debye sound velocity.

Due to the small size of the garnet Brillouin zone, the acoustic modes can cross with optical modes even below 10 meV at ambient conditions (Baima et al, 2016, Papagelis et al, 2002). This leads to a narrow range for the parabolic fit of the low-energy part of pDOS, thus we carried it out from 4 to 7-10 meV depending on the pressure (Fig. 4). The data below 4 meV lie under the strong elastic peak in the NIS spectrum, so data points affected by the elastic peak subtraction are not used for the fitting. The upper limit of the fitted interval is determined by the deviation of the pDOS data from parabolic dependence. The phonon spectrum shifts to higher energies with increasing pressure, so the parabolic region is extended at higher pressures.

The Debye sound velocity can be expressed as

$$\frac{3}{V_D^3} = \frac{1}{V_p^3} + \frac{2}{V_s^3} \tag{2}$$

where V_p is the average velocity of the *primary* (compression) wave and V_s is the average velocity of the *secondary* (shear) wave. There is additional relationship between V_p and V_s:

$$V_p = \sqrt{\frac{K + 4/3G}{\rho}} \qquad V_s = \sqrt{\frac{G}{\rho}}$$
$$=> \frac{K}{\rho} = V_k^2 = V_p^2 - \frac{4}{3}V_s^2 \tag{3}$$

where K is the adiabatic bulk modulus, G is the shear modulus and ρ is the density. The density was determined using the equation of state (EoS) from Ismailova et al (2017), which was measured on the same material that we studied. Besides, the isothermal bulk modulus K_T was used instead of adiabatic bulk modulus (Table 1). The latter introduces a negligible error, as K_T is only slightly lower than K at ambient temperature (for example, for andradite the difference is 0.7 %, Jiang et al, 2004).

Generally speaking, the equations (1),(2),(3) are valid for elastically isotropic media. The use of them is justified, as garnets have very small elastic anisotropy (Erba et al, 2014). The system of equations (2) and (3) has an approximate solution according to the corrected formula from Sturhahn and Jackson (2007):

$$V_p = \sqrt{1.002V_k^2 - 0.104V_kV_D + 1.208V_D^2}, \qquad V_s = 0.952V_D - 0.041V_k \tag{4}$$

Fig. 5 shows the obtained values of V_p and V_s as function of pressure. For the data point at 56 GPa we report only Debye sound velocity (Table 1) as the bulk modulus of the sample is unknown due to the spin crossover of Y-site octahedral iron in this pressure range (Ismailova et al, 2017). A linear fit gives the following pressure dependencies of sound velocities at ambient temperature:

$$V_p = 7.43(9) + 0.039(4) \times P, \qquad V_s = 3.56(12) + 0.012(6) \times P \tag{5}$$

Here, V_p and V_s are in km/s and pressure is in GPa. The magnitudes of sound velocities are substantially lower than for all other garnet end-members considered so far, while the pressure derivatives of both V_p and V_s are comparable (Fig. 5).

4 Discussion

In petrological models of the upper mantle and MTZ, iron ions are conventionally assumed to be divalent. This is also a common assumption when reducing electron microprobe data of natural samples from the deep mantle. In the case of garnet, Fe^{2+} is assigned to the X-site. It is therefore important to estimate the extent to which the presence of Fe in the Y-site can influence sound velocities of the complex garnet solid solution. The most important consequences would be for the seismic profile in the 400-600 km depth interval where pyroxene completely dissolves into garnet and the volume fraction of the latter reaches a maximum (Wood et al, 2013).

Experimental studies have shown that, in the presence of both Mg and Fe in the majorite solid solution, there is a strong preference to balance Si^{4+} in the Y-site by Mg^{2+} (not Fe^{2+}) (Kiseeva et al, 2018, McCammon and Ross, 2003). Moreover, in the presence of Al, Fe^{2+} was not detected in the Y-site at all. Therefore, for further discussion only end-members with ferric iron in the octahedral site are important.

4.1 Garnets with Y-site Fe^{3+}: skiagite and khoharite

Among garnets of interest, only the elastic properties of andradite have been studied in detail (Jiang et al, 2004). Due to the lack of experimental data for pure skiagite, we will estimate its elastic moduli based on solid solution considerations.

For a solid solution formed by atomic substitution on multiple distinct crystallographic sites, the unknown elastic moduli and sound velocities of end-members can be estimated from solid solutions with a particular composition. Let us consider the hypothetical solid solution $(Fe_{2.4}Ca_{0.6})(Fe_{0.4}Al_{1.6})(SiO_4)_3$ for estimation of sound velocities of pure skiagite. The composition has two equivalent representations using end-members: 20% And + 80% Alm ≡ 20% Gro + 20% Ski + 60% Alm (Gro refers to grossular — $Ca_3Al_2(SiO_4)_3$). From Fig. 5 and a comparison of sound velocities of these end-members, one can see that the first representation should lead to sound velocities higher than almandine lines. As the second representation is equivalent, it is obvious that skiagite should balance grossular relative to the almandine line.

Assuming the validity of Vegard's law, we obtain $a = 11.73$ Å for pure skiagite (unit cell parameters of almandine, andradite and grossular were taken from Arimoto et al (2015), Jiang et al (2004), Rodehorst et al (2002), respectively). The unit cell parameter is in excellent agreement with experimental data (11.73 Å, Woodland et al, 1999, Woodland and Ross, 1994).

A widely used assumption for the pyralspite (pyrope-almandine-spessartine) series (Erba et al, 2014) is that elastic moduli of the solid solution depend linearly on those of the end-members.

A recent *ab initio* investigation verified this assumption for the grossular-andradite solid solution (Lacivita et al, 2014). Using this assumption for skiagite gives an aggregate adiabatic bulk modulus of 156.6 GPa, a shear modulus of 76.4 GPa, and Poisson's ratio of 0.29. For these calculations we used the aggregate elastic moduli known from the literature for almandine (Arimoto et al, 2015) and andradite (Jiang et al, 2004), as well as the average of values for grossular published by Kono et al (2010) and Gwanmesia et al (2014). The calculated bulk modulus is in good agreement with the experimental isothermal bulk modulus of 157(3) GPa (Woodland et al, 1999); hence we consider our approximation to be valid and use the calculated moduli to obtain the values $V_p = 7.52$ km/s and $V_s = 4.09$ km/s for skiagite at ambient conditions (plotted in Fig. 5 as black diamonds). Comparing our experimental data of skiagite-iron-majorite solid solution and estimated sound velocities of pure skiagite (Fig. 5), one can see that the presence of iron-majorite strongly decreases V_s. This fact suggest non-linear behavior for the studied solid solution (the isothermal bulk modulus values also show non-linear behavior for this composition, see Ismailova et al, 2017). The cause of this behavior requires further investigation.

Recently reported majoritic inclusions in host garnet from an eclogite xenolith (Xu et al, 2017) contain a considerable amount (from 40 to 48 % depending on the particular end-member representation) of khoharite, $Mg_3Fe_2(SiO_4)_3$. This Y-site Fe^{3+} end-member may therefore also be relevant for the Earth's mantle. However, there is no experimental data at all for this garnet; only a single theoretical study (Milman et al, 2001).

We can estimate khoharite sound velocities in a similar way as performed above for skiagite. The hypothetical solid solution with composition $(Mg_{2.4}Ca_{0.6})(Al_{1.6}Fe_{0.4})(SiO_4)_3$ can be represented as 20% And + 80% Pyr ≡ 20% Gro + 20% Kho + 60% Pyr (Pyr refers to pyrope — $Mg_3Al_2(SiO_4)_3$). Elastic moduli and the unit cell parameter of pyrope were taken from Chantel et al (2016) (results of "global" fit) and Hazen and Finger (1978), respectively. We obtain the following values for khoharite: $a = 11.66$ Å, $\rho = 3.859$ g/cm^3, $K = 153.9$ GPa, $G = 73.4$ GPa. The sound velocities for khoharite at ambient conditions are then $V_p = 8.08$ km/s and $V_s = 4.36$ km/s (plotted in Fig. 5 as cyan squares). As seen in the figure, khoharite also has lower sound velocities compared to other silicate garnets, but occupies an intermediate position between andradite and skiagite in the series of garnets with Y-site Fe^{3+}.

Skiagite and khoharite are particularly relevant to the properties of Ca-depleted solid solutions. For instance, such garnets can be formed in harzburgite rock whose existence in the MTZ was proposed by Irifune et al (2008). Indeed, the garnet inclusions from Xu et al (2017) that contain a large proportion of khoharite have a low amount of CaO, but their genesis is unclear. In the following discussion we will therefore consider only the inclusions from Kiseeva et al (2018).

4.2 Influence of Y-site Fe^{3+} on sound velocities of garnet from MTZ

As a representative example of Y-site Fe^{3+} influence, we consider the JF-55A inclusion (formation depth of 440 km) with pyroxenitic composition from the Jagersfontein kimberlite (Kiseeva et al, 2018). This is the most oxidized garnet from the series, so it is ideal as a limiting case. Based on electron microprobe and Mössbauer data, the composition of JF-55A from single-crystal structure refinement is $(Ca_{0.57}Na_{0.06}Fe^{2+}_{0.42}Mg_{1.97})(Al_{1.01}Fe^{3+}_{0.15}Si_{0.44}Mg_{0.38})(SiO_4)_3$ (Kiseeva et al, 2018). Therefore, the end-member representation is 3% Na-maj + 38% Mg-maj + 27% Pyr + 13% Alm + 11.5% Gro + 7.5% And.

In the original publication, all iron was assumed to be ferrous in the reduction of electron microprobe data (Tappert et al, 2005). There is no unique chemical formula that can be written from these data. Indeed, it is impossible to derive a composition without excess cations or the presence

of vacancies based on normal assumptions about site charges. To proceed, we consider the following end-member representation: 3% Na-maj + 38% Mg-maj + 27% Pyr + 16% Alm + 16% Gro.

Using the experimentally determined unit cell parameter of JF-55A (Kiseeva et al, 2018), we obtain densities of 3.673 and 3.638 g/cm^3 for the actual and "Fe^{2+} only" compositions, respectively. Elastic moduli and pressure derivatives of Mg-majorite were taken from Sinogeikin and Bass (2002). We neglect the Na-majorite contribution to the elastic moduli as there is no experimental data on the pressure derivative of its shear modulus. This term enters symmetrically in both representations, so it will not appreciably influence the relative difference between them.

The differences between the two representations are the amount of almandine and grossular, and the presence of andradite. From Fig. 5 one can see that consideration of Y-site Fe^{3+} should decrease the resulting sound velocities. Indeed, the calculations for composition with Fe^{3+} give $V_p = 8.88$ km/s and $V_s = 4.98$ km/s (Fig. 5), while for the "Fe^{2+} only" composition the result is $V_p = 8.96$ km/s and $V_s = 5.03$ km/s at ambient conditions. Therefore, Y-site ferric iron decreases sound velocities by 1 % in this case. At 20 GPa and 300 K the difference remains 0.08 and 0.05 km/s for V_p and V_s, respectively. In terms of the 400—600 km depth interval in the preliminary reference Earth model (Dziewonski and Anderson, 1981), it corresponds to a 16 km depth difference.

However, if instead of using the experimental unit cell parameter for both compositions, the values calculated using Vegard's law are used (average unit cell parameters of Na- and Mg-majorite were taken from Bindi et al (2011) and Angel et al (1989), respectively), the difference in the velocities decreases to 0.05 and 0.03 km/s at ambient conditions for V_p and V_s, respectively. Moreover, the non-uniqueness of the "Fe^{2+} only" composition substantially spreads the range of this difference. We also note that current uncertainties in the determination of elastic moduli and their derivatives exceed such small differences. A striking example is the shear modulus of pyrope. In recent HPHT ultrasonic interferometry experiments in a multi-anvil press, the obtained values are 89.1(5) and 93.2(1) (Chantel et al (2016) and Zou et al (2012), respectively).

5 Conclusions

In this study we performed an ambient temperature high-pressure NIS investigation of skiagite (77 mol. %)-iron-majorite solid solution. The determined sound velocities are significantly lower than sound velocities of the silicate garnet end-members, grossular, pyrope, Mg-majorite, andradite, and almandine. We also estimated the sound velocities of two end-members with Fe^{3+} in the Y-site: skiagite and khoharite. Comparison of the NIS-data-derived values of sound velocities with those estimated for pure skiagite demonstrates that the iron-majorite component decreases the sound velocities, especially V_s. The neglect of Y-site Fe^{3+} may decrease sound velocities of garnet solid solution relevant to MTZ up to 1 % relative to a composition with only Fe^{2+} in the X-site.

References

Achterhold K, Keppler C, Ostermann A, Van Bürck U, Sturhahn W, Alp E, Parak F (2002) Vibrational dynamics of myoglobin determined by the phonon-assisted Mössbauer effect. Phys Rev E 65(5):051,916

Angel R, Finger L, Hazen R, Kanzaki M, Weidner D, Liebermann R, Veblen D (1989) Letter. Structure and twinning of single-crystal $MgSiO_3$ garnet synthesized at 17 GPa and 1800 °C. Am Mineral 74(3-4):509–512

Arimoto T, Gréaux S, Irifune T, Zhou C, Higo Y (2015) Sound velocities of $Fe_3Al_2Si_3O_{12}$ almandine up to 19 GPa and 1700 K. Phys Earth Planet Inter 246:1–8

Baima J, Ferrabone M, Orlando R, Erba A, Dovesi R (2016) Thermodynamics and phonon dispersion of pyrope and grossular silicate garnets from ab initio simulations. Phys Chem Miner 43(2):137–149

Bindi L, Dymshits AM, Bobrov AV, Litasov KD, Shatskiy AF, Ohtani E, Litvin YA (2011) Letter. Crystal chemistry of sodium in the Earth's interior: The structure of $Na_2MgSi_5O_{12}$ synthesized at 17.5 GPa and 1700 °C. Am Mineral 96(2-3):447–450

Chantel J, Manthilake GM, Frost DJ, Beyer C, Ballaran TB, Jing Z, Wang Y (2016) Elastic wave velocities in polycrystalline $Mg_3Al_2Si_3O_{12}$-pyrope garnet to 24 GPa and 1300 K. Am Mineral 101(4):991–997

Chumakov A, Rüffer R (1998) Nuclear inelastic scattering. Hyperfine Interact 113(1):59–79

Dewaele A, Torrent M, Loubeyre P, Mezouar M (2008) Compression curves of transition metals in the Mbar range: Experiments and projector augmented-wave calculations. Phys Rev B 78(10):104,102

Dziewonski AM, Anderson DL (1981) Preliminary reference Earth model. Phys Earth Planet Inter 25(4):297–356

Erba A, Mahmoud A, Orlando R, Dovesi R (2014) Elastic properties of six silicate garnet end members from accurate ab initio simulations. Phys Chem Miner 41(2):151–160

Gwanmesia GD, Wang L, Heady A, Liebermann RC (2014) Elasticity and sound velocities of polycrystalline grossular garnet ($Ca_3Al_2Si_3O_{12}$) at simultaneous high pressures and high temperatures. Phys Earth Planet Inter 228:80–87

Hazen RM, Finger LW (1978) Crystal structures and compressibilities of pyrope and grossular to 60 kbar. Am Mineral 63(3-4):297–303

Hu M, Sturhahn W, Toellner T, Hession P, Sutter J, Alp E (1999) Data analysis for inelastic nuclear resonant absorption experiments. Nucl Instrum Methods Phys Res, Sect A 428(2):551–555

Hu MY, Sturhahn W, Toellner TS, Mannheim PD, Brown DE, Zhao J, Alp EE (2003) Measuring velocity of sound with nuclear resonant inelastic X-ray scattering. Phys Rev B 67(9):094,304

Irifune T, Ringwood A (1993) Phase transformations in subducted oceanic crust and buoyancy relationships at depths of 600–800 km in the mantle. Earth Planet Sci Lett 117(1-2):101–110

Irifune T, Sekine T, Ringwood A, Hibberson W (1986) The eclogite-garnetite transformation at high pressure and some geophysical implications. Earth Planet Sci Lett 77(2):245–256

Irifune T, Higo Y, Inoue T, Kono Y, Ohfuji H, Funakoshi K (2008) Sound velocities of majorite garnet and the composition of the mantle transition region. Nature 451(7180):814–817

Ismailova L, Bobrov A, Bykov M, Bykova E, Cerantola V, Kantor I, Kupenko I, McCammon C, Dyadkin V, Chernyshov D, Pascarelli S, Chumakov A, Dubrovinskaia N, Dubrovinsky L (2015) High-pressure synthesis of skiagite-majorite garnet and investigation of its crystal structure. Am Mineral 100(11-12):2650–2654

Ismailova L, Bykov M, Bykova E, Bobrov A, Kupenko I, Cerantola V, Vasiukov D, Dubrovinskaia N, McCammon C, Hanfland M, Glazyrin K, Liermann HP, Chumakov A, Dubrovinsky L (2017) Effect of composition on compressibility of skiagite-Fe-majorite garnet. Am Mineral 102(1):184–191

Jiang F, Speziale S, Shieh SR, Duffy TS (2004) Single-crystal elasticity of andradite garnet to 11 GPa. J Phys: Condens Matter 16(14):S1041

Kiseeva ES, Vasiukov DM, Wood BJ, McCammon C, Stachel T, Bykov M, Bykova E, Chumakov A, Cerantola V, Harris JW, Dubrovinsky L (2018) Oxidised iron in garnets from the mantle transition zone. Nat Geosci 11:144–147

Kohn V, Chumakov A (2000) DOS: Evaluation of phonon density of states from nuclear resonant inelastic absorption. Hyperfine Interact 125(1-4):205–221

Kohn V, Chumakov A, Rüffer R (1998) Nuclear resonant inelastic absorption of synchrotron radiation in an anisotropic single crystal. Phys Rev B 58(13):8437

Kono Y, Gréaux S, Higo Y, Ohfuji H, Irifune T (2010) Pressure and temperature dependences of elastic properties of grossular garnet up to 17 GPa and 1650 K. J Earth Sci 21(5):782–791

Lacivita V, Erba A, Dovesi R, D'Arco P (2014) Elasticity of grossular–andradite solid solution: an *ab initio* investigation. Phys Chem Chem Phys 16(29):15,331–15,338

Litasov KD, Ohtani E (2005) Phase relations in hydrous MORB at 18–28 GPa: implications for heterogeneity of the lower mantle. Phys Earth Planet Inter 150(4):239–263

McCammon C, Ross N (2003) Crystal chemistry of ferric iron in (Mg,Fe)(Si,Al)O_3 majorite with implications for the transition zone. Phys Chem Miner 30(4):206–216

Milman V, Akhmatskaya E, Nobes R, Winkler B, Pickard C, White J (2001) Systematic *ab initio* study of the compressibility of silicate garnets. Acta Crystallogr, Sect B: Struct Sci 57(2):163–177

Mittal R, Chaplot S, Choudhury N, Loong CK (2000) Inelastic neutron scattering and lattice-dynamics studies of almandine $Fe_3Al_2Si_3O_{12}$. Phys Rev B 61(6):3983

Mittal R, Chaplot S, Choudhury N (2001) Lattice dynamics calculations of the phonon spectra and thermodynamic properties of the aluminosilicate garnets pyrope, grossular, and spessartine $M_3Al_2Si_3O_{12}$ (M = Mg, Ca, and Mn). Phys Rev B 64(9):094,302

Momma K, Izumi F (2011) VESTA 3 for three-dimensional visualization of crystal, volumetric and morphology data. J Appl Crystallogr 44(6):1272–1276

Papagelis K, Kanellis G, Ves S, Kourouklis G (2002) Lattice dynamical properties of the rare earth aluminum garnets ($RE_3Al_5O_{12}$). Phys Status Solidi B 233(1):134–150

Ricolleau A, Perrillat Jp, Fiquet G, Daniel I, Matas J, Addad A, Menguy N, Cardon H, Mezouar M, Guignot N (2010) Phase relations and equation of state of a natural MORB: Implications for the density profile of subducted oceanic crust in the Earth's lower mantle. J Geophys Res: Solid Earth 115(B8)

Ringwood A (1991) Phase transformations and their bearing on the constitution and dynamics of the mantle. Geochim Cosmochim Acta 55(8):2083–2110

Rodehorst U, Geiger CA, Armbruster T (2002) The crystal structures of grossular and spessartine between 100 and 600 K and the crystal chemistry of grossular-spessartine solid solutions. Am Mineral 87(4):542–549

Rohrbach A, Ballhaus C, Golla-Schindler U, Ulmer P, Kamenetsky VS, Kuzmin DV (2007) Metal saturation in the upper mantle. Nature 449(7161):456–458

Rüffer R, Chumakov AI (1996) Nuclear resonance beamline at ESRF. Hyperfine Interact 97(1):589–604

Sinogeikin SV, Bass JD (2002) Elasticity of majorite and a majorite-pyrope solid solution to high pressure: Implications for the transition zone. Geophys Res Lett 29(2)

Sturhahn W, Chumakov A (1999) Lamb–Mössbauer factor and second-order Doppler shift from inelastic nuclear resonant absorption. Hyperfine Interact 123(1-4):809–824

Sturhahn W, Jackson JM (2007) Geophysical applications of nuclear resonant spectroscopy. In: Ohtani E (ed) Advances in High-pressure Mineralogy, Geological Society of America

Tappert R, Stachel T, Harris JW, Muehlenbachs K, Ludwig T, Brey GP (2005) Diamonds from Jagersfontein (South Africa): messengers from the sublithospheric mantle. Contrib Mineral Petrol 150(5):505–522

Wood BJ, Kiseeva ES, Matzen AK (2013) Garnet in the Earth's Mantle. Elements 9(6):421–426

Woodland A, Koch M (2003) Variation in oxygen fugacity with depth in the upper mantle beneath the Kaapvaal craton, Southern Africa. Earth Planet Sci Lett 214(1):295–310

Woodland A, Angel R, Koch M, Kunz M, Miletich R (1999) Equations of state for $Fe_3^{2+}Fe_2^{3+}Si_3O_{12}$ "skiagite" garnet and Fe_2SiO_4-Fe_3O_4 spinel solid solutions. J Geophys Res: Solid Earth 104(B9):20,049–20,058

Woodland AB, Ross CR (1994) A crystallographic and Mössbauer spectroscopy study of $Fe_3^{2+}Al_2Si_3O_{12}$-$Fe_3^{2+}Fe_2^{3+}Si_3O_{12}$, (almandine-"skiagite") and $Ca_3Fe_2^{3+}Si_3O_{12}$-$Fe_3^{2+}Fe_2^{3+}Si_3O_{12}$ (andradite-"skiagite") garnet solid solutions. Phys Chem Miner 21(3):117–132

Xu C, Kynickỳ J, Tao R, Liu X, Zhang L, Pohanka M, Song W, Fei Y (2017) Recovery of an oxidized majorite inclusion from Earth's deep asthenosphere. Sci Adv 3(4):e1601,589

Zhou C, Gréaux S, Nishiyama N, Irifune T, Higo Y (2014) Sound velocities measurement on $MgSiO_3$ akimotoite at high pressures and high temperatures with simultaneous in situ X-ray diffraction and ultrasonic study. Phys Earth Planet Inter 228:97–105

Zou Y, Irifune T, Gréaux S, Whitaker ML, Shinmei T, Ohfuji H, Negishi R, Higo Y (2012) Elasticity and sound velocities of polycrystalline $Mg_3Al_2(SiO_4)_3$ garnet up to 20 GPa and 1700 K. J Appl Phys 112(1):014,910

Table 1: Extracted parameters from the NIS spectra and elastic moduli of skiagite-iron-majorite solid solution. These parameters are "averaged" values for the two crystallographic sites (see main text). The isothermal bulk moduli were taken from (Ismailova et al, 2017).

Pressure (GPa)	Lamb-Mössbauer factor	Vibrational amplitude (Å)	Mean internal energy (meV)	Specific heat (k_B/atom)	Entropy (k_B/atom)	Norm. mean force constant (N/m)	Debye velocity (km/s)	Isothermal bulk modulus (GPa)	Shear modulus (GPa)	Poisson's ratio
10^{-4}	0.710(3)	0.1389(3)	85.0(2)	2.705(7)	3.50(3)	201(4)	3.97(14)	160(5)	57(4)	0.34
14(1)	0.78(1)	0.120(3)	87(1)	2.65(2)	3.1(1)	240(20)	4.3(2)	218(2)	72(7)	0.35
27(1)	0.80(1)	0.114(3)	88(1)	2.62(2)	3.0(1)	260(30)	4.5(3)	268(3)	82(10)	0.36
37(1)	0.80(1)	0.114(3)	87(1)	2.63(2)	3.0(1)	250(30)	4.3(3)	304(5)	77(11)	0.38
45(2)	0.82(1)	0.107(3)	90(1)	2.55(2)	2.8(1)	320(30)	4.7(4)	334(7)	96(17)	0.37
56(3)	0.84(1)	0.101(3)	94(1)	2.44(2)	2.5(1)	420(40)	4.8(5)	–	–	–

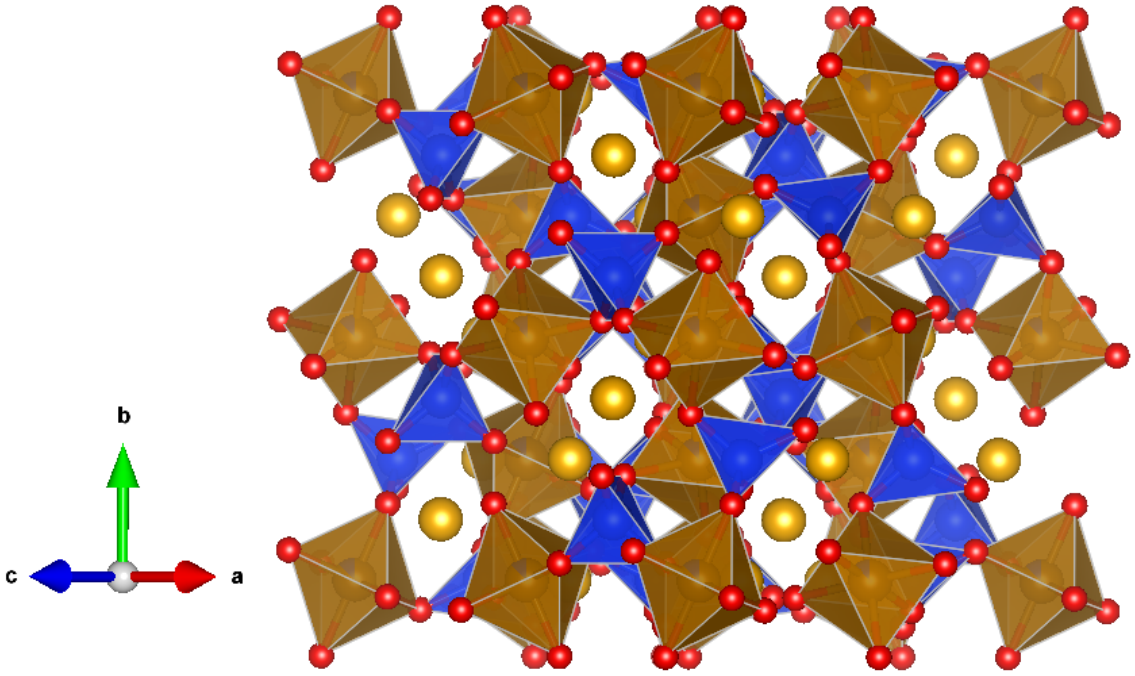

Figure 1. Crystal structure of skiagite-Fe-majorite solid solution. The corner-shared alternating Si-tetrahedra (Z-site) and (Fe,Si)-octahedra (Y-site) form a framework in the garnet structure. The distorted cubic voids (X-site) are populated by divalent iron (depicted as yellow isolated atoms). The structure is visualized using VESTA software (Momma and Izumi, 2011).

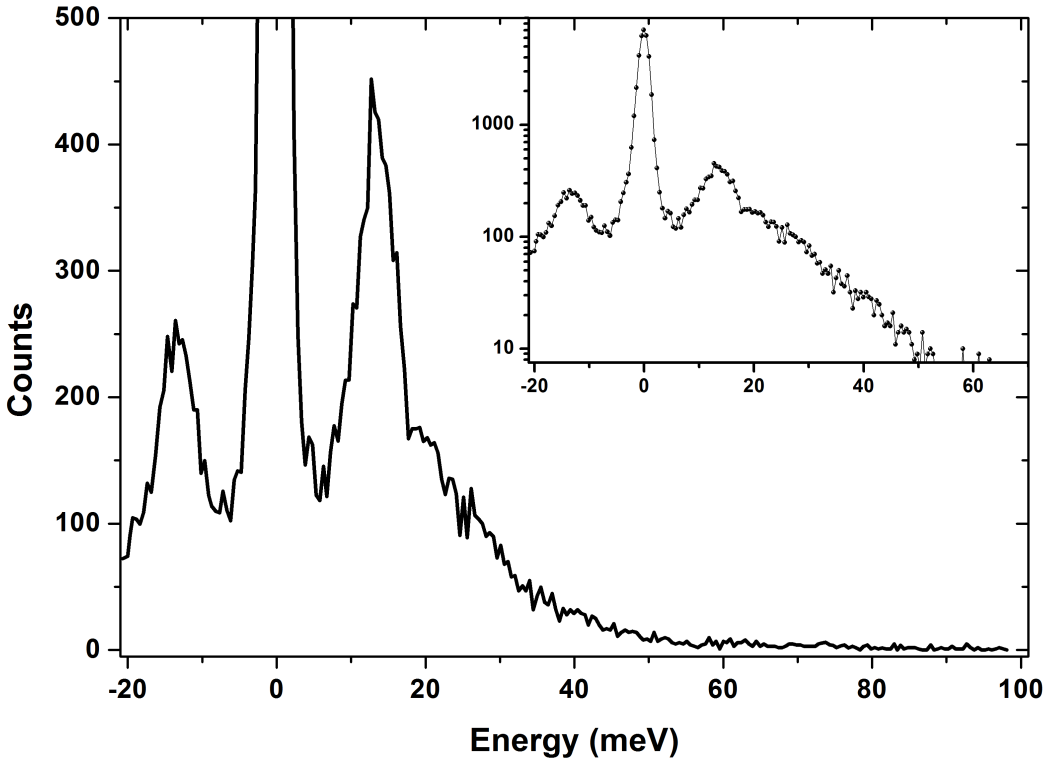

Figure 2. Raw NIS spectrum of skiagite-iron-majorite solid solution at ambient conditions. The elastic peak at 0 meV is surrounded by phonon creation (positive energy) and annihilation (negative energy) wings. The inset shows same spectrum in logarithmic scale.

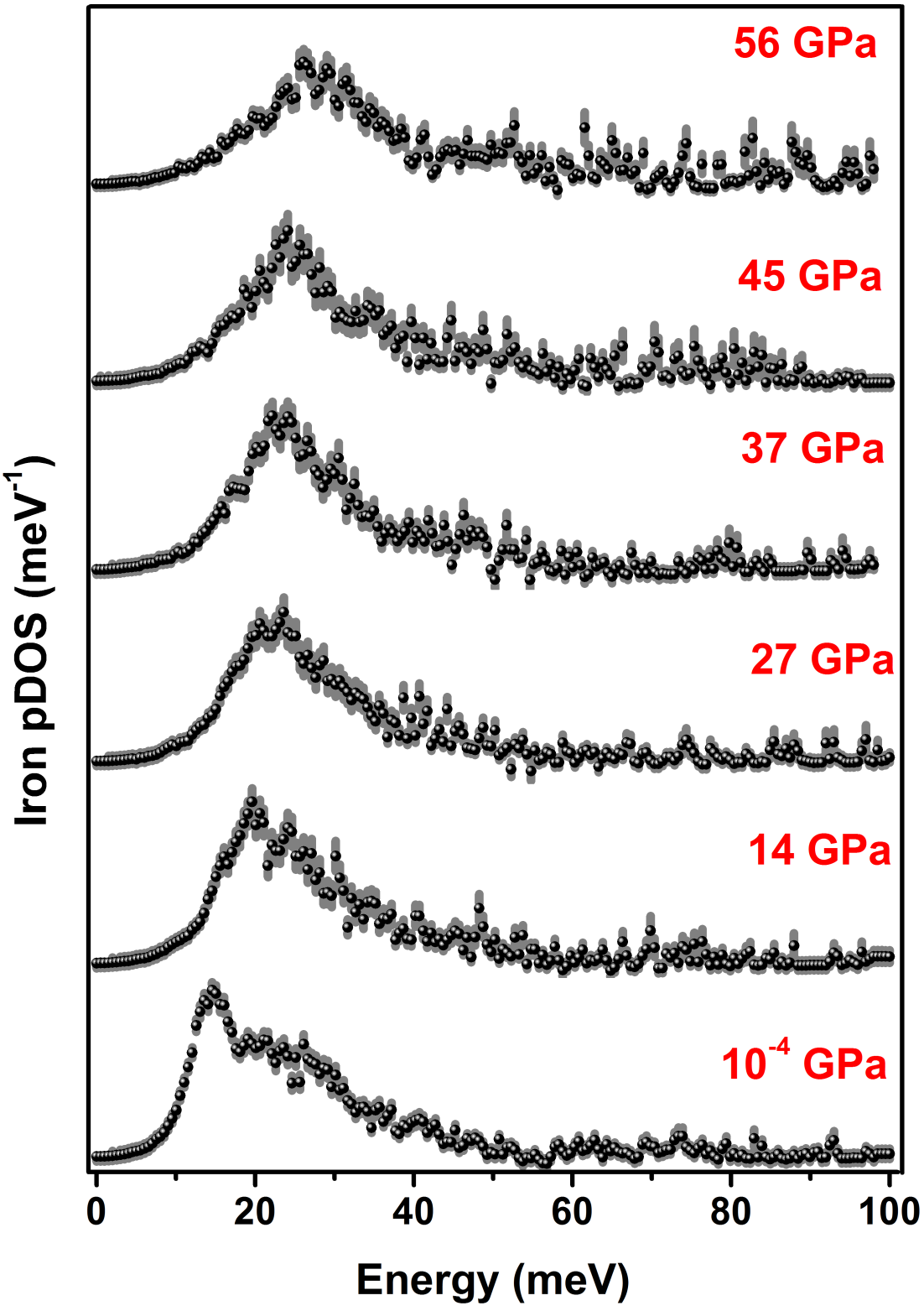

Figure 3. Pressure evolution of the extracted pDOS. Vertical grey bars are the standard deviations.

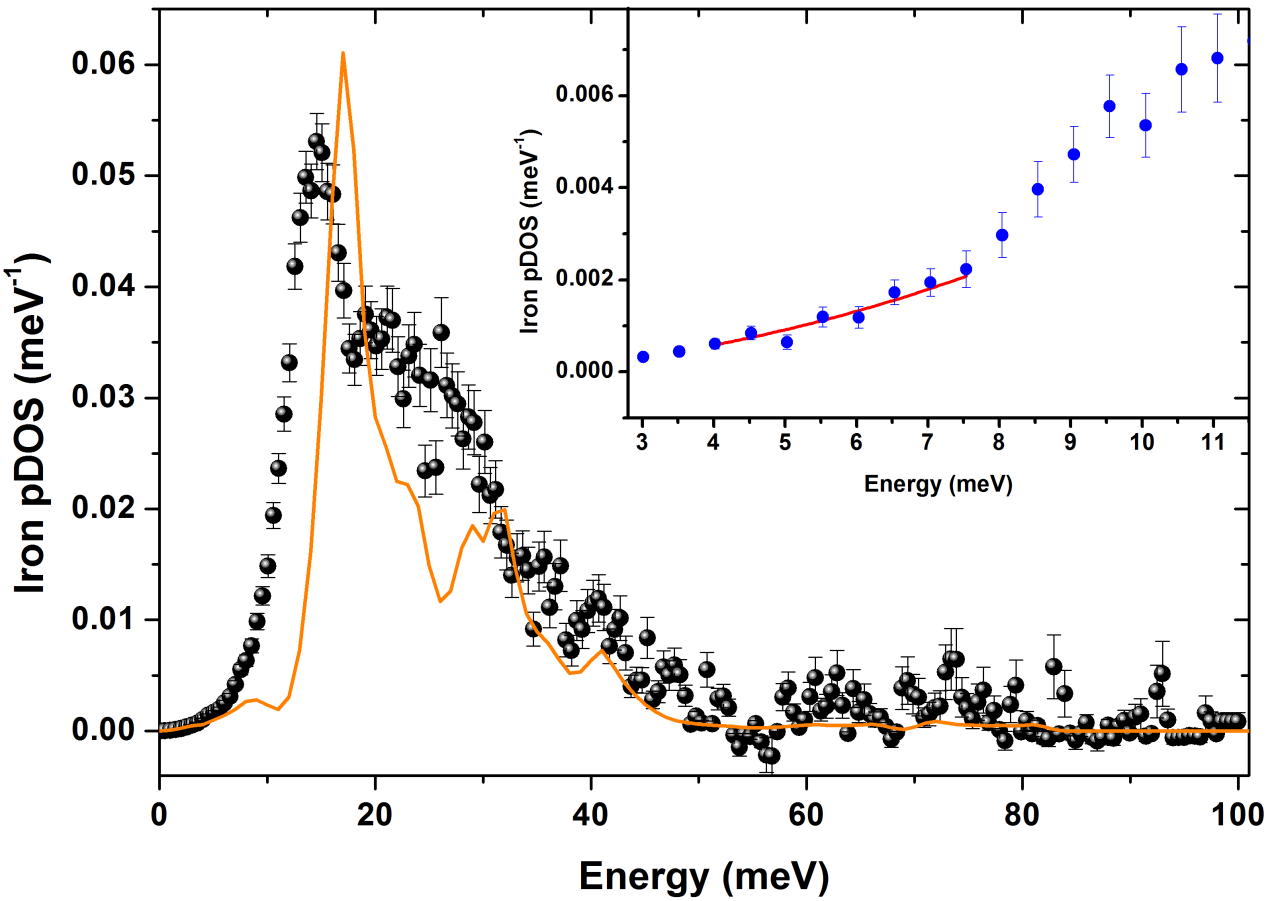

Figure 4. Iron pDOS of skiagite-iron-majorite solid solution at ambient conditions. The yellow line is the calculated pDOS of X-site Fe^{2+} in almandine (Mittal et al, 2000). Comparing it with our experimental pDOS, one can judge that the 15 meV peak is dominated by vibrations of X-site Fe^{2+}. The dip on the almandine pDOS around 11 meV is a calculation artefact, see Fe pDOS in a subsequent paper of the same group (Mittal et al, 2001). The inset shows example of the parabolic fit for the low-energy part of the experimental pDOS at 27 GPa.

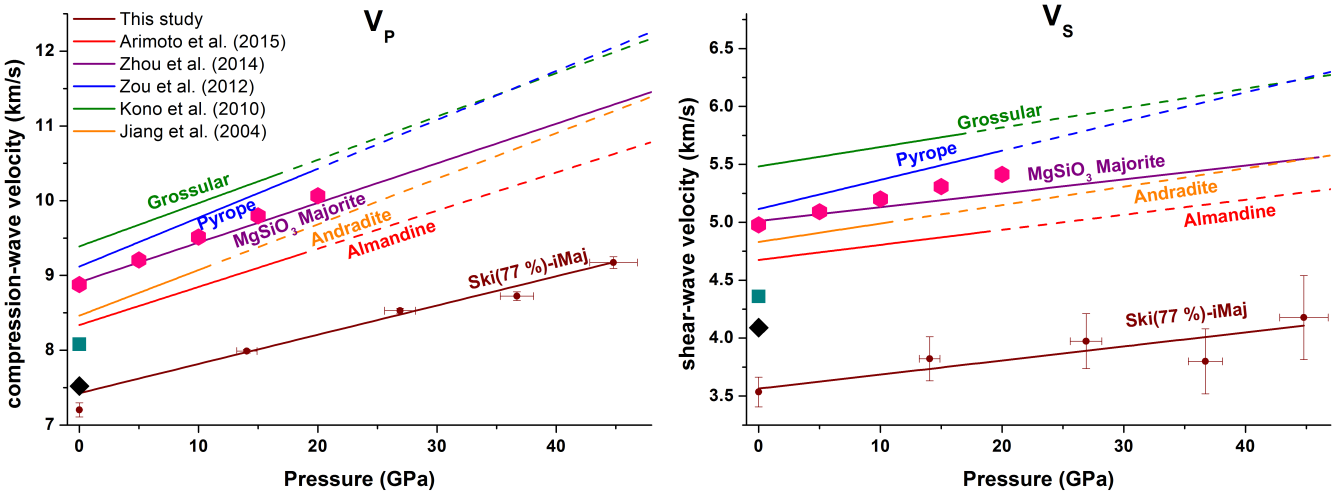

Figure 5. Sound velocities of skiagite-iron-majorite solid solution and some silicate garnet end-members as a function of pressure at ambient temperature. The black diamonds, cyan squares and pink hexagons are estimated sound velocities of pure skiagite, khoharite and JF-55A inclusion (correct composition with Y-site Fe^{3+}), respectively (see main text). The solid lines conform to the pressure range investigated in the corresponding studies while dashed lines designate regions of extrapolation.

Sound velocities of skiagite-iron-majorite solid solution to 56 GPa probed by Nuclear Inelastic Scattering

Physics and Chemistry of Minerals

D.M. Vasiukov*[a,b], L. Ismailova[c], I. Kupenko[d], V. Cerantola[e], R. Sinmyo[b], K. Glazyrin[f], C. McCammon[b], A.I. Chumakov[e], L. Dubrovinsky[b], N. Dubrovinskaia[a]

[a]*Laboratory of Crystallography, Universität Bayreuth, Universitätsstr. 30, D-95447 Bayreuth, Germany*
[b]*Bayerisches Geoinstitut, Universität Bayreuth, Universitätsstr. 30, D-95447 Bayreuth, Germany*
[c]*Skolkovo Institute of Science and Technology, Skolkovo Innovation Center, ul. Nobelya 3,143026 Moscow, Russia*
[d]*Institut für Mineralogie, Universität Münster, Corrensstr. 24, D-48149 Münster, Germany*
[e]*ESRF-The European Synchrotron CS40220 38043 Grenoble Cedex 9 France*
[f]*Photon Science, Deutsches Elektronen-Synchrotron, Notkestr. 85, D-22603 Hamburg, Germany*

*vasyukov@physics.msu.ru

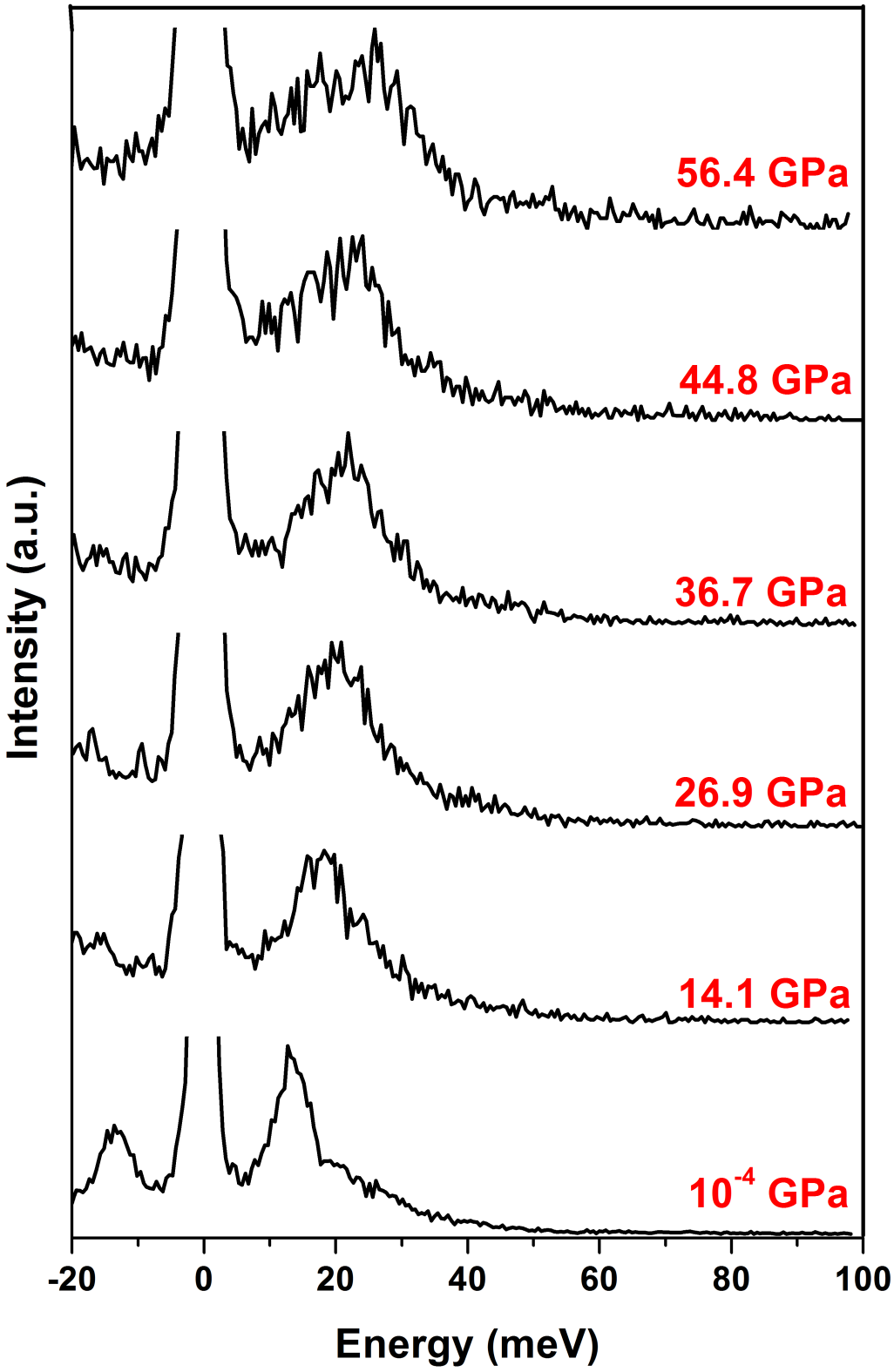

Figure 1. Pressure evolution of the raw NIS spectra of skiagite-iron-majorite solid solution at ambient temperature.

Oxidised iron in garnets from the mantle transition zone

Ekaterina S. Kiseeva[1,*], Denis M. Vasiukov[2], Bernard J. Wood[1], Catherine McCammon[3], Thomas Stachel[4], Maxim Bykov[3], Elena Bykova[3,5], Alexander Chumakov[6], Valerio Cerantola[6], Jeff W. Harris[7], Leonid Dubrovinsky[3]

[1] – Department of Earth Sciences, University of Oxford, Oxford OX1 3AN, UK

[2] – Laboratory of Crystallography, University of Bayreuth, D-95440 Bayreuth, Germany

[3] – Bayerisches Geoinstitut, Universität Bayreuth, D-95440 Bayreuth, Germany

[4] – Department of Earth and Atmospheric Sciences, University of Alberta, Edmonton, AB, T6G 2E3, Canada

[5] – DESY Photon Science, Notkestrasse 85, DE-22607 Hamburg, Germany

[6] – ESRF-The European Synchrotron, CS 40220, 38043, Grenoble, Cedex 9, France

[7] – School of Geographical and Earth Sciences, University of Glasgow, Glasgow, G12 8QQ, UK

*corresponding author, kate.kiseeva@earth.ox.ac.uk

Abstract

The oxidation state of iron in Earth's mantle is well known to depths of approximately 200km, but has not been characterised in samples from the lowermost upper mantle (200-410 km depth) or the transition zone (410-660 km). Natural samples from the deep (>200km) mantle are extremely rare, and are usually only found as inclusions in diamonds. Here we use Synchrotron Mössbauer Source spectroscopy complemented by single crystal X-ray

diffraction to measure the oxidation state of Fe in inclusions of ultra-high pressure majoritic garnet in diamond. The garnets show a pronounced increase in oxidation state with depth, with $Fe^{3+}/(Fe^{3+}+Fe^{2+})$ increasing from 0.08 at approximately 240 km depth to 0.30 at approximately 500 km depth. The latter majorites, which come from pyroxenitic bulk compositions, are twice as rich in Fe^{3+} as the most oxidised garnets from the shallow mantle. Corresponding oxygen fugacities are above the upper stability limit of Fe metal. This implies that the increase in oxidation state is unconnected to disproportionation of Fe^{2+} to Fe^{3+} plus Fe^{0}. Instead, the Fe^{3+} increase with depth is consistent with the hypothesis that carbonated fluids or melts are the oxidising agents responsible for the high Fe^{3+} contents of the inclusions.

Introduction

The Earth's peridotitic upper mantle contains about 6.3wt% Fe[1] dominantly stored as Fe^{2+} in the main rock forming minerals, olivine, pyroxene, spinel and garnet. Analyses of these minerals from peridotite xenoliths and less abundant mantle pyroxenites using Mössbauer spectroscopy indicate that the Fe^{3+} content of fertile upper mantle is very low with $Fe^{3+}/(Fe^{3+}+Fe^{2+})$ ~0.036[2]. In the case of ferric iron, spinel is a major host in the uppermost mantle and Fe^{3+} contents of this mineral are sufficiently high to be used to calculate the oxygen fugacity recorded by mantle peridotites using the olivine-orthopyroxene-spinel oxybarometer[3]. The results indicate that the subcontinental lithospheric upper mantle exhibits oxygen fugacities close to the reference FMQ (fayalite-magnetite-quartz buffer)[3,4], while peridotites from close to subduction zones are about 1 log fO_2 unit higher and suboceanic peridotites about 1 log unit lower than FMQ[2]. At pressures above 2.8 GPa, spinel is replaced by garnet as

the aluminous phase in peridotite. Mössbauer data on xenoliths from the deeper parts of the lithosphere[5] indicate a general increase in $Fe^{3+}/(Fe^{2+}+Fe^{3+})$ of garnet with depth, with values of around 0.04 corresponding to about 100 km depth while at 200 km depth this ratio is ~ 0.1. When translated to oxygen fugacity, however, these results indicate a decline relative to FMQ with depth because of the increased stability of ferric iron in garnet at high pressure[6]. Extrapolation of the data to higher pressures implies that the FeO-Fe (IW) buffer curve could be crossed in the mantle at depths below 250 km[5,7], leading to the possibility of Fe-rich metal being stabilised in the mantle transition zone. This is an important suggestion, consistent with observations of Fe-rich metallic inclusions in diamond from depths of the base of the lithospheric mantle[8,9] and >360 km[10]. Similar deep diamonds contain inclusions of majoritic garnet, the major silicate inclusion from the transition zone. Given the role of garnet as a key host for Fe^{3+} in the upper mantle, it is important to determine how the Fe^{3+} contents and oxygen fugacities recorded by garnet inclusions in diamond from depths >250 km relate to those derived from upper mantle xenoliths (from <200 km) and to the apparent stability of Fe-rich alloys and other indicators of ultra-reduced conditions[11] in some very high pressure assemblages. The purpose of our study was, therefore, to determine how the oxidation state of iron in garnet (included in diamond) from the mantle varies as a function of depth and to translate measured oxidation states to oxygen fugacities.

Sample analysis

In order to determine the oxidation state of Fe in garnet inclusions in diamond, we used single crystal X-ray diffraction analysis (beamline P02 at PETRA III, Hamburg) combined with Synchrotron Mössbauer Source (SMS) spectroscopy (beamline ID18

at the European Synchrotron Radiation Facility, Grenoble). The diamonds were polished to expose the garnet prior to analysis. We obtained spectra (Extended Data Figs. 1-2 and Extended Data Table 1) of 13 small (0.1-0.3 mm in diameter) majoritic inclusions in diamonds from the Jagersfontein kimberlite (South Africa) (Extended Data Fig. 3). The inclusions were initially studied by X-ray diffraction and confirmed as predominantly monophase garnet single crystals or (in very few cases) as aggregates of single crystals (Extended Data Tables 2-3). There is good agreement between determinations of $Fe^{3+}/(Fe^{2+}+Fe^{3+})$ using Mössbauer spectroscopy and single crystal X-ray refinement as well as calculations based on composition assuming stoichiometry (Extended Data Table 4). In several samples an unexpectedly high content of ferric iron was detected (up to ~30% of total iron) and requires further detailed consideration.

Source lithology of majorites and their ferric iron content

In the commonest case of a single garnet inclusion there is no unique geobarometer enabling pressure to be unequivocally determined. However, at pressures beyond 7.5 GPa coexisting pyroxene dissolves progressively into garnet as the majoritic components $(Mg,Fe)_4Si_4O_{12}$ and $Na_2MgSi_5O_{12}$. The concentrations of these components in majoritic garnet give an equilibrium pressure provided pyroxene is present in the source[12]. In the absence of pyroxene in the source, the derived pressure is a minimum estimate. In subducted basaltic lithologies the pyroxene to garnet transformation produces a garnetite of ~95% majoritic garnet and ~5% stishovite at about 500 km depth[13,14], while in rocks with peridotitic composition majoritic garnet forms a bimineralic rock with the high-pressure form of $(Mg,Fe)_2SiO_4$ (wadsleyite or ringwoodite)[15]. There are, however, significant compositional differences between

garnets from the two end-member lithologies, with the $(Mg,Fe)_4Si_4O_{12}$ substitution dominating in peridotitic rocks while basaltic or eclogitic compositions produce garnet with considerable amounts of $Na_2MgSi_5O_{12}$ component (Fig. 1). Perhaps surprisingly, the compositions of most inclusions from diamond appear to come from a third rock type, pyroxenite, which is intermediate in composition between peridotite and eclogite[16]. Pyroxenite lenses are common in mantle peridotites[17] and considered to be produced by reaction between peridotitic and eclogitic compositions, possibly through the agency of carbonated melts[18,19]. Although following the "peridotitic" trend of Fig 1, pyroxenitic garnets are lower in Cr_2O_3 and Mg# (=Mg/Mg+Fe) and higher in CaO than peridotitic garnets. The garnet inclusions we have studied are, in common with most other majorite inclusions, pyroxenitic in composition in that they follow the peridotite "trend" on a plot of M^{2+} versus $(M^{4+}+M^{5+})$ (Fig. 1), but are low in Cr_2O_3 (0.03-0.34 wt%) and Mg# (0.65-0.81) and high in CaO (4.62-11.2 wt%). As far as we are aware, no majoritic garnets of peridotitic composition have yet been reported as inclusions in diamond from the mantle transition zone. This implies a genetic connection, explored in more detail elsewhere[18,19] between the minor mantle rock type pyroxenite, and the diamond host.

Our measurements show an increase in $Fe^{3+}/(Fe^{2+}+Fe^{3+})$ with increasing amount of majorite substitution and hence pressure (Fig. 2). Assuming the presence of pyroxene in the pyroxenitic diamond substrates, garnet compositions yield pressures of formation of 7.7-17.9 GPa using the Beyer and Frost majorite geobarometer[12]. These are minimum pressures, however, because majoritic garnet equilibrium with pyroxene has not been demonstrated in our samples. Interestingly, Figure 2 shows that $Fe^{3+}/(Fe^{2+}+Fe^{3+})$ is extremely well correlated with calculated pressure, increasing from 0.08 at 7.7 GPa to values between 0.30 at 16 GPa and 0.27 at 18 GPa. Note that

at least 3 of these 13 garnets were formed at (minimum) pressures of 13 to 18 GPa and, therefore crystallised in the transition zone (410-660 km depth). It is also interesting to note that our measured $Fe^{3+}/(Fe^{2+}+Fe^{3+})$ values define a clear extension of the trend apparent in the data from peridotite xenoliths crystallised at lower pressures and that Fe from the transition zone garnets is at least twice as oxidised as in any garnet from xenoliths of subcratonic lithospheric mantle.

Oxygen fugacity in the mantle transition zone

In order to estimate the oxygen fugacities represented by these Fe^{3+}- bearing inclusions we looked for the simplest equilibrium available containing the fewest number of activities undefined by garnet composition:

$$2Ca_3Al_2Si_3O_{12} + 4/3Fe_3Al_2Si_3O_{12} + 2.5Mg_4Si_4O_{12} + O_2 = 2Ca_3Fe_2Si_3O_{12} + 10/3Mg_3Al_2Si_3O_{12} + 4SiO_2 \quad (1)$$

Garnet Garnet Garnet Garnet Garnet

In this case we need to define the activity of SiO_2, which we assumed was slightly (0.01 log units) above the forsterite-enstatite equilibrium and hence consistent with the garnets being close to equilibrium with peridotite. Although we recognise that this is a crude assumption, we show below that it yields (correctly) oxygen fugacities consistent with the stability of metallic Fe in experiments performed in iron capsules on similar compositions by Rohrbach et al[26]. We took thermodynamic data for equilibrium (1) from the database of Holland and Powell and Holland et al[27,28] and calculated oxygen fugacities for pressures given by the Beyer-Frost geobarometer[12] at temperatures corresponding to a mantle adiabat with a potential temperature of 1350°C[29] (Methods). Results (Fig. 3) indicate that the analysed garnets correspond to

oxygen fugacities from ~0.26 log fO_2 units below to about 3 log fO_2 units above the Fe-FeO (IW) buffer, implying that they were not in equilibrium with Fe metal and not oxidised by disproportionation of Fe^{2+} to Fe^{3+} plus Fe^0 (Methods). We checked our calculation method and assumptions using data from experiments in which garnets were synthesised in equilibrium with Fe metal and their Fe^{3+} contents measured[26]. In this case (Fig 3), 4 of the 5 experiments give calculated oxygen fugacities, as expected, just below Fe-FeO equilibrium. This test indicates that our methods are reasonably accurate and our conclusions justified, even though uncertainties in activity expressions imply about 1 log unit of uncertainty in absolute fO_2 (methods). Note that any actual error in activity expressions would lead to all points moving in the same direction, thus preserving the trends of Figure 3.

Since Fe^{2+} disproportionation appears not to be responsible, the source of the oxidising agent which generated the high $Fe^{3+}/(Fe^{2+}+Fe^{3+})$ ratios of the transition zone garnets is of considerable interest. It has previously been suggested that the pyroxenite substrates in which the garnets and their host diamonds crystallised were generated by reaction between subducted eclogite and peridotite aided by carbonate melt[18,19] and that diamond and oxidised majoritic garnet are products of this interaction. For this reason we compare our results (Fig. 3) to a carbon-carbonate equilibrium relevant to the deeper upper mantle:

$$Mg_2Si_2O_6 + 2MgCO_3 = 2Mg_2SiO_4 + 2C + 2O_2 \quad (EMOD) \quad (2)$$

enstatite magnesite olivine diamond

We used tabulated thermodynamic data[27,28] and corrected for the effect of the phase change from olivine to wadsleyite at ~13 GPa. Figure 3 shows that our inclusions are in the (reduced) diamond stability field and that they approach EMOD with increasing pressure, which means that oxidation of Fe^{2+} during reduction of carbonate in a fluid

or melt phase is a plausible mechanism for generating the Fe^{3+} present in the garnets, as also suggested in a recent study[30]. The inclusions have $\delta^{18}O_{VSMOW}$ values between +8.6 and +10‰[31], consistent with a protolith which contains a substantial proportion of subducted oceanic crust, although it is no longer eclogitic. The LREE depleted and fairly flat chondrite normalised MREE-HREE patterns[32] of the majoritic garnet inclusions suggest that during subduction, their protolith was chemically depleted in incompatible trace elements, including LREE, during partial melting in the garnet stability field.

In conclusion, we have shown that, in the upper mantle and transition zone, there is a systematic increase with depth in the oxidation state of iron in garnet from pyroxenitic bulk compositions. Although the volumetric proportion of pyroxenite in this part of the mantle is unknown, we note that these are the only available garnet inclusions that demonstrably come from the mantle transition zone and are hence the only indication of oxygen fugacity and oxidation state in this region of the mantle. The deepest samples (from~500 km depth) have $Fe^{3+}/(Fe^{3+}+Fe^{2+})$ of 0.30, more than double the ferric iron content of any garnet from the shallower (<200 km) peridotitic mantle. These ferric iron contents correspond to oxygen fugacities above the Fe-FeO (IW) buffer, which means that the high Fe^{3+} contents were not generated by disproportionation of Fe^{2+} to Fe^{3+} and Fe^{0}. With increasing depth relative oxygen fugacities increase and approach the carbon-carbonate equilibrium, suggesting that carbonate was the oxidising agent responsible for generating the high Fe^{3+} of these mantle garnets.

References

1 McDonough, W. F. & Sun, S. S. The Composition of the Earth. *Chemical Geology* **120**, 223-253 (1995).

2 Canil, D. *et al.* Ferric iron in peridotites and mantle oxidation states. *Earth and Planetary Science Letters* **123**, 205-220, doi:10.1016/0012-821x(94)90268-2 (1994).

3 Wood, B. J., Bryndzia, L. T. & Johnson, K. E. Mantle oxidation state and Its relationship to tectonic environment and fluid speciation. *Science* **248**, 337-345, doi:10.1126/science.248.4953.337 (1990).

4 Frost, D. J. & McCammon, C. A. The redox state of Earth's mantle. *Annual Review of Earth and Planetary Sciences* **36**, 389-420 (2008).

5 Woodland, A. B. & Koch, M. Variation in oxygen fugacity with depth in the upper mantle beneath the Kaapvaal craton, Southern Africa. *Earth and Planetary Science Letters* **214**, 295-310 (2003).

6 Gudmundsson, G. & Wood, B. J. Experimental tests of garnet peridotite oxygen barometry. *Contributions to Mineralogy and Petrology* **119**, 56-67, doi:10.1007/bf00310717 (1995).

7 Ballhaus, C. Is the upper mantle metal-saturated. Earth and Planetary Science Letters 132, 75-86, doi:Doi 10.1016/0012-821x(95)00047-G (1995).

8 Jacob, D. E., Kronz, A. & Viljoen, K. S. Cohenite, native iron and troilite inclusions in garnets from polycrystalline diamond aggregates. *Contributions to Mineralogy and Petrology* **146**, 566-576, doi:10.1007/s00410-003-0518-2 (2004).

9 Sobolev, N. V., Efimova, E. S. & Pospelova, L. N. Native iron in diamonds of Yakutia and its paragenesis. *Geologiya I Geofizika* **22**, 25-28 (1981).

10 Smith, E. M. *et al.* Large gem diamonds from metallic liquid in Earth's deep mantle. *Science* **354**, 1403-1405, doi:10.1126/science.aal1303 (2016).

11 Golubkova, A., Schmidt, M. W. & Connolly, J. A. D. Ultra-reducing conditions in average mantle peridotites and in podiform chromitites: a thermodynamic model for moissanite (SiC) formation. *Contributions to Mineralogy and Petrology* **171**, 1-17, doi:10.1007/s00410-016-1253-9 (2016).

12 Beyer, C. & Frost, D. J. The depth of sub-lithospheric diamond formation and the redistribution of carbon in the deep mantle. *Earth and Planetary Science Letters* **461**, 30-39, doi:http://dx.doi.org/10.1016/j.epsl.2016.12.017 (2017).

13 Irifune, T. & Ringwood, A. E. in *High-Pressure Research in Mineral Physics* Vol. 1 (eds M.H. Manghnani & Y Syono) 235-246 (Terra Scientific, 1987).

14 Wood, B. J., Kiseeva, E. S. & Matzen, A. K. Garnet in the Earth's Mantle. *Elements* **9**, 421-426 (2013).

15 Irifune, T. & Ringwood, A. E. Phase transformations in a harzburgite composition to 26 GPa - implications for dynamical behavior of the subducting slab. *Earth and Planetary Science Letters* **86**, 365-376 (1987).

16 Kiseeva, E. S. *et al.* Metapyroxenite in the mantle transition zone revealed from majorite inclusions in diamonds. *Geology* **41**, 883-886, doi:Doi 10.1130/G34311.1 (2013).

17 Pearson, D. G., Davies, G. R. & Nixon, P. H. Geochemical constraints on the petrogenesis of diamond facies pyroxenites from the Beni Bousera peridotite massif, North Morocco. *Journal of Petrology* **34**, 125-172 (1993).

18 Kiseeva, E. S., Wood, B. J., Ghosh, S. & Stachel, T. The pyroxenite-diamond connection. *Geochemical Perspectives Letters* **2**, 1-9, doi:http://dx.doi.org/10.7185/geochemlet.1601 (2016).

19 Thomson, A. R., Walter, M. J., Kohn, S. C. & Brooker, R. A. Slab melting as a barrier to deep carbon subduction. *Nature* **529**, 76-79 (2016).

20 Canil, D. & ONeill, H. S. C. Distribution of ferric iron in some upper-mantle assemblages. *Journal of Petrology* **37**, 609-635, doi:Doi 10.1093/Petrology/37.3.609 (1996).

21 Goncharov, A. G., Ionov, D. A., Doucet, L. S. & Pokhilenko, L. N. Thermal state, oxygen fugacity and C-O-H fluid speciation in cratonic lithospheric mantle: New data on peridotite xenoliths from the Udachnaya kimberlite, Siberia. *Earth and Planetary Science Letters* **357**, 99-110, doi:10.1016/j.epsl.2012.09.016 (2012).

22 Lazarov, M., Woodland, A. B. & Brey, G. P. Thermal state and redox conditions of the Kaapvaal mantle: A study of xenoliths from the Finsch mine, South Africa. *Lithos* **112**, 913-923, doi:10.1016/j.lithos.2009.03.035 (2009).

23 Luth, R. W., Virgo, D., Boyd, F. R. & Wood, B. J. Ferric iron in mantle-derived garnets - implications for thermobarometry and for the oxidation state of the mantle. *Contributions to Mineralogy and Petrology* **104**, 56-72, doi:Doi 10.1007/Bf00310646 (1990).

24 McCammon, C. & Kopylova, M. G. A redox profile of the Slave mantle and oxygen fugacity control in the cratonic mantle. *Contributions to Mineralogy and Petrology* **148**, 55-68 (2004).

25 Kopylova, M. G., Beausoleil, Y., Goncharov, A., Burgess, J. & Strand, P. Spatial distribution of eclogite in the Slave cratonic mantle: The role of subduction. *Tectonophysics* **672**, 87-103, doi:10.1016/j.tecto.2016.01.034 (2016).

26 Rohrbach, A. *et al.* Metal saturation in the upper mantle. *Nature* **449**, 456-458 (2007).

27 Holland, T. J., Hudson, N. F., Powell, R. & Harte, B. New thermodynamic models and calculated phase equilibria in NCFMAS for basic and ultrabasic compositions through the transition zone into the uppermost lower mantle. *Journal of Petrology* **54**, 1901-1920, doi:Doi 10.1093/Petrology/Egt035 (2013).

28 Holland, T. J. B. & Powell, R. An improved and extended internally consistent thermodynamic dataset for phases of petrological interest, involving a new equation of state for solids. *Journal of Metamorphic Geology* **29**, 333-383, doi:Doi 10.1111/J.1525-1314.2010.00923.X (2011).

29 Mckenzie, D. & Bickle, M. J. The volume and composition of melt generated by extension of the lithosphere. *Journal of Petrology* **29**, 625-679 (1988).

30 Xu, C. *et al.* Recovery of an oxidized majorite inclusion from Earth's deep asthenosphere. *Science Advances* **3**, doi:10.1126/sciadv.1601589 (2017).

31 Ickert, R. B., Stachel, T., Stern, R. A. & Harris, J. W. Extreme ^{18}O-enrichment in majorite constrains a crustal origin of transition zone diamonds. *Geochemical Perspectives Letters* **1**, 65-74, doi:http://dx.doi.org/10.7185/geochemlet.1507 (2015).

32 Tappert, R. *et al.* Diamonds from Jagersfontein (South Africa): messengers from the sublithospheric mantle. *Contributions to Mineralogy and Petrology* **150**, 505-522 (2005).

Corresponding author.

Correspondence and requests for materials should be address to Ekaterina S. Kiseeva, email: kate.kiseeva@earth.ox.ac.uk**.**

Acknowledgements.

We thank Tim Holland for checking some of our calculations and Dan Frost for providing his spreadsheet for oxygen fugacity calculations using garnet equilibria, Andreas Schönleber for discussion of XRD results and Dariia Simonova for assistance during Mössbauer experiments. We acknowledge support from European Research Council grant 267764 to BJW and the NERC grant NE/L010828/1 to ESK. Financial support was provided to LD and CM through grants from the DFG and BMBF. We acknowledge the European Synchrotron Radiation Facility for provision of synchrotron radiation facilities.

Author contributions.

Work was initiated and planned by ESK and LD. TS and JH provided the samples and their detailed description. MB, DV, EB and LD performed the X-ray diffraction measurements. DV, MB, EB, and LD processed and analysed the diffraction data. DV, VC, AC and CM collected, processed and analysed the Mössbauer spectra. ESK and BW interpreted the data, performed the thermodynamic calculations and prepared the manuscript. All co-authors read, commented and approved of the manuscript.

Figure captions

Figure 1. ***Chemical composition (in cations per 12-oxygen formula unit) of majoritic garnet inclusions in diamonds worldwide (literature data from ref. 16).*** *Inclusions studied here from the Jagersfontein kimberlite are shown by red circles. In order to compare compositions with those of previous studies, all iron has been calculated as* Fe^{2+}*. Uncertainties are estimated at 1% relative for microprobe analysis and shown as indicative error bars.*

Fig. 2. ***Ferric iron contents of majoritic garnets from Jagersfontein diamonds compared to lithospheric garnets from peridotite xenoliths.*** *All ferric iron contents determined by Mössbauer spectroscopy*[5,20-25]. Uncertainty in pressure calculations (0.86 GPa) was taken from ref. 12.

Fig. 3. ***Calculated oxygen fugacities (see methods) of the majoritic inclusions and of garnets crystallised in coexistence with Fe metal***[26]***.*** *The data are plotted relative to the EMOD and Fe-FeO (IW) buffers. Uncertainty in absolute oxygen fugacity is estimated at ±1 log unit with relative uncertainty approximately ±0.3 log units (methods).*

METHODS

Samples. The garnet inclusions in diamonds investigated in this study originate from the Jagersfontein kimberlite in South Africa (more details about the host diamonds, compositions, rare earth element (REE) patterns *etc.* are given in Ref. 32). The inclusions were released by crushing the host diamonds, mounted in epoxy disks with 0.7 mm thickness supported by brass rings and then polished. All measurements described here were performed on the samples mounted in epoxy. The size of the inclusions studied vary from about 60 μm in diameter and 20 μm thick to 300 μm in lateral dimensions and about 300 μm thick.

Mössbauer spectroscopy. Mössbauer absorption spectra were collected at ambient temperature at the Nuclear Resonance beamline (ID18) at the European Synchrotron Radiation Facility (Grenoble, France) using a Synchrotron Mössbauer Source (SMS)[33]. The experiment was conducted in transmission geometry and folded spectra contain 512 channels. The typical beam size was 16 × 20 μm^2 full width at half maximum (FWHM). The line width of the SMS was determined before and after collection of each spectrum of the sample by measuring the reference single line absorber ($K_2Mg^{57}Fe(CN)_6$). More information about sample mounting and alignment procedure is given in Ref. 34. Each spectrum was collected for 4 to 12 hours.

The Mössbauer spectra were fitted using MossA software[35] version 1.01a with the full transmission integral assuming a Lorentzian-squared line shape of the SMS. The fitted parameters were centre shift (CS), FWHM, intensity (area), quadrupole splitting (QS), and component intensity ratio of the main doublet (*a*12, where the asymmetry is due to the Goldanskii-Karyagin effect for iron located in the distorted cubic X-position of the garnet structure, see Ref. 36; there is no effect for iron in the

361 octahedral Y-site). The centre shift values are reported relative to α-iron at ambient
362 conditions. Iron cations in two crystallographically distinct sites in the garnet
363 structure may have different recoil-free-fractions ("*f*-factors")[37,38]. The Debye
364 approximation was used to correct for the different *f*-factors, where values of the
365 effective Debye temperatures for X- and Y-sites were taken from Refs. 37 and 38.
366 Additional absorption in the JF-22A spectrum was fit to a quadrupole doublet and
367 assigned to Fe^{2+} in clinopyroxene based on the hyperfine parameters.
368 X-ray optical components at the ID18 beamline, contain very small amounts (ppm
369 level) of iron. Generally, this amount of iron does not affect SMS spectra due to the
370 strong signal from the sample. However, due to the small size of the samples studied
371 and the low natural abundance of ^{57}Fe, the signal from the sample was sufficiently
372 weak that spectral contamination from iron in the X-ray optical components could be
373 detected. In order to account for this effect at each experimental run (i.e., for different
374 combinations of X-ray optical components), SMS spectra were measured without any
375 sample so that Mössbauer absorption due to the optical components could be
376 accurately determined for each of the garnet SMS spectra.
377 The Mössbauer spectra of studied inclusions do not show the presence of Fe^{2+} in the
378 Y-site. This agrees with the results of McCammon and Ross[39], who conclude that in
379 majoritic garnet there is a strong preference to balance Si^{4+} in the Y-site by Mg^{2+}
380 (rather than Fe^{2+}).
381 **X-ray diffraction**. X-ray diffraction (XRD) measurements were performed at the
382 Extreme Conditions Beamline P02.2 at PETRA III (Hamburg, Germany)[40]. Data
383 were acquired with a PerkinElmer XRD1621 flat panel detector, X-ray beam-size
384 $5 \times 8\ \mu m^2$ (FWHM), and wavelength $\lambda = 0.29464$ Å. XRD "wide-scan" images were
385 collected during continuous rotation of the samples from –20 to +20° on the omega

axis; single crystal data collection experiments were performed by narrow 0.5° scanning ω-scanning in the range from -35° to $+35^{\circ}$. Data integration and absorption corrections were performed with CrysAlisPro[41] software version 171.38.43. Refinement was performed using the JANA2006[42] version from 25.10.2015.

XRD data analysis. Analysis of diffraction patterns shows that all garnet inclusions studied are single crystals, mostly mono-domain, where only samples JF-58B and JF-22A contain more than two domains (but all with the same lattice parameters within measurement uncertainty). Within the detection limits of X-ray diffraction, all samples except for three are monomineralic. Samples JF-44B and JF-58B show the presence of a small amount of polycrystalline phase(s) (strongest intensity of impurity powder diffraction lines are within 0.5% of the (420) diffraction line of garnet). Sample JF-84A contains single crystal domains of clinopyroxene (space group *C*2/*c*, *a* = 9.650(4), *b* = 8.828(2), *c* = 5.2481(11) Å, β = 106.91(3), V = 427.8(2) Å^3). However, its relative phase fraction is negligible and its presence does not affect the structure refinement of XRD data. The contribution to the Mössbauer spectrum is negligible within the statistics of the data.

The structural analysis of garnets is a well established method to study the distribution of elements over different crystallographic sites. For this study the amount of iron in the different structural positions is particularly relevant. Accurate structure refinements provide an average atomic scattering factor in the different crystallographic sites, thus imposing constraints on the types and amounts of elements in the sites. Silicate garnets have the general formula $X^{2+}_3\,Y^{3+}_2(SiO_4)_3$ and crystallize in the cubic structure ($Ia\bar{3}d$ space group). The octahedral Y-site is usually populated by a trivalent cation (Al^{3+}, Fe^{3+}, Cr^{3+}) and at high pressure could accommodate (as in majorite) Si^{4+} (balanced by Mg^{2+}, in particular). Divalent cations

411 (Mg^{2+}, Ca^{2+}, Fe^{2+}, Mn^{2+}, etc.) occupy the distorted X-site. Natural samples have
412 complex chemical compositions. Even if one assumes that the contributions by Na,
413 Mn, Cr, and Ti to diffraction intensity are negligible (total up to ~3 at% in some
414 samples), it is not possible to simultaneously refine the occupancies of four different
415 atoms (Mg, Fe, Al, Si) in the Y site and three atoms (Ca, Mg, Fe) in the X-site. Based
416 on the known crystal chemistry of silicate garnet, all structural positions may be
417 assumed to be fully occupied and charge (valence) balanced. Unambiguous
418 refinements of iron occupancy in the X- and Y-sites are not possible and require
419 information about the amount of other components from chemical analysis. We tested
420 different combinations of constraints for sample JF-22a, and all give the same
421 outcome within uncertainty (~0.5%). In the final model, we performed structural
422 refinements of all garnets with the following composition constraints: (*i*) each
423 crystallographic site of garnet is fully occupied, (*ii*) only O, Si, Mg, Al, Fe and Ca are
424 considered and the presence of other elements is neglected, (*iii*) in the Y-site, Mg, Si
425 and Al are refined as a single "Al" atom (X-ray scattering by equiproportional
426 mixture of Si and Mg approximately the same as scattering by Al), and (*iiii*) the
427 amount of Ca in the X-site is fixed based on the microprobe data.

428 Overall, there is good (within 3σ) agreement between determinations of Fe^{3+} content
429 in all garnets studied by Mössbauer spectroscopy and X-ray diffraction as well as
430 calculations based on composition assuming stoichiometry. We note that the Fe^{3+}
431 content derived from Mössbauer spectroscopy is systematically higher than the
432 amount obtained from X-ray diffraction data. The reasons for this minor
433 inconsistency could be simplifications (assumptions) made during the structural
434 refinements and/or complications in the analysis of overlapping components in SMS
435 spectra (in particular the impurity signal from iron in the X-ray optical components).

Thermodynamic calculations. All end-member thermodynamic data for our calculations, except that of the Fe-FeO (IW) reaction were taken from the work of Holland and Powell and Holland et al[27,28]. We used the equilibrium:

$$2Ca_3Al_2Si_3O_{12} + 4/3Fe_3Al_2Si_3O_{12} + 2.5Mg_4Si_4O_{12} + O_2 = 2Ca_3Fe_2Si_3O_{12} + 10/3Mg_3Al_2Si_3O_{12} + 4SiO_2 \quad (1)$$

Garnet Garnet Garnet Garnet Garnet

to estimate the oxygen fugacities at which the garnet inclusions were formed. Since the inclusions do not contain a SiO_2 phase we need to estimate the activity of this component. We approximated this activity using end-member data for the reaction:

$$Mg_2SiO_4 + SiO_2 = Mg_2Si_2O_6 \quad (2)$$

Olivine/wadsleyite Enstatite

Coexistence of olivine and enstatite, as in a mantle peridotite, defines the activity of SiO_2. In this case we used stishovite as our SiO_2 end member so that SiO_2 activities are expressed relative to this standard state. Since we do not observe olivine and orthopyroxene in the garnet inclusions we arbitrarily raised SiO_2 activity by 0.01 log units relative to olivine (wadsleyite above 13 GPa) stability.

Using a standard state of the pure phase at the pressure and temperature of interest we followed the methods of Stagno et al[43] to compute activities of the $Ca_3Al_2Si_3O_{12}$, $Fe_3Al_2Si_3O_{12}$, $Mg_3Al_2Si_3O_{12}$ and $Ca_3Fe_2Si_3O_{12}$ components from the compositions of the garnet inclusions. For the majorite component $Mg_4Si_4O_{12}$ we computed activities from the garnet compositions using 2 possible expressions:

$$RT\ln a^{gt}_{Mg_4Si_4O_{12}} = RT\ln 4x^{c3}_{Mg}x^{o2}_{Si} + RT\ln g^{gt}_{Mg_4Si_4O_{12}}$$
$$RT\ln a^{gt}_{Mg_4Si_4O_{12}} = RT\ln 4x^{c3}_{Mg}.x^{o}_{Mg}x^{o}_{Si} + RT\ln g^{gt}_{Mg_4Si_4O_{12}} \quad (3)$$

457 In equation 3, $x^c_{Mg}, x^o_{Mg}, x^o_{Si}$ refer to the atomic fractions of Mg and Si in the cubic
458 (c) and octahedral (o) sites and the factor 4 normalises so that pure $Mg_4Si_4O_{12}$ has
459 activity 1.0. The first expression assumes stoichiometric substitution of $Mg_4Si_4O_{12}$
460 into garnet so that there are equal mole fractions of Mg and Si on the octahedral site.
461 The second expression is more realistic in allowing for different fractions of Mg and
462 Si on the octahedral sites, but is impossible to compute exactly because the
463 partitioning of Fe^{2+} and Mg between cubic and octahedral sites cannot be determined
464 exactly by either stoichiometry or XRD.

465 The activity coefficient, $g^{gt}_{Mg_4Si_4O_{12}}$ was calculated using the regular solution
466 parameters from Holland et al[27]. Note, however, that these contain no reciprocal
467 terms[43] and no terms involving Fe^{3+}.

468 We used our analyses to assign atoms to sites in the normal way:

469 Cubic: Ca, Mg, Fe^{2+}, Mn
470 Tetrahedral: Si
471 Octahedral, Al, Cr, Fe^{3+}, excess Si from tetrahedral and excess (Mg+Fe^{2+}) from
472 cubic.

473 We then computed activities using both expressions (3) and, since the octahedral site
474 is smaller than the cubic site assumed either that all of the excess cubic site atoms
475 were Mg (smaller than Fe^{2+}) or that they were 75% Mg and 25% Fe^{2+}. Use of the first
476 activity expression in (3) yields the highest oxygen fugacities and it is these, which
477 are shown on Figure 3. Use of the second expression with all "excess" cubic atoms as
478 Mg yields values on average 0.6 log$f$$O_2$ units lower, while the allocation of 75% of
479 the excess cubic atoms to Mg and 25% to Fe^{2+} means that average oxygen fugacities

480 are 0.9 logf_{O2} units lower than shown. However, the addition of activity coefficient
481 terms, currently unknown, for octahedral site interactions involving Mg, Si and Fe^{3+}
482 would, we believe, tend to shift calculated oxygen fugacities to values higher than
483 shown. Hence we consider that the simpler activity expression of (3) provides a
484 reasonable compromise. In support of this conclusion we observe that 4 of the 5 iron
485 metal-saturated experiments of Rohrbach et al[26] plot correctly in the Fe stability field
486 of Figure 3 and that only one of our 13 inclusions plots just into the Fe stability field.
487 It should also be noted that, although the absolute uncertainties must be of the order
488 of 1 log unit in fO_2, errors in the activity expressions would shift all points up and
489 down by similar amounts, thus preserving the trends observed in Figure 3. Relative
490 uncertainties are thus estimated by the differences in calculated fO_2 between the
491 majorite inclusions and the Fe-metal saturated experiments of Rohrbach et al.[26]
492 shown in Fig 3. Relative uncertainties must be about $\pm$0.3 log units or less in order to
493 preserve the clear distinctions between the 2 sets of data.

494 Data for the IW (Fe-FeO) buffer[44] at 1 atmosphere were fitted to 1/T to enable
495 extrapolation to high temperature. They were extrapolated in pressure using the
496 Murnaghan equation of state with volumes, thermal expansion coefficients and bulk
497 moduli from a Handbook of Physical Constants[45].

498 **Data availability.** CCDC 1588374 to 1588386 contain the supplementary
499 crystallographic data for this paper. The data can be obtained free of charge from the
500 Cambridge Crystallographic Data Centre via www.ccdc.cam.ac.uk/structures. The
501 Mössbauer spectra and the thermodynamic calculations are available from the
502 corresponding author upon request.

Methods References

33 Potapkin, V. *et al.* The 57Fe synchrotron Mössbauer source at the ESRF. *Journal of synchrotron radiation* **19**, 559–569 (2012).

34 Nestola, F. *et al.* Synchrotron Mössbauer Source technique for in situ measurement of iron-bearing inclusions in natural diamonds. *Lithos* **265**, 328-333, doi:http://dx.doi.org/10.1016/j.lithos.2016.06.016 (2016).

35 Prescher, C., McCammon, C. & Dubrovinsky, L. MossA: a program for analyzing energy-domain Mössbauer spectra from conventional and synchrotron sources. *Journal of Applied Crystallography* **45**, 329–331 (2012).

36 Geiger, C. A. *et al.* A combined temperature dependent ^{57}Fe Mössbauer and single crystal X-ray diffraction study of synthetic almandine: evidence for the Goldanskii-Karyagin effect. *Physics and Chemistry of Minerals* **19**, 121-126 (1992).

37 Lyubutin, I. & Dodokin, A. Temperature dependence of Mössbauer effect for Fe^{2+} in dodecahedral coordination in garnet. . *SOVIET PHYSICS CRYSTALLOGRAPHY, USSR* **15**, 1091 (1971).

38 Lyubutin, I., Dodokin, A. & Belyaev, L. Temperature dependence of Mössbauer effect for octahedral iron atoms in garnets. *SOVIET PHYSICS SOLID STATE, USSR* **12**, 1100 (1970).

39 McCammon, C. A. & Ross, N. L. Crystal chemistry of ferric iron in (Mg, Fe)(Si,Al)O_3 majorite with implications for the transition zone. *Physics and Chemistry of Minerals* **30**, 206-216, doi:Doi 10.1007/S00269-003-0309-3 (2003).

40 Liermann, H. P. *et al.* The extreme conditions beamline P02.2 and the extreme conditions science infrastructure at PETRA III. *Journal of synchrotron radiation* **22**, 908-924, doi:10.1107/S1600577515005937 (2015).

41 Agilent Technologies. CrysAlisPro Software system (2013).

42 Petříček, V., Dušek, M. & Palatinus, L. Crystallographic computing system JANA2006: general features. *Zeitschrift für Kristallographie-Crystalline Materials* **229**, 345–352 (2014).

43 Stagno, V., Ojwang, D. O., McCammon, C. A. & Frost, D. J. The oxidation state of the mantle and the extraction of carbon from Earth's interior. *Nature* **493**, 84-88, doi:Doi 10.1038/Nature11679 (2013).

44 Holmes, R. D., O'Neill, H. S. C. & Arculus, R. J. Standard Gibbs free energy of formation for Cu_2O, NiO, CoO, and Fe_xO: high-resolution electrochemical measurements using zirconia solid electrolytes from 900-1400 K. *Geochimica Et Cosmochimica Acta* **50**, 2439-2452, doi:Doi 10.1016/0016-7037(86)90027-X (1986).

45 Ahrens, T. J. in *Mineral Physics and Crystallography, A Handbook of Physical Constants, AGU Reference Shelf* (American Geophysical Union, 1995).

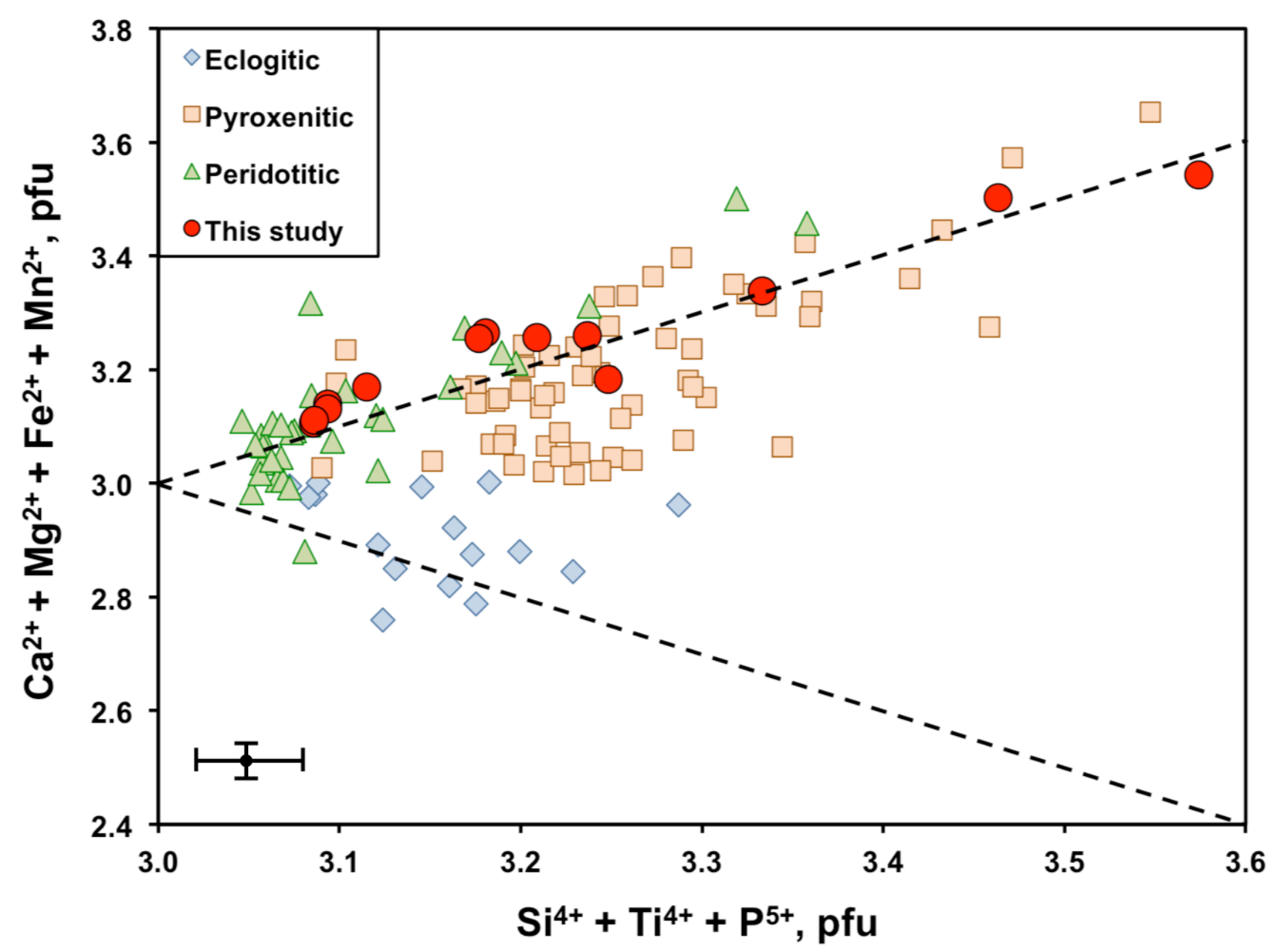
Eclogitic
Pyroxenitic
Peridotitic
This study
3.8
3.6
3.4
3.2
3.0
2.8
2.6
2.4
3.0
3.1
3.2
3.3
3.4
3.5
3.6
Ca2+ + Mg2+ + Fe2+ + Mn2+, pfu
Si4+ + Ti4+ + P5+, pfu

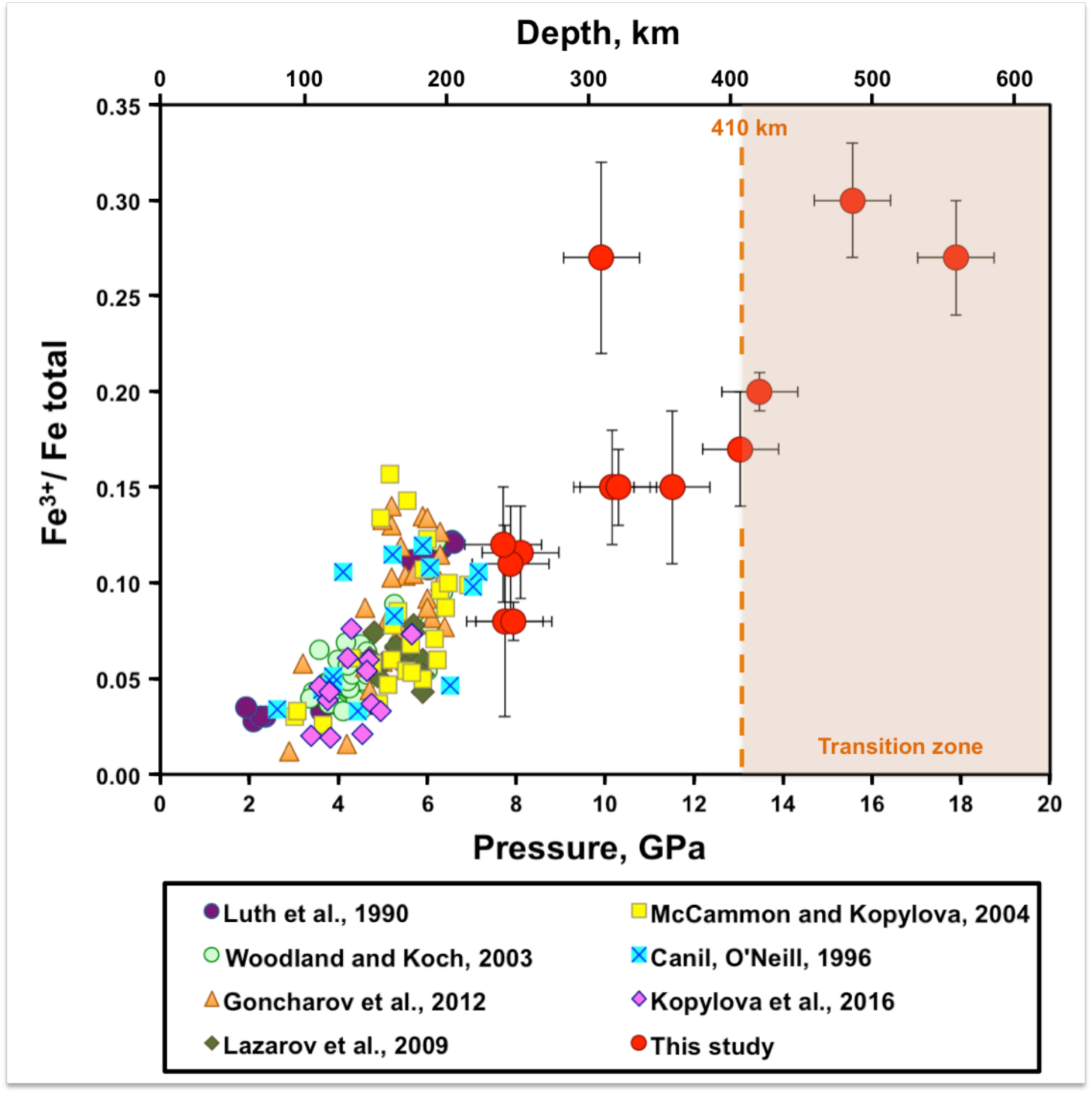
Depth, km
0
100
200
300
400
500
600
410 km
Transition zone
Fe3+/ Fe total
0.35
0.30
0.25
0.20
0.15
0.10
0.05
0.00
0
2
4
6
8
10
12
14
16
18
20
Pressure, GPa
Luth et al., 1990
McCammon and Kopylova, 2004
Woodland and Koch, 2003
Canil, O'Neill, 1996
Goncharov et al., 2012
Kopylova et al., 2016
Lazarov et al., 2009
This study

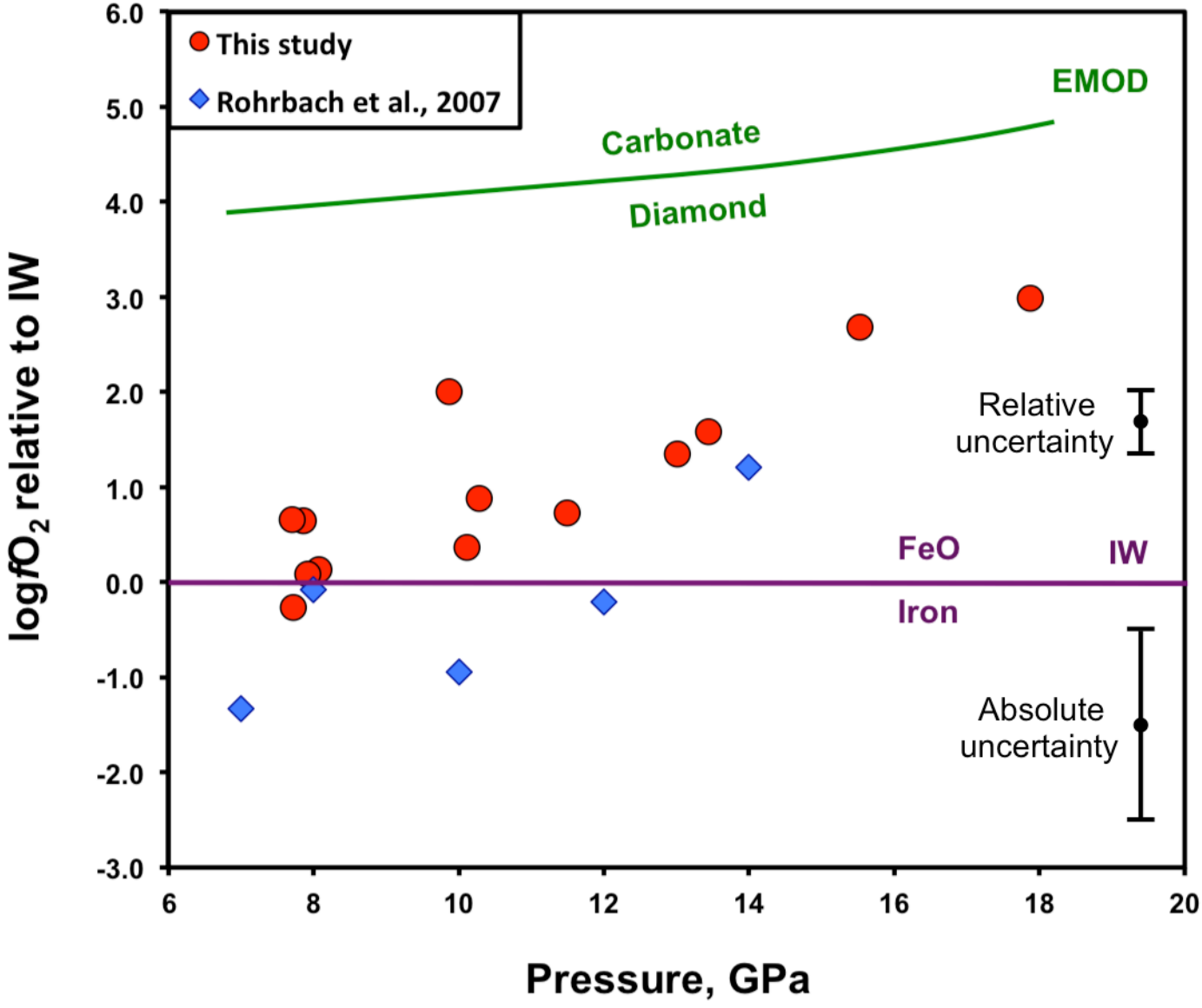
This study
Rohrbach et al., 2007
EMOD
Carbonate
Diamond
Relative uncertainty
FeO
IW
Iron
Absolute uncertainty
logfO_2 relative to IW
Pressure, GPa
6.0
5.0
4.0
3.0
2.0
1.0
0.0
-1.0
-2.0
-3.0
6
8
10
12
14
16
18
20

Oxidised iron in garnets from the mantle transition zone

Ekaterina S. Kiseeva[1,*], Denis M. Vasiukov[2,3], Bernard J. Wood[1], Catherine McCammon[3], Thomas Stachel[4], Maxim Bykov[3], Elena Bykova[3,5], Alexander Chumakov[6], Valerio Cerantola[6], Jeff W. Harris[7], Leonid Dubrovinsky[3]

[1] – Department of Earth Sciences, University of Oxford, Oxford OX1 3AN, UK

[2] – Laboratory of Crystallography, University of Bayreuth, D-95440 Bayreuth, Germany

[3] – Bayerisches Geoinstitut, Universität Bayreuth, D-95440 Bayreuth, Germany

[4] – Department of Earth and Atmospheric Sciences, University of Alberta, Edmonton, AB, T6G 2E3, Canada

[5] – DESY Photon Science, Notkestrasse 85, DE-22607 Hamburg, Germany

[6] – ESRF-The European Synchrotron, CS 40220, 38043, Grenoble, Cedex 9, France

[7] – School of Geographical and Earth Sciences, University of Glasgow, Glasgow, G12 8QQ, UK

*corresponding author, kate.kiseeva@earth.ox.ac.uk

Supplementary Table 1. **Hyperfine parameters of the garnet inclusions**.

Components	JF-1A		JF-9A		JF-37A		JF-37B	
	Fe^{2+} X-site	Fe^{3+} Y-site	Fe^{2+} X-site	Fe^{3+} Y-site	Fe^{2+} X-site	Fe^{3+} Y-site	Fe^{2+} X-site	Fe^{3+} Y-site
CS (mm/s)	1.285(3)	0.34(4)	1.282(5)	0.26(6)	1.280(5)	0.35(7)	1.278(4)	0.28(6)
FWHM (mm/s)	0.26(2)	0.25(17)	0.27(3)	0.2(2)	0.25(3)	0.25	0.24(2)	0.4(3)
Int (%)	87(3)	13(3)	88(3)	12(3)	91(5)	9(5)	86(3)	14(3)
QS (mm/s)	3.547(6)	0.33(8)	3.55(1)	0.48(8)	3.551(9)	0.2(2)	3.552(7)	0.4(1)
a12	0.480(7)	–	0.48(1)	–	0.481(9)	–	0.477(9)	–

Components	JF-39A		JF-42A		JF-44B		JF-50A	
	Fe^{2+} X-site	Fe^{3+} Y-site	Fe^{2+} X-site	Fe^{3+} Y-site	Fe^{2+} X-site	Fe^{3+} Y-site	Fe^{2+} X-site	Fe^{3+} Y-site
CS (mm/s)	1.259(3)	0.282(15)	1.279(4)	0.34(4)	1.290(7)	0.38(5)	1.279(2)	0.31(3)
FWHM (mm/s)	0.20(2)	0.21(15)	0.25(2)	0.28(13)	0.23(5)	0.2(2)	0.236(16)	0.20(13)
Int (%)	77.9(12)	22.1(12)	81(2)	19(2)	83(4)	17(4)	90.8(1.5)	9.2(1.5)
QS (mm/s)	3.524(6)	0.39(2)	3.545(7)	0.45(5)	3.519(13)	0.30(9)	3.548(5)	0.35(6)
a12	0.487(7)	–	0.471(8)	–	0.475(14)	–	0.474(5)	–

Components	JF-55A		JF-58A		JF-58B		JF-84A	
	Fe^{2+} X-site	Fe^{3+} Y-site	Fe^{2+} X-site	Fe^{3+} Y-site	Fe^{2+} X-site	Fe^{3+} Y-site	Fe^{2+} X-site	Fe^{3+} Y-site
CS (mm/s)	1.248(6)	0.31(2)	1.273(3)	0.32(3)	1.282(9)	0.320	1.275(6)	0.320
FWHM (mm/s)	0.25(4)	0.14(6)	0.25(2)	0.29(14)	0.24(7)	0.34(24)	0.23(4)	0.2(2)
Int (%)	67(3)	33(3)	83(2)	17(2)	71(5)	29(5)	84(4)	16(4)
QS (mm/s)	3.516(12)	0.42(3)	3.528(7)	0.30(8)	3.52(2)	0.3(1)	3.545(12)	0.51(8)
a12	0.477(13)	–	0.484(8)	–	0.50(2)	–	0.459(12)	–

Components	JF-22A		
	Fe^{2+} X-site	Fe^{3+} Y-site	Fe^{2+} cpx
CS (mm/s)	1.226(12)	0.27(7)	1.15(8)
FWHM (mm/s)	0.26(8)	0.3(2)	0.300
Int (%)	47(5)	29(4)	24(4)
QS (mm/s)	3.493(25)	0.300	2.07(16)
a12	–	–	–

CS: centre shift relative to α-Fe, FWHM: full width at half maximum of the absorber line, Int: relative area, QS: quadrupole splitting, a12: doublet area asymmetry.

Supplementary Table 2. **Crystal structure data of garnet inclusions.**

Inclusion	**JF-1A**	**JF-9A**	**JF-22A**	**JF-37A**	**JF-37B**	**JF-39A**	**JF-42A**	**JF-44B**
Chemical formula	$Al_{1.925}Ca_{0.478}Fe_{0.777}Mg_{1.82}Si_3O_{12}$	$Al_{1.952}Ca_{0.474}Fe_{0.838}Mg_{1.736}Si_3O_{12}$	$Al_{1.847}Ca_{0.444}Fe_{0.702}Mg_{2.006}Si_3O_{12}$	$Al_{1.948}Ca_{0.501}Fe_{0.78}Mg_{1.77}Si_3O_{12}$	$Al_{1.938}Ca_{0.497}Fe_{0.792}Mg_{1.773}Si_3O_{12}$	$Al_{1.886}Ca_{0.45}Fe_{0.631}Mg_{2.033}Si_3O_{12}$	$Al_{1.875}Ca_{0.883}Fe_{0.808}Mg_{1.435}Si_3O_{12}$	$Al_{1.893}Ca_{0.616}Fe_{0.716}Mg_{1.775}Si_3O_{12}$
Crystal system, space group	Cubic, $Ia\bar{3}d$							
Temperature (K)	293							
a (Å)	11.54866 (9)	11.54697 (8)	11.56570 (8)	11.55093 (7)	11.55114 (8)	11.54816 (9)	11.61383 (8)	11.57482 (7)
V (Å^3)	1540.26 (2)	1539.59 (2)	1547.09 (2)	1541.17 (2)	1541.25 (2)	1540.06 (2)	1566.49 (2)	1550.75 (2)
Z	8							
F(000)	1717	1723	1706	1719	1720	1695	1746	1719
Radiation type	Synchrotron, λ = 0.29464 Å							
μ (mm^{-1})	0.26	0.27	0.25	0.26	0.26	0.24	0.28	0.26
Crystal size (mm)	0.16 × 0.10 × 0.03	0.16 × 0.10 × 0.02	0.11 × 0.07 × 0.02	0.13 × 0.10 × 0.05	0.17 × 0.10 × 0.05	0.23 × 0.15 × 0.05	0.12 × 0.12 × 0.07	0.08 × 0.08 × 0.02
No. of measured, independent and observed [$I > 3\sigma(I)$] reflections	4006, 464, 398	3184, 456, 398	4116, 448, 417	4296, 443, 394	3477, 439, 376	3614, 438, 380	4095, 447, 381	3970, 448, 381
R_{int}	0.021	0.028	0.030	0.026	0.023	0.015	0.023	0.025
θ values (°)	θ_{max} = 16.8, θ_{min} = 1.8	θ_{max} = 16.9, θ_{min} = 1.8	θ_{max} = 16.9, θ_{min} = 1.8	θ_{max} = 16.9, θ_{min} = 1.8	θ_{max} = 16.8, θ_{min} = 1.8	θ_{max} = 17.0, θ_{min} = 1.8	θ_{max} = 16.9, θ_{min} = 1.8	θ_{max} = 16.7, θ_{min} = 1.8
$(\sin\theta/\lambda)_{max}$ (Å^{-1})	0.982	0.985	0.984	0.985	0.982	0.989	0.984	0.975
Range of h, k, l	h = -21→19, k = -19→9, l = -21→21	h = -16→6, k = -20→19, l = -17→21	h = -16→19, k = -21→20, l = -21→16	h = -8→17, k = -18→20, l = -19→19	h = -20→21, k = -21→19, l = -15→9	h = -14→19, k = -21→20, l = -21→17	h = -21→20, k = -5→15, l = -20→20	h = -21→13, k = -19→18, l = -21→18
R [$F^2 > 2\sigma(F^2)$], $wR(F^2)$, S	0.023, 0.030, 1.60	0.027, 0.033, 1.89	0.028, 0.037, 2.38	0.020, 0.031, 1.85	0.022, 0.030, 1.56	0.026, 0.035, 1.95	0.022, 0.031, 1.70	0.024, 0.032, 1.86
No. of parameters	20							
No. of restraints	0							
No. of constraints	8							
CCDC reference No.	1588374	1588375	1588376	1588377	1588378	1588379	1588380	1588381

Supplementary Table 2. **Crystal structure data of garnet inclusions (continued)**.

Inclusion	**JF-50A**	**JF-55A**	**JF-58A**	**JF-58B**	**JF-84A**
Chemical formula	$Al_{1.938}Ca_{0.377}Fe_{0.815}Mg_{1.871}Si_3O_{12}$	$Al_{1.855}Ca_{0.57}Fe_{0.56}Mg_{2.015}Si_3O_{12}$	$Al_{1.894}Ca_{0.36}Fe_{0.886}Mg_{1.86}Si_3O_{12}$	$Al_{1.882}Ca_{0.355}Fe_{0.89}Mg_{1.873}Si_3O_{12}$	$Al_{1.908}Ca_{0.493}Fe_{0.722}Mg_{1.877}Si_3O_{12}$
Crystal system, space group	Cubic, $Ia\bar{3}d$				
Temperature (K)	293				
a (Å)	11.53228 (7)	11.57663 (7)	11.53956 (7)	11.54779 (18)	11.55837 (9)
V (Å^3)	1533.72 (2)	1551.48 (2)	1536.62 (2)	1539.91 (4)	1544.15 (2)
Z	8				
F(000)	1715	1698	1721	1721	1712
Radiation type	Synchrotron, λ = 0.29464 Å				
μ (mm^{-1})	0.26	0.23	0.27	0.27	0.25
Crystal size (mm)	0.22 × 0.18 × 0.08	0.20 × 0.10 × 0.08	0.30 × 0.30 × 0.30	0.18 × 0.10 × 0.03	0.09 × 0.06 × 0.02
No. of measured, independent and observed [$I > 3\sigma(I)$] reflections	3646, 420, 366	4193, 438, 392	3732, 440, 394	4173, 440, 361	4306, 412, 357
R_{int}	0.022	0.021	0.034	0.021	0.026
θ values (°)	θ_{max} = 16.8, θ_{min} = 1.8	θ_{max} = 16.8, θ_{min} = 1.8	θ_{max} = 17.0, θ_{min} = 1.8	θ_{max} = 16.7, θ_{min} = 1.8	θ_{max} = 16.9, θ_{min} = 1.8
$(\sin\theta/\lambda)_{max}$ (Å^{-1})	0.983	0.983	0.992	0.974	0.984
Range of *h*, *k*, *l*	*h* = -6→15, *k* = -21→22, *l* = -21→21	*h* = -21→22, *k* = -22→21, *l* = -13→6	*h* = -22→15, *k* = -21→21, *l* = -15→20	*h* = -22→21, *k* = -21→20, *l* = -17→12	*h* = -18→9, *k* = -22→21, *l* = -21→22
R [$F^2 > 2\sigma(F^2)$], *wR*(F^2), *S*	0.027, 0.036, 2.09	0.027, 0.036, 2.34	0.023, 0.032, 1.81	0.031, 0.038, 2.07	0.022, 0.029, 1.77
No. of parameters	20				
No. of restraints	0				
No. of constraints	8				
CCDC reference No.	1588382	1588383	1588384	1588385	1588386

The chemical formula is the obtained model (see Methods) used for the crystal structure refinement. The constraints are (i) fixed amount of Ca, (ii) identical anisotropic displacement parameters (ADP), and (iii) fixed total occupation number (equal to 1) for atoms populating the same crystallographic position.

Supplementary Table 3. **X-ray refinement of Fe^{3+} content of sample JF22a**.

X-site	Y-site	$Fe^{3+}/\Sigma Fe$ (%)
Fully occupied Ca amount fixed to microprobe data Mg occupancy refined	Fully occupied Mg, Si, Al refined as single Al atom	21.8(4)
Fully occupied Mg amount fixed to microprobe data Ca occupancy refined.	Fully occupied Mg, Si, Al refined as single Al atom	21.7(4)
Fully occupied Mg occupancy refined Fe occupancy refined	Fully occupied Mg, Si, Al refined as single Al atom	21.5(4)
Fully occupied Ca amount fixed to microprobe data Mg occupancy refined	Fully occupied Mg and Si amount fixed to microprobe data Al and Fe occupancy refined	22.3(4)
Fully occupied Ca amount fixed to microprobe data Mg occupancy refined	Fully occupied Al amount fixed to microprobe data Mg and Si constrained to have same abundance Fe and (Mg+Si) amounts refined	22.1(4)

Rows indicate different refinements of single crystal diffraction data using the indicated constraints.

Supplementary Table 4. **Inclusion compositions**.

Sample	Pressure (GPa)	Si (pfu)	Mg (pfu)	Al (pfu)	Ca (pfu)	Fe (pfu)	Fe by XRD (pfu)	Fe^{3+}/Fe_{tot} by MS (%)	Y-site Fe/Fe_{tot} by XRD (%)	Fe^{3+}/Fe_{tot} by EMPA (%)
JF-37B	7.7	3.08(3)	1.82(2)	1.77(2)	0.50(1)	0.79(1)	0.79	12(3)	7.8(4)	11(6)
JF-37A	7.7	3.08(3)	1.83(2)	1.77(2)	0.50(1)	0.79(1)	0.78	8(5)	6.7(4)	11(6)
JF-09A	7.9	3.08(3)	1.75(2)	1.80(2)	0.48(1)	0.86(1)	0.84	11(3)	5.7(3)	10(6)
JF-50A	7.9	3.08(3)	1.91(2)	1.79(2)	0.38(1)	0.80(1)	0.82	8(1)	7.6(4)	10(6)
JF-01A	8.1	3.11(3)	1.90(2)	1.71(2)	0.48(1)	0.77(1)	0.78	12(2)	9.7(4)	13(7)
JF-58B	9.9	3.16(3)	1.99(2)	1.57(2)	0.36(1)	0.89(1)	0.89	27(5)	13.3(3)	17(10)
JF-44B	10.2	3.19(3)	1.91(2)	1.52(2)	0.62(1)	0.71(1)	0.72	15(3)	14.9(3)	14(8)
JF-58A	10.3	3.16(3)	1.98(2)	1.56(2)	0.36(1)	0.90(1)	0.89	15(2)	12.0(3)	18(11)
JF-84A	11.5	3.21(3)	2.04(2)	1.48(1)	0.49(1)	0.71(1)	0.72	15(4)	12.7(3)	16(9)
JF-42A	13.0	3.22(3)	1.48(1)	1.52(2)	0.89(1)	0.80(1)	0.81	17(3)	15.5(4)	12(7)
JF-39A	13.5	3.32(3)	2.22(2)	1.30(1)	0.45(1)	0.66(1)	0.63	20(1)	18.0(4)	17(10)
JF-55A	15.6	3.44(3)	2.35(2)	1.01(1)	0.57(1)	0.57(1)	0.56	30(3)	25.9(5)	29(18)
JF-22A	17.9	3.55(4)	2.36(2)	0.83(1)	0.45(1)	0.72(1)	0.70	27(3)	21.7(4)	22(14)

Cation abundance based on 12 oxygen anions calculated from major element compositions from electron microprobe data reported in Ref. 26. XRD: X-ray diffraction, MS: Mössbauer spectroscopy, EMPA: calculation based on electron microprobe data assuming stoichiometry

Supplementary Figure 1. **Mössbauer spectra of garnet inclusions JF-1A, JF-9A, JF-22A, JF-37A, JF-37B, JF-39A, JF-42A and JF-44B**. The bluish-green doublet corresponds to Fe^{2+} on the X-site and the orange doublet indicates Fe^{3+} located on the Y-site. The dark red component corresponds to iron in the X-ray optics on ID18 at ESRF. The green doublet in **c** with smaller splitting corresponds to Fe^{2+} in clinopyroxene. The pink line indicates the residual of the fit.

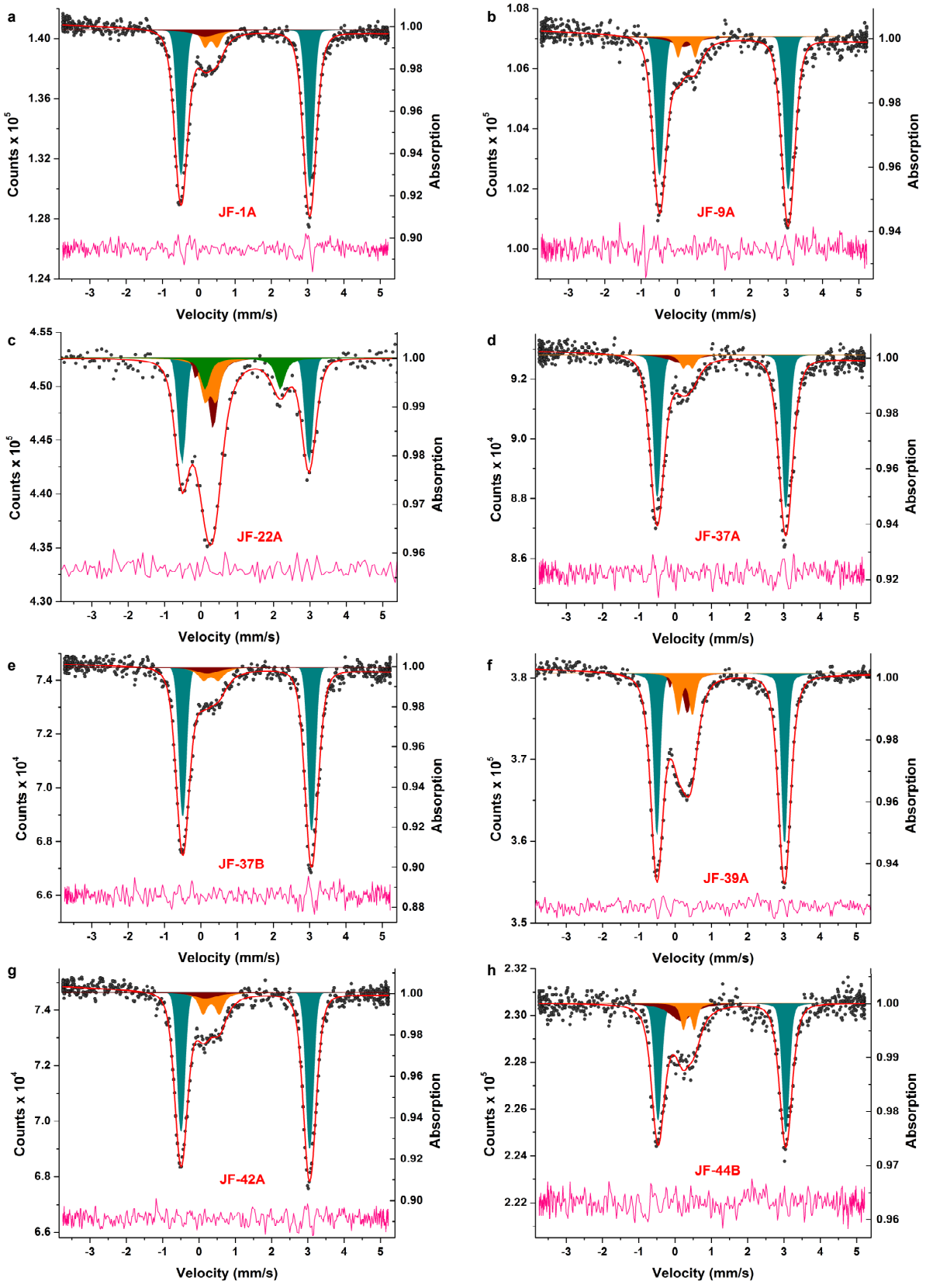

Supplementary Figure 2. **Mössbauer spectra of garnet inclusions JF-50A, JF-55A, JF58A, JF-58B and JF-84a**. The colours are the same as in Supplementary Figure 1.

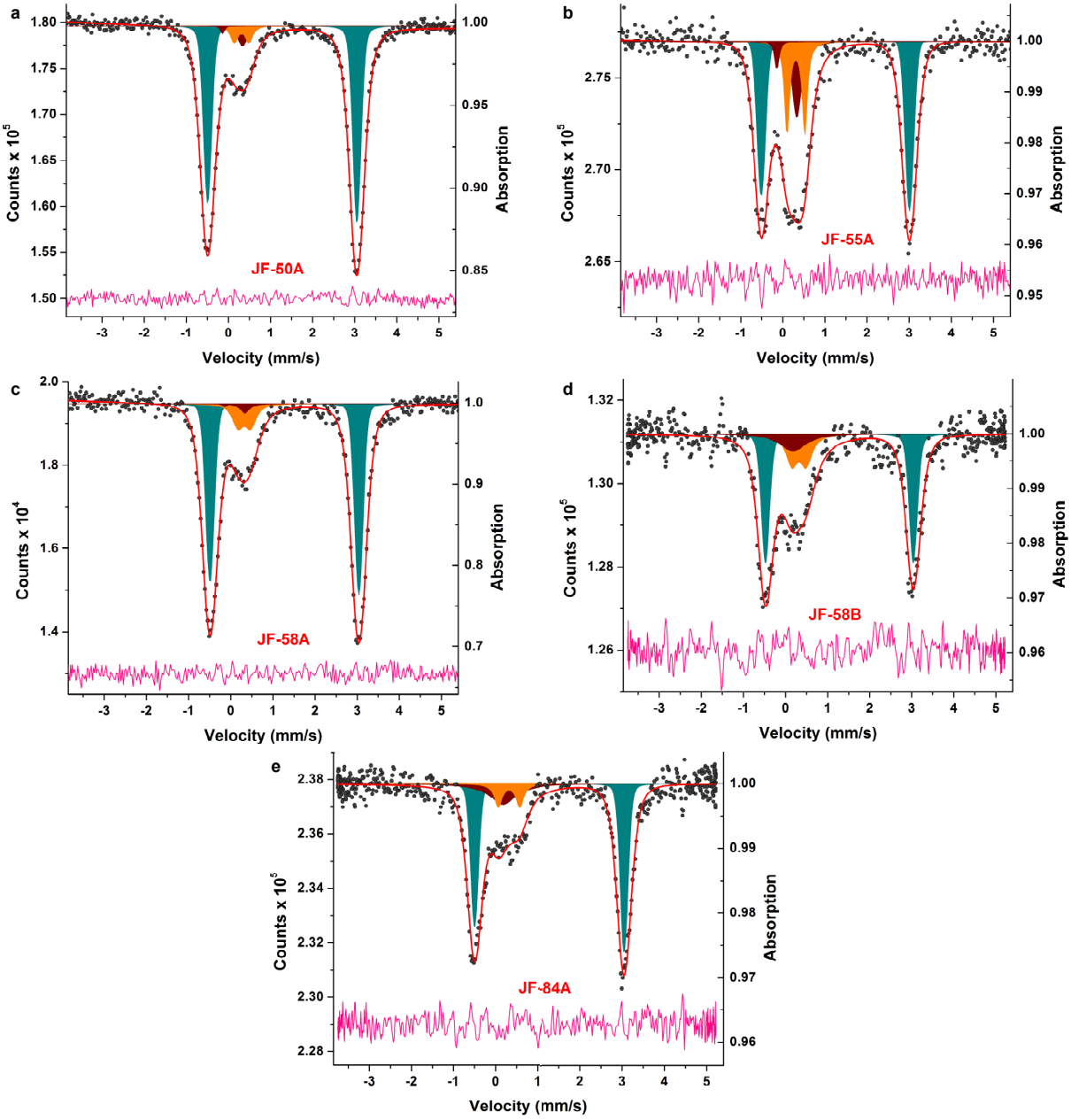

Supplementary Figure 3. **Photos of garnet inclusions.** Epoxy mount with seven inclusions (marked by red circles) is shown on the left. The right image shows inclusion JF-55A under higher magnification. The photos were made on a Leica M205 C stereo microscope equipped with a Leica DFC450 digital camera.

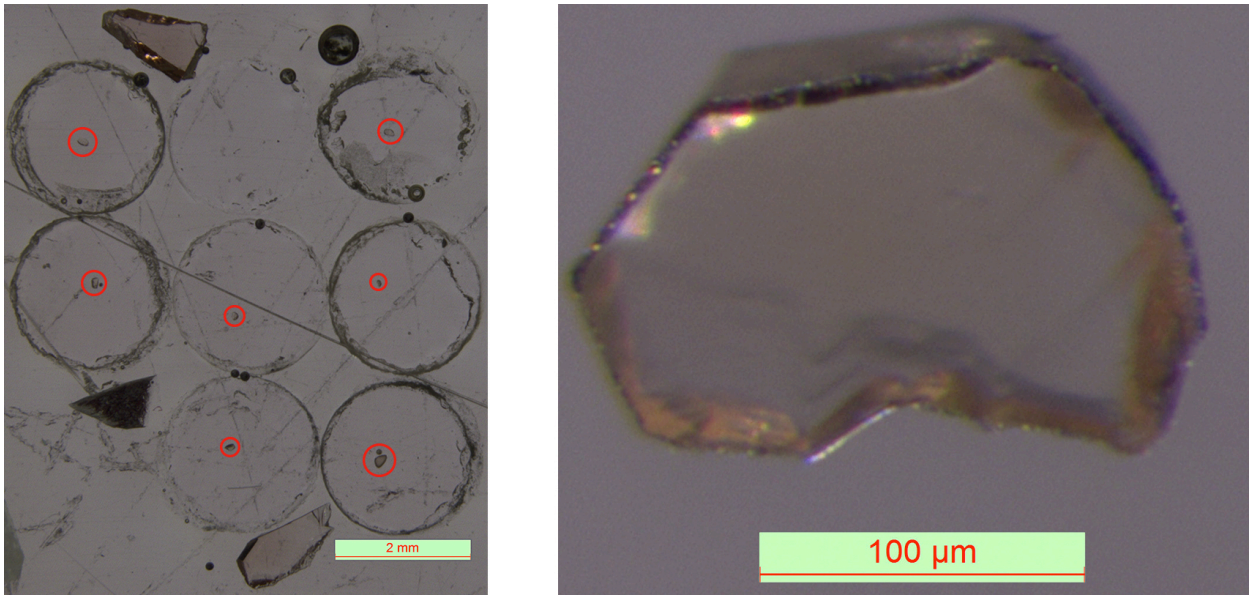

Pressure-induced spin transition of Fe^{3+} in oxygen octahedra

D. M. Vasiukov,[1,2,*] L. Dubrovinsky,[2] I. Kupenko,[3] V. Cerantola,[4]
G. Aprilis,[1,2] L. Ismailova,[5] E. Bykova,[6] C. McCammon,[2]
C. Prescher,[7] A. I. Chumakov,[4] and N. Dubrovinskaia[1]

[1]*Laboratory of Crystallography, Universität Bayreuth, D-95440 Bayreuth, Germany*
[2]*Bayerisches Geoinstitut, Universität Bayreuth, D-95440 Bayreuth, Germany*
[3]*Institut für Mineralogie, Universität Münster, D-48149 Münster, Germany*
[4]*ESRF-The European Synchrotron CS40220 38043 Grenoble Cedex 9 France*
[5]*Skolkovo Institute of Science and Technology,*
Skolkovo Innovation Center, 143026 Moscow, Russia
[6]*Photon Science, Deutsches Elektronen-Synchrotron, D-22607 Hamburg, Germany*
[7]*Institut für Geologie und Mineralogie,*
Universität zu Köln, D-50674 Köln, Germany

(Dated: June 22, 2018)

Abstract

High pressure can provoke spin transitions in transition metal-bearing compounds. These transitions are of high interest not only for fundamental physics and chemistry, but also may have important implications for geochemistry and geophysics of the Earth and planetary interiors. Here we have carried out a comparative study of the pressure-induced spin transition in compounds with trivalent iron, octahedrally coordinated by oxygen. High-pressure single-crystal Mössbauer spectroscopy data for $FeBO_3$, Fe_2O_3 and $Fe_3(Fe_{1.766(2)}Si_{0.234(2)})(SiO_4)_3$ are presented together with detailed analysis of hyperfine parameter behavior. The structural data show that the spin transition is closely related to the volume of the iron octahedron. The transition starts when volumes reach 8.9–9.3 $Å^3$, which corresponds to pressures of 45–60 GPa, depending on the compound. Based on phenomenological arguments we conclude that the spin transition can proceed only as a first-order phase transition in magnetically-ordered compounds. An empirical rule for prediction of cooperative behavior at the spin transition is proposed. The instability of iron octahedra, together with strong interactions between them in the vicinity of the critical volume, may trigger a phase transition in the metastable phase. We find that the isomer shift of high spin iron ions depends linearly on the octahedron volume with approximately the same coefficient, independent of the particular compounds and/or oxidation state. For eight-fold coordinated Fe^{2+} we observe a significantly weaker nonlinear volume dependence.

PACS numbers: 75.30.Wx, 76.80.+y, 61.50.Ks

I. INTRODUCTION

The spin transition in transition metal compounds, also known as spin crossover[1] (the first observation[2] published in 1931), is an important phenomenon that can cause drastic changes in physical properties of materials, including alterations in volume, compressibility and electrical conductivity. During a spin transition from high spin (HS) to low spin (LS), the ionic radii change dramatically (for example[3], for Fe^{2+} from 78 to 61 pm, and Fe^{3+} from 64.5 to 55 pm) that leads to a reduction of chemical bond lengths and may cause structural changes. Reduction of the radii means that the LS ion can substitute for other cations without significant change in the crystal structure, which is important for chemistry and especially for geochemistry as it may lead to variations in partitioning of elements (particularly iron, one of the most abundant elements in the Earth and a component of major mantle-forming minerals). Magnetic properties are also affected: for example, octahedrally-coordinated ferrous iron (Fe^{2+}) in the LS state is diamagnetic. Such versatile behavior has motivated ongoing attempts to find practical applications for this phenomenon, for instance, as storage media and in displays[4], temperature-sensitive contrast agents for magnetic resonance imaging[5], and as a mechanical actuator[6] (see review [7]).

Thermally-induced spin transition is a frequent phenomenon in coordination complexes with suitable ligands when the crystal-field splitting parameter D_q is close to the mean spin-pairing energy E_p. Most of such compounds are complexes of iron (see the recent review [8] on this topic).

A *pressure-induced* spin transition can be observed even in compounds with small ambient D_q, because the crystal-field splitting parameter increases upon compression. However, until recently such investigations were rare. The swift development of the diamond anvil cell (DAC) technique yielded several striking discoveries, such as, for example, spin crossover in ferropericlase at lower mantle conditions[9]. Mössbauer spectroscopy (MS) coupled with single crystal X-ray diffraction (XRD) is an extremely powerful combination for investigation of spin transitions. High-pressure crystallography using synchrotron facilities with focused high-energy X-rays and fast 2D detectors, and use of DACs with a large opening angle[10] enable careful investigation of the geometry of the FeO_6 octahedron before and after the spin transition and provide a basis to search for correlations between crystal chemistry and hyperfine parameters of the compounds under investigation.

In this paper we focus on ferric iron (Fe^{3+}) octahedrally coordinated by oxygen for the following reasons: (*i*) the $Fe^{3+}O_6$ octahedron is a common structural element in different compounds and minerals (iron-containing garnets, perovskite-structured materials including ferrites, simple (Fe_2O_3) and complex oxides, etc.), (*ii*) this polyhedron is of interest for physics, as a spin transition in an ion with d^5-configuration may provoke an insulator-metal transition[11], and (*iii*) high quality experimental data on spin transitions in some $Fe^{3+}O_6$-containing compounds are already available. Complemented by our new experimental results, these data may be useful for a comparative analysis aimed at establishing regularities in the pressure-induced spin transition of trivalent iron in the oxygen octahedron. The following compounds were examined: iron borate ($FeBO_3$), hematite (Fe_2O_3), skiagite-rich garnet ($Fe_5(SiO_4)_3$), goethite (FeOOH), calcium ferrite ($CaFe_2O_4$) and andradite ($Ca_3Fe_2(SiO_4)_3$) (Table I).

$FeBO_3$ has a calcite ($CaCO_3$)-type structure ($R\bar{3}c$ space group, no. #167)[19,20]. At ambient conditions the structure consists of slightly distorted corner-shared oxygen octahedra enclosing ferric iron and BO_3 triangles oriented in the structure perpendicular to the 3-fold axis (see section III A). Iron borate is antiferromagnetic with weak ferromagnetism due to a small canting of iron spins from antiparallel alignment[21] with Néel point $T_N = 348$ K Ref. [22 and 23]. A nuclear forward scattering (NFS) study[24] showed that $FeBO_3$ undergoes a phase

TABLE I. List of compounds examined in the present work. References to literature data used in the comparative analysis are provided. Hereafter an em dash means the absence of data.

Chemical compound	Crystallographic data	Mössbauer spectroscopy data kind of material/reference
$FeBO_3$	Ref. [12]	powder, conventional MS, and single-crystal, MS with synchrotron Mössbauer source (SMS)/this study
Fe_2O_3	Ref. [13]	single-crystal, MS with SMS/ this study
$Fe_3(Fe_{1.766(2)}Si_{0.234(2)})(SiO_4)_3$	Ref. [14]	single-crystal, MS with SMS/ this study
FeOOH	Ref. [15]	powder/Ref. [15]
$CaFe_2O_4$	Ref. [16]	powder/Ref. [17]
$Ca_3Fe_2(SiO_4)_3$	Ref. [18]	—

transition to a nonmagnetic state at 46 GPa. Single-crystal MS data[25] led to the conclusion that it is a HS→LS transition. A recent detailed high-pressure single-crystal XRD study[12] confirmed earlier suppositions[26,27] that it is an isosymmetric transition[28]. Thus, $FeBO_3$ is an excellent reference compound for investigation of relations between crystal chemistry and hyperfine parameters of trivalent iron as a function of pressure and geometry of the $Fe^{3+}O_6$ octahedron.

Hematite is a well-known iron sesquioxide (Fe_2O_3) with a corundum-type (Al_2O_3) structure consisting only of $Fe^{3+}O_6$ octahedra (see section III B). Each octahedron connects with three neighbors via edges in honeycomb-like layers and the layers are interconnected through common triangular faces of octahedra[29] (space group $R\bar{3}c$, no. #167). It is antiferromagnetic (canted-type at ambient conditions) with a high Néel temperature[30] of 948 K. Upon compression at ambient temperature up to about 100 GPa, it undergoes three phase transformations: pressure-induced Morin transition[31] with reorientation of the iron magnetic moments and loss of canting at 1.7 GPa, structural transition to the ζ-Fe_2O_3 phase with a triclinic, distorted-perovskite structure[32,33] (space group $P\bar{1}$, no. #2) at 54 GPa, and a transition to the orthorhombic θ-Fe_2O_3 phase[33] (space group $Aba2$, no. #41) at 67 GPa. The perovskite-type phase consists of two types of iron coordination polyhedra — octahedra and bicapped triangular prisms. The structural details of this phase are still not fully clarified because of its low triclinic symmetry and difficulties in collecting a sufficiently full XRD dataset in the DAC[33]. The orthorhombic phase contains ferric iron in distorted triangular prisms only and Fe^{3+} is in a LS state, as suggested by the available XRD and MS data[33,34]. There is only limited information about the behavior of trivalent iron at the spin transition in Fe_2O_3 polymorphs, and we provide here new experimental data.

Skiagite is an iron end-member in the silicate garnet family with ideal chemical formula $Fe_3^{2+}Fe_2^{3+}(SiO_4)_3$. Samples used in the present study are a solid solution of skiagite and iron-majorite ($Fe_3(FeSi)(SiO_4)_3$), which have been described in Ref. [35]. Their exact chemical composition $Fe_3(Fe^{3+}_{1.532(2)}Fe^{2+}_{0.234(2)}Si^{4+}_{0.234(2)})(SiO_4)_3$ was determined from single-crystal XRD and microprobe analysis[35]. This composition corresponds to approximately 23 mol % of iron majorite component in the samples. The skiagite-majorite solid solution has a cubic crystal structure (space group $Ia\bar{3}d$, no. #230). The cubic X-site (Wyckoff position 24c) is populated by ferrous iron (see section III C), whereas Fe^{3+} and ($Fe^{2+}Si^{4+}$) share the octahedral position (Y-site, 16a). XRD data[14] revealed isosymmetric crossover at room

temperature (RT) accompanied by a drop of the octahedron volume above 50 GPa. We collected Mössbauer spectra of the skiagite-majorite sample on compression up to 90 GPa and found that the spectra change in the same pressure range where XRD data indicate the phase transition. Although iron occupies two structural positions and has multiple electronic states, our new data allowed unambiguous interpretation of the mechanism and origin of this transition.

Goethite (α-FeOOH) is a widespread mineral with a diaspore-type (α-AlOOH) structure[36] (space group *Pnma*, no. #62). Iron octahedra share edges to form double chains along the *c*-axis (in *Pbnm* setting), which are further linked in a three-dimensional structure by sharing vertices. At ambient conditions goethite is a collinear antiferromagnet[37,38] with Néel temperature $T_N = 393$ K, Ref. [39]. A sharp spin transition accompanied by hydrogen bond symmetrization was observed at 45 GPa, Ref. [15].

Calcium ferrite ($CaFe_2O_4$, recently discovered as the mineral harmunite[40]) belongs to the orthorhombic crystal system[41] (space group *Pnma*, no. #62). Calcium has eight-fold coordination and ferric iron populates two crystallographically nonequivalent octahedra with different degrees of distortion. These two different octahedra form infinite double chains along the *c*-axis (in *Pbnm* settings). Each chain contains octahedra of only one type. Within the chains octahedra share edges and different chains are linked by common vertices of octahedra. At ambient pressure calcium ferrite undergoes a phase transition to an antiferromagnetic state bellow 200 K, Ref. [42]. In previous work[16] an isosymmetric phase transition was observed above 50 GPa and explained by a spin transition of trivalent iron. Recently, this was associated with a Mott transition[17].

Andradite ($Ca_3Fe_2(SiO_4)_3$) is a member of the garnet family. In this garnet structure, calcium is located in the cubic site (X-site) and ferric iron fully occupies the octahedral position (Y-site). Spin crossover in andradite takes place between 60 GPa and 70 GPa, Ref. [18].

Here we present our new high-pressure single-crystal MS data for $FeBO_3$, Fe_2O_3, and $Fe_3(Fe_{1.766(2)}Si_{0.234(2)})(SiO_4)_3$ and analyze the behavior of hyperfine parameters at spin transitions of ferric iron. We also discuss possible structural changes coupled with spin transitions, analyze the compressibility of the ferric iron octahedron, and the relationship between the isomer shift and the polyhedron volume.

The manuscript is organized as follows. First, new experimental data are presented, follo-

wed by a detailed analysis of hyperfine parameter behavior at the spin transition. Then, the compressibility of the ferric iron octahedron is determined and possible structural changes coupled with the spin transition are discussed. Finally, the dependence of the center shift[43] on polyhedron volume is examined.

II. EXPERIMENTAL DESCRIPTION

Iron borate single crystals were grown from a $^{57}Fe_2O_3$–B_2O_3–PbO/PbF_2 flux as described in Ref. [44]. Hematite single crystals studied in the present work were taken from the same synthesis batch as the crystals used in Ref. [33]. Skiagite-iron-majorite single crystals were synthesized in a multi-anvil apparatus at 9.5 GPa and 1100 °C from a powdered mixture of chemically pure oxides ($^{57}Fe_{1-x}O$, $^{57}Fe_2O_3$ and SiO_2) identically to the procedure described in Ref. [35].

High-quality single crystals with an average size of $\sim 30 \times 30 \times 5$ μm^3 for iron borate and hematite, and $\sim 10 \times 10 \times 5$ μm^3 for skiagite-iron-majorite were pre-selected on a three-circle Bruker diffractometer equipped with a SMART APEX CCD detector and a high-brilliance Rigaku rotating anode (Rotor Flex FR-D, Mo-K_α radiation) with Osmic focusing X-ray optics.

For pressure generation BX90 DACs[45] were used. The size of diamond culets was 250 μm. Rhenium gaskets were pre-indented down to a thickness of ≈ 30 μm and holes of ≈ 130 μm diameter were drilled in the center of indents. The cells with sample and a small ruby sphere placed in the pressure chamber were loaded with Ne (Ar for $FeBO_3$ single-crystal experiment) by means of a gas-loading system[46]. Pressure in the pressure chamber was estimated before and after MS measurements by the ruby fluorescence method[47] and an average value was taken and the deviation was included in the uncertainty.

Mössbauer absorption spectra of powdered $FeBO_3$ were collected using a conventional WissEL spectrometer in constant-acceleration mode with a nominal 10 mCi ^{57}Co(Rh) point source at 19 °C. The folded spectra consist of 256 channels. The single-crystal Mössbauer experiments with iron borate, hematite and skiagite were performed at ambient temperature (22 °C) at the Nuclear Resonance beamline[48] (ID18) at the European Synchrotron Radiation Facility (ESRF) using the synchrotron Mössbauer source[49]. The SMS is the pure nuclear reflection of a $^{57}FeBO_3$ crystal which is mounted on a velocity transducer and operated

in sinusoidal mode. The SMS is linearly polarized due to polarization of the synchrotron radiation. In this case the folded spectra contain 512 channels. The average beam spot size for these experiments was $8 \times 13\ \mu\text{m}^2$. The line width of the SMS was determined before and after collection of each spectrum of the samples by measurements of the reference single line absorber ($K_2Mg^{57}Fe(CN)_6$). All experiments were conducted in transmission geometry.

The Mössbauer spectra were fitted using *MossA* software[50], version 1.01a. Spectra from the conventional radioactive source were processed using pseudo-Voigt line shapes. For processing of spectra collected with SMS, a transmission integral fit was used assuming a Lorentzian-squared line shape of the SMS and a Lorentzian line shape of the absorber. All center shifts were calibrated relative to α-Fe at ambient conditions.

The visualization of the structures and calculation of the distortions of polyhedra were performed using VESTA software[51], version 3.3.2. Calculations of the equations of state (EoS) were performed using EosFit7[52].

III. RESULTS

A. Iron borate

Recent high-pressure single-crystal XRD experiments[12] with $FeBO_3$ showed a sharp transition with large volume discontinuity at 50 ± 2 GPa[53] and confirmed earlier supposition[26,27] that it is an isosymmetric phase transition. The single crystal XRD data provide important information about geometrical characteristics of the $Fe^{3+}O_6$ octahedron. At ambient conditions the iron octahedron is slightly trigonally elongated along the 3-fold axis. Under compression this distortion diminishes and completely disappears around 36 GPa. At the transition, the octahedron volume decreases by 10.5 %, which is a clear indication of the transition to LS state. The octahedron remains ideal across the transition and it is only above 56 GPa that a trigonal compression along the 3-fold axis begins to increase slowly[12].

Mössbauer spectra of iron borate were collected from ambient pressure to 70 GPa. The evolution of the Mössbauer spectra is shown in Fig. 1b. At ambient conditions the spectrum consists of one magnetic component with the following hyperfine parameters: center shift (CS) $\delta_{CS} = 0.398(8)$ mm/s, quadrupole shift[54] $\varepsilon = 0.098(9)$ mm/s and hyperfine magnetic field $H_{hf} = 34.86(6)$ T. Up to 48.5 GPa there are no substantial changes of the

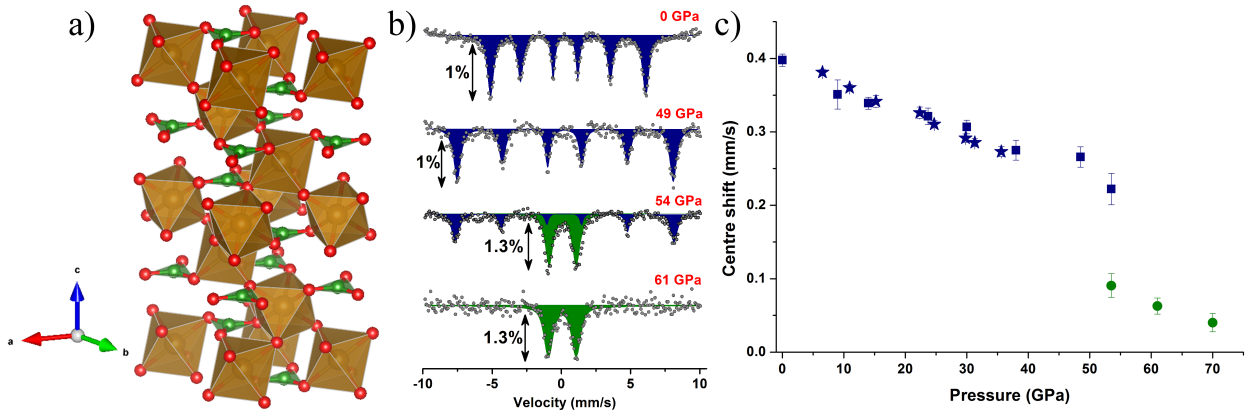

FIG. 1. a) Structure of $FeBO_3$ comprised by corner-shared $Fe^{3+}O_6$ octahedra and BO_3 triangles perpendicular to the 3-fold axis. b) Pressure evolution of iron borate Mössbauer spectra at RT. At ambient pressure the spectrum is a single magnetic sextet (blue) that demonstrates increasing H_{hf} at compression up to 54 GPa, then a paramagnetic doublet (green) appears that can be attributed to LS Fe^{3+}. At 61 GPa only the paramagnetic doublet remains. c) The doublet has a center shift lower by $\approx$ 0.13 mm/s than the sextet. The squares and circles correspond to the experiment with powder sample measured using a radioactive Mössbauer source and the stars are data from the single-crystal experiment measured using SMS. Hereafter, if error bars are not visible they are smaller than the symbol size.

spectrum, only an increase in hyperfine field (Fig. 2b) and decrease in CS (Fig. 1c).

The quadrupole shift gradually decreases with increasing pressure and becomes close to zero above 30 GPa. Such behavior can be understood if one takes into account the above-mentioned changes in the octahedron distortion. With pressure increase the trigonal distortion decreases and becomes zero above 35 GPa. This means that there is no lattice contribution to the electric field gradient (EFG) from the first coordination sphere. However, there is still a lattice contribution from the next coordination spheres as the iron Wyckoff position (6b) does not have cubic symmetry. The quadrupole shift alters accordingly. Indeed, ε above 35 GPa is small but non-zero.

The iron ions are on the 3-fold axis; therefore the EFG should be symmetric, i.e., the asymmetry parameter $\eta = 0$ and the principal component V_{zz} of the EFG tensor is collinear with the 3-fold axis[55]. As the magnetic moments lie in the plane perpendicular to the 3-fold axis and remain in the plane until the spin transition occurs[24,25], the angle θ between H_{hf} and

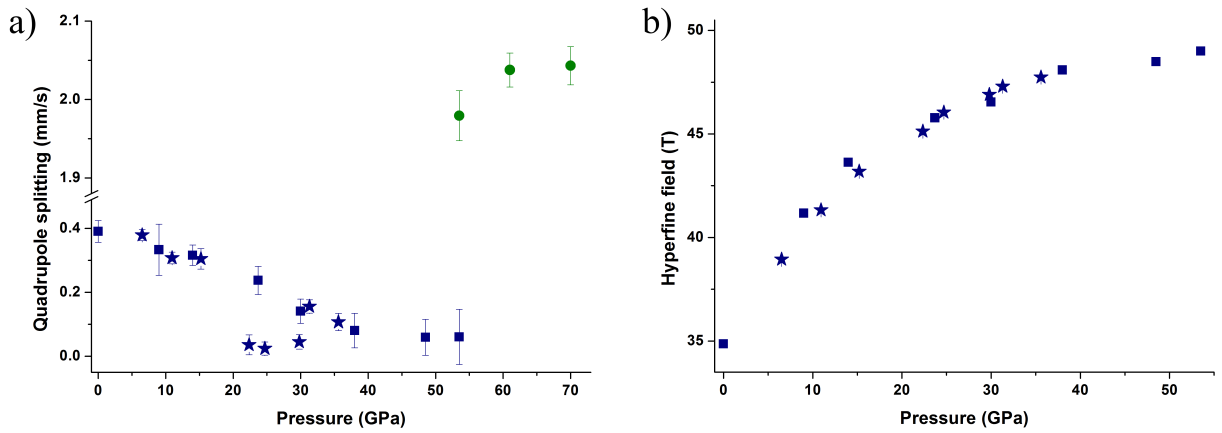

FIG. 2. a) Pressure dependence of $|\Delta E_Q|$ in $FeBO_3$. The values for the doublet (green) and sextet (blue) differ by one order of magnitude at 54 GPa. b) The growth of hyperfine field over the entire pressure range indicates an increase of Néel temperature of $FeBO_3$. The squares and circles correspond to the experiment with powder sample measured using a conventional Mössbauer source and the stars are data from the single-crystal experiment measured using SMS. The colors conform to those in Figs. 1b and 1c.

V_{zz} of the EFG remains constant, and we can convert ε to the quadrupole splitting (QS) ΔE_Q to obtain comparable values for HS and LS states. In our case the quadrupole shift in the high-field condition ($g_N \mu_N H_{hf} \gg eQV_{zz}/2$) is[56]

$$\varepsilon = \frac{eQV_{zz}}{2}\left(\frac{3\cos^2\theta - 1}{4}\right) = \Delta E_Q \left(\frac{3\cos^2\theta - 1}{4}\right), \tag{1}$$

where Q is the quadrupole moment of the nucleus and e is the elementary charge. For $\theta = 90°$, $\varepsilon = -\Delta E_Q/4$ and, as the quadrupole shift is positive, the V_{zz} in $FeBO_3$ is negative. The respective $|\Delta E_Q|$ is plotted in Fig. 2a.

At 54(1) GPa a new paramagnetic doublet appears with $\delta_{CS} = 0.09(2)$ mm/s (≈ 0.13 mm/s lower than the CS of the magnetic sextet, Fig. 1c) and $|\Delta E_Q| = 1.98(3)$ mm/s, which is one order of magnitude larger than ΔE_Q before the transition (Fig. 2a). Parameters of the doublet correspond to the low-spin state of the iron ion, $^2T_{2g}$. At 61 GPa the magnetic sextet disappears completely, and only the doublet is observed up to 70 GPa. Our results are in general agreement with the previous study[25], although our data show smoother pressure dependencies of the hyperfine parameters, and higher pressure (5 ± 2 GPa difference) of the transition compared to Ref. 25.

B. Iron sesquioxide

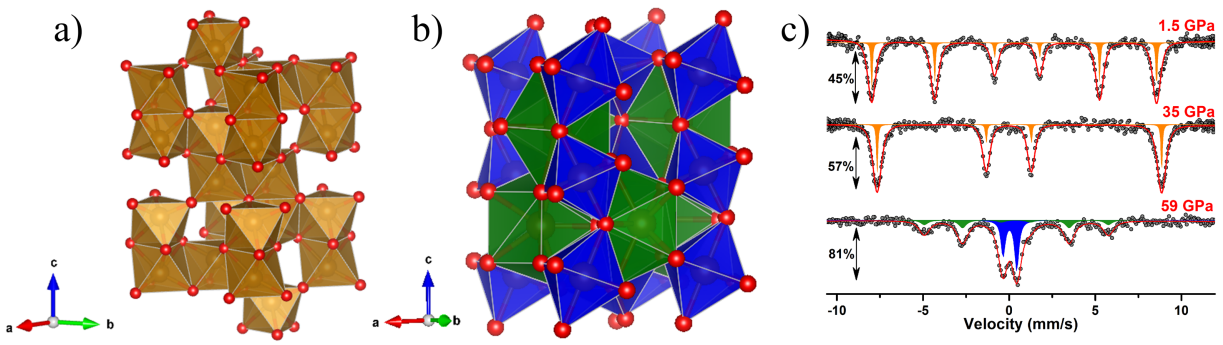

FIG. 3. a) Structure of α-Fe_2O_3 (hematite) is builded by FeO_6 octahedra. b) At 54 GPa α-Fe_2O_3 undergoes a phase transition to ζ-Fe_2O_3 with distorted perovskite-type structure that consists of octahedra (B-position) and bicapped trigonal prisms (A-position). c) The single magnetic sextet of hematite before (1.5 GPa) and after (35 GPa) Morin transition. The spin-flop Morin transition results in a disappearance of the 2nd and 5th lines due to the particular orientation of the single crystal relative to the incident beam (see text). The spectrum of the ζ-Fe_2O_3 (59 GPa) is a superposition of a doublet and sextet with smaller hyperfine field.

The Mössbauer spectrum of α-Fe_2O_3 (hematite, Fig. 3a) is a single magnetic sextet of HS ferric iron (Fig. 3c). At ambient temperature hematite undergoes a pressure-induced spin-flop Morin transition[31] at 1.7 GPa. At this transition the spins flip 90° from the basal plane to the direction collinear with the 3-fold axis without change in the atomic arrangement. The noticeable effect of this transition is the disappearance of the 2nd and 5th lines of the sextet in the Mössbauer spectrum (Fig. 3c) due to the use of a single-crystal sample: in this particular experiment the angle between the wave vector of the γ-ray and the magnetic moments is close to zero after the transition. The hyperfine magnetic field increases by 1.0(1) T and ε changes from $-0.086(7)$ to $+0.189(6)$ mm/s, which is in good agreement with data for the Morin transition at ambient pressure[57].

There is no significant change in the hematite spectrum with further compression up to 49 GPa. The δ_{CS} expectedly decreases (Fig. 4a) and H_{hf} is reduced from 52.26(5) T to 50.15(6) T. Note that the latter behavior is not related to the reduction of the Néel temperature[58], but is caused by a decrease in the H_{hf} saturation value with pressure increase (a similar behavior was observed in $FeBO_3$, Ref [59]). Although single-crystal XRD expe-

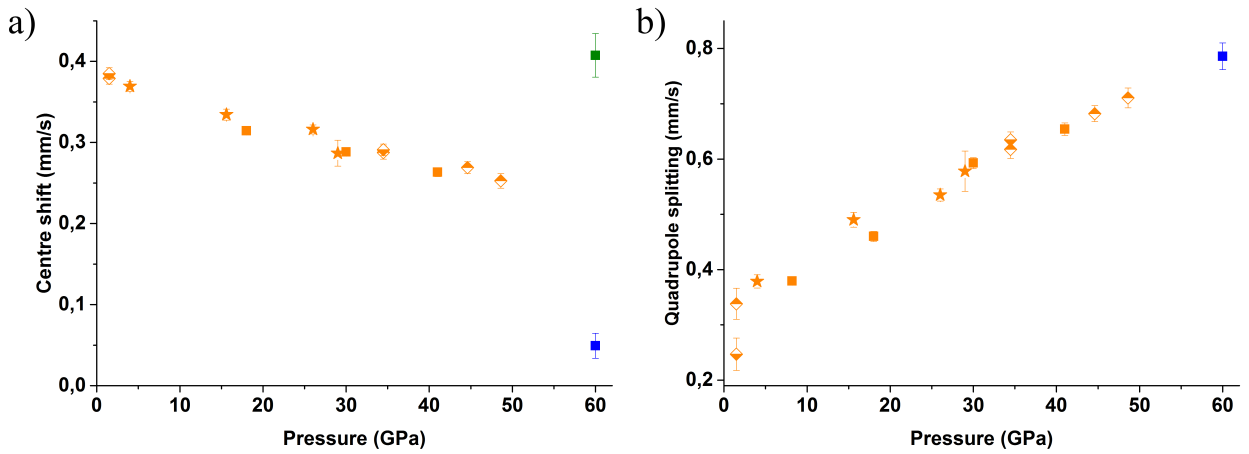

FIG. 4. Pressure dependence of Fe_2O_3 hyperfine parameters. a) δ_{CS} of the ζ-Fe_2O_3 doublet (blue) is lower by ≈ 0.2 mm/s compared to δ_{CS} of HS Fe^{3+} before the transition (orange). δ_{CS} of the ζ-Fe_2O_3 sextet (green) is larger than δ_{CS} of α-Fe_2O_3 at ambient pressure. b) ΔE_Q of the ζ-Fe_2O_3 doublet is close to ΔE_Q of α-Fe_2O_3 before the transition. The colors conform to those in Fig. 3c. Squares, stars and half-filled diamonds correspond to data from three different DACs. Half-up and half-down filled symbols distinguish two different crystals in the third DAC.

riments[13] did not detect any significant changes in the octahedral distortion up to 25 GPa, the ε value almost doubles up to 0.355(9) mm/s at 49 GPa. Because iron is located on the 3-fold axis in α-Fe_2O_3, we can convert the quadrupole shift to ΔE_Q (similar to $FeBO_3$ in section III A). The result is plotted in Fig. 4b.

New components related to the ζ-Fe_2O_3 appear on Mössbauer spectra above 49 GPa. Single-crystal XRD experiments show that this phase has triclinic symmetry[33] (space group $P\bar{1}$). The obtained structure of ζ-Fe_2O_3 (in monoclinic symmetry) belongs to the perovskite-type group[32] (Fig. 3b) where Fe cations occupy trigonal prisms (A-site) and octahedra (B-site). A representative spectrum of ζ-Fe_2O_3 at 59(1) GPa shows a superposition of a doublet ($\delta_{CS} = 0.05(2)$ mm/s and $\Delta E_Q = 0.79(3)$ mm/s, blue in Fig. 3c) and a new magnetic sextet ($\delta_{CS} = 0.41(3)$ mm/s, $\varepsilon = 0.02(3)$ mm/s, $H_{hf} = 33.1(2)$ T, green in Fig. 3c). The drop in δ_{CS} ($\approx$0.2 mm/s) relative to α-Fe_2O_3 (Fig. 4a) and the coexistence with a magnetic sextet indicate that the doublet corresponds to LS Fe^{3+}. The δ_{CS} of the magnetic sextet corresponds to HS Fe^{3+} and the increment in CS (Fig. 4a) can be related to the increase in coordination number. This peculiar coexistence of spin states in ζ-Fe_2O_3 and subsequent phase transition in the Fe_2O_3 system require further investigation and will be published

elsewhere.

C. Skiagite-iron-majorite solid solution

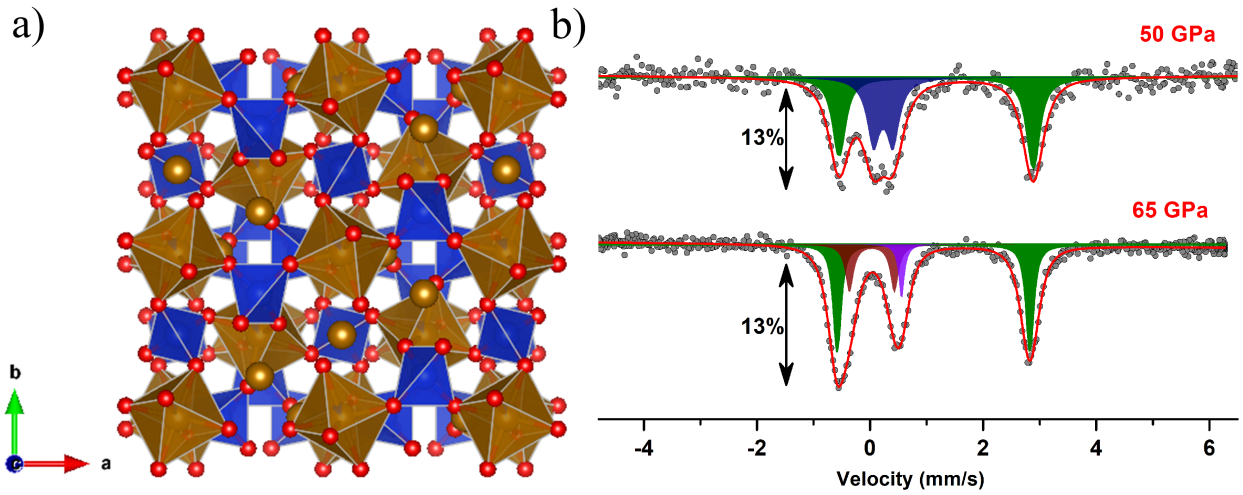

FIG. 5. a) Skiagite-iron-majorite solid solution with typical garnet structure. Its framework is formed by corner-shared SiO_4 tetrahedra (Z-site, blue) and (Fe,Si)O_6 octahedra (Y-site, gold), and the distorted cubic voids (X-site) are populated by Fe^{2+}. In the pressure range 50−60 GPa, skiagite-iron-majorite solid solution undergoes an isosymmetric phase transition with ≈ 10 % discontinuity in the (Fe,Si)O_6 volume[14]. b) Mössbauer spectra of skiagite-majorite solid solution before (50 GPa) and after (65 GPa) spin crossover. The green doublet corresponds to the X-site with HS Fe^{2+}, the blue and brown doublets correspond to the Y-site with HS and LS Fe^{3+}, respectively, and the violet singlet corresponds to the LS Y-site Fe^{2+}.

Below 50 GPa the Mössbauer spectrum of the studied solid solution is a superposition of two paramagnetic doublets corresponding to ferrous iron in the X-site and ferric iron in the Y-site (Fig. 5b). At 1.4 GPa the hyperfine parameters are δ_{CS} = 1.292(9) mm/s, ΔE_Q = 3.49(2) mm/s for X-site Fe^{2+} and δ_{CS} = 0.36(2) mm/s, ΔE_Q = 0.25(4) mm/s for Y-site Fe^{3+}, which is in excellent agreement with Ref. [35]. As the garnet structure is cubic, even in the case of single-crystal Mössbauer experiments the doublet components should have equal areas for any orientation[60]. A small asymmetry of the X-site doublet areas appears due to the Gol'danskii-Karyagin effect (GKE)[61]. Note that the GKE is not possible for the Y-site, as all diagonal elements of the mean-square displacement tensor are

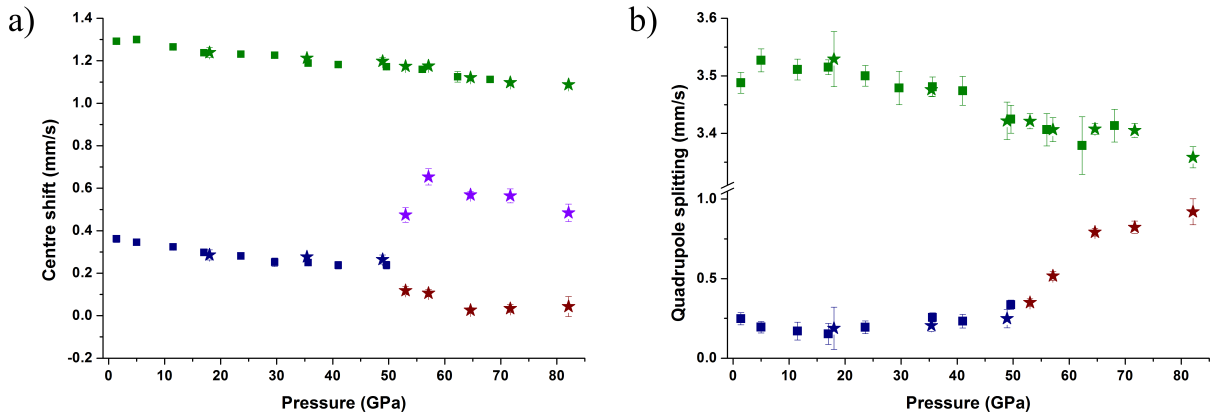

FIG. 6. Pressure dependence of center shift (a) and quadrupole splitting (b). The hyperfine parameters of X-site Fe^{2+} (green) show monotone behavior over the entire all pressure range. Above 50 GPa, the CS of Y-site Fe^{3+} decreases with simultaneous growth of QS (blue and brown points). The colors conform to those in Fig. 5b and the squares and stars correspond to two independent experiments.

equal due to the symmetry of this position.

The signal from Y-site Fe^{2+} is not detected in the Mössbauer spectra, despite the sample containing 23 mol. % of iron-majorite (hence, the expected Fe^{3+}:Fe^{2+} ratio in the Y-site should be $\approx$ 7:1). Apparently, the small amount of octahedral divalent iron is below the statistical accuracy of the data. The interpretation that the Y-site doublet (blue, Fig. 5b) is the signal from iron in a mixed valence state is implausible. Mixed valence components are observed in compounds where iron polyhedra (participating in intervalence charge transfer) are connected through common edges or faces[62], which is not the case for iron populating the octahedral position in the garnet structure (see Fig. 5a).

The Mössbauer spectra do not change substantially with compression up to 50 GPa. Above this pressure the Fe^{3+} component starts to transform into an asymmetric doublet with higher quadrupole splitting (Fig. 5b). The changes develop up to 65 GPa, so the transformation pressure range is consistent with that determined from the XRD data[14] within experimental error. Between these pressures the Y-site component shows dynamical broadening which indicates interconversion between spin states comparable with precession times ($\sim 10^{-8}$ s) of the nuclear quadrupole moment of the excited state of ^{57}Fe.

Because the structure of skiagite-iron-majorite preserves the cubic symmetry over the

entire investigated pressure range, the intensities of the Y-site doublet lines should remain equal after spin crossover[60]. To describe the new feature (strong asymmetry of the new doublet) one could add a singlet to the more intense line of the new doublet and interpret it as iron in a different electronic state in the octahedral position (Fig. 5b, spectrum at 65 GPa). Indeed the value of the center shift of the singlet (0.57(2) mm/s at 65 GPa) is close to values characteristic for LS Fe^{2+} in oxygen octahedra[63,64]. This observation could be an indication that octahedral ferrous iron undergoes a HS→LS transition. Because of the collapse of the doublet into a singlet, the intensity of this component increases by a factor of two, hence its signal may become observable.

The asymmetry of the Y-site doublet above 50 GPa could also result from a dynamical Jahn-Teller effect of LS Fe^{3+}, because in the low-spin state, ferric iron has the orbitally degenerate state $^2T_{2g}$. There are several equivalent distortions that remove the degeneracy, and the iron octahedron can resonate between them. It could lead to non-trivial modifications of the line shape, if the hopping characteristic time between equivalent distorted configurations is close to the characteristic measurement time[65].

We note, however, that while the proposed explanations of the asymmetry of the doublet described above are ambiguous and further work (for example, low-temperature MS) may be required to fully explain the observations, this uncertainty does not affect our major conclusions in any way. The brown doublet (Fig. 5b) remains the signal of trivalent iron in the octahedral site. The hyperfine parameters of ferric iron during the transition change in the following way: at 65 GPa CS drops from 0.24 (at 50 GPa) to 0.03 mm/s and the QS value increases from 0.34 to 0.8 mm/s (Figs. 6a and 6b). These changes are consistent with typical trends for spin transitions of ferric iron. Hyperfine parameters of divalent iron in the cubic position vary monotonically up to 90 GPa (Figs. 6a and b).

IV. DISCUSSION

A. Hyperfine parameters at spin transitions in $Fe^{3+}O_6$ octahedra

Data on the hyperfine parameters of ferric iron in compounds of interest before and after the spin transition are compiled in Table II. All considered compounds demonstrate similar behavior through spin transitions. The main features are *(i)* drop in CS value, *(ii)*

TABLE II. Hyperfine parameters of ferric iron in the studied compounds before and after the pressure-induced spin transition. All parameters refer to ambient temperature if not given explicitly.

Compound	${}^{HS}\delta_{CS} - {}^{LS}\delta_{CS}$, mm/s	ΔE_Q, mm/s		H_{hf}, T	
		before	after	before	after
$FeBO_3$	0.13(3)	0.06(9)	1.98(3)	49.0(2)	0
$Fe_3(Fe_{1.766}Si_{0.234})(SiO_4)_3$	0.19(2)	0.25(6)	0.89(1)	0	0
$CaFe_2O_4$	0.16(3) at 5 K	0.6 & 1.2	1.1 & 1.6	47.6 & 45.4 at 5 K	0
FeOOH	0.3 at 6 K	—	2.5 at 50 K	49 at 6 K	7.2 at 6 K
Fe_2O_3	0.22(3)	0.71(2)	0.76(3)	50.15(6)	0

disappearance of magnetic order at room temperature, and *(iii)* LS state of ferric iron ion characterized by doublet with higher quadrupole splitting (relative to the values of HS Fe^{3+}).

There is a large spread of QS values of the Fe^{3+} LS state at RT: from 0.76 mm/s in Fe_2O_3 to 2.5 mm/s in FeOOH (at 50 K). Note that the lowest value of ΔE_Q is significantly smaller than the corresponding value of 1.9 mm/s reported for LS Fe^{3+} in coordination complexes[66]. There is only a scarce amount of data for H_{hf} of $Fe^{3+}O_6$ in the LS state. Magnetic ordering was observed in FeOOH with LS Fe^{3+} that showed a hyperfine field of 7.2 T at 6 K (Table II, but it is not clear if H_{hf} was saturated) and magnetism was also reported in $FeBO_3$ below 50 K, Ref [59]. In the latter case perturbations of NFS spectra were detected, but it was not possible to fit them satisfactorily. Moreover, spin transitions in Fe^{3+} can lead to metallization[11] with disappearance of magnetic moments (as in the case of $CaFe_2O_4$, Ref. [17]). It is clear that further systematic studies of magnetic ordering in phases containing high-pressure LS trivalent iron are required. See Supplemental Material at [URL] for more detailed discussion of ΔE_Q and H_{hf} behavior at spin transition. The changes in δ_{CS} are considered below.

1. Isomer shift

As mentioned in the introduction, the centre shift is the sum of the isomer shift and the second-order Doppler shift. The physical meaning of the isomer shift (IS) in MS is a measure

of the electron density at the probe nucleus which is almost fully created by s-electrons (with relativistic considerations there is also a minor p-electron contribution)[67]. One can write it in such form

$$\delta_{IS} = \frac{2\pi}{3} Ze^2[\langle r_e^2\rangle - \langle r_g^2\rangle]\Delta\psi^2(0) = \alpha \cdot \Delta\psi^2(0), \tag{2}$$

where Z is the proton number, $\langle r_{e,g}^2\rangle$ is the mean-squared nuclear radius of the excited and ground states, respectively, and $\Delta\psi^2(0)$ is the difference in electron density at the nucleus between the measured and reference compounds. The constant α is negative in the case of ^{57}Fe.

The difference in IS between HS and LS states has been known since the early days of Mössbauer spectroscopy[67]. As HS and LS ions have different radii, the metal-ligand bonds should be shorter for the LS configuration and, accordingly, an increased covalency of chemical bonds. This suggests that in the LS state, the occupancy of $4s$-orbitals increase which leads to higher electron density at the nucleus and to lower δ_{IS}. However, modern density functional theory (DFT) calculations have not found a correlation between the IS value and $4s$-Löwdin population[68]. In that paper the general inference was made that the metal-ligand bond length is important and that shorter bonds result in lower IS. In any event, bond length is a determinant factor and the IS value is necessarily lower for the LS iron ion.

2. Second-order Doppler shift and center shift

The second-order Doppler shift results in reduction of γ-ray energy due to relativistic time dilation in the reference frame associated with the moving nucleus [67]

$$\delta_{SOD} = -\frac{\langle v^2\rangle}{2c^2} E_\gamma = -\frac{\langle \epsilon_k\rangle}{Mc^2} E_\gamma, \tag{3}$$

where E_γ is the γ-quantum energy, $\langle v^2\rangle$ is the mean-squared velocity of the nucleus in the crystal, M is the nuclear mass, c is the speed of light and $\langle \epsilon_k\rangle$ is the mean kinetic energy of the nucleus. Under the assumption that the nucleus is a harmonic oscillator, the mean kinetic energy is half of the vibrational internal energy and the SOD shift depends linearly on the internal energy of the nucleus. At the HS→LS transition the magnitude of δ_{SOD} should increase as the decrease of the iron ionic radius causes a reduction of the polyhedron

volume and, accordingly, leads to an increase in the force constants. Therefore, changes in δ_{SOD} will have the same sign as changes in the isomer shift.

Value of the SOD shift can be determined by means of nuclear inelastic scattering (NIS) data. From the NIS spectrum one can extract the partial phonon density of states (pDOS) of the Mössbauer isotope and the vibrational internal energy can be directly determined by integrating the pDOS function[69]

$$\epsilon_v = \frac{3}{2}\int_0^\infty E \coth\left(\frac{E}{2k_BT}\right)\mathcal{D}(E)dE, \tag{4}$$

where $\mathcal{D}(E)$ is the iron pDOS, k_B is the Boltzmann constant and T is the temperature.

For the compounds in this study, only NIS data for the skiagite–iron-majorite solid solution are published[70]. Because iron occupies two different structural positions in this garnet, the corresponding pDOS is an average function of both. Nevertheless, these data can yield a reasonable estimate of changes in SOD shift at the spin transition of Y-site Fe^{3+} as δ_{CS} of X-site Fe^{2+} does not show any evident anomalies in the vicinity of spin crossover (Fig. 6a). There is a 4 meV increase of vibrational internal energy[70] between 45 and 56 GPa that corresponds to 0.011(4) mm/s change in δ_{SOD}. This is below 10 % of the observed variation in center shift upon HS-LS crossover.

One can also use siderite ($FeCO_3$) data[71] to crosscheck this estimation. Siderite is isostructural with iron borate and contains carbon and ferrous iron instead of boron and ferric iron, respectively. Siderite also undergoes a HS→LS transition at similar pressures ($\approx$ 45 GPa) and with similar changes in unit cell and octahedron volumes[72,73]; hence the phonon properties of the crystal lattice should be similar to those of $FeBO_3$. Siderite NIS data show a 4 meV discontinuity in vibrational internal energy at the spin transition[71], and the respective δ_{SOD} change is 0.011(2) mm/s, similar to the estimation for the skiagite-iron-majorite solid solution. Thus, our estimates suggest that reduction of δ_{CS} at the pressure-induced spin transition of Fe^{3+} at ambient temperature is mainly caused by the isomer shift. The SOD contribution is not higher than 10 %.

As a reference value of IS change at the spin transition in the $Fe^{3+}O_6$ octahedron, we choose the change in iron borate (0.13(3) mm/s) for the following reasons: (*i*) the transition is isosymmetric (as distinct to the case of hematite), (*ii*) the transition is first-order, i.e., abrupt (unlike in skiagite-iron-majorite, for example), and (*iii*) Mössbauer spectra were measured at room temperature so the influence of changes in the second-order Doppler

(SOD) shift should be minimal.

The difference in CS values between HS and LS states is half the difference observed in coordination complexes[66] ($\sim$ 0.2 mm/s). The smaller difference is probably related to smaller changes in the octahedral volume of $Fe^{3+}O_6$ (compare changes in bond length for different ligands in Ref. 66, Table 1). The relatively large discontinuity in values for FeOOH (Table II) might be related to hydrogen bond symmetrization and corresponding significant changes of the zero-motion contribution to the SOD shift (because the measurements were performed at 6 K, see discussion in Ref. 74).

B. Structure data

1. *Volume of $Fe^{3+}O_6$ octahedron at spin transition*

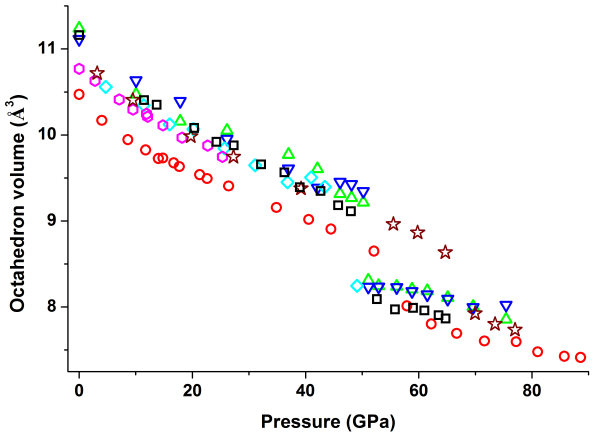

FIG. 7. Volume of $Fe^{3+}O_6$ octahedra as a function of pressure for different compounds. Black squares correspond to iron borate, red circles to skiagite, green and blue triangles to two different structural positions in calcium ferrite, cyan diamonds to goethite, magenta hexagons to hematite and brown stars to andradite.

Fig. 7 shows the dependence of the octahedron volumes in the studied compounds as a function of pressure. One can see that the spin transition of Fe^{3+} starts in the pressure range 45–60 GPa and over a remarkably narrow range of octahedron volume — 8.9–9.3 Å^3. This suggests that the spin transition is controlled by the electronic density inside the octahedron.

In crystal field theory the crystal field splitting parameter determines the strength of

TABLE III. Crystal field parameters and the estimated polyhedron volumes at transition onset.

Compound	$10D_q$ (cm^{-1})	B (cm^{-1})	β	V_0 (Å^3)	V_t from eq. (5) (Å^3)	exp. V_t (Å^3)
$FeBO_3$	12700[75]	680	0.68	11.16	9.0	9.1
Fe_2O_3	14000[76]	540	0.54	10.77	10.2	9.0
FeOOH	15320[76]	590	0.59	10.81	10.3	9.3
$Ca_3Fe_2(SiO_4)_3$	12600[77]	593	0.59	10.88	9.2	8.9

the electrostatic potential created by anions and is directly related to the distance between cation and anions ($D_q \propto r^{-5}$ for an ideal octahedron, ch. 2 in Ref. 78). Using Tanabe-Sugano diagrams[79] one can estimate the transition bond length at which the spin transition should happen. So, for the octahedron volume we can write:

$$V_t = V_0 \left(\frac{D_q^0}{D_q^t} \right)^{3/5}, \tag{5}$$

where V is the octahedron volume, and the indices 0 and t correspond to ambient pressure and at the spin transition, respectively. The results of this estimation for the compounds under consideration are collected in Table III. One can see that this simplest model overestimates the transition volume notably in the case of hematite and goethite. If predictions would be accurate, the spin transition in these compounds would take place at 20–25 GPa. Note that this discrepancy is not related to covalent effects. The degree of covalency can be estimated using the nephelauxetic ratio β (smaller values of β indicate more covalent bonds, while unity means a purely ionic bond). Despite the fact that hematite and goethite are more covalent than iron borate, Eq. (5) predicts nearly the correct octahedron volume for andradite, which has the same nephelauxetic ratio as hematite (Table III).

This problem is most likely related to octahedral distortions. In both hematite and goethite, octahedral Fe-O bonds divide into two groups (three bonds in each) with different lengths: approximately 1.95 and 2.10 Å at ambient conditions. Electrostatic potentials with symmetry lower than cubic contain additional terms that have different power dependencies on r (for instance, the term $\propto r^{-3}$ for a trigonally distorted octahedron, see ch. 2 in Ref. 78). Therefore, consideration of the proper electrostatic potentials for hematite and goethite should lead to a correct estimation of the transition volumes, but such an examination is beyond the scope of this work.

TABLE IV. Equation of state parameters of the HS ferric iron octahedron in the studied compounds. The Birch-Murnagham (BM) EoS of both 2nd and 3rd order was used. For calcium ferrite, the average volume of two octahedra (for iron in two distinct crystallographic positions) was used. K_0 and K_0' are the isothermal bulk modulus and its first pressure derivative, respectively.

Compound	EoS order	V_0 (Å^3)	K_0 (GPa)	K_0'
$FeBO_3$	3rd	11.16(fixed)	166(9)	3.8(6)
	2nd	11.14(5)	166(8)	4
$CaFe_2O_4$	3rd	11.18 (fixed)	170(10)	5.2(8)
	2nd	11.18(fixed)	186(2)	4
$Ca_3Fe_2(SiO_4)_3$	3rd	10.88(1)	202(4)	3.62(16)
	2nd	10.89(1)	194(2)	4
Fe_2O_3	3rd	10.77(1)	200(20)	5(3)
	2nd	10.77(1)	209(6)	4
FeOOH	3rd	10.75(fixed)	202(11)	5(1)
	2nd	10.75(fixed)	214(4)	4

In all studied compounds, iron octahedra show very similar compressibility (Fig. 7). Skiagite-iron-majorite solid solution data deviate from the rest of the examined compounds due to the mixed population of the Y-site by iron and silicon, because the SiO_6 octahedron is significantly smaller than one for $Fe^{3+}O_6$ (for example, in the ilmenite- and perovskite-type $MgSiO_3$ polymorphs the volume is around 7.64 Å^3 at ambient conditions[80,81]). Hence, XRD provides an average picture with a reduced volume of the (Fe,Si)O_6 octahedron (Fig. 7). At the spin crossover, the volume of iron octahedra decreases and approaches that of the silicon octahedra, and the difference between the average volume of the (Fe,Si)O_6 octahedra and the rest of the data becomes small above 60 GPa (Fig. 7).

The isothermal bulk moduli of $Fe^{3+}O_6$ octahedra in different compounds at ambient conditions vary between 170 and 210 GPa (Table IV). The K_0 value correlates with the octahedron volume at ambient pressure and, apparently, it is related to the length of Fe-O bonds (the shorter the bond, the more incompressible the octahedron). In the vicinity of the spin transition the average value of K is around 400 GPa (iron borate has the lowest value of 340(20) GPa). Currently, only iron borate and calcium ferrite have sufficient data

points above the spin transition for estimation of the LS octahedron EoS[12,16]. For $FeBO_3$ the parameters of the EoS (BM, 2nd order) are V_0 = 9.6(4) Å^3 and K_0 = 225(65) GPa, and for $CaFe_2O_4$ they are V_0 = 9.4(2) Å^3 and K_0 = 320(50) GPa. As LS ferric iron has a significantly smaller ionic radius, one can expect that the elastic moduli should increase at the HS→LS transition. Indeed, an EoS comparison of HS and LS $Fe^{3+}O_6$ octahedra shows that at 50 GPa, the bulk modulus changes from 340(20) GPa to 410(70) GPa and from 400(20) GPa to 510(50) GPa for $FeBO_3$ and $CaFe_2O_4$, respectively.

2. Cooperativity at spin transition

Available single-crystal XRD data show that pressure-induced spin transitions in inorganic compounds have a strong tendency to result in isosymmetric transitions. From the phenomenological theory of phase transitions, it follows that they can proceed either as first-order transitions or, beyond the critical point, as a crossover (supercritical manner) in which there is no discontinuity in any free-energy derivative[82].

The abundance ratio of different spin states would be controlled by Boltzmann factor if the cations change spin states independently. However, because cations in different spin states have different ionic radii, a spin transition of one ion introduces a strain field into the crystal lattice (one can consider the ion in a different spin state as an impurity). The coupling of the cations with this strain field determines the strength of cooperative behavior at the spin transition and, accordingly, the critical temperature (T_{cp}) at which the first-order phase transition is changed by crossover behavior. In general, the elastic interaction between impurities in a crystal is complex and may even lead to superstructures with cations coexisting in different spin states[83]. However, to our knowledge, no single-crystal XRD study of pressure-induced spin transition has observed such superstructures. We therefore limit our discussion to simple isosymmetric transitions, as they involve all principal features of the spin-transition phenomenon.

In the crossover regime, there is *dynamical spin state equilibrium* at the spin transition, so cations permanently change their spin state. The characteristic time of these changes (t_s) is an important parameter, since different experimental techniques have different characteristic measurement times (t_m, 10^{-8} s for ^{57}Fe MS). Hence, depending on the ratio t_s/t_m, one technique can show an averaged spin state while another can show the *apparent* static

coexistence of spin states. Because phase coexistence is an inherent feature of first-order phase transitions, it is not necessarily a trivial task to determine which mechanism of spin transition is observed. In this respect diffraction techniques have an advantage, because they average over ensemble and not time period. Hence if a spin transition proceeds in a first-order manner, one can see peak splitting corresponding to spin-domains with different volumes (see siderite example in Ref. 72), while for crossover it will be simply a single phase with averaged volume. In addition, results of powder DAC experiments should be considered with caution because of the tendency to broaden the transition region (see comparison of powder and single-crystal experiments in Ref. 64).

For the compounds under study (Table I) the condition of cooperativity is as follows: if iron octahedra share common oxygen atoms and form an infinite framework, the compound shows strong cooperative behavior at pressure-induced spin transitions (by "strong" we mean that the critical point lies above room temperature). If this condition is fulfilled there are favorable conditions for magnetic ordering by means of superexchange interactions. Indeed, all such studied compounds in the HS state are magnetically ordered at room temperature in the vicinity of the spin transition (see Table I in supplemental material). However, if the magnetic ordering disappears in the LS state, when, strictly speaking, the transition could not be isosymmetric, because at such transition the symmetry relative to time reversal is changed. This leads to important consequences: (*i*) the spin transition in magnetically-ordered compounds can only proceed as a first-order phase transition, and (*ii*) the temperature of the critical point cannot be lower than the Néel (Curie) temperature of the HS phase in the vicinity of the spin transition. These conclusions are valid if the spin transition is the driving force of the transition.

Among the studied compounds, only the spin transitions in the Y-site of the garnet structure (andradite and skiagite–iron-majorite solid solution) show explicit crossover behavior at room temperature within $\sim$ 10 GPa. This is in agreement with the formulated cooperativity condition, since Y-site octahedra do not share oxygen atoms (Fig. 5a). Note that this is a clear structure feature, where the spin transition of Mn^{3+} (d^4 configuration) in the octahedral site of the hydrogarnet henritermierite proceeds in the same way[84].

An interesting transition takes place in yttrium iron garnet (YIG) $Y_3Fe_5O_{12}$ in which ferric iron populates both the Y-sites and tetrahedral Z-sites. Although YIG is isostructural to the garnets discussed above, it undergoes a different phase transition. At pressures

characteristic for the $Fe^{3+}O_6$ spin transition (50 ± 1 GPa), there is an abrupt irreversible amorphization of this garnet[85,86] that is not related to the mechanical instability[86]. YIG remains ferrimagnetic ($T_C = 559$ K at ambient conditions) up to the amorphization, so a spin transition according to our phenomenological arguments can proceed only in a first-order manner.

The $Fe^{3+}O_4$ tetrahedron is a "metastable" polyhedron at high pressure due to the relatively large ionic radius of ferric iron (49 pm *vs* 26 pm of Si^{4+}, Ref. [3]) and the general tendency to increase coordination number with pressure[87]. Indeed, XRD and Mössbauer data of YIG after pressure-induced amorphization show evidence that all iron cations have six-fold coordination[85,88]. Moreover, YIG is metastable at room temperature above 31 GPa and transforms to the perovskite structure (in which the minimum cation coordination number is six) upon heating[86], which is typical behavior for members of the garnet family. There is a large kinetic barrier between the garnet and perovskite structures, which, to our knowledge, cannot be overcome by any garnet at room temperature. Therefore, it is the instability of HS $Fe^{3+}O_6$ octahedra upon reaching the critical volume that serves as a trigger for this amorphization, allowing the kinetic barrier to be overcome (partially in this case). The cooperative behavior of iron octahedra might be crucial for the process. Indeed, spin transition by crossover does not lead to such consequences for the garnet examples above (although they are also certainly metastable at spin crossover pressures).

In the case of solid solutions, the highest T_{cp} value will be seen in the iron end-member. Reduction of the amount of iron in the system will decrease the cooperativity of iron octahedra and, accordingly, the critical point temperature. In natural systems pressure-induced spin transitions are inferred to occur in the Earth and exoplanet interiors. In view of the above considerations the iron spin transition in the Earth's mantle should tend to crossover behavior for the following reasons: (*i*) mantle minerals are solid solutions with relatively low concentrations of iron that promote a decrease of the cooperativity of iron ions, and (*ii*) the temperatures of the mantle are high (> 2000 K) at spin-transition pressures.

C. Center shift *vs* polyhedron volume

Single-crystal XRD experiments provide a unique opportunity to study the dependence of CS on the polyhedron volume (Figs. 8 and 9). In addition to the compounds measured

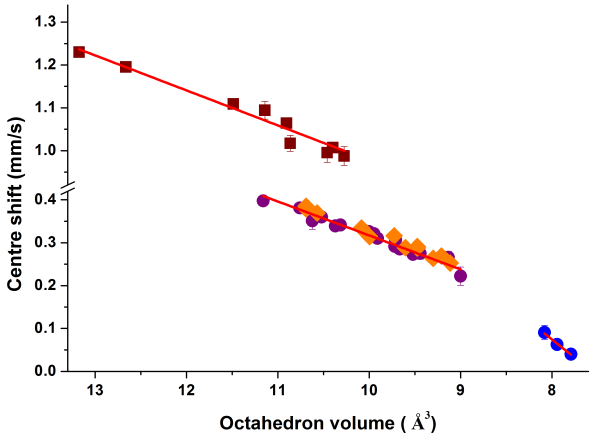

FIG. 8. Center shift as a function of the octahedron volume showing a linear dependence. Purple and blue circles are data of $FeBO_3$ (HS and LS, respectively), orange diamonds correspond to α-Fe_2O_3, and brown squares belong to $FeCO_3$ (single-crystal data from Ref. 64). The red lines are linear fits to the underlying points (the middle line is a fit of the $FeBO_3$ HS points). In the HS state, slope values are the same for both ferric ($FeBO_3$, α-Fe_2O_3) and ferrous ($FeCO_3$) iron ions. The LS state in iron borate is more sensitive to changes of octahedron volume.

in this work, we also used for comparison single-crystal Mössbauer data of $FeCO_3$[64]. Using structure data from Ref. 72 we obtained the following 2nd BM EoS parameters for the $Fe^{2+}O_6$ octahedron in $FeCO_3$: $V_0 = 13.17(4)$ Å^3 and $K_0 = 108(3)$ GPa. Hence the octahedron of ferrous iron is larger by ~ 2 Å^3 at ambient conditions (see Fig. 7) and more compressible relative to ferric iron octahedra.

In all studied compounds the CS value varies linearly with octahedron volume. It is interesting that for the HS octahedra, linear fits have the same slope (Fig. 8) within uncertainty, regardless of valence state: 0.079(4), 0.079(5) and 0.082(4) mm/s·Å^{-3} for $FeBO_3$, α-Fe_2O_3 and $FeCO_3$, respectively. Y-site Fe^{3+} in skiagite-iron-majorite solid solution shows the same linear dependence in the HS state (Fig. 9a) with a slope of 0.087(6) mm/s·Å^{-3}, but one should note the systematic error in this value because the average $(Fe,Si)O_6$ volume was used.

This similarity of slopes suggests that the volume dependence of CS is governed by the same mechanism in all investigated compounds. The noted difference in pressure dependence of isomer shift between Fe^{2+} and Fe^{3+} compounds[89] is therefore simply related to the higher compressibility of ferrous iron (at least in the case of octahedral coordination). High-pressure

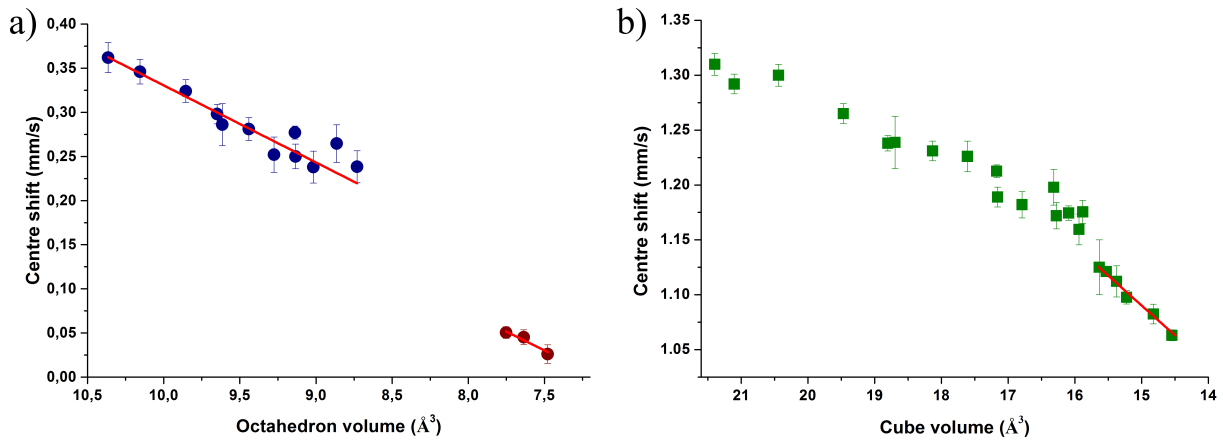

FIG. 9. Volume dependence of CS in skiagite-iron-majorite solid solution. a) CS of Y-site HS Fe^{3+} (blue circles) also depends linearly on octahedron volume, but LS data (brown circles) show almost the same slope in contrast to $FeBO_3$. b) CS of X-site Fe^{2+} (in distorted cube) has a much weaker non-linear dependence. The red lines are linear fits to the underlying points.

NIS data of siderite[71] show that δ_{SOD} also depends linearly on the octahedron volume with a slope of 0.0050(1) mm/s·Å^{-3}, which is 6 % of the observed volume dependence of δ_{CS}.

The data clearly show that the CS discontinuity between the two spin states is caused not only by the volume difference, but also by changes in the electronic configuration, because the LS δ_{CS} do not follow HS δ_{CS} volume dependence (Fig. 8 and 9a). In the LS state δ_{CS} is more sensitive to volume changes in the $FeBO_3$ case (0.17(7) mm/s·Å^{-3}, Fig. 8,), while LS Fe^{3+} in skiagite-iron-majorite shows roughly the same slope (0.09(2) mm/s·Å^{-3}) as the HS state (Fig. 9a). The number of data points is too small, however, for definite conclusions. Also note that in the latter case the CS values can be affected by strong overlap with singlet component (Fig. 5b).

The skiagite-iron-majorite data demonstrate that volume dependence of CS is distinct for different coordination polyhedra. The volume dependence of δ_{CS} of the cubic X-site Fe^{2+} is nonlinear in the investigated pressure range and considerably weaker than for the case of the octahedron (Fig. 9b). A linear fit of the data below 16 Å^3 (pressure above 60 GPa) has a slope of 0.054(3) mm/s·Å^{-3}.

Based on the obtained volume dependence for δ_{CS} and compressibility data (section IV B 1) we can constrain the possible range of CS values for the HS Fe cations coordinated by oxygen octahedra. The average decrease in δ_{CS} before the beginning of the pressure-induced spin

transition is 0.15 ± 0.03 mm/s for Fe^{3+} and 0.25 ± 0.05 mm/s for Fe^{2+}. The δ_{CS} of LS state Fe after the pressure-induced spin transition should be smaller by 0.28 ± 0.05 mm/s for Fe^{3+} and 0.55 ± 0.1 mm/s for Fe^{2+} compared to δ_{CS} of HS state Fe at ambient pressure.

V. CONCLUSIONS

We performed a comparative study of the spin transition in $Fe^{3+}O_6$ octahedra in a number of different compounds using MS in combination with single-crystal XRD data. Analysis of the obtained data shows that the most universal and unambiguous evidence of the HS→LS transition among hyperfine parameters is a drop of the center shift value (≥ 0.13 mm/s). One significant advantage is the temperature independence of the drop, which is not the case for quadrupole splitting, since for the studied case the QS values for the LS state can be close to HS values before spin transition. However, the temperature dependence of ΔE_Q within the LS state can be a reliable indicator.

Structural data reveal that for all studied compounds, the spin transition begins within a narrow range of octahedral volumes: 8.9–9.3 Å^3. Taking into account the compressibility of the $Fe^{3+}O_6$ octahedra, this volume range corresponds to a 45–60 GPa pressure range. The simple ideal octahedral model from crystal field theory predicts transition volumes with reasonable accuracy, but highly distorted octahedra require a more elaborate approach.

Spin transitions usually lead to isosymmetric structural transitions. Two scenarios are possible: supercritical, crossover behavior or first-order phase transition. The degree of cooperativity in the behavior of the iron octahedra (controlled by elastic interactions between ions in different spin states) plays a crucial role, determining the position of the critical point on the phase diagram. From phenomenological arguments, it follows that in magnetically-ordered compounds the spin transition can proceed only in a first-order manner. Moreover, experiments show that cooperative behavior is preserved at least at room temperature if iron octahedra share common oxygen atoms. We argue that instability of iron octahedra on reaching the critical volume, together with cooperative behavior, is important for metastable phases as it may promote the overcoming of kinetic barriers, even at low temperatures. We note that these conclusions are applicable in general to spin transition phenomenon, regardless of the specific transition ion.

We have demonstrated that the center shift of HS iron depends linearly on octahedral

volume with the same slope, regardless of oxidation state (0.08 mm/s·Å^{-3}). NIS data show that the SOD contribution to this dependence is less than 10 %. Such data can be used for determination of the isomer shift calibration constant. The center shift of ferrous iron in cubic coordination is less sensitive to the volume changes and the dependence is nonlinear.

ACKNOWLEDGMENTS

Authors are grateful to Prof. V. Dmitriev and Dr. D. Chernyshov for fruitful discussion and Dr. E. Greenberg for provided data. We thank the European Synchrotron Radiation Facility for provision of synchrotron radiation (ID18). N.D. thanks the German Research Foundation (Deutsche Forschungsgemeinschaft, DFG, projects no. DU 954-8/1 and DU 954-11/1) and the Federal Ministry of Education and Research, Germany (BMBF, grants no. 5K13WC3 and 5K16WC1) for financial support. L.D. acknowledges DFG funding through projects the CarboPaT Research Unit FOR2125.

---

* vasyukov@physics.msu.ru

[1] Hereafter, the term "spin crossover" is only used for the case when a spin transition progresses by a supercritical manner, see section IV B 2.

[2] L. Cambi and L. Szegö, Eur. J. Inorg. Chem. **64**, 2591 (1931).

[3] R. Shannon, Acta Crystallogr., Sect. A: Cryst. Phys., Diffr., Theor. Gen. Crystallogr. **32**, 751 (1976).

[4] O. Kahn and C. J. Martinez, Science **279**, 44 (1998).

[5] R. N. Muller, L. Vander Elst, and S. Laurent, J. Am. Chem. Soc. **125**, 8405 (2003).

[6] H. J. Shepherd, I. A. Gural'skiy, C. M. Quintero, S. Tricard, L. Salmon, G. Molnár, and A. Bousseksou, Nat. Commun. **4** (2013).

[7] G. Molnár, L. Salmon, W. Nicolazzi, F. Terki, and A. Bousseksou, J. Mater. Chem. C **2**, 1360 (2014).

[8] P. Gütlich, Eur. J. Inorg. Chem. **2013**, 581 (2013).

[9] J. Badro, G. Fiquet, F. Guyot, J.-P. Rueff, V. V. Struzhkin, G. Vankó, and G. Monaco, Science **300**, 789 (2003).

[10] R. Boehler and K. De Hantsetters, High Pressure Res. **24**, 391 (2004).

[11] S. Ovchinnikov, J. Exp. Theor. Phys. **107**, 140 (2008).

[12] E. Greenberg, To be published.

[13] P. Schouwink, L. Dubrovinsky, K. Glazyrin, M. Merlini, M. Hanfland, T. Pippinger, and R. Miletich, Am. Mineral. **96**, 1781 (2011).

[14] L. Ismailova, M. Bykov, E. Bykova, A. Bobrov, I. Kupenko, V. Cerantola, D. Vasiukov, N. Dubrovinskaia, C. McCammon, M. Hanfland, K. Glazyrin, H.-P. Liermann, A. Chumakov, and L. Dubrovinsky, Am. Mineral. **102**, 184 (2017).

[15] W. Xu, E. Greenberg, G. K. Rozenberg, M. P. Pasternak, E. Bykova, T. Boffa-Ballaran, L. Dubrovinsky, V. Prakapenka, M. Hanfland, O. Y. Vekilova, S. I. Simak, and I. A. Abrikosov, Phys. Rev. Lett. **111**, 175501 (2013).

[16] M. Merlini, M. Hanfland, M. Gemmi, S. Huotari, L. Simonelli, and P. Strobel, Am. Mineral. **95**, 200 (2010).

[17] E. Greenberg, G. K. Rozenberg, W. Xu, M. P. Pasternak, C. McCammon, K. Glazyrin, and L. S. Dubrovinsky, Phys. Rev. B **88**, 214109 (2013).

[18] A. Friedrich, B. Winkler, W. Morgenroth, J. Ruiz-Fuertes, M. Koch-Müller, D. Rhede, and V. Milman, Phys. Rev. B **90**, 094105 (2014).

[19] I. Bernal, C. Struck, and J. G. White, Acta Crystallogr. **16**, 849 (1963).

[20] R. Diehl, Solid State Commun. **17**, 743 (1975).

[21] M. Petrov, A. Paugurt, G. Smolenskii, S. Kizhaev, and M. Chizhov, Fiz. Tverd. Tela **14**, 109 (1972).

[22] R. Wolfe, A. Kurtzig, and R. LeCraw, J. Appl. Phys. **41**, 1218 (1970).

[23] M. Eibschütz, L. Pfeiffer, and J. Nielsen, J. Appl. Phys. **41**, 1276 (1970).

[24] I. Troyan, A. Gavrilyuk, V. Sarkisyan, I. Lyubutin, R. Rüffer, O. Leupold, A. Barla, B. Doyle, and A. Chumakov, JETP Lett. **74**, 24 (2001).

[25] V. Sarkisyan, I. Troyan, I. S. Lyubutin, A. Gavrilyuk, and A. Kashuba, JETP Lett. **76**, 664 (2002).

[26] A. G. Gavriliuk, I. Trojan, R. Boehler, M. Eremets, A. Zerr, I. S. Lyubutin, and V. Sarkisyan, JETP Lett. **75**, 23 (2002).

[27] K. Parlinski, Eur. Phys. J. B **27**, 283 (2002).

[28] At isosymmetric transition the space group preserves and the atoms do not change their Wyckoff

positions. In the literature it is also often called isostructural.

[29] R. Blake, H. RE, T. Zoltai, and L. W. Finger, Am. Mineral. **51**, 123 (1966).

[30] C. Shull, W. Strauser, and E. Wollan, Phys. Rev. **83**, 333 (1951).

[31] S. Klotz, T. Strässle, and T. Hansen, EPL **104**, 16001 (2013).

[32] E. Bykova, M. Bykov, V. Prakapenka, Z. Konôpková, H.-P. Liermann, N. Dubrovinskaia, and L. Dubrovinsky, High Pressure Res. **33**, 534 (2013).

[33] E. Bykova, L. Dubrovinsky, N. Dubrovinskaia, M. Bykov, C. McCammon, S. Ovsyannikov, H.-P. Liermann, I. Kupenko, A. Chumakov, R. Rüffer, M. Hanfland, and V. Prakapenka, Nat. Commun. **7** (2016).

[34] M. Pasternak, G. K. Rozenberg, G. Y. Machavariani, O. Naaman, R. Taylor, and R. Jeanloz, Phys. Rev. Lett. **82**, 4663 (1999).

[35] L. Ismailova, A. Bobrov, M. Bykov, E. Bykova, V. Cerantola, I. Kantor, I. Kupenko, C. McCammon, V. Dyadkin, D. Chernyshov, S. Pascarelli, A. Chumakov, N. Dubrovinskaia, and L. Dubrovinsky, Am. Mineral. **100**, 2650 (2015).

[36] H. Yang, R. Lu, R. T. Downs, and G. Costin, Acta Crystallogr., Sect. E: Struct. Rep. Online **62**, i250 (2006).

[37] J. Forsyth, I. Hedley, and C. Johnson, J. Phys. C: Solid State Phys. **1**, 179 (1968).

[38] A. Szytuła, A. Burewicz, Ž. Dimitrijević, S. Kraśnicki, H. Rżany, J. Todorović, A. Wanic, and W. Wolski, Phys. Status Solidi B **26**, 429 (1968).

[39] Ö. Özdemir and D. J. Dunlop, Geophys. Res. Lett. **23**, 921 (1996).

[40] I. O. Galuskina, Y. Vapnik, B. Lazic, T. Armbruster, M. Murashko, and E. V. Galuskin, Am. Mineral. **99**, 965 (2014).

[41] B. Decker and J. Kasper, Acta Crystallogr. **10**, 332 (1957).

[42] L. Corliss, J. Hastings, and W. Kunnmann, Phys. Rev. **160**, 408 (1967).

[43] We note that the center shift extracted from Mössbauer spectra is the sum of isomer and second-order Doppler shifts ($\delta_{CS} = \delta_{IS} + \delta_{SOD}$).

[44] M. Kotrbová, S. Kadečková, J. Novák, J. Brádler, G. Smirnov, and Y. V. Shvydko, J. Cryst. Growth **71**, 607 (1985).

[45] I. Kantor, V. Prakapenka, A. Kantor, P. Dera, A. Kurnosov, S. Sinogeikin, N. Dubrovinskaia, and L. Dubrovinsky, Rev. Sci. Instrum. **83**, 125102 (2012).

[46] A. Kurnosov, I. Kantor, T. Boffa-Ballaran, S. Lindhardt, L. Dubrovinsky, A. Kuznetsov, and

B. H. Zehnder, Rev. Sci. Instrum. **79**, 045110 (2008).

[47] A. Dewaele, M. Torrent, P. Loubeyre, and M. Mezouar, Phys. Rev. B **78**, 104102 (2008).

[48] R. Rüffer and A. I. Chumakov, Hyperfine Interact. **97**, 589 (1996).

[49] V. Potapkin, A. I. Chumakov, G. V. Smirnov, J.-P. Celse, R. Rüffer, C. McCammon, and L. Dubrovinsky, J. Synchrotron Radiat. **19**, 559 (2012).

[50] C. Prescher, C. McCammon, and L. Dubrovinsky, J. Appl. Crystallogr. **45**, 329 (2012).

[51] K. Momma and F. Izumi, J. Appl. Crystallogr. **44**, 1272 (2011).

[52] R. J. Angel, M. Alvaro, and J. Gonzalez-Platas, Z. Kristallogr. - Cryst. Mater. **229**, 405 (2014).

[53] Hereafter the error notation $A \pm \sigma$ means that the probability density of the error has continuous uniform distribution over the interval $[A - \sigma, A + \sigma]$, as distinct from the notation $A(\sigma)$ where the Gaussian distribution of the error is implied and σ is one standard deviation.

[54] Quadrupole shift is a pair-wise shift of the magnetic sextet lines due to the quadrupole interaction. In the literature, 2ε is often referred to as quadrupole shift.

[55] M. Cohen and F. Reif, Solid State Phys. **5**, 321 (1957).

[56] P. Gütlich, E. Bill, and A. Trautwein, *Mössbauer Spectroscopy and Transition Metal Chemistry: Fundamentals and Applications* (Springer Berlin Heidelberg, 2010).

[57] L. Tobler, W. Kündig, and I. Savić, Hyperfine Interact. **10**, 1017 (1981).

[58] I. Kupenko, To be published.

[59] A. Gavriliuk, I. Trojan, I. Lyubutin, S. Ovchinnikov, and V. Sarkissian, J. Exp. Theor. Phys. **100**, 688 (2005).

[60] H. Spiering, in *Mössbauer Spectroscopy Applied to Inorganic Chemistry*, Modern Inorganic Chemistry, Vol. 1, edited by G. Long (Plenum Press, New York, 1984).

[61] C. Geiger, T. Armbruster, G. Lager, K. Jiang, W. Lottermoser, and G. Amthauer, Phys. Chem. Miner. **19**, 121 (1992).

[62] G. Amthauer and G. R. Rossman, Phys. Chem. Miner. **11**, 37 (1984).

[63] I. Y. Kantor, L. Dubrovinsky, and C. McCammon, Phys. Rev. B **73**, 100101 (2006).

[64] V. Cerantola, C. McCammon, I. Kupenko, I. Kantor, C. Marini, M. Wilke, L. Ismailova, N. Solopova, A. Chumakov, S. Pascarelli, and L. Dubrovinsky, Am. Mineral. **100**, 2670 (2015).

[65] I. Bersuker and I. Ogurtson, Fiz. Tverd. Tela **10**, 3651 (1968), [Sov. Phys. Solid State, **10**(12) 2894, (1969)].

[66] M. Nihei, T. Shiga, Y. Maeda, and H. Oshio, Coord. Chem. Rev. **251**, 2606 (2007).

[67] N. Greenwood and T. Gibb, *Mössbauer Spectroscopy* (Chapman and Hall Ltd, London, 1971).

[68] F. Neese, Inorg. Chim. Acta **337**, 181 (2002).

[69] W. Jones and N. March, *Theoretical Solid State Physics: Perfect lattices in equilibrium*, Dover Books on Physics Series (Dover Publications, 1985) p.237.

[70] D. Vasiukov, L. Ismailova, I. Kupenko, V. Cerantola, R. Sinmyo, K. Glazyrin, C. McCammon, A. Chumakov, L. Dubrovinsky, and N. Dubrovinskaia, Phys. Chem. Miner. **45**, 397 (2018).

[71] S. Chariton, Private communication.

[72] B. Lavina, P. Dera, R. T. Downs, W. Yang, S. Sinogeikin, Y. Meng, G. Shen, and D. Schiferl, Phys. Rev. B **82**, 064110 (2010).

[73] M. Merlini and M. Hanfland, High Pressure Res. **33**, 511 (2013).

[74] F. Menil, J. Phys. Chem. Solids **46**, 763 (1985).

[75] A. Malakhovskii and I. Edelman, Phys. Status Solidi B **74**, K145 (1976).

[76] D. M. Sherman and T. D. Waite, Am. Mineral. **70**, 1262 (1985).

[77] R. Burns, *Mineralogical Applications of Crystal Field Theory*, 2nd ed., Cambridge Topics in Mineral Physics and Chemistry (Cambridge University Press, 1993).

[78] B. N. Figgis and M. Hitchman, *Ligand field theory and its applications*, Special topics in inorganic chemistry (Wiley-VCH, 2000).

[79] Y. Tanabe and S. Sugano, J. Phys. Soc. Jpn. **9**, 753 (1954); **9**, 766 (1954).

[80] H. Horiuchi, M. Hirano, E. Ito, and Y. Matsui, Am. Mineral. **67**, 788 (1982).

[81] H. Horiuchi, E. Ito, and D. Weidner, Am. Mineral. **72**, 357 (1987).

[82] A. G. Christy, Acta Crystallogr., Sect. B: Struct. Sci. **51**, 753 (1995).

[83] D. Khomskii and U. Löw, Phys. Rev. B **69**, 184401 (2004).

[84] A. Friedrich, B. Winkler, W. Morgenroth, A. Perlov, and V. Milman, Phys. Rev. B **92**, 014117 (2015).

[85] A. G. Gavriliuk, V. Struzhkin, I. S. Lyubutin, M. Eremets, I. Trojan, and V. Artemov, JETP Lett. **83**, 37 (2006).

[86] C. V. Stan, J. Wang, I. S. Zouboulis, V. Prakapenka, and T. S. Duffy, J. Phys.: Condens. Matter **27**, 405401 (2015).

[87] R. Hazen and L. Finger, *Comparative crystal chemistry: temperature, pressure, composition, and the variation of crystal structure*, ch. 10, III.

[88] I. S. Lyubutin, A. G. Gavriliuk, I. Trojan, and R. Sadykov, JETP Lett. **82**, 702 (2005); however

Fe^{3+} likely remains in the HS state as there is no drop in CS value for octahedrally-coordinated iron and on decompression the hyperfine parameters do not show any significant changes.

[89] D. Williamson, in *Mössbauer isomer shifts*, edited by G. Shenoy and F. Wagner (North-Holland Publ., 1978).

Pressure-induced spin pairing transition of Fe^{3+} in oxygen octahedra

Supplemental Material

D.M. Vasiukov[1,2], L. Dubrovinsky[2], I. Kupenko[3], V. Cerantola[4], G. Aprilis[1,2], L. Ismailova[5], E. Bykova[6], C. McCammon[2], C. Prescher[7], A.I. Chumakov[4], N. Dubrovinskaia[1]

[1]*Laboratory of Crystallography, Universität Bayreuth, Universitätsstr. 30, D-95447 Bayreuth, Germany*

[2]*Bayerisches Geoinstitut, Universität Bayreuth, Universitätsstr. 30, D-95447 Bayreuth, Germany*

[3]*Institut für Mineralogie, Universität Münster, Corrensstr. 24, D-48149 Münster, Germany*

[4]*ESRF-The European Synchrotron CS40220 38043 Grenoble Cedex 9 France*

[5]*Skolkovo Institute of Science and Technology, Skolkovo Innovation Center, ul. Nobelya 3,143026 Moscow, Russia*

[6]*Photon Science, Deutsches Elektronen-Synchrotron, Notkestr. 85, D-22603 Hamburg, Germany*

[7]*Institut für Geologie und Mineralogie, Universität zu Köln, D-50674 Köln, Germany*

vasyukov@physics.msu.ru

Hyperfine magnetic field

Table 1: Estimated Néel temperatures from Bloch's law in the vicinity of the HS→LS transition in the studied compounds.

Compound	T_N at ambient pressure, K	T_N just below transition, K
$FeBO_3$	348, [1,2]	690
FeOOH	393, [3]	649
$CaFe_2O_4$	200, [4]	370
Fe_2O_3	948, [5]	1675

At the HS→LS transition in octahedral coordination, the spin of ferric iron changes from 5/2 to 1/2. This means a huge drop of the iron magnetic moment, but Fe^{3+} remains paramagnetic in the LS state as distinct from LS Fe^{2+}. Accordingly, the transition should cause a large decrease in Néel (Curie) temperature. Indeed, in all studied compounds that were magnetically ordered in the HS state, the disappearance of magnetic ordering or a large decrease in the H_{hf} value at the spin transition are observed.

Reliable experimental information about the T_N pressure dependence is unfortunately absent. To estimate the magnetic critical temperature in the vicinity of the spin transition for the compounds under study, one can apply Bloch's law [6]:

$$T_N \propto J \propto V^{(-10/3)}, \tag{1}$$

where J is the exchange integral. For V it is more reasonable to use the volume of the octahedron instead of the unit cell volume as it better determines the overlapping of electronic wave functions. The obtained estimates are listed in Table 1. Using the mean-field

approximation and assuming that the exchange integral does not change substantially, one can obtain that the Néel temperature after the spin transition will be 3/35 of T_N before the transition [7]. Although the constancy of the exchange integral through the spin transition is doubtful[1], this result is satisfactory for rough estimates. The factor 3/35 means that existence of magnetic order at room temperature after the spin transition requires that the Néel temperature before the transition should be around 3500 K. Even the large T_N in hematite (1675 K, Table 1) is substantially less than this value.

The hyperfine magnetic field results from interaction of the nuclear spin with electronic cloud[2] and can be expressed as a sum of three contributions: Fermi contact interaction (H_c) and a dipolar interaction with orbital and spin momenta (H_L and H_S, respectively) of the electrons [8]:

$$H_{hf} = H_c + H_L + H_S, \tag{2}$$

$$H_c = \frac{8\pi}{3} g_e \mu_B \langle \mathbf{S} \rangle \sum_{ns} \left[\left| \psi^{\uparrow}_{ns}(0) \right|^2 - \left| \psi^{\downarrow}_{ns}(0) \right|^2 \right], \tag{3}$$

$$H_L = g_e \mu_B \langle \frac{1}{r^3} \rangle \langle \mathbf{L} \rangle, \tag{4}$$

$$H_S = g_e \mu_B \langle 3\mathbf{r}(\mathbf{S} \cdot \mathbf{r}) \frac{1}{r^5} - \mathbf{S} \frac{1}{r^3} \rangle, \tag{5}$$

where g_e is the electron spin g-factor, μ_B is the Bohr magneton, $\left| \psi^{\uparrow\downarrow}_{ns}(0) \right|^2$ is the electron density at the nucleus for a given ns shell with spin parallel or antiparallel to the expectation value of the net electronic spin $\langle \mathbf{S} \rangle$, $\langle \mathbf{L} \rangle$ is the expectation value of the orbital momentum and r is the radial coordinate of electrons. As all terms in eq. (2) depend on $\langle \mathbf{S} \rangle$ or $\langle \mathbf{L} \rangle$, the corresponding H_{hf} of Fe^{3+} in HS and LS configurations should be significantly different.

The saturation H_{hf} value of HS ferric iron in oxygen octahedra (electronic term $^6A_{1g}$) is usually around 50–55 T. For this electronic configuration the orbital momentum is absent, the saturation value of $\langle \mathbf{S} \rangle$ is 5/2 and the observed hyperfine field arises mainly from the Fermi contact interaction term. In the LS state ($^2T_{2g}$ term) the saturated values of $\langle \mathbf{S} \rangle$ or $\langle \mathbf{L} \rangle$ can reach 1/2 and 1, respectively. So in this case H_c should be around 11 T, but H_L and H_S can now also have comparable values. As H_L and H_S may have different signs relative to H_c, the resulting hyperfine fields may lie in the 0 to 20 T range.

Quadrupole splitting

The main parameter of Mössbauer spectra that is usually used to discriminate between HS and LS states is the quadrupole splitting (especially for the Nuclear Forward Scattering experiments). The strength of the quadrupole interaction depends on the electric field gradient created at the nucleus by the electron cloud (electronic contribution) and by neighboring ions (lattice contribution) [8]:

$$q = (1 - R)q_e + (1 - \gamma_\infty)q_i, \tag{6}$$

[1]for instance, through the spin transition the σ hopping integral $t_{pd\sigma}$ for corner-shared octahedra will be replaced by the significantly smaller π hopping $t_{pd\pi}$

[2]there is also a magnetic field from dipolar interactions with magnetic moments of neighboring atoms but its value is usually less than 1 T and can be neglected

where q, q_e and q_i are the electric field gradient (total, electronic and lattice contributions, respectively), and R and γ_∞ are the Sternheimer factors of shielding and antishielding, respectively. Since the electric field gradient (EFG) is proportional to r^{-3}, firstly, the electronic part generally is the dominant contribution to the EFG and secondly, in the case where the lattice contribution plays a main role the EFG will be mainly dominated by the first coordination sphere (since the second neighbors at $2r$ distance produce an EFG that is 8 times weaker).

As fully-filled or half-filled e_g and t_{2g} orbitals do not produce an EFG (see Table 4.2 in Ref. [9]), the quadrupole splitting in the case of HS Fe^{3+} is mainly related to the lattice contribution and is generally small. In octahedrally coordinated Fe^{3+} in the LS state, the electron term is $^2T_{2g}$ with one unpaired electron on the t_{2g} level and, therefore, for ferric iron at the spin transition the main contribution to the EFG changes from lattice to electronic (for ferrous iron the situation is opposite). This should cause a significant increase in the QS value and, indeed, this tendency is observed in all compounds with the exception of Fe_2O_3 (Table II in the manuscript) where the polyhedron type may changes.

The analysis of the EFG in LS Fe^{3+} is analogous to the approach for HS Fe^{2+} [10]. The additional electron on the t_{2g} level is replaced by a hole and the EFG will be controlled by t_{2g} manifold splitting and temperature. This explains the spread of QS values in the LS state through the different degrees of octahedral distortion in the studied compounds. The temperature dependence of ΔE_Q for LS Fe^{3+} has been observed for FeOOH and $CaFe_2O_4$ [11, 12].

Table 2: The obtained hyperfine parameters of $FeBO_3$ at RT. In the HS state we provide values of the quadrupole shift (ε), whereas in the LS state the quadrupole splitting values (ΔE_Q) are given.

P,GPa	δ_{CS}, mm/s	$\varepsilon/\Delta E_Q$, mm/s	H_{hf}, T
HS state			
1E-4	0.398(8)	0.098(9)	34.86(6)
9	0.35(2)	0.08(2)	41.17(14)
14	0.339(8)	0.079(8)	43.63(6)
23.7	0.32(1)	0.06(1)	45.78(9)
30	0.307(9)	0.04(1)	46.54(7)
38	0.275(14)	0.020(14)	48.09(11)
48.5	0.266(14)	0.015(14)	48.49(11)
53.5	0.22(2)	0.02(2)	49.00(15)
LS state			
53.5	0.09(2)	1.98(3)	0
61	0.06(1)	2.04(2)	0
70	0.04(1)	2.043(24)	0

Table 3: The obtained hyperfine parameters of α-Fe_2O_3 at RT.

P,GPa	δ_{CS}, mm/s	ε, mm/s	H_{hf}, T
DAC 1			
8.2	–	0.190(4)	52.19(7)
18	0.314(5)	0.230(5)	52.10(3)
30	0.288(5)	0.296(5)	51.53(4)
41	0.263(6)	0.327(6)	50.85(4)
DAC 2			
4	0.369(6)	0.189(6)	52.27(5)
15.6	0.334(7)	0.245(7)	52.16(5)
26	0.316(6)	0.268(6)	51.87(4)
29	0.29(2)	0.29(2)	51.54(15)
DAC 3, Crystal 1			
1.5	0.379(7)	-0.085(7)	51.25(6)
34.5	0.288(8)	0.309(8)	51.20(5)
44.6	0.269(7)	0.341(7)	50.54(5)
48.6	0.253(9)	0.355(9)	50.15(6)
DAC 3, Crystal 2			
1.5	0.385(7)	-0.062(7)	51.36(6)
34.5	0.291(7)	0.318(7)	51.24(4)

Table 4: The obtained hyperfine parameters of skiagite-iron-majorite solid solution at RT.

P,GPa	δ_{CS}, mm/s	ΔE_Q, mm/s	δ_{CS}, mm/s	ΔE_Q, mm/s
DAC 1	X-site HS Fe^{2+}		Y-site HS Fe^{3+}	
1.4	1.292(9)	3.49(2)	0.36(2)	0.25(4)
5	1.30(1)	3.53(2)	0.346(14)	0.20(4)
11.5	1.265(9)	3.51(2)	0.32(1)	0.17(6)
17	1.238(7)	3.52(1)	0.30(1)	0.15(7)
23.6	1.231(9)	3.50(2)	0.28(1)	0.19(4)
29.7	1.226(14)	3.48(3)	0.25(2)	–
35.6	1.189(9)	3.48(2)	0.250(14)	0.26(3)
41	1.18(1)	3.47(3)	0.24(2)	0.23(4)
49.6	1.17(1)	3.43(3)	0.24(2)	0.34(3)
	X-site HS Fe^{2+}		Y-site LS Fe^{3+}	
56	1.160(14)	3.41(3)	0.17(15)	0.6(3)
62.3	1.13(3)	3.38(5)	0.13(13)	1.0(2)
68.1	1.112(14)	3.41(3)	0.12(6)	0.76(13)
DAC 2	X-site HS Fe^{2+}		Y-site HS Fe^{3+}	
18	1.24(2)	3.52(5)	0.29(2)	0.19(13)
35.4	1.212(6)	3.48(1)	0.277(7)	0.21(4)
48.9	1.20(2)	3.42(3)	0.27(2)	0.25(6)
	X-site HS Fe^{2+}		Y-site LS Fe^{3+}	
53	1.174(7)	3.42(1)	0.12(2)	0.35(2)
57.1	1.18(1)	3.41(2)	0.11(2)	0.52(3)
64.6	1.121(5)	3.41(1)	0.03(1)	0.79(3)
71.7	1.098(6)	3.41(1)	0.03(2)	0.82(4)
82.1	1.088(9)	3.36(2)	0.04(5)	0.92(8)
90.1	1.063(5)	3.38(1)	0.041(9)	0.89(2)

References

[1] R Wolfe, AJ Kurtzig, and RC LeCraw. Room-temperature ferromagnetic materials transparent in the visible. *J. Appl. Phys.*, 41(3):1218–1224, 1970.

[2] M Eibschütz, L Pfeiffer, and JW Nielsen. Critical-point behavior of $FeBO_3$ single crystals by Mössbauer effect. *J. Appl. Phys.*, 41(3):1276–1277, 1970.

[3] Özden Özdemir and David J Dunlop. Thermoremanence and Néel temperature of goethite. *Geophys. Res. Lett.*, 23(9):921–924, 1996.

[4] LM Corliss, JM Hastings, and W Kunnmann. Magnetic phase equilibrium in chromium-substituted calcium ferrite. *Phys. Rev.*, 160(2):408, 1967.

[5] CG Shull, WA Strauser, and EO Wollan. Neutron diffraction by paramagnetic and antiferromagnetic substances. *Phys. Rev.*, 83(2):333, 1951.

[6] Daniel Bloch. The 10/3 law for the volume dependence of superexchange. *J. Phys. Chem. Solids*, 27(5):881–885, 1966.

[7] AG Gavriliuk, IA Trojan, IS Lyubutin, SG Ovchinnikov, and VA Sarkissian. High-pressure magnetic properties and P–T phase diagram of iron borate. *J. Exp. Theor. Phys.*, 100(4):688–696, 2005.

[8] NN Greenwood and TC Gibb. *Mössbauer Spectroscopy*. Chapman and Hall Ltd, London, 1971.

[9] P. Gütlich, E. Bill, and A.X. Trautwein. *Mössbauer Spectroscopy and Transition Metal Chemistry: Fundamentals and Applications*. Springer Berlin Heidelberg, 2010.

[10] Robert Ingalls. Electric-field gradient tensor in ferrous compounds. *Phys. Rev.*, 133(3A):A787, 1964.

[11] Weiming Xu, Eran Greenberg, Gregory Kh Rozenberg, Moshe P Pasternak, Elena Bykova, Tiziana Boffa-Ballaran, Leonid Dubrovinsky, Vitali Prakapenka, Michael Hanfland, Olga Yu Vekilova, Sergei I Simak, and Igor A Abrikosov. Pressure-induced hydrogen bond symmetrization in iron oxyhydroxide. *Phys. Rev. Lett.*, 111(17):175501, 2013.

[12] Eran Greenberg, Gregory Kh Rozenberg, Weiming Xu, Moshe P Pasternak, Catherine McCammon, Konstantin Glazyrin, and Leonid S Dubrovinsky. Mott transition in $CaFe_2O_4$ at around 50 GPa. *Phys. Rev. B*, 88(21):214109, 2013.

Iron behaviour in Fe,Al-bearing bridgmanite between 35–80 GPa

D.M. Vasiukov*[a,b], J. van Driel[c], E. Bykova[d], M. Bykov[d], G. Aprilis[a,b], V. Cerantola[e], I. Kupenko[f], C. McCammon[b], A. Schönleber[a], K. Glazyrin[d], V. Prakapenka[g], H.-P. Liermann[d], M. Hanfland[e], A.I. Chumakov[e], L. Dubrovinsky[b], N. Dubrovinskaia[a]

[a] *Laboratory of Crystallography, Universität Bayreuth, Universitätsstr. 30, D-95447 Bayreuth, Germany*

[b] *Bayerisches Geoinstitut, Universität Bayreuth, Universitätsstr. 30, D-95447 Bayreuth, Germany*

[c] *Department of Earth Sciences, University College London, WC1E 6BT London, UK*

[d] *Photon Science, Deutsches Elektronen-Synchrotron, Notkestr. 85, D-22603 Hamburg, Germany*

[e] *ESRF-The European Synchrotron CS40220 38043 Grenoble Cedex 9 France*

[f] *Institut für Mineralogie, Universität Münster, Corrensstr. 24, D-48149 Münster, Germany*

[g] *Center for Advanced Radiation Sources, University of Chicago, Chicago, Illinois 60637, USA.*

*vasyukov@physics.msu.ru

The changes in the electronic states of iron in bridgmanite are crucial for the chemical and physical properties of the lower mantle. Here we present results of the *in situ* synthesis of bridgmanite in the laser-heated diamond anvil cell in pressure range from 35 to 86 GPa. Our experiments revealed that the $Fe^{3+}/\Sigma Fe$ ratio in bridgmanite depends on the iron oxidation state of the precursor that was used. We demonstrated that Fe^{3+} in bridgmanite is formed due to Fe^{2+} disproportionation in case of synthesis from a reduced precursor at pressures below 60 GPa. All products of the iron disproportionation reaction, including Fe metal, were identified *in situ*. The $Fe^{3+}/\Sigma Fe$ ratio in bridgmanite synthesized from a reduced precursor at pressures between 35 and 60 GPa and $\sim$ 2400 K is about 25 %. In bridgmanite synthesized at 86 GPa and $\sim$ 2800 K, Fe^{3+} adopts the low-spin state and the $Fe^{3+}/\Sigma Fe$ ratio reaches 60 %. However, despite this high Fe^{3+} content, we could not detect the presence of Fe metal, which leaves open the question regarding the origin of the large amount of Fe^{3+}. We argue that the appearance of the doublet with extremely high quadrupole splitting in Mössbauer spectra of bridgmanite above 30 GPa is related not to the spin transition of Fe^{2+} in the pseudo-dodecahedral site, but to a transition between the non-degenerate and Jahn-Teller active electronic terms without any change in the spin quantum number.

Keywords Bridgmanite · Fe^{2+} disproportionation · Iron electronic states · X-ray diffraction · Mössbauer spectroscopy

1 Introduction

The Earth's lower mantle can be assumed as a primarily triminerallic rock consisting of Fe,Al-bearing $MgSiO_3$ bridgmanite, (Mg,Fe)O ferropericlase and $CaSiO_3$ perovskite. While the exact mineral proportions are not well constrained, the estimates of bridgmanite part range from 75 wt.% and higher (Murakami et al, 2012, Ricolleau et al, 2009).

Bridgmanite crystallizes in the distorted $GdFeO_3$-type perovskite structure (space group *Pbnm*) with two cationic sites (pseudo-dodecahedral A-site and octahedral B-site, see Fig. 1) and can adopt iron in both +2 and +3 oxidation states. Ferrous iron partitions between ferropericlase and bridgmanite in lower mantle whereas bridgmanite is a principal host for ferric iron (McCammon, 1997).

In bridgmanite Fe^{2+} substitutes Mg^{2+} in the large A-site. Multianvil experiments show that the Al^{3+} presence significantly enhance the $Fe^{3+}/\Sigma Fe$ ratio (Lauterbach et al, 2000) that is attributed to a energetically favorable charge-coupled substitution Fe_A^{3+}–Al_B^{3+} (the subscript designates crystallographic site). Indeed, the direct determination of site occupancies from the single-crystal diffraction data show that Fe^{3+} also prefers A-site (Vanpeteghem et al, 2006).

At lower mantle pressures the Fe^{2+} and Fe^{3+} in bridgmanite undergo electronic transitions. Above 30 GPa Mössbauer data show appearance of a new Fe_A^{2+} doublet with high quadrupole splitting ($\Delta E_Q > 3$ mm/s). This new component was initially interpreted as an intermediate spin state ($S = 1$) of Fe_A^{2+} (Lin et al, 2008, McCammon et al, 2008). However, the first-principle theoretical calculations do not support this conjecture but show that ferrous iron remains in the high-spin state at pressures of the lower mantle and component with high quadrupole splitting is related to the different local oxygen arrangement around Fe_A^{2+} (Bengtson et al, 2009, Hsu et al, 2010). Regarding Fe_A^{3+} both experimental and theoretical works are in agreement that ferric iron in the A-site remains in the HS state at P–T conditions of the lower mantle (Glazyrin et al, 2014, Hsu et al, 2012).

However at moderate pressures (above 50 GPa) the LS state of Fe^{3+} in the B-site can be stabilized and this may lead to redistribution of ferric iron between A- and B-sites. Such diffusion process requires high temperatures and will not be visible at room temperature compression experiments. To date, the possible redistribution of ferric iron remains a debatable topic, and while theoretical calculations support this possibility (Hsu et al, 2012) the different experimental studies came to the opposite conclusions (for instance, see Catalli et al, 2010, Glazyrin et al, 2014).

These changes in the iron electronic states may have far-reaching consequences for the

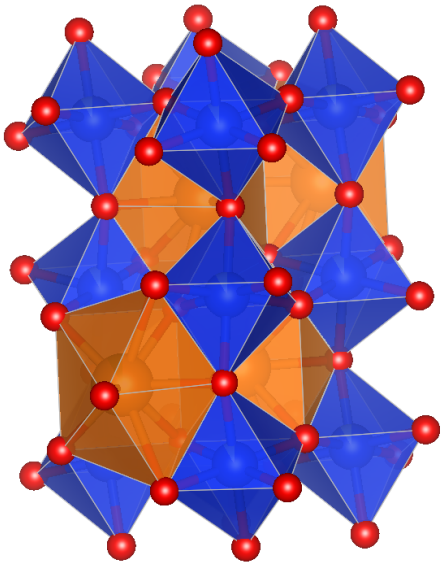

Figure 1. Crystal structure of bridgmanite. Its perovskite-like framework is formed by corner-shared octahedra populated by Si^{4+} and Al^{3+} (B-site, blue) with large 8-12 coordinated cavities occupied by Mg^{2+} and Fe^{2+} (A-site, orange). The Fe^{3+} can occupy both sites depending on the electronic state.

physical and chemical properties of lower mantle (e.g. density, compressibility, transport properties etc., see Lin et al, 2013) because of bridgmanite abundance. To date however, our understanding of iron behavior in bridgmanite is largely based on multianvil experiments (so pressures about 25 GPa that correspond to a thin layer on the top of lower mantle) and many estimations of lower mantle properties just assume validity of these results to higher pressures.

The particularly important parameter for the composition of lower mantle is a $Fe^{3+}/\Sigma Fe$ ratio in bridgmanite. The Al-bearing bridgmanite synthesized in multianvil press contains a large amount of Fe^{3+} ($Fe^{3+}/\Sigma Fe \geq 50$ %) independently of oxygen fugacity (f_{O_2}, see Frost et al, 2004). These data led to the conclusion that the lower mantle with a typical bulk silicate earth composition should contain about 1 wt% of a metallic Fe-rich alloy due to the disproportionation reaction of ferrous iron Frost et al (2004). However, the $Fe^{3+}/\Sigma Fe$ ratio in bridgmanite can vary with pressure (especially taking into account the possible stabilization of LS Fe_B^{3+}) that would directly affect the presence of the Fe-rich alloy in the lower mantle and the partitioning of Fe between ferropericlase and bridgmanite.

Recently, the modelling of seismic wave velocities based on elasticity data of Fe,Al-bearing bridgmanite in Kurnosov et al (2017) shows the divergence with Preliminary Reference Earth Model (PREM, Dziewonski and Anderson, 1981) at depths below 1200 km that led to a proposal that Fe^{3+} content in bridgmanite decreases with depth. Indeed, Shim et al

(2017) found significant variations of $Fe^{3+}/\Sigma Fe$ ratio with synthesis pressure in bridgmanite synthesized *in situ* in the laser-heated diamond anvil cell (DAC).

Here we present experimental study of bridgmanite crystallized *in situ* in laser-heated DAC from a glass with different Fe^{3+} content. Because to date there are no *in situ* evidences for the Fe^{2+} disproportionation in DAC the especial attention was paid to confirm presence of all outcomes of the iron disproportionation reaction.

2 Methods

As a precursor for the *in situ* bridgmanite synthesis in DAC two kind of glass with $Fe^{3+}/\Sigma Fe$ ratio 2(1) and 47(3) % were used (hereinafter referred as reduced and oxidized glass, respectively). Initially, the oxidized glass was prepared from mixed oxides in furnace at 1600 °C. Then it was used as a precursor for preparation of reduced glass in gas mixing furnace with CO/CO_2 atmosphere (45/55) at 1000 °C. The desired composition for the reduced glass was $Mg_{0.88}Fe_{0.09}Al_{0.06}Si_{0.97}O_3$ (or 56.4% SiO_2, 34.3% MgO, 6.3% FeO, 3% Al_2O_3 in wt.%) that corresponds to an expected mantle composition and the crystallization from such composition can give a stoichiometric bridgmanite with only Fe^{2+}.

The chemical composition of the synthesized glass were characterized using wavelength-dispersive X-ray microprobe analysis (JEOL JXA-8200; focused beam; accelerating voltage of 15 keV and beam current of 15 nA). The iron oxidation state was determined using transmission Mössbauer (WissEL spectrometer operated in constant-acceleration mode with a nominal 25 mCi $^{57}Co(Rh)$ source at 19 °C). The compositions of the oxidized and reduced glass are $Mg_{0.841(4)}Fe_{0.087(5)}Al_{0.059(3)}Si_{0.982(4)}O_3$ and $Mg_{0.871(8)}Fe_{0.090(5)}Al_{0.062(5)}Si_{0.973(4)}O_3$, respectively, that is close to the target stoichiometry.

The products of the synthesis in DAC and electronic states of iron were controlled by synchrotron X-ray diffraction (XRD) and Mössbauer spectroscopy, respectively (the summary of performed experiments is given in Table 1). We used the piston-cylinder BX90 DAC (Kantor et al, 2012) equipped with Boehler-Almax diamonds (Boehler and De Hantsetters, 2004) to increase the opening angle for diffraction experiments. The sample was put to pressure chamber inside rhenium gasket together with a small ruby sphere. The cells were loaded by neon or argon using a gas loading system of Bayerisches Geoinstitut (Kurnosov et al, 2008). In case of Mössbauer experiments the pressure inside DAC was determined using ruby fluorescence method (Dewaele et al, 2008) while during XRD experiments we used the equation of state of pressure medium (Fei et al, 2007). For the glass crystallization we used the double-sided laser heating system operated in continuous-wave mode (Aprilis et al, 2017,

Table 1: List of the performed experiments and data collection. Notes: Mj: majorite; Brd: bridgmanite; Stish: Stishovite.

Glass type	Synth. P, GPa	T, K	Möss.		XRD		Confirmed phases
			after LH	decompr.	powder	SC	
Oxid.	15	up to 1900			×	×	Mj
Red.	35	2500		×	×	×	Brd+Stish+α-Fe
Oxid.	45		×				Brd
Red.	45		×				Brd
Red.	48	2350	×				Brd
Oxid.	49		×		×		Brd
Red.	59		×	×			Brd+α-Fe
Red.	78	2400	×	×	×		Brd+Stish+α-Fe
Red.	86	2800	×	×	×		Brd+Stish

Kupenko et al, 2012). The system uses two near-infrared fiber lasers ($\lambda = 1070 \pm 10$ nm) and a π-shapers to form a Gaussian TEM_{00} beam into a flat-top one (Laskin and Laskin, 2011) that minimizes the effects of the thermophoresis (also known as thermal diffusion, see Sinmyo and Hirose, 2010).

The Mössbauer transmission spectra were collected at the Nuclear Resonance beamline Rüffer and Chumakov (1996) (ID18) at the European Synchrotron Radiation Facility (ESRF) using the synchrotron Mössbauer source (SMS, Potapkin et al, 2012). The SMS is the pure nuclear reflection of a $^{57}FeBO_3$ crystal mounted on a velocity transducer and operated in sinusoidal mode. The SMS is linearly polarized due to polarization of the synchrotron radiation. The average beam spot size for these experiments was $15 \times 20\,\mu m^2$. The line width of the SMS was controlled before and after each measurement using the reference single line absorber ($K_2Mg^{57}Fe(CN)_6$). The Mössbauer spectra were fitted using *MossA* software (Prescher et al, 2012), version 1.01a. The transmission integral fit was used assuming a Lorentzian-squared line shape of the SMS. All center shifts were calibrated relative to α-Fe at ambient conditions.

XRD experiments were performed on the Extreme Conditions Beamline P02.2 at PETRA III, Hamburg, Germany (PerkinElmer XRD1621 flat panel detector, $\lambda = 0.29$ Å) and on the 13-IDD beamline at the advanced photon source (APS), Chicago, USA (MAR165 CCD detector, $\lambda = 0.33$ Å). The beam spot size were $5 \times 8\ \mu m^2$ and $3 \times 4\ \mu m^2$, respectively. The powder diffraction patterns were collected during continuous ω rotation of $\pm 35°$; for

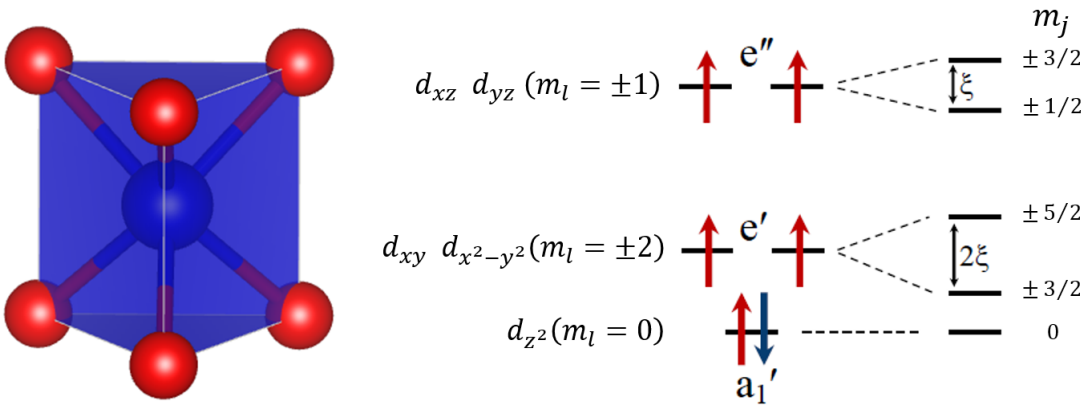

Figure 2. Crystal field splitting in a trigonal prism, the z-axis is collinear to the 3-fold axis of the trigonal prism. Note that in case of the high-spin state of d^6 configuration there is a competition between ${}^5E'$ and ${}^5A_1'$ electronic terms for the ground state because of the spin-orbit splitting of e' level.

single-crystal structure refinement the step scans were collected by ω-scanning in the range from $-35°$ to $+35°$ with $0.5°$ step. Data integration and absorption corrections were performed with CrysAlisPro software version 171.38.43. Structure refinement was done using the JANA2006 (Petříček et al, 2014) version from 25.10.2015.

3 Results and discussion

3.1 Change in the ground state of the A-site Fe^{2+}

In discussion of the possible spin states of the Fe_A^{2+} the crystal field splitting scheme of the cuboctahedron is used in literature (Lin et al, 2013). However, the real coordination polyhedron of the bridgmanite A-site is a bicapped trigonal prism which has considerably different splitting scheme of the d-orbitals. Let us approximate crystal fields splitting of the A-site by trigonal prism (Huisman et al, 1971, Fig. 2). The influence of two capping atoms can be considered as a small perturbation because of their longer Fe-O distances and be neglected in the first approximation. The validity of this assumption is supported by results of the molecular orbital analysis in Burdett et al (1978) where the obtained crystal field splitting scheme of bicapped trigonal prism is similar to the trigonal prism.

In agreement with previous Mössbauer studies at pressures above 30 GPa apart from the ambient Fe_A^{2+} doublet (violet in Fig. 3b) we observe appearance of a new doublet with high quadrupole splitting (> 3.7 mm/s, see Fig. 4a). As mentioned in the introduction there are

two interpretations of this component: an intermediate spin state of Fe_A^{2+} (Lin et al, 2008, McCammon et al, 2008) or Fe_A^{2+} in different local oxygen arrangement (Bengtson et al, 2009, Hsu et al, 2010).

Looking on Fig. 2, it is easy to see that spin transition of d^6 configuration should lead to LS state with $S = 0$ and appearance of any intermediate spin state is unlikely. However, the HS-LS transition can be excluded because both Fe_A^{2+} doublets with high and low quadrupole splitting (Fig. 4a) have the same center shift values. Recently, we show that beginning of the spin transition is directly related to the volume of the iron coordination polyhedron (Vasiukov et al, 2017). Therefore, because the metal-ligand distance and magnitude of the crystal field splitting are similar for both octahedral and trigonal prismatic coordination (Huisman et al, 1971), any spin transition in A-site with large Fe-O distances are unlikely at moderate pressures.

There is another possible electronic transition which can be responsible for the appearance of new Fe_A^{2+} doublet. The energy difference between a_1' and e' levels (Fig. 2) depends in a sensitive way on the geometry of trigonal prism (as D_{3h} point group allows arbitrary height of the trigonal prism). Moreover, crystal field of the trigonal prism does not quench orbital moment of the d-orbitals and e' level can be splitted by strong spin-orbit coupling with magnitude 2ξ (Fig. 2). As result, it is not self-evident which electronic term, $^5E'$ or $^5A_1'$, will be adopted as ground state.

Therefore, we conclude that the appearance of the Fe_A^{2+} doublet with high quadrupole splitting is related to the transition between these electronic terms. Such interpretation is in agreement with theoretical predictions (Bengtson et al, 2009, Hsu et al, 2010) because $^5E'$ term is a Jahn-Teller active state and, due to Jahn-Teller theorem, will have a different local ligand arrangement comparing to the non-degenerated $^5A_1'$ term. The difference in quadrupole splitting between these two terms can be enhanced by mixing of $3d$-orbitals (see Burdett et al, 1978).

3.2 *In situ* evidence of the iron disproportionation reaction

The abundance of bridgmanite and its strong preference to accommodate Fe^{3+} make the redox reaction generating trivalent iron important for the composition of lower mantle. For instance, the proposed 1 wt.% Fe metal in lower mantle (based on multiavnil experiments, Frost et al, 2004) is a reduced product of the Fe^{2+} disproportionation. However, multianvil press does not provide a closed system with respect to oxygen so the Fe metal could be reduced by some other agent. The DAC is a closed system and appearance of metallic iron

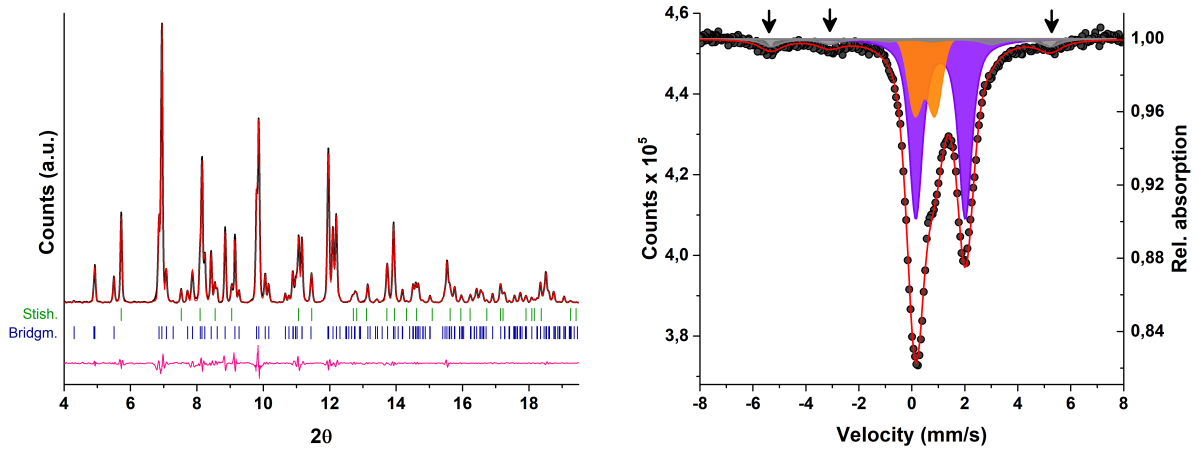

Figure 3. Powder XRD pattern and Mössbauer spectrum of the decompressed sample synthesized from reduced glass at 35 GPa and 2500 K. While the bridgmanite dominates diffraction pattern, the first two peaks of stishovite, (110) and (101), are clearly visible. On the Mössbauer spectrum, apart from Fe^{2+}_A and Fe^{3+}_A in bridgmanite (violet and orange doublets, respectively), one can see signal of α-iron (grey sextet). The evident sextet lines (1st, 2nd and 6th), which are not overlapped with bridgmanite components, are marked by arrows.

in synthesis of bridgmanite from reduced precursor would be a strong evidence of the Fe^{2+} disproportionation.

The disproportionation of ferrous iron in a simple ionic form is $3Fe^{2+} \rightarrow 2Fe^{3+} + Fe^0$. However, taking into account that we are dealing with Fe^{2+} in bridgmanite, the complete reaction is

$$3Fe^{2+}SiO_3 \rightarrow Fe^{3+}Fe^{3+}O_3 + 3SiO_2 + Fe^0 \quad (1)$$

and Fe^{2+} disproportionation produces 3 moles of stishovite for every mole of iron metal. Taking into account that the precursor is comprised by 90 % of $MgSiO_3$, the Fe metal should be the least abundant phase in the synthesized sample and difficult for identification.

In our experiments, the powder diffraction pattern of the samples synthesized from reduced precursor is dominated by bridgmanite and stishovite is also clearly visible (Fig. 3a). The presence of Fe metal could not be reliably established since its diffraction peaks would overlap with bridgmanite ones. The Rietveld refinement cannot be used in this case because laser heating in DAC produces polycrystalline sample with some preferred orientation.

The similar problem appears when one fit Mössbauer spectra of the synthesized sample at high pressures because the expected singlet of ε-Fe would totally overlap with strong bridgmanite signal. However, this problem can be overcome at decompression as Fe metal transforms to another allotrope, α-Fe, which is ferromagnetic with distinguishable magnetic

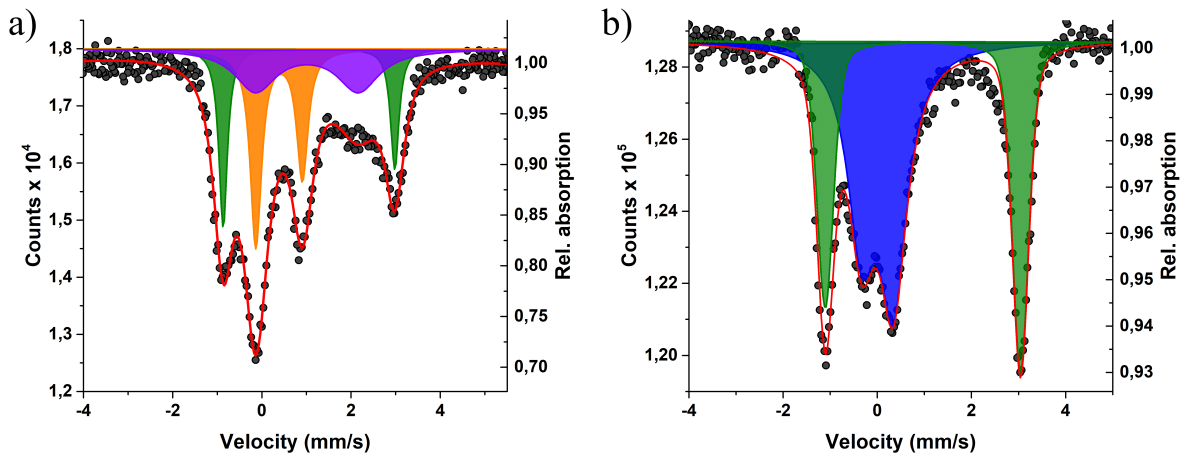

Figure 4. Examples of Mössbauer spectra of bridgmanite after synthesis at high pressures. These bridgmanites were synthesized from oxidized precursor at 45 GPa (a) and reduced precursor at 86 GPa (b). The green doublet corresponds to the different electronic term of Fe_A^{2+} (see text) while the blue doublet is low-spin Fe^{3+}, most likely in the B-site. The rest components conform to those in Fig. 3.

sextet. Indeed, on the Mössbauer spectrum of the decompressed sample one can distinctly see separate peaks of the α-Fe sextet (Fig. 3b). These results unambiguously confirm that the iron disproportionation produces Fe^{3+} in this case.

3.3 Evolution of the iron oxidation state with synthesis pressure

We were able to identify all products of the Fe^{2+} disproportionation in the syntheses from reduced precursor at pressures between 35 and 60 GPa. The Fe^{3+} content in the synthesized bridgmanite is rather constant in this pressure interval, about 20–25 % (Fig. 5). The experiments with oxidized glass around 50 GPa show that $Fe^{3+}/\Sigma Fe$ ratio is higher in this case than in bridgmanite synthesized from reduced glass (Fig. 5), but Fe^{3+} content is slightly decreases relative to the precursor value (from 47(3) to 37(4)%). This points out on the absence of Fe^{2+} disproportionation in this case and, indeed, stishovite peaks were not detected by XRD.

At pressures above 30 GPa the three-doublet model (two doublets correspond to Fe_A^{2+} in different electronic ground states and on doublet of Fe_A^{3+}, for instance see Fig. 4a) was sufficient to describe bridgmanite signal in Mössbauer spectra. However, the sample synthesized at 86 GPa (Fig. 4b) show spectrum that is quantitatively different from spectra of the samples synthesized at lower pressures. In this case the spectrum is superposition of only two doublets, one is the high-pressure electronic term of Fe_A^{2+} and another is a new doublet

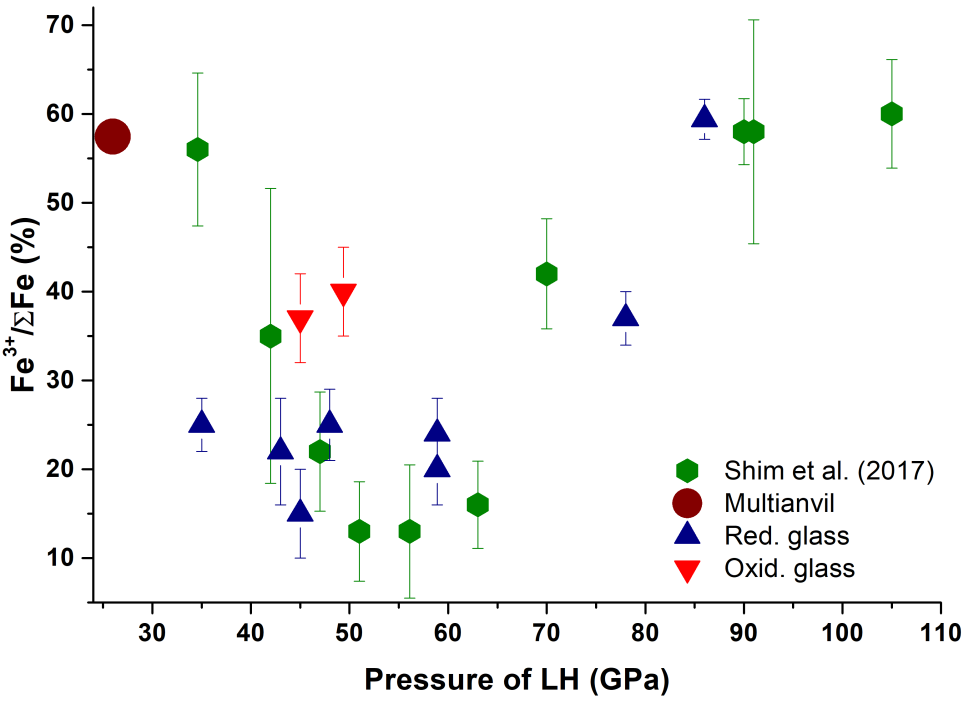

Figure 5. Dependence of the $Fe^{3+}/\Sigma Fe$ ratio in bridgmanite on the synthesis pressure. Our results are compared with data from Shim et al (2017). The multianvil point corresponds to the average Fe^{3+} content in bridgmanite synthesized from both oxidized and reduced glass in multianvil press at different oxygen fugacities. These results will be published elsewhere.

with $\delta_{CS} = 0.00(2)$ mm/s and $\Delta E_Q = 0.68(2)$ mm/s (at 87 GPa and RT) which was not observed at lower pressures. The doublet with similar hyperfine parameters was observed in McCammon et al (2010) after laser heating of majorite at 125 GPa and in Kupenko et al (2015) after laser heating of bridgmanite above 40 GPa. In the former work this doublet was interpreted as a LS Fe^{2+}_A, whereas authors of the latter work treat it as a LS Fe^{3+}_B.

The center shift of the blue doublet is lower by 0.35 mm/s than the corresponding value of HS Fe^{3+}_A around 50 GPa. The volume dependence of center shift cannot explain such big difference. According to results in Vasiukov et al (2017), center shift of 0.00(2) mm/s is too low to correspond with any electronic state of Fe^{2+}, even with its low-spin state, but it is close to characteristic values of LS Fe^{3+} in oxygen octahedron. As mentioned in introduction, the theoretical studies predict redistribution of ferric iron between A- and B-sites above 50 GPa (Hsu et al, 2012). Therefore, we interpret the blue doublet in Fig. 4b as LS Fe^{3+}_B in agreement with work Kupenko et al (2015).

This stabilization of LS Fe^{3+} together with redistribution of iron between A- and B-site apparently has a significant effect on the $Fe^{3+}/\Sigma Fe$ ratio in the synthesized bridgmanite

(Fig. 5). While our data show rather constant Fe^{3+} content between 35 and 60 GPa ($\sim$ 25 %) there is a clear increase of $Fe^{3+}/\Sigma Fe$ ratio above this pressure interval. Generally, our results are in agreement with recent work Shim et al (2017). However, authors of this study did not observe the doublet of LS Fe^{3+}_B at high pressures, so it is not clear whether increase of $Fe^{3+}/\Sigma Fe$ ratio above 60 GPa in our and Shim et al (2017) work has the same cause.

We also note that there is no space for ε-Fe singlet on the spectrum of the sample synthesized at 86 GPa (Fig. 4b) and we do not observe any sign of α-Fe in Mössbauer spectrum of the decompressed sample. In principle, Fe^{3+} in bridgmanite can be produced by another possible type of redox reaction where Mg, Al or Si are reduced with formation of bridgmanite with cationic vacancies. Any of these three compounds will be difficult to detect by powder XRD as strong bridgmanite signal should obscure their peaks. However, our powder XRD data show presence of stishovite which should not appear in such redox reactions. Therefore, the question regarding the redox reaction which produces the large amount of Fe^{3+} at pressures above 60 GPa remains open.

4 Conclusions

In this work we have studied evolution of iron electronic states in bridgmanite and how $Fe^{3+}/\Sigma Fe$ ratio depends on the synthesis pressure. We propose new interpretation for electronic transition of Fe^{2+}_A around 30 GPa, namely, that it is transition between different electronic terms with same spin quantum number. We unambiguously demonstrated that ferric iron is produced by Fe^{2+} disproportionation in case of synthesis from reduced precursor, identifying all products of this reaction *in situ*. In case of syntheses from reduced precursor the Fe^{3+} content in bridgmanite is constant (about 20–25%) up to 60 GPa and increases above this pressure. In synthesis at 86 GPa we observe appearance of LS Fe^{3+}_B that means redistribution of iron cation between A- and B-sites in bridgmanite structure. However, we did not find iron metal in this case and, therefore, the cause of increase in $Fe^{3+}/\Sigma Fe$ ratio above 60 GPa requires further experiments.

References

Aprilis G, Strohm C, Kupenko I, Linhardt S, Laskin A, Vasiukov D, Cerantola V, Koemets E, McCammon C, Kurnosov A, et al (2017) Portable double-sided pulsed laser heating system for time-resolved geoscience and materials science applications. Rev Sci Instrum 88(8):084,501

Bengtson A, Li J, Morgan D (2009) Mössbauer modeling to interpret the spin state of iron in (Mg,Fe)SiO_3 perovskite. Geophys Res Lett 36(15)

Boehler R, De Hantsetters K (2004) New anvil designs in diamond-cells. High Pressure Res 24(3):391–396

Burdett JK, Hoffmann R, Fay RC (1978) Eight-coordination. Inorganic Chemistry 17(9):2553–2568

Catalli K, Shim SH, Prakapenka VB, Zhao J, Sturhahn W, Chow P, Xiao Y, Liu H, Cynn H, Evans WJ (2010) Spin state of ferric iron in $MgSiO_3$ perovskite and its effect on elastic properties. Earth Planet Sci Lett 289(1-2):68–75

Dewaele A, Torrent M, Loubeyre P, Mezouar M (2008) Compression curves of transition metals in the Mbar range: Experiments and projector augmented-wave calculations. Phys Rev B 78(10):104,102

Dziewonski AM, Anderson DL (1981) Preliminary reference Earth model. Phys Earth Planet Inter 25(4):297–356

Fei Y, Ricolleau A, Frank M, Mibe K, Shen G, Prakapenka V (2007) Toward an internally consistent pressure scale. PNAS 104(22):9182–9186

Frost DJ, Liebske C, Langenhorst F, McCammon CA, Trønnes RG, Rubie DC (2004) Experimental evidence for the existence of iron-rich metal in the Earth's lower mantle. Nature 428(6981):409

Glazyrin K, Ballaran TB, Frost D, McCammon C, Kantor A, Merlini M, Hanfland M, Dubrovinsky L (2014) Magnesium silicate perovskite and effect of iron oxidation state on its bulk sound velocity at the conditions of the lower mantle. Earth Planet Sci Lett 393:182–186

Hsu H, Umemoto K, Blaha P, Wentzcovitch RM (2010) Spin states and hyperfine interactions of iron in (Mg,Fe)SiO_3 perovskite under pressure. Earth Planet Sci Lett 294(1-2):19–26

Hsu H, Yonggang GY, Wentzcovitch RM (2012) Spin crossover of iron in aluminous $MgSiO_3$ perovskite and post-perovskite. Earth Planet Sci Lett 359:34–39

Huisman R, De Jonge R, Haas C, Jellinek F (1971) Trigonal-prismatic coordination in solid compounds of transition metals. J Solid State Chem 3(1):56–66

Kantor I, Prakapenka V, Kantor A, Dera P, Kurnosov A, Sinogeikin S, Dubrovinskaia N, Dubrovinsky L (2012) BX90: A new diamond anvil cell design for X-ray diffraction and optical measurements. Rev Sci Instrum 83(12):125,102

Kupenko I, Dubrovinsky L, Dubrovinskaia N, McCammon C, Glazyrin K, Bykova E, Ballaran TB, Sinmyo R, Chumakov A, Potapkin V, Kantor A, Rüffer R, Hanfland M, Crichton W, Merlini M (2012) Portable double-sided laser-heating system for Mössbauer spectroscopy and X-ray diffraction experiments at synchrotron facilities with diamond anvil cells. Rev Sci Instrum 83(12):124,501

Kupenko I, McCammon C, Sinmyo R, Cerantola V, Potapkin V, Chumakov A, Kantor A, Rüffer R, Dubrovinsky L (2015) Oxidation state of the lower mantle: *In situ* observations of the iron electronic configuration in bridgmanite at extreme conditions. Earth Planet Sci Lett 423:78–86

Kurnosov A, Kantor I, Boffa-Ballaran T, Lindhardt S, Dubrovinsky L, Kuznetsov A, Zehnder BH (2008) A novel gas-loading system for mechanically closing of various types of diamond anvil cells. Rev Sci Instrum 79(4):045,110

Kurnosov A, Marquardt H, Frost D, Ballaran TB, Ziberna L (2017) Evidence for a Fe^{3+}-rich pyrolitic lower mantle from (Al, Fe)-bearing bridgmanite elasticity data. Nature 543(7646):543

Laskin A, Laskin V (2011) πShaper–refractive beam shaping optics for advanced laser technologies. In: J. Phys.: Conf. Ser., IOP Publishing, vol 276, p 012171

Lauterbach S, McCammon C, Van Aken P, Langenhorst F, Seifert F (2000) Mössbauer and ELNES spectroscopy of (Mg,Fe)(Si,Al)O_3 perovskite: a highly oxidised component of the lower mantle. Contrib Mineral Petrol 138(1):17–26

Lin JF, Watson H, Vankó G, Alp EE, Prakapenka VB, Dera P, Struzhkin VV, Kubo A, Zhao J, McCammon C, Evans WJ (2008) Intermediate-spin ferrous iron in lowermost mantle post-perovskite and perovskite. Nat Geosci 1(10):688

Lin JF, Speziale S, Mao Z, Marquardt H (2013) Effects of the electronic spin transitions of iron in lower mantle minerals: Implications for deep mantle geophysics and geochemistry. Rev Geophys 51(2):244–275

McCammon C (1997) Perovskite as a possible sink for ferric iron in the lower mantle. Nature 387(6634):694

McCammon C, Kantor I, Narygina O, Rouquette J, Ponkratz U, Sergueev I, Mezouar M, Prakapenka V, Dubrovinsky L (2008) Stable intermediate-spin ferrous iron in lower-mantle perovskite. Nat Geosci 1(10):684

McCammon C, Dubrovinsky L, Narygina O, Kantor I, Wu X, Glazyrin K, Sergueev I, Chumakov A (2010) Low-spin Fe^{2+} in silicate perovskite and a possible layer at the base of the lower mantle. Phys Earth Planet Inter 180(3-4):215–221

Murakami M, Ohishi Y, Hirao N, Hirose K (2012) A perovskitic lower mantle inferred from high-pressure, high-temperature sound velocity data. Nature 485(7396):90

Petříček V, Dušek M, Palatinus L (2014) Crystallographic computing system JANA2006: general features. Z Kristallogr - Cryst Mater 229(5):345–352

Potapkin V, Chumakov AI, Smirnov GV, Celse JP, Rüffer R, McCammon C, Dubrovinsky L (2012) The ^{57}Fe synchrotron Mössbauer source at the ESRF. J Synchrotron Radiat 19(4):559–569

Prescher C, McCammon C, Dubrovinsky L (2012) MossA: a program for analyzing energy-domain Mössbauer spectra from conventional and synchrotron sources. J Appl Crystallogr 45(2):329–331

Ricolleau A, Fei Y, Cottrell E, Watson H, Deng L, Zhang L, Fiquet G, Auzende AL, Roskosz M, Morard G, Prakapenka V (2009) Density profile of pyrolite under the lower mantle conditions. Geophys Res Lett 36(6)

Rüffer R, Chumakov AI (1996) Nuclear resonance beamline at ESRF. Hyperfine Interact 97(1):589–604

Shim SH, Grocholski B, Ye Y, Alp EE, Xu S, Morgan D, Meng Y, Prakapenka VB (2017) Stability of ferrous-iron-rich bridgmanite under reducing midmantle conditions. Proc Natl Acad Sci 114(25):6468–6473

Sinmyo R, Hirose K (2010) The Soret diffusion in laser-heated diamond-anvil cell. Phys Earth Planet Inter 180(3-4):172–178

Vanpeteghem CB, Angel R, Ross N, Jacobsen S, Dobson D, Litasov K, Ohtani E (2006) Al, Fe substitution in the $MgSiO_3$ perovskite structure: A single-crystal X-ray diffraction study. Phys Earth Planet Inter 155(1-2):96–103

Vasiukov DM, Dubrovinsky L, Kupenko I, Cerantola V, Aprilis G, Ismailova L, Bykova E, McCammon C, Prescher C, Chumakov AI, Dubrovinskaia N (2017) Pressure-induced spin pairing transition of Fe^{3+} in oxygen octahedra. arXiv preprint arXiv:171003192v1

Iron behaviour in Fe,Al-bearing bridgmanite between 35–80 GPa

Supplemental Material

D.M. Vasiukov*[a,b], J. van Driel[c], E. Bykova[d], M. Bykov[d], G. Aprilis[a,b], V. Cerantola[e], I. Kupenko[f], C. McCammon[b], A. Schönleber[a], K. Glazyrin[d], V. Prakapenka[g], H.-P. Liermann[d], M. Hanfland[e], A.I. Chumakov[e], L. Dubrovinsky[b], N. Dubrovinskaia[a]

[a]*Laboratory of Crystallography, Universität Bayreuth, Universitätsstr. 30, D-95447 Bayreuth, Germany*
[b]*Bayerisches Geoinstitut, Universität Bayreuth, Universitätsstr. 30, D-95447 Bayreuth, Germany*
[c]*Department of Earth Sciences, University College London, WC1E 6BT London, UK*
[d]*Photon Science, Deutsches Elektronen-Synchrotron, Notkestr. 85, D-22603 Hamburg, Germany*
[e]*ESRF-The European Synchrotron CS40220 38043 Grenoble Cedex 9 France*
[f]*Institut für Mineralogie, Universität Münster, Corrensstr. 24, D-48149 Münster, Germany*
[g]*Center for Advanced Radiation Sources, University of Chicago, Chicago, Illinois 60637, USA.*

*vasyukov@physics.msu.ru

Table 1: The Mössbauer parameters of iron cations in the synthesized bridgmanite samples at RT. The absence of the uncertainty means that the parameter was fixed. The Mössbauer spectrum of bridgmanite synthesized at 78 GPa also contains 25 % of iron hydride.

P, GPa		δ_{CS}, mm/s	Γ, mm/s	Area, %	ΔE_Q, mm/s	δ_{CS}, mm/s	Γ, mm/s	Area, %	ΔE_Q, mm/s	δ_{CS}, mm/s	Γ, mm/s	Area, %	ΔE_Q, mm/s
LH	Measur.												
		Fe_A^{2+}, HP ground state, high ΔE_Q				Fe_A^{2+}, ambient ground state				Fe_A^{3+}			
Oxidized precursor													
45	42	1.060(9)	0.30(4)	29(3)	3.83(2)	1.03(7)	1.1(2)	37(5)	2.1(2)	0.38(1)	0.34(4)	34(3)	1.05(3)
49.4	51.4	1.02(1)	0.23(5)	31(3)	3.70(3)	0.9(1)	0.6(2)	30(5)	2.3(2)	0.34(5)	0.34(7)	40(4)	1.1(1)
Reduced precursor													
35	10^{-4}	–	–	–	–	1.09(3)	0.60(3)	67(3)	1.87(5)	0.50(5)	0.64(4)	23(3)	0.75(10)
45	45	1.02(1)	0.22(4)	42(6)	3.82(2)	1.11(9)	0.7(3)	37(8)	1.9(2)	0.38(9)	0.24	14(4)	1.1(2)
43	48	1.02(1)	0.20(9)	33(6)	3.78(5)	1.14(5)	0.5(2)	34(8)	2.0(1)	0.38	0.3(2)	19(5)	1.05
48	48	1.05(2)	0.14(7)	22(3)	3.79(3)	1.21(4)	0.7(1)	40(3)	2.4(1)	0.38	1.1(4)	23(2)	1.05
59	59	1.04(1)	0.22(6)	19(3)	3.77(3)	1.09(2)	0.67(7)	53(3)	2.32(5)	0.55(3)	0.40(8)	19(2)	0.65(4)
59	59	1.04(1)	0.20(6)	19(3)	3.80(3)	1.2(4)	0.68(8)	48(3)	2.3(9)	0.4(9)	0.6(2)	22(2)	0.8
78	80	0.992(4)	0.15(2)	22(2)	4.14(1)	0.98(4)	0.8(2)	16(3)	2.8(1)	0.35(2)	0.52(6)	37(3)	0.99(3)
		Fe_A^{2+}, HP ground state, high ΔE_Q				Fe_A^{2+}, ambient ground state				LS Fe_B^{3+}			
86	88	0.969(5)	0.24(3)	41(2)	4.15(1)	–	–	–	–	0.00(2)	0.50(7)	59(2)	0.68(2)

(Eidesstattliche) Versicherungen und Erklärungen

(§ 9 Satz 2 Nr. 3 PromO BayNAT)

Hiermit versichere ich eidesstattlich, dass ich die Arbeit selbstständig verfasst und keine anderen als die von mir angegebenen Quellen und Hilfsmittel benutzt habe (vgl. Art. 64 Abs. 1 Satz 6 BayHSchG).

(§ 9 Satz 2 Nr. 3 PromO BayNAT)

Hiermit erkläre ich, dass ich die Dissertation nicht bereits zur Erlangung eines akademischen Grades eingereicht habe und dass ich nicht bereits diese oder eine gleichartige Doktorprüfung endgültig nicht bestanden habe.

(§ 9 Satz 2 Nr. 4 PromO BayNAT)

Hiermit erkläre ich, dass ich Hilfe von gewerblichen Promotionsberatern bzw. -vermittlern oder ähnlichen Dienstleistern weder bisher in Anspruch genommen habe noch künftig in Anspruch nehmen werde.

(§ 9 Satz 2 Nr. 7 PromO BayNAT)

Hiermit erkläre ich mein Einverständnis, dass die elektronische Fassung meiner Dissertation unter Wahrung meiner Urheberrechte und des Datenschutzes einer gesonderten Überprüfung unterzogen werden kann.

(§ 9 Satz 2 Nr. 8 PromO BayNAT)

Hiermit erkläre ich mein Einverständnis, dass bei Verdacht wissenschaftlichen Fehlverhaltens Ermittlungen durch universitätsinterne Organe der wissenschaftlichen Selbstkontrolle stattfinden können.

…….
Ort, Datum, Unterschrift